TESIS DOCTORAL

Systematic Study of the Interaction between Ion Beams and Plasmas via Spatial-Temporal Simulations in the context of Nuclear Fusion by Ion Fast Ignition.

Pablo Rodríguez Beltrán

Julio de 2024 en Las Palmas de Gran Canaria

UNIVERSIDAD Ð LAS PALMAS Ð GRAN CANARIA
Departamento de Física
Programa de Doctorado en Calidad Ambiental y Recursos Naturales

Universidad de Las Palmas de Gran Canaria
Programa de Doctorado en Calidad Ambiental y Recursos Naturales
Escuela de Doctorado de la ULPGC

Lugar y fecha: Las Palmas de Gran Canaria, en julio de 2024.
Título de la tesis: *Systematic Study of the Interaction between Ion Beams and Plasmas via Spatial-Temporal Simulations in the context of Nuclear Fusion by Ion Fast Ignition.*
Doctorando: Pablo Rodríguez Beltrán
Directores: Dr. Juan Miguel Gil de la Fe & Dr. Rafael Rodríguez Pérez

Firma del doctorando:

Firma del director:

Firma del codirector:

Para mis padres y *familia*.

Agradecimientos

En primer lugar, quisiera dar las gracias al Dr. Juan Miguel Gil de la Fe, por su guía en lo académico, su persistencia y su apoyo en estos duros años. Sus enseñanzas me han dado una mejor perspectiva sobre cómo hacer ciencia, aprehender y asimilar las nociones de la física, así como afrontar la vida. Junto a Juan Miguel, quiero agradecer su dedicación al Dr. Rafael Rodríguez Pérez y a la Dra. Guadalupe Espinosa Vivas. Agradezco además al resto de miembros del departamento que han apoyado esta tesis.

A nivel científico y personal, quiero manifestar mi gratitud a los doctores Alexandre Vazdekis, Miguel Cerviño y Michael Beasley, además del resto de personal del IAC. Sus consejos y formación han permitido que pueda superar las dificultades que ha supuesto desarrollar esta tesis. Asimismo, por su inestimable ayuda en lo académico, debo mentar a Maitane Urrutia Aparicio, Isaac Alonso Asensio y Javi Sánchez Sierras, que más adelante volverán a ser mencionados por la amistad que guardamos.

El interés por la ciencia que me ha llevado a escribir esta tesis, no sería posible sin las muy tempranas enseñanzas de mis dos profesores de instituto, Carlos y David. Después, innumerables profesores del grado de Física, junto a aquellos del master SIANI, impidieron que esa llama se apagara. Se merece especial mención Claudia, porque sin ella no hubiera conocido a mi director de tesis.

Fuera de lo académico, mi familia, en especial mis padres, han sido responsables directos de que yo pueda estar donde estoy hoy en día. Me hubiera sido completamente imposible terminar la carrera, el master y este doctorado sin su respaldo. Su amor, cuidado y enseñanza son impagables. Os quiero mucho a los dos. El resto de mi familia se merece un cálido recuerdo también, entre ellos, Paloma, Mª José y Antonio, Tina y Paco, Pablo y Rosa María, Pedro y Sonsoles, Arturo y Pilar, Antuan, Patricia, Paquito, Pedro Jr., Carlos, Pilar, Amparos y Arturito. Todos estos allegados, y otros tantos más, se preocuparon

con mucho cariño por mí estos años. Por último, quiero dedicar un pensamiento a mis abuelos y Mª Cándida, que, allá donde estén, espero se sientan felices y orgullosos del trabajo que he hecho.

Como segunda familia, mis amigos han sido un apoyo fundamental durante estos años. En los momentos más oscuros me dieron un rayo de luz y me cuidaron, muchas veces sin saberlo. El Café 7, con todos sus habitantes, ha sido un refugio más días de los que puedo recordar. Por ese motivo, me gustaría dedicar unas breves palabras de agradecimiento a las personas que me han aguantado en el día a día: a Esther y Fiti, que me introdujeron en este otro hogar y me han sacado las mayores sonrisas; a Davide, por enseñarme a ser más fuerte; a Betsa, por el vodka y las incontables risas; a Nerea, por la ternura que me infunde; a Sergio, por las lecciones de vida y llevarme la contraria; a Flor, por salvarme la vida en los meses más críticos; a Ángel, por esos abrazos que llenan; a Cris, por los mejores peores chistes que han rozado mis oídos; a Zoe, por ser el angelito que me distrajo de mis ansiedades siempre con una sonrisa; a Irene, que juega conmigo y me cuida a la vez; a Alejandro, por ser un hermano en música y espíritu; a David, por sacarme las mejores conversaciones cuando necesito salir de mi cabeza; a Adán, que sin él no podría hacer la defensa; a Zaida, por esa sonrisa que me alegra el día; a Fajardo, por la ligereza que me contagia; a Joa, que me amparó y dio cariño todo el tiempo que pudo y supo; a Abián, que me baja a la tierra con su sabiduría ancestral; a Pedro, Abraham, Agustín y Sergio, por sus consejos de vida; a Yisem, Brito, Val, Adrián, Alana, Marcos, Dodo, Pablo Humanes, Amanda, Hannah e Ingrid, porque tengo la tranquilidad de que puedo contar con ellos; a Cris y Tristana, que me obligan a ver el lado bueno de las cosas; a Paula, Sergio, Gema, Yeray, Laura, Lolo, María, que, por su forma de ver la vida, me enseñan como ser mejor; a Cuco y Amanda Leona, que me alegran el día cada vez que aparecen y me hacen las preguntas más curiosas; a Villo y Xclusifs, que son dos *rara avis* que tienen un corazón enorme con el que me han cuidado; a Jose Ramón, Diego y Semo, por ser compañeros de batallas cuando nadie más estaba; y como no me da tiempo ni imaginación para todos los que faltan, por el cariño que les tengo, quiero mencionar a Lena, Ale filólogo, Bea, Raquel, Clemente, Aarón, Gary, Elde, Dalila, Jorge, Joaquín, David-jefe, Pablo-piano, Jose, Víctor, Mehdi, M, Aday, Rocío, Candy y resto de criaturas de la noche.

Mis compañeros de armas, tanto de la carrera como del doctorado, se merecen una mención por el camino compartido. Me viene a la mente: Salva, Dani, Eduardo, Luis, Rafa, Paco, Pablo, Facu, Rubén, Guayente, Andrea, Ayoze, Laura Scholtz, Iveth, Maialen, Nuria, Rosa-el-amor-de-mi-vida, Isabel, Elham, Sarah, Tereza, Manolo, Raúl, Alessandra, Regina, entre otros. Recuerdo, también, a mis compañeros de la beca de verano del IAC, mis queridos Alberto,

Joanna, Nuria, Alessandra y Facu. De especial ayuda, tanto científica como personal, han sido: Isaac, Elena, Martín, los años compartidos con ellos no los olvidaré; Alberto, camarada indispensable en estos años de doctorado; Ricardo y Maitane, que me han dado esperanza cuando no sabía a quién acudir; y Fernando, que me ha enseñado una forma diferente y mejor de ver la vida. Finalmente, no pueden faltar Javi, Lore y Vega, una familia que me hace creer en que la vida puede ser mejor. En particular, Javi, te agradezco las decenas de horas hablando de física, filosofía y del corazón. Eres de las pocas personas con las que desnudo mi alma.

Sería desconsiderado olvidar a otros grupos que me han escoltado en esta senda. Durante mis años viviendo en Gran Canaria, la compañía de Paula, Alberto, Javi, Orlando y Wilmer fueron de especial apoyo. Del grupo de informáticos, que me presentó el bueno de Ray, he recibido mucha ayuda y cariño. Sin nombrar a todos, porque son muchos, me gustaría mentar a Néstor, Sebas, Rafa, Sergio, Andy, Jenni, Gabriela, Edu, Martita, Pablo, Elena, Nicole, Catu, Laura Brito, Sumaya, Cidoncha, Andrea, Yeray, David, Airam, Laura, Carla y el resto de L'Medines. Quiero recordar a los trabajadores del Malamutem: Mayara, Martín y Emma. Su comida y calidez me ha llenado en muchos días tristes, tanto la tripa como el corazón. El equipo y extrabajadores del Tintín también se han ganado un hueco en mi corazón, su amabilidad me ha acompañado en los últimos meses. A los raveros que han hecho que mi ilusión por la música no se extinga. Me acuerdo de Darwin e Indira, Raw, Miriam, Palmester, Mimosa y Portu, entre otros. Asimismo, mando un abrazo a Belimar, Pables, Alec, Cristina, Mel, Marta, Neli y Sonia. Como dedicatoria parasocial, numerosos artistas y creadores han llenado las largas horas de trabajo con su arte y gracia. Se lo agradezco sin mesura. En último lugar, pero no por eso menos importante, quiero agradecer a Víctor, que lleva a mi lado desde que tengo memoria, y a Joako, que ha sido como un hermano sin compartir sangre. Quizás no esté nombrando alguien que merece estar aquí. De ser así, lamento el olvido, pero estoy seguro de que os llevo en el corazón y querría que estuvierais aquí.

Por cada abrazo. Por cada sonrisa. Por cada lágrima. Por cada palabra. Por cada día. Muchas gracias a todos.

Pablo

Resumen

Desde el siglo pasado, la humanidad ha investigado e intentado alcanzar el difícil objetivo de crear fusión nuclear controlada, para así, acceder a una fuente de energía limpia y rentable. Con esta tesis, pretendemos continuar esta tarea, centrándonos, específicamente, en la fusión nuclear por confinamiento inercial mediante la técnica llamada "ignición rápida por iones" (*ion fast ignition*). La ignición rápida por iones consiste en aplicar un potente haz de iones para calentar e inflamar una cápsula de combustible de deuterio-tritio, precomprimida y en estado de plasma, creando así un punto caliente (*hot-spot*) que inicia la reacción de fusión. Separar las fases de compresión y calentamiento permite optimizar ambas de forma individual, así como ganar más control sobre la deposición de energía. Sin embargo, la ignición rápida con iones se enfrenta a varios retos que requieren un estudio más profundo.

Por consiguiente, en el contexto de la ignición rápida por iones, la contribución principal de esta tesis consiste en proveer un paquete computacional y un estudio sistemático de la interacción entre el haz de iones y el plasma en distintos escenarios de interés, así como un análisis sistemático preliminar de la ganancia conseguida tras la ignición. Para llevar a cabo este objetivo, hemos modelado una simulación espacio-temporal unidimensional de la deposición de energía del haz y del calentamiento del combustible. Con estos cálculos, podemos obtener la distribución de temperaturas del plasma, y, de ahí, extraer ciertas características clave que permiten describir el *hot-spot* creado y predecir de su evolución posterior. Presentamos resultados para una amplia gama de valores de interés, centrándonos en un plasma de deuterio-tritio en concentración equimolar. Es posible modelar este combustible para distintas temperaturas iniciales, densidades y radios, incluso, incluyendo las impurezas desprendidas de la cápsula a diferentes concentraciones. Asimismo, hemos considerado diferentes tipos de haces de iones, tanto monoenergéticos como cuasi-monoenergéticos, varias especies iónicas, distintos radios de haz, energías de proyectil y flujos.

En esencia, con este estudio exhaustivo de la ignición rápida, establecemos un vínculo entre las características del haz aplicado y el estado del plasma calentado tras la interacción. Esto es muy práctico en dos sentidos: a la hora de diseñar un experimento, podemos predecir el estado del plasma resultante o, por el contrario, si el objetivo es crear un tipo específico de *hot-spot*, podemos averiguar los parámetros de entrada necesarios, tanto para el haz de iones como para el plasma. Que sepamos, este enfoque no ha sido explorado profundamente en la literatura existente.

Abstract

Since the last century, humanity has researched and attempted the challenging goal of creating nuclear fusion in a controlled environment and, thus, accessing a clean and cost-effective energy source. In this thesis, we aim to continue this endeavour, focusing specifically on the scenario of inertial confinement nuclear fusion through the ion fast ignition approach. Ion fast ignition scheme uses a powerful, focused ion beam to rapidly heat and ignite a pre-compressed deuterium-tritium fuel pellet in a plasma state, creating a hot-spot that initiates the fusion reaction. By decoupling the compression and heating phases, it is possible to optimize both and keep control over the energy deposition. However, ion fast ignition encounters several challenges that require further study.

Therefore, in the context of the ion fast ignition scheme, the main contribution of this thesis is to provide a computational package and a systematic study of the interaction between the ion beam and the plasma in different scenarios, as well as a preliminary systematic analysis of the gain achieved after the ignition. This is carried out through a spatial-temporal one-dimensional simulation of the deposition of energy from the beam and the heating of the fuel. After this calculation, we retrieve the distribution of temperatures of the plasma, from which we extract key features to characterise the hot-spot created and the prediction of its posterior evolution. We present results for a wide range of values of interest, focusing on a deuterium-tritium plasma in equimolar concentration. This fuel can be modelled for various temperatures, densities, and radii, including impurities from the pellet at different concentrations. Additionally, we incorporate different types of fast ion beams, both monoenergetic and quasi-monoenergetic, across various ionic species, different beam radii, projectile energies, and fluxes.

In essence, our systematic and comprehensive study of the fast ignition, establishes a clear link between the characteristics of the applied beam and the

resulting plasma state. This is highly useful in two ways: when designing an experiment, we can predict the resulting plasma state, or conversely, if the goal is to create a specific type of hot-spot, we can provide the necessary input parameters, for both the ion beam and the plasma. To the best of our knowledge, this approach has not been extensively explored in the existing literature.

Contents

1

Introduction

From the earliest days of philosophy, some of the greatest minds in history contemplated the concept of matter in an attempt to define it. The ancient cultures already regarded matter as a vague notion: what remains beneath the changing appearances of the things of nature. The natural philosophy of atomism is of the most important ones in this sense, proposing that the physical universe is composed of fundamentally indivisible components known as atoms. This concept appeared in both ancient Greek and Indian philosophical traditions, such as Leucippus and Democritus (5th century BC, Destrée, 2003) and Kanada (6th century BC, Durant, 2011). Other philosophical currents considered the *elements* to be the foundations of the material world, namely fire, water, air, and earth. Empedocles considered that almost all things were composed of these four elements, while Aristotle claimed that atoms could not build up elements, as the latter were the prime and continuous material that remains (Aristotle & Aristotle, 1933). Conversely, Plato believed that elements were composed of different arrangements of atoms. Even further, he thought elements could not be the most basic level of reality, but something that were univocally unchanging, which he considered that should be mathematical. According to this theory, the properties of each element arose from the unique shapes, sizes, and movements of the atoms comprising them. For instance, fire was thought to consist of small, light, and fast-moving atoms, while earth was composed of large, heavy, and slow-moving atoms (Pohle, 1971; Cornford, 2014).

Later on, atomism was revived by rationalist Mechanicism in the 17th and 18th century, which provided the basic theoretical support for the birth of modern physical science. In the early 19th century, chemists and other natural philosophers observed experimental evidence of particles constituting chemical

matter. Initially considered indivisible, these particles were named "atoms" by Dalton (1817), drawing upon the longstanding concept from atomist philosophy. Consequently, the composition of atoms were discovered: electrons by Thomson (1897), atomic nucleus and protons by Rutherford (1911) and Rutherford (1919), as well as neutrons by Chadwick (1932). Despite the thin connection to ancient atomism, elementary particles have emerged as a contemporary counterpart to philosophical atoms. It is curious that, figuratively, some of the concepts that the ancient Greeks elaborated were not so far from the idea of primal building blocks that constitute most of observable reality. Their elements are also analogous to our currently defined states of matter: air would correspond to gas, water to liquid, earth to solid and fire to plasma.

Consequently, throughout the history of physics, the exploration of the physical properties of matter has consistently held a central position, serving as a cornerstone of the discipline. While the gas, liquid, and solid states are the most commonly encountered forms of matter, significant attention has been devoted to investigating the plasma state since the latter half of the twentieth century. The interest in this topic grew once this state of matter began to be identified (Crookes, 1879; Langmuir, 1928; Kamenetskii, 1972) and its utility for different applications discovered (Committee et al., 1995; Chu & Lu, 2013). Accordingly, contemporary history gathers numerous studies addressing plasmas, establishing it as the most abundant form of ordinary matter in the universe (Piel, 2010; Chu & Lu, 2013).

Plasma consists of both neutral components (such as atoms, molecules, neutrons, and photons) and charged components (including ions, free electrons, and protons). In such state, collective effects arise from the interactions between the particles of the system, leading to behaviours and properties at the macroscopic scale, that cannot be described by considering each element in isolation. Unlike gases, liquids, and solids, plasma does not naturally occur under ordinary conditions on the surface of the Earth; instead, it must be artificially generated through methods such as heating or the application of strong electromagnetic fields. In nature, plasma is primarily associated with phenomena such as stellar interiors and atmospheres, the rarified intracluster medium, and intergalactic regions. Additionally, plasma can be produced in laboratory settings and nuclear fusion facilities.

Figure 1.1 illustrates the various types of plasma based on temperature and free electron density, highlighting the extensive range of plasma phenomena observed in nature and subject to scientific inquiry. The study of plasma physics includes numerous lines of research, among which we are going to focus on the interaction between particle beams with high energy density plasma. In the particular case of this thesis, we work in the mainframe of a plasma thought

for nuclear fusion as an energy source, where densities are in the order of 10^{21} particles per cubic meter and temperatures that reach 10 to more than 1000 million Kelvin.

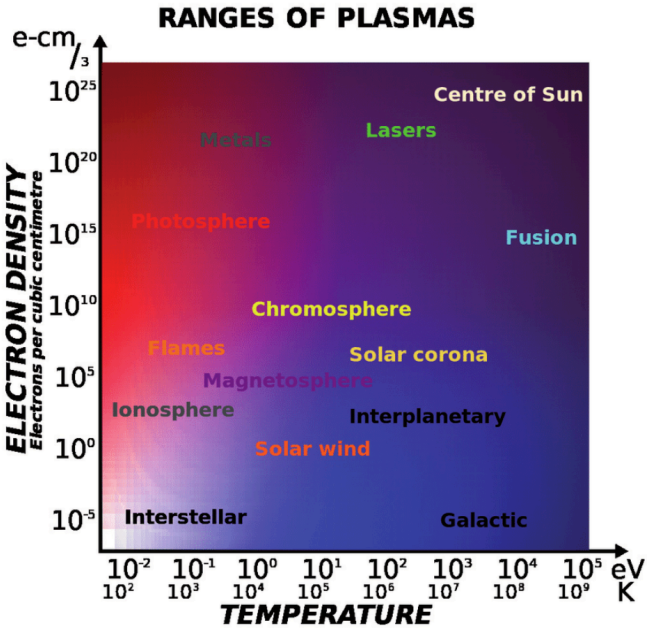

FIGURE 1.1— Diagram with the classification of plasmas depending on its temperature and free electron density. Source: Alam (2013).

The current world is in great need of an energy supply that can meet its escalating demand for energy. Fossil fuels, which have been relied upon for centuries, are both limited and harmful to the environment. Moreover, new ecological regulations further constrain the use of these traditional energy sources, as, for example, the 2023 United Nations Climate Change Conference. Considering these conditions, we have various unlimited options available. Among them, we find the nuclear fusion energy, breeder fission nuclear reactors, solar energy, wind power, hydropower and bioenergy, among others. While the latter four have been useful in reducing pollution from sources like fossil fuels and fission, they are unlikely to fully satisfy the global energy demand. On the other hand, fission breeder reactors produce extremely dangerous radioactive waste, posing significant risks if not managed properly. This leaves nuclear fusion as the most promising candidate for a future source of unlimited and clean energy.

In a fusion reaction, two lighter atomic nuclei combine to form other particles as byproducts. These byproducts include heavier nuclei and subatomic

particles (neutrons or protons), releasing enormous amounts of energy in the process. Two common proposed fuels for such reactions are isotopes of hydrogen: deuterium and tritium. Deuterium can be found in abundance in seawater, while tritium is harder to find naturally, although it can be produced artificially by, for instance, exposing lithium to energetic neutrons.

Luckily for humanity, the path for achieving such process has been already taken for decades. Since the early 1920s the concept of nuclear fusion was proposed and then associated to the generation of energy from stars (Eddington, 1979). Years after, experiments on Earth began to explore the possibilities of nuclear power, starting with the experiments associated to the fission atomic bomb and, later, the first artificial nuclear fusion detonation of the bomb "Ivy Mike" in 1952, triggered, in turn, by a fission weapon (established as Ulam-Teller process). Simultaneously, the civil and controlled used of both nuclear energies was being investigated. In 1942 the earliest fission reactor was achieved (Chicago Pile-1), then, a decade later, the first nuclear power plants were created. Similarly, the first nuclear fusion reactions were achieved in laboratories in the decade of the 1950s, along with prototype reactors. Subsequently, these reactors have significantly improved over the years[1]. Currently, net positive reactions have been accomplished, as well as transient or pulsed periods of net power (e.g. Woodward, 2022; Frank Fleschner, 2023). For the future, the challenge is to build nuclear plants of sustained nuclear fusion and, afterwards, demonstrating commercial viability as a cost-effective electricity source for the metropolis and the industry field.

In the quest for nuclear fusion, extensive research is being conducted to address the many obstacles that remain unsolved. Different fields contribute with their knowledge, including theoretical studies that describe accurately the plasma, computational simulations that predict the processes, experimentation in real reactors, production of the material to be fused, creation of containers capable of withstanding such high energies, and the drivers that ignite the plasma, among others. All these aspects are interconnected, functioning like gears in a mechanism, so collaboration is crucial to ensure success.

In this context, the current thesis focuses on one particular facet: among the various proposed methods for generating nuclear fusion in a reactor, one of them is known as inertial confinement fusion (ICF), where the plasma is compressed and heated. Within ICF, we explore an alternative technique that achieves ignition by applying a powerful final beam to the fuel. This approach is

[1]For a more detailed narration of the history of nuclear power, some recommended literature could be, for example, Char & Csik (1987); Segre (1989); Bodansky (2007); Stacey (2010); Rhodes (2012); Stacey (2018) and Barbarino (2020).

generally called fast ignition (FI) or ion fast ignition (IFI) if ion projectiles are applied. In FI, the compression and heating phases are decoupled, optimising the energy deposition and the control over fusion reactions. However, FI faces challenges in achieving efficient energy transfer and compression of the fusion fuel. Although this scheme is not currently one of the most popular choices, studying the different pathways that could lead to successful nuclear fusion is of substantial importance. With this work, we model the interaction between the ion beam and the plasma, simulating how the fuel is heated, its primary characteristics, and its initial evolution. Through various scenarios, we present a systematic analysis of the plasma conditions after applying the beam and anticipate its progress. Thus, the bottom line objective of this thesis consists in determining the beam characteristics needed to achieve a heated plasma with certain properties. Simulating the connection between beam attributes and the resulting plasma is crucial for advancing FI.

To effectively present all the generated knowledge, this thesis is organized as follows: in Chapter 2, we provide a general review of the context of this thesis as described above; in Chapter 3, we then detail our model and study methodology; in Chapters 4, 5, 6, and 7, we derive numerous results under varying conditions utilizing our model, which are presented and discussed; finally, in Chapter 8, we present the conclusions.

2

Nuclear fusion overview and state of the art

This chapter collects the physical foundations necessary to describe the main processes that take place to obtain energy from nuclear fusion. We present the nuclear fusion reactions, the different schemes to achieve the nuclear fusion and, in particular, the ion fast ignition approach, which involves the ion beam, the plasma, and the interaction of both. Finally, the motivations, objectives and thesis outline are presented. It is mandatory addressing that this segment of the thesis synthesizes and builds upon the findings and insights from existing literature (among others, Atzeni & Meyer-Ter-Vehn, 2004; Fuentes, 2018), which we recommend consulting for delving further on the subject.

As outlined in the Introduction, a plasma is a compound of both neutral particles (atoms, molecules, neutrons, photons, etc) and charged components (ions, electrons, protons, etc), which present collective effects, such as large-range interactions. In this sense, a comprehensive analysis of the system from a physical standpoint would require a complete examination of both microscopic and macroscopic perspectives, as described below.

On one side, the microscopic description implies:

- The investigation of the internal atomic structure, focusing on the energy levels and wave functions of the ions influenced by the surrounding plasma. This involves solving the Dirac equation in a quantum relativistic scenario or the Schrödinger equation in a non-relativistic one.
- Determining the cross-sections (probabilities) and reactivity rates (num-

ber of processes per time) for each possible process. This allows calculating the collisional and radiative processes occurring within the plasma, such as ionizations resulting from electron or ion impacts, as well as the excitation of ions through photon absorption, among others.

- Examining of the populations of the various components within the plasma. This involves employing methods such as atomic kinetic transport or collisional-radiative equations to compute the spatial and temporal distribution of ion and atom populations across each charge state and ground and excited configurations. Additionally, it also encompasses the utilization of radiative transport equations to determine the energy distribution for photons.

- Describing of the dynamic interaction ions suffer within, this is, with other charged particles (electrons or ions) or external fields like electromagnetic fields. In such processes, the ions transfer energy to the surrounding plasma constituents, losing energy and slowing down, therefore, it is necessary understanding the types of collisions involved.

On the other side, the macroscopic description implies:

- Investigating the radiative properties of the plasma, based on the parameters determined in the microscopic analysis.

- Examining the state equations of the plasma concerning temperature and density variations, applying statistical physic principles.

- Analysing the spatio-temporal evolution of various fields, including temperature, density, and pressure, considering initial and boundary conditions. This study employs fluid mechanics principles, along with hydrodynamic equations interacting with electromagnetic radiation.

- Considering the slowing down of ions in plasma on a macroscopic level, such that, particle collisions, scattering, and collective plasma phenomena are described. The rate of ion slowing down depends on factors such as the ion energy, plasma density, temperature, or any other.

The preceding microscopic and macroscopic descriptions point out the extensive complexity of this study. Moreover, as the plasma is a compound of huge amounts of interacting particles, some equations to describe the system are coupled. As such, simulating plasma properties at high energy densities requires the development of complex theoretical models and their computation to

generate extensive databases under different conditions. These plasma properties entail the computation of an extensive array of atomic levels (approximately 10^5) and atomic processes (approximately 10^7). Additionally, it is mandatory to solve the set of coupled rate equations that determine the average ionization of the plasma and the population of atomic levels. This array of equations must be resolved for each plasma condition, including density and temperature, thus, approximately 10^3 profiles of plasma conditions are required for a hydrodynamic simulation. Consequently, employing certain approximations becomes necessary to disentangle these equations. This illustrates a comprehensive analysis of the system. However, our work does not necessarily address all the previous bullet points, as we focus on certain aspects relevant to fusion plasmas within the context of a fast ignition scheme. In our cases of study, the density and temperature of the plasma are such that all the particles are fully ionized. As a consequence, neither atomic structure nor kinetic are required for the investigation. In the following sections, we will provide a description of the physics involved.

2.1 Binding energy and nuclear reactions

The first point we should address is the origin of the energy of a nuclear reaction. In nuclear physics and particle physics, the strong interaction or strong nuclear force, is responsible for attaching neutrons and protons to create atom nuclei, by means of the "nuclear binding energy". This binding energy appears when finding that the mass of an atomic nucleus is lower than the combined masses of its constituent individual protons and neutrons. This difference is named "mass defect", and, for an atom of atomic number Z, atomic mass number A and atomic mass m, it is calculated as $\Delta m = Zm_{\mathrm{p}} + (A - Z)m_{\mathrm{n}} - m$ (m_p and m_n are the proton and neutron masses, respectively). As the mass can be categorised as energy, this discrepancy in mass can be calculated with the famous Einstein equation, $E = \Delta mc^2$, where E represents the nuclear binding energy, c is the speed of light, and Δm is the difference in mass.

For an exothermic nuclear reaction (either fission or fusion), it is necessary that the mass of the reactants is larger than the mass of the products, or, in other words, the binding energy of the products must be larger. In this sense, the energy released in the reaction is calculated as:

$$Q = \left(\sum_i m_i - \sum_f m_f \right) c^2, \tag{2.1}$$

being m_i and m_f the set of reactants and products, respectively.

A general description of a fusion reaction involves two reactants X_1 and X_2 to produce a more massive particle X_3 and lighter one X_4, as well as energy if the reaction is exothermic, so:

$$X_1 + X_2 \rightarrow X_3 + X_4 + Q. \tag{2.2}$$

Due to the law of conservation of momentum, the energy released during the reaction is attributed to products inversely proportional to their masses. It can be calculated by solving the set of equations $Q = 1/2 m_3 v_3^2 + 1/2 m_4 v_4^2$ and $Q = 1/2 m_\mathrm{r} v_\mathrm{r}^2$, being the reduced mass $m_\mathrm{r} = m_3 m_4/(m_3 + m_4)$ and the modulus of the relative velocity $v_\mathrm{r} = |v_3 - v_4|$.

In the particular case of the reaction that is considered in this work we have:

$$D + T \rightarrow \alpha + n + Q_\mathrm{DT}. \tag{2.3}$$

Here, the reactants, deuterium and tritium, are two isotopes of hydrogen with one proton and two and three neutrons in its nucleus, respectively. In this fusion process, the components are found in the form of a high temperature plasma, and, therefore, highly ionized. Consequently, the products are a neutron and an α-particle, this is, a helium nucleus consisting of two protons and two neutrons. Thus, taking into account the masses of every component:

$$\begin{cases} m_\mathrm{D} = 2.01355 \text{ amu}, \\ m_\mathrm{T} = 3.01605 \text{ amu}, \\ m_\alpha = 4.0026 \text{ amu}, \\ m_\mathrm{n} = 1.00867 \text{ amu}, \end{cases} \tag{2.4}$$

we find that $Q_\mathrm{DT} = 17.58$ MeV. Then, computing the pair of equations above, we find $Q_\alpha = 3.52$ MeV and $Q_\mathrm{n} = 14.06$ MeV.

Certain magnitudes are necessary for analysing the nuclear reactions. Among them, the cross-section, $\sigma_\mathrm{fus}(v)$, quantifies the likelihood of the reaction occurring for two particles. If the reactants have a distribution of relative velocities, $f(v)$, as in a thermal distribution, then, averaging over this distribution, with the cross-section and the velocities, returns the "reactivity" or "reaction rate"[1]:

$$\langle \sigma_\mathrm{fus} v \rangle = \int_0^\infty \sigma_\mathrm{fus}(v) v f(v) dv. \tag{2.5}$$

[1]Literature does not agree on denoting $\langle \sigma_\mathrm{fus} v \rangle$. For instance, in Atzeni & Meyer-Ter-Vehn (2004) and 'Nuclear fusion', Wikipedia contributors (2024), $\langle \sigma_\mathrm{fus} v \rangle$ is named "averaged reactivity" and the reaction rate (fusions per volume per time) is the reactivity times the product of the reactant number densities $n_1 n_2 \langle \sigma_\mathrm{fus} v \rangle$. On the contrary, in Gus'kov et al. (2011), $\langle \sigma_\mathrm{fus} v \rangle$ is referred as "reaction rate".

This represents the probability of reaction per unit time per unit density of the target nuclei. In this sense, Deuterium-Tritium (DT) is the most promising fuel for nuclear fusion in a reactor. It presents favourable cross-sections, while simultaneously presenting a highly exothermic reaction, releasing a significant amount of energy. Moreover, the DT reaction has the largest reactivity and its ignition temperature is relatively low compared to other fusion combinations. Additionally, it yields a large number of neutrons, which can sustain the fusion process and facilitate the breeding of tritium fuel from lithium. To illustrate this, we show some common controlled fusion fuel reactions, in Table 2.1, along with their respective energy release and their cross-sections at 10 keV and 100 keV. Furthermore, in Fig. 2.1 we show the cross-sections at the centre-of-mass energy and the reactivity as functions of temperature for different reactions (Atzeni & Meyer-Ter-Vehn, 2004).

Reaction	Q [MeV]	$\sigma_{\mathrm{fus}(10\,\mathrm{keV})}$ [10^{-24} cm^2]	$\sigma_{\mathrm{fus}(100\,\mathrm{keV})}$ [10^{-24} cm^2]
$D + T \rightarrow \alpha + n$	17.59	$2.72{\cdot}10^{-2}$	3.43
$D + D \rightarrow T + p$	4.04	$2.81{\cdot}10^{-4}$	$3.3{\cdot}10^{-2}$
$D + D \rightarrow^3 He + n$	3.27	$2.78{\cdot}10^{-4}$	$3.7{\cdot}10^{-2}$
$D + D \rightarrow^4 He$	23.85	-	-
$T + T \rightarrow \alpha + 2n$	11.33	$7.9{\cdot}10^{-4}$	$3.4{\cdot}10^{-2}$

TABLE 2.1— Main controlled fusion fuels with their energy release and their cross-section at 10 keV and 100 keV (source: Atzeni & Meyer-Ter-Vehn, 2004)

Among the examples provided, it is demonstrated that the DT reaction has the second-largest energy release, superior cross-section values, and the highest possible reaction rate. Besides DT, other fuels have been considered, named advanced (or alternate) fusion fuels, involving reactions between hydrogen isotopes and light nuclei (such as Helium, Lithium and Boron). Advanced fusion fuels offer certain benefits, and their characteristics might be comparable to those of the DT. However, burning such fuels appears exceedingly difficult, as they have higher ignition temperatures (Miley, 1982).

In this context, it is necessary to discuss the feasibility of obtaining and using the DT as a fusion fuel source. Most of the following information can be retrieved from Keçebaş & Kayfeci (2019).

On the one hand, deuterium is stable and abundant in nature. It is found in water, specifically in the form of heavy water (^2H_2O). However, heavy water is present in ordinary water at very low concentrations, with approximately one molecule of heavy water for every 6,400 molecules of ordinary water. Hence, the oceans serve as the largest source of heavy water on Earth. Nevertheless, due

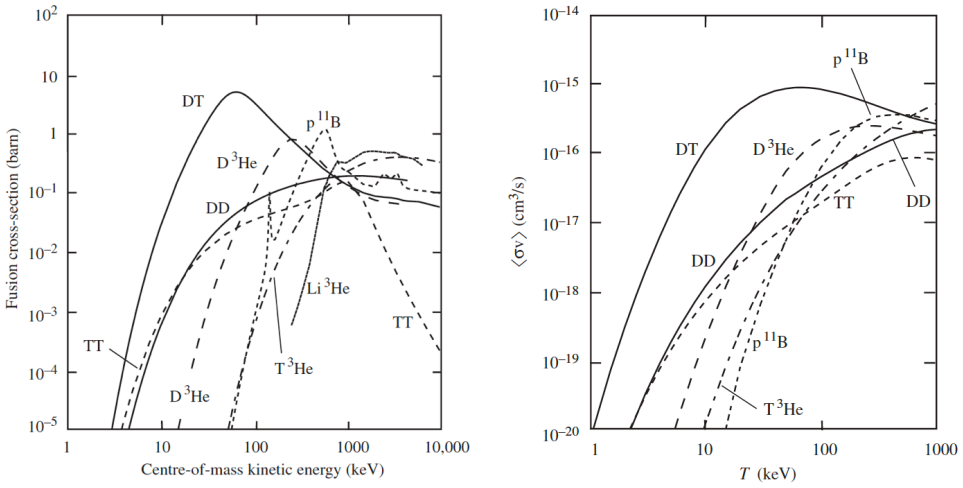

FIGURE 2.1— Left: Cross-sections (1 barn = 10^{24} cm^2) for fusion reactions relevant to controlled fusion energy as a function of the center-of-mass energy. The DD curve aggregates the cross-sections of different branches of the reaction. Right: Averaged reaction reactivity plotted against temperature for different controlled fusion reactions. Source: Atzeni & Meyer-Ter-Vehn (2004).

to its low concentration, heavy water must undergo extraction and purification processes to obtain deuterium in significant quantities. Heavy water is separated from common water through processes such as the Girdler sulphide process[2], differential distillation[3], or other methods (Waltham, 2002). Then, deuterium is isolated via electrolysis[4], being the overall reaction ${}^2H_2O \rightarrow 2H_2 + O_2$. Additionally, deuterium can be separated from ordinary hydrogen through isotopic separation techniques. One common method is differential distillation, which takes advantage of the slight difference in boiling points between deuterium and ordinary hydrogen. In this process, liquid hydrogen is repeatedly evaporated and condensed, with each cycle enriching the concentration of deuterium in the remaining liquid.

On the other hand, tritium, being a radioactive isotope with a half-life of

[2]The Girdler sulphide process is a method for the industrial-scale production of heavy water by catalytic exchange between hydrogen sulphide and water.

[3]The differential distillation process is a method for separating isotopes based on their different boiling points.

[4]Making an electric current flow through the water. At the cathode (negative electrode), water molecules gain electrons and are thereby reduced to form hydrogen gas. Conversely, at the anode (positive electrode), water molecules lose electrons and are oxidized to form oxygen gas.

$\sim$12.3 years, is not as easily found as deuterium. Tritium is mainly available in Earth's atmosphere in small amounts, formed by the interaction of gases with cosmic rays. Among other techniques, it can be produced artificially by irradiating lithium or boron plates (Vasaru, 1993). In this sense, it is common to retrieve tritium from nuclear reactors, where it appears as a low-abundance byproduct of the fission of lithium in breeder ceramics (Rubel, 2019). Another. less common, procedure to acquire tritium involves inducing deuterium to capture high-energy neutrons (Whitlock, 2010). Finally, the decay product of tritium, helium-3, can be converted back to tritium if it reacts with a neutron and expels a proton. The cross-section of this reaction is sufficiently large and can happen in nuclear reactors (MIT, 2004; Shea & Morgan, 2010). Regardless of the approach used, tritium needs to be separated later from the rest of products of their respective reactions through any necessary chemical process.

2.2 Schemes to achieve nuclear fusion

To achieve nuclear fusion reactions on Earth, aiming for a sustained energy production, different schemes have been proposed. Here, we present a collection of these schemes, classified by the method chosen for confining the plasma. Broadly speaking, there are two major branches in the field of controlled fusion: magnetic confinement fusion (MCF) and inertial confinement fusion (ICF). It is worth noting that MCF has a longer tradition in Europe and Asia, while ICF is typically associated with the United States of America.

2.2.1 Magnetic confinement fusion

The magnetic confinement fusion scheme uses magnetic fields to confine fusion fuel in the form of a plasma. In this case, sets of coils are distributed in a toroid shape to create magnetic fields that trap the ions and the stripped electrons in currents. The components of the fuel are forced to follow the field lines without touching the walls of the container, reaching temperatures of millions of degrees and fusing. Two of the most historically relevant schemes within MCF are the Stellarators and the Tokamaks, which will be explained as follows.

2.2.1.a Stellarators

Stellarators were one of the pilot approaches for MCF, proposed by Spitzer (1951), based on non-circular bent sections following a helix shape around the central line of the toroid (see left panel from Fig. 2.2). In theory, this configuration should prevent the particles from drifting away in each revolution of the circuit, keeping the plasma continuously circulating. Some experimental attempts were carried out during the decade of the 1950s, but the idea was

progressively abandoned due to its complex shape and a lack of efficiency, in favour of Tokamaks (see next section). This design has been retaken again in 2015, with, for instance, the innovative use of Wendelstei 7-X reactor from Germany, the Helically Symmetric Experiment (HSX) in the US, and the Large Helical Device in Japan. The advancements of technology, as the use of superconducting magnetic coils, aim to achieve intrinsic stability without relying on plasma current, making them potentially more stable for long-duration plasma confinement. In fact, on February of 2023, Wendelstein 7-X achieved a significant milestone by generating a plasma that reached for the first time an energy turnover[5] in the order of gigajoule units during eight minutes (Frank Fleschner, 2023).

2.2.1.b Tokamaks

Tokamaks and Stellerators both employ a similar concept to keep the plasma flowing in the circuit. The first designs of Tokamaks date back to the late 1960s in the Soviet Union. The main difference is that Tokamaks typically rely on the plasma current induced by the toroidal magnetic field to help confine and stabilize the plasma, instead of being inherently stable as the Stellerators. Additionally, Tokamaks present a simpler geometry and construction, where instead of considering spiralled or torsed coils, a non-circular flat cross-section is used (see right panel from Fig. 2.2).

In the new millennia, Tokamak-type reactors have been the spearhead of nuclear fusion research, as a leading candidate for a practical fusion reactor (Freidberg, 2008). Currently, ITER (International Thermonuclear Experimental Reactor) is one of the most ambitious Tokamak projects, presently under construction in Cadarache, France. It is supposed to reach unprecedented thermal power, greater than the injected thermal power. The timeline for ITER consisted on completing its construction and working with its first plasma by 2025, then start the operation of deuterium-tritium by 2035[6] (ITER, 2023).

Several prototype reactors have been built, such as: JET (Joint European Torus) at UK, being one of the largest reactors; WEST ("W" Environment in Steady-state Tokamak, formerly Tore Supra) located at the Cadarache facility in France, is designed to test and develop technologies for ITER; EAST (Experimental Advanced Superconducting Tokamak) in China and KSTAR (Korea Superconducting Tokamak Advanced Research) in Korea are both of the most

[5] The energy turnover is a result from the coupled heating power multiplied by the duration of the discharge. The energy turnover achieved, of 1.3 gigajoule, is associated to an average heating power of 2.7 megawatts, whereby the discharge lasted 480 seconds.

[6] Delays in this timeline were already warned and are set to be revised (World-Nuclear-News, 2023).

advanced Tokamaks reactors in Asia. Looking further into the future, DEMO is a proposed experimental reactor intended to demonstrate the net production of electric power from nuclear fusion by 2050 or later.

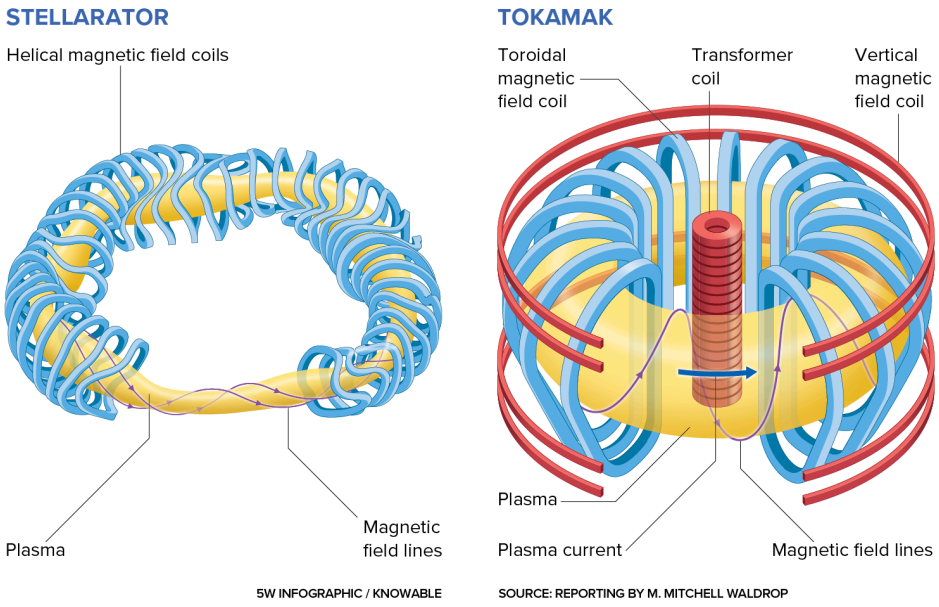

FIGURE 2.2— Structural representation of two MCF devices: Stellarator (left) and Tokamak (right). Source: Mitchell (2023).

2.2.2 Inertial confinement fusion

The inertial confinement fusion scheme consists of compressing a target shell or pellet of DT to a point of enough density and temperature for the fuel to ignite, then, burn and generate a small nuclear explosion. Generally, the container for the fuel is a sphere which is compressed by a set of beams (laser or particles) called *driver*. The energy from the driver is concentrated on the target outer layer, creating an explosion outwards. This produces an opposite reaction force in the form of shock waves that travel through the target. Sufficiently powerful shock waves compress and heat the fuel to induce fusion. The resulting burning emulates stellar conditions, briefly resembling the detonation of a thermonuclear bomb, albeit within a more controlled and less energetically intense environment compared to its military counterpart. In a nuclear plant, continuous energy production requires the replacement of each detonated shell with another, like a four-stroke engine:

1. Intake (of air and gasoline for a cylinder in an engine; of DT for a reactor).
2. Compression (of the air-gasoline mixture by the piston; of the DT fuel by laser beams).
3. Combustion of the compressed fuel (by the spark plug in an engine; by the final part of the implosion or other methods).
4. Exhaust (disposal of the remaining fuel and backwards movement of the piston; disposal of the reaction remnants, as well as the energy deposition created by the burning).

Then, the cycle repeats again (see Fig. 2.3). The nuclear energy released by each explosion should be absorbed by the walls of the reactor, which, with a cooling system, is used to create a traditional vapour cycle able to activate a turbine.

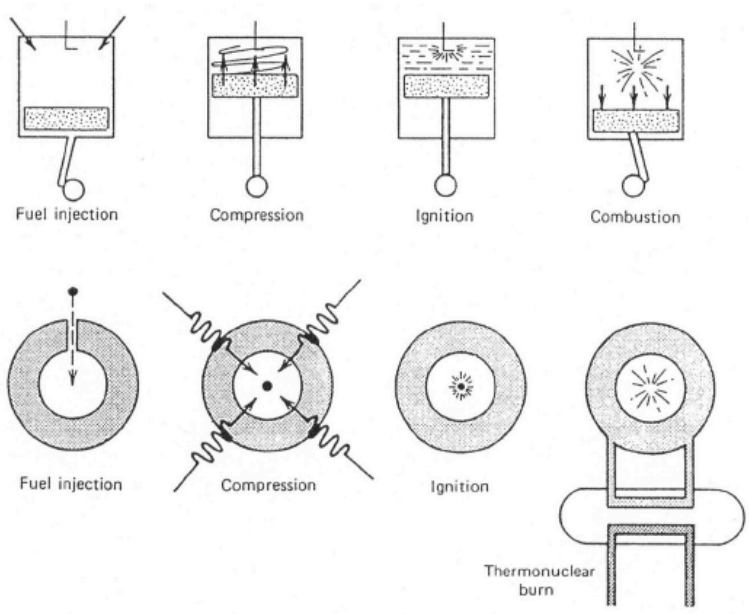

FIGURE 2.3— The analogy of a four-stroke sequence of a combustion engine of an automobile (top row) and the one of an inertial confinement fusion reactor (bottom row). Source: Duderstadt & Moses (1982).

Completing this process is not exempt of problems, most of them shared with the MFC approach (Guo, 2023). Heating and compressing the fuel up to temperatures so high that the thermal velocity of the nuclei is enough to

surpass the electrostatic repulsion is highly difficult and requires large amounts of input energy. Additionally, the pellet that contains the fuel should keep the nuclei gathered enough time for the fusion to occur without dismantling due to the extreme conditions. In the case of ICF, the drivers must be finely tuned, in order to compress the target symmetrically and avoid instabilities. Then, the components of the reactor should be resistant enough to withstand the high temperatures, intense radiation and neutron flux. This imposes stringent requirements on materials and engineering in order to avoid degradation over time. At last, the fusion process must release more energy than is required to sustain it, achieving a net energy gain, so there is a positive energy balance. None of these problems are present in the detonation of a thermonuclear weapon, where the fusion explosion begins with the detonation of the fission primary stage and then the energy is openly liberated. Thus, during more than half a century, effort have been made to confine the fuel, ignite and properly absorb the energy from the fusion.

In order to differentiate this scheme from others it is commonly named "standard ICF" and, as it is explained in the following subsections, it can be carried out in two modes: direct and indirect. In addition, in recent decades, two other ignition schemes have become relevant in ICF: shock ignition and fast ignition with electrons or ions. For a deeper understanding of the theoretical aspects of the ICF, we strongly recommend the book of Atzeni & Meyer-Ter-Vehn (2004). This thesis is framed within this context, focusing specifically on the Fast Ignition scheme based on ions (IFI), which is one of the methods employed to compress and heat fusion fuel for initiating fusion reactions. Some of these methods are explained as follows.

2.2.2.a Direct drive

Historically, the direct drive approach has been the primary method proposed within ICF, so it closely aligns with its most fundamental concepts. It originated in the 1960s but under classified status, only being declassified in the 1970s (Nuckolls et al., 1972).

In this scheme, the beams radially strike the spherical target to achieve uniform compression from all sides (see left panel of Fig. 2.4). Initially, lasers were proposed as the primary beams, with particle beams later suggested as an alternative driver. The fuel is contained within a thin capsule, absorbing energy from the driver beams. The vaporization of the capsule leads to an outward explosion of the shell, generating, in turn, an inward force pressure reaction. This compression should heat the target centre up to a sufficiently high temperature for the fuel to ignite. Subsequently, this ignition would initiate

a reaction that is expected to propagate from the centre to the entire sphere (Craxton et al., 2015; Campbell et al., 2021; Tao et al., 2023; Hu et al., 2024).

The initial concept of central hot-spot ignition represented a pivotal realization that inertial confinement fusion (ICF) could serve as a feasible pathway to achieving fusion, specially during the early 1970s, offering a relatively straightforward approach and a relatively simple arrangement. However, despite its promising potential, the development of this technology faced several challenges. Firstly, the process must be completed within an incredibly brief timeframe, typically less than a nanosecond, to avoid natural capsule disruption. Secondly, it is crucial to keep a uniform implosion, to prevent asymmetry arising from hydrodynamic diversions, such as Rayleigh–Taylor instability. Thirdly, the drivers must deliver high amounts of energy within minuscule areas and timeframes, constraining the size of the beams to an extremely narrow diameter (Atzeni & Meyer-Ter-Vehn, 2004). Lastly, meeting the demanding temperature and compression requirements of this approach has been proven difficult, as the energy input from the beams often exceeds the energy output from fusion, making it challenging to achieve significant gains. Several attempts have been carried out, as, for instance, the OMEGA experiments at the Laboratory for Laser Energetics (see Fig. 2.5) of the National Ignition Facility (Lawrence Livermore National Laboratory, USA; McCrory et al. 2001).

2.2.2.b Indirect drive

The indirect drive scheme appears as an alternative to the direct drive. In this approach, the fuel is located within a cylindrical container, typically made of gold and commonly denoted as *hohlraum*, with its top and bottom open. Instead of directly targeting the fuel, laser beams are pointed towards the unlatched top and bottom of the cylinder (see right panel of Fig. 2.4). The energy from the beams heats the interior walls of the cylinder until it re-emits X-rays that compress the capsule. These X-rays have a more uniform front, reducing the asymmetries of the implosion, and the beams can be larger and less precise. However, one of the main disadvantages of this approach is that much of the delivered energy is used to heat the cylinder, resulting in a lower end-to-end energy efficiency compared to direct drive.

Despite numerous attempts over decades, various projects employing this methodology did not achieve success until two pivotal experiments supervised by the National Ignition Facility (Lawrence Livermore National Laboratory, US) demonstrated its viability. These experiments, conducted in the winter of 2022 (Woodward, 2022) and the summer of 2023 (Wilson, Tom and Hancock, Alice, 2023), recorded the first-ever net energy production through nuclear fu-

sion. They produced more fusion energy than the energy input from the laser beams, achieving an efficiency on the order of 1%.

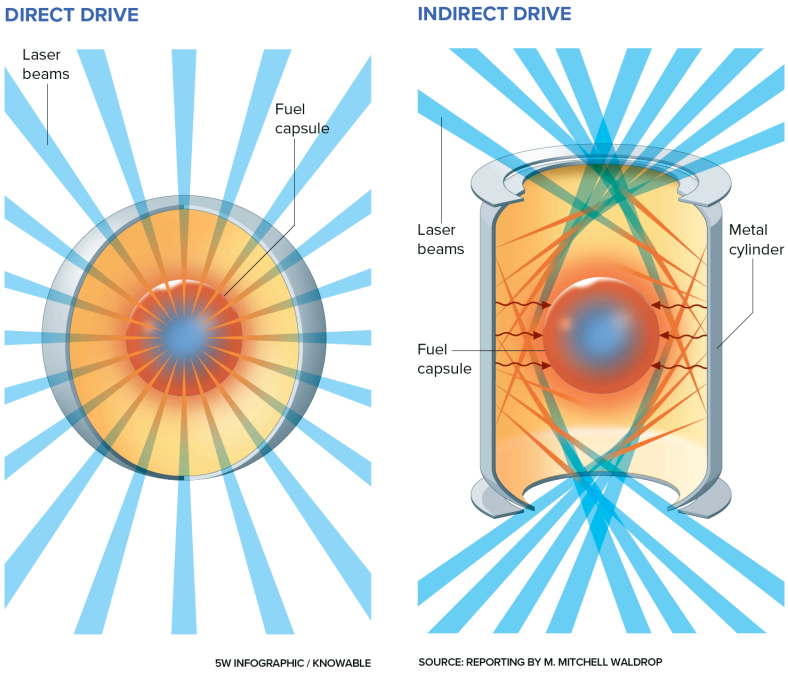

FIGURE 2.4— Visual representation of two ICF approaches: direct drive (left) and indirect drive (right). Source: Mitchell (2023).

2.2.2.c Shock ignition

Proposed by Betti et al. (2007), the shock ignition scheme resembles the direct drive approach until certain conditions are achieved in the plasma. The process is divided into two phases: first, a typical ICF early compression, similar to that of direct drive, followed by the application of an additional driver (such as a laser, electron beam, or similar pulse) to create a shock wave orders of magnitude stronger. This separation of the compression process from the final heating, where ignition is achieved, offers the advantage of reducing the compression requirements and utilizing more efficient energy deposition mechanisms. Additionally, some theoretical and experimental findings claim that these approach enhances ignition conditions (Theobald et al., 2008), as demonstrated, for instance, at the OMEGA Laser Facility (Rochester, New York, Ribeyre et al., 2011). An illustrative scheme of this approach is shown in Fig. 2.7.

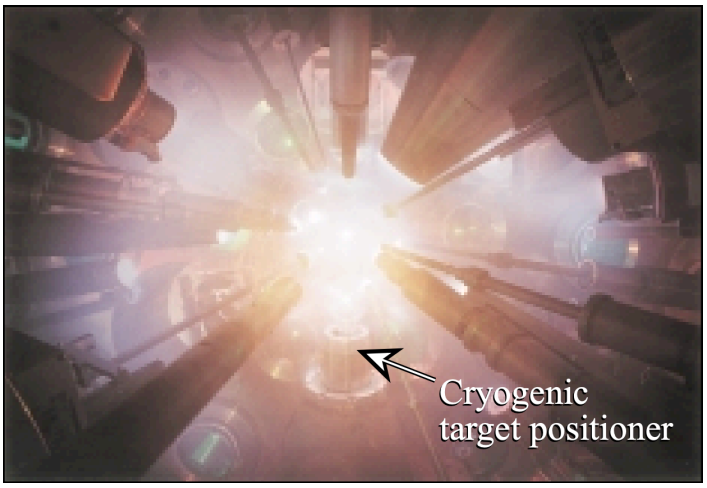

FIGURE 2.5— Photograph of the OMEGA target chamber. The "cryogenic target positioner" refers to a deuterium-filled capsule suspended by strands to minimize the mass of support structure mass and provide a relatively stiff positioning. Source: McCrory et al. (2001).

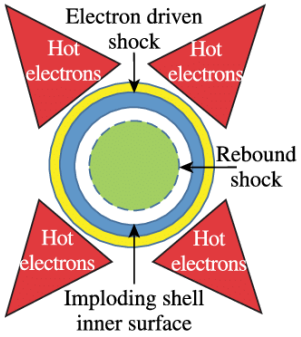

FIGURE 2.6— Visual representation of the shock ignition scheme (Shang et al., 2017).

2.2.2.d Electron or ion fast ignition

Fast ignition (FI) is a promising alternative for achieving nuclear fusion within the inertial confinement fusion (ICF) scheme (Tabak & Callaham-Miller, 1998; Roth et al., 2001; Roth, 2009). Given its significance, this work focuses on studying the ion fast ignition approach in detail. Similar to the shock ignition scheme, FI divides the fusion process into two distinct steps: compression and heating, each of which can be optimized independently. The steps of this process

are illustrated in Fig. 2.7.

First, the FI approach takes advantage of the ICF compression up to an optimal point of size and density, without excessively heating it. The compression pulse typically lasts for 10-15 ps, which is shorter than in direct drive. Following this phase, commonly referred to as "precompression", the majority of the fuel is found in a condensed and stagnated state, noted as the core (Kodama et al., 2001; Betti & Zhou, 2005). Additionally, the process generates a region of less dense plasma surrounding the fuel sphere, known as the corona. In this context, traditional direct drive methods would experience significant losses due to this surrounding plasma, thereby increasing the driver requirements.

Second, after this precompression phase, a powerful particle beam is used to provide additional energy directly to the core of the fuel. It is important to note that, in fast ignition, this relies on a separate and rapid heating pulse, while shock ignition primarily employs shock waves to achieve ignition. The beam applied creates a heated volume within the plasma. If any region of such volume is able to ignite the nuclear fusion process, then, the burning will start and spread to the rest of the fuel. The region capable of initiating the process is called "hot-spot".

Some approaches consider using a preceding laser pulse to dig the corona before the last beam shot. Alternatively, others propose using a cone embedded in the corona, enabling the beam to go directly into the denser core. A variation of this cone approach incorporates a small pellet of fuel at the apex of the device, initiating a preliminary pre-explosion that also moves inward towards the larger fuel mass.

Regarding the power beam, the original proposal for fast ignition (FI) involved an electron-based scheme (Tabak et al., 1994). However, it was limited by the high electron divergences, kinetic energy constraints and sensitivity (Robinson et al., 2008; Green et al., 2008; Debayle et al., 2010; Kemp & Divol, 2012). Meanwhile, FI by laser-driven ion beams, known as IFI, offers a much more localized energy deposition, a stiffer ion transport, with the possibility of beam focusing, and a better understood and controlled ion-plasma interaction (Tabak & Callaham-Miller, 1998; Roth et al., 2001; Roth, 2009; Tabak et al., 2014). At first, the proposed projectiles of the beam were light ions, such as protons. However, these ions deposit most of their energy at the edge of the fuel, resulting in an asymmetrical geometry of the heated plasma (Roth et al., 2001). Later, heavier projectiles were suggested. Their interaction with the plasma is semi-transparent at the edge, allowing for deposition of most of their energy in the centre of the fuel, which optimises a symmetrical propagation and explosion (Gus'kov et al., 2014a).

Initially, the ion beams studied exhibited a Maxwellian energy distribution.

However, recent advancements have led to the proposal of quasi-monoenergetic ion beams for IFI (Fernandez et al., 2009). Quasi-monoenergetic ions have several advantages over ions with Maxwellian energy distributions, such as a better coupling with compressed fuel (Honrubia et al., 2009) and the possibility to place the ion source far from the fuel without the need for re-entrant cones (Fernandez et al., 2009). Ion beams are often generated by irradiating plates of diverse materials and accelerating the detached ions. The ion beam used for the final ignition can be optimized, in order to achieve the desired conditions for the plasma and the burning, and to reduce system requirements. This scheme and its simulated results will be examined thoroughly from Chapter 3 to 7.

Currently, several research facilities worldwide are actively experimenting with Fast Ignition nuclear fusion, notably: the High Power Laser Energy Research Facility (HiPER), located across multiple institutions in Europe; GEKKO XII at the Institute of Laser Engineering (ILE) in Osaka, Japan; or the Laboratory for Laser Energetics (LLE) in Rochester, USA. Nonetheless, fast ignition faces its particular challenges, such as achieving an optimal deposition of energy in the target, avoiding unnecessary losses and properly transporting the fast electrons or ions through the plasma without creating divergences or instabilities (Guo, 2023).

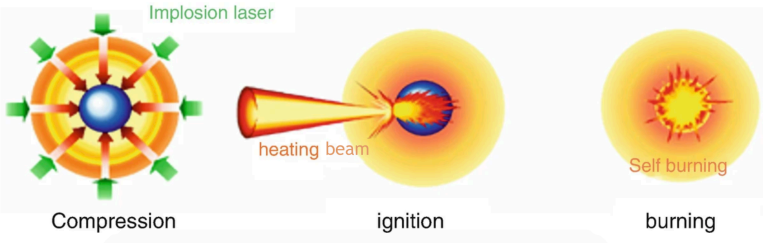

FIGURE 2.7— Visual representation of the steps in the FI approach (Moynihan & Bortz, 2023).

2.3 Detailed description of the ion fast ignition approach

This section offers a physical description of the target-projectile system and the posterior heated plasma forecast. Initially, we introduce the Hamiltonian governing the dynamic evolution of its particles. Subsequently, we provide a description of the system through different approaches of the dynamic model. We present the expressions governing the interaction between the beam and the previously discussed plasma, describing its behaviour in both temporal and spatial domains. Some of these ideas have been taken and revised from

Rodríguez-Beltrán (2018). Finally, we address the preliminary evolution of the plasma and its capacity to ignite and continue the burning.

2.3.1 IFI approach: the ion beam-plasma interaction

2.3.1.a Hamiltonian and dynamic equations

The fundamental point for modelling the interaction between a plasma and an ion beam (considering just a single projectile) is the Hamiltonian of the system. This Hamiltonian consists of a plasma target Hamiltonian term H_{T}, a non-relativistic projectile Hamiltonian term H_{P}, and its target-projectile potential energy interaction term $V_{\mathrm{P-T}}$, which is switched at a certain time with a step function $\theta(t - t_0)$, where t_0 is the instant when the interaction begins. The Hamiltonian is written as:

$$H = H_{\mathrm{T}} \; + \; H_{\mathrm{P}} \; + \; \theta(t - t_0) \cdot V_{\mathrm{P-T}} \; (\vec{\mathbf{R}}, \{\vec{S}, \vec{s}, \vec{\mathbf{s}}\}), \tag{2.6}$$

where:

$$H_{\mathrm{P}} = \frac{\mathbf{P}^2}{2m_{\mathrm{P}}} \quad \text{and} \quad H_{\mathrm{T}} = H_{\mathrm{CM}} + H_{\mathrm{bound}} + H_{\mathrm{free}} + H_{\mathrm{int}},$$

where $\vec{\mathbf{R}}$, $\vec{\mathbf{P}}$ and m_{P} are the position, the momentum and the mass of the projectile, respectively. The plasma coordinates are:

$$\{\vec{S}, \vec{s}, \vec{\mathbf{s}}\} = \{\vec{S}_1 ... \vec{S}_{N_i} \; ; \; \vec{s}_{1,1} ... \vec{s}_{1,N_{b,i}} \; ... \; \vec{s}_{N_i,1} ... \vec{s}_{N_i,N_{b,i}} \; ; \; \vec{\mathbf{s}}_1 ... \vec{\mathbf{s}}_{N_e}\},$$

these components can be associated with the coordinates of the ion mass centres ($\vec{S}$), the bound electrons of these ions ($\vec{s}$, relative to its mass centre), and the free electrons ($\vec{\mathbf{s}}$). Here, N_i is the number of ions in the plasma, $N_{\mathrm{b},j}$ is the number of bound electrons of the j^{th} ion and N_{e} is the number of free electrons. The Hamiltonian of the target plasma H_{T} is divided into four parts: the first two terms represent each ion system, which is divided into its mass centre (H_{CM}, usually approximated as the nucleus) and the bound electrons per each ion (H_{bound}), the third term represents the free electrons of the plasma (H_{free}) and the fourth term takes into account the interaction between the other three Hamiltonians (H_{int}).

Once the Hamiltonian has been introduced, the goal of this section is to describe the dynamics of the system. Because of the large number of particles in the plasma, the problem is highly complex, and as a result there are different possible approximations to solve the Hamiltonian given by Eq. 2.6.

On the one hand, the Hamiltonian could be approached within a molecular dynamic framework, that is, solving the Newtonian or Hamiltonian equations

of each component of the plasma and the beam. This should be computed simultaneously, as the equations are coupled due to the interactions. In this description, the dynamic equations for the i^{th} component of the system (whether the ions of the beam, ions of the plasma or the free electrons) are given in the Hamiltonian formalism by:

$$\dot{\vec{r}}_i = \frac{\partial H}{\partial \vec{p}_i}; \quad \dot{\vec{p}}_i = -\frac{\partial H}{\partial \vec{r}_i}. \tag{2.7}$$

Or, in the Newtonian formalism by:

$$\vec{F}_i = \frac{d\vec{p}_i}{dt}; \quad \vec{v}_i = \frac{d\vec{r}_i}{dt}, \tag{2.8}$$

where $\vec{r}_i$ and $\vec{p}_i$ are the position and momentum either of the beam or the plasma particles, and $\vec{F}_i$ represents the force over the i^{th} component due to the interaction with the rest of particles of the system. This detailed description would entail high computational costs due to the large number of coupled equations that need to be solved.

On the other hand, an alternative approach involves using a statistical description, which consists of solving the Liouville equation of the system. By doing so, it becomes possible to derive, from the Hamiltonian of Eq. 2.6, the probability density $\boldsymbol{\rho}(\{\vec{r},\vec{p}\},t)$ in the phase space $\{\vec{r},\vec{p}\}$ of the system. Thus, in a statistical context, the average of a magnitude $A(\{\vec{r},\vec{p}\},t)$ in a volume Ω of the phase space, can be calculated as:

$$\langle A\rangle_{\{\vec{r},\vec{p}\}} = \int_\Omega d\vec{r}_1...d\vec{r}_n\ d\vec{p}_1...d\vec{p}_n\ dt\ \boldsymbol{\rho}(\{\vec{r},\vec{p}\},t)\ A(\{\vec{r},\vec{p}\},t); \qquad (d\vec{r} = d^3r). \tag{2.9}$$

Expression 2.9 can be expressed in terms of the distribution function in the phase space of one particle, $f(\vec{r},\vec{p},t)$, defined as the integral of $\boldsymbol{\rho}(\{\vec{r},\vec{p}\},t)$ over all the coordinates except one. Also, it can be approximated from the kinetic or Boltzmann equations, where the correlations between three or more particles are despised. In the last case, the average of a magnitude could be calculated as:

$$\langle A\rangle_{\vec{r},\vec{p}} = \int_\Omega d\vec{r}\ d\vec{p}\ dt\ f(\vec{r},\vec{p},t)\ A(\vec{r},\vec{p},t). \tag{2.10}$$

Now that we have presented the possible descriptions of the system, we can select the most suitable one for the purposes of our problem. In this work, we focus on analysing the dynamic of the ion beam within the plasma. Thus, we will study the projectile under a classical deterministic dynamic description in the Newtonian formalism. Additionally, it is assumed that the particles of the beam do not interact with each other, and therefore, its behaviour is ruled

by its interaction with the plasma particles. This interaction yields a force ($\vec{F}_{T-P} = \vec{F}_i$) from the plasma acting on the i^{th} projectile, given by:

$$\vec{F}_{T-P} \equiv \vec{F}_i = -\vec{\nabla} V_i, \quad \text{with } V_i = \sum_j V_{T-P_{ij}}, \tag{2.11}$$

where $V_{T-P_{ij}}$ represents the potential experienced by the particle i^{th} of the ion beam due to its interaction with a j^{th} particle of the plasma.

In our model, this force (F_{T-P}) is considered as a statistical average over the plasma coordinates, in the context of Eq. 2.10, but in the phase space of the plasma. With this description, all the contributions from the plasma components to the interaction are averaged, avoiding large computational work. When studying the dynamics of the projectile, we focus on the change in its kinetic energy as it dives in the plasma. As explained in the next section, the variation of this energy is related to the averaged force mentioned early.

2.3.1.b Ion beam energy loss and stopping power

In the experiments that explore the interaction between an ion beam and a plasma, the ion projectiles gradually lose their energy as they penetrate the target plasma. Considering a point-like projectile (with its internal structure neglected) described by classical dynamics, a key observable for quantification is the kinetic energy loss ΔE of the projectile. This loss is empirically determined by comparing the energy of the projectile before and after passing through the plasma.

A much more detailed magnitude is the stopping power Sp, defined as the energy loss of the projectile per unit of path-length:

$$Sp = -\frac{dE}{ds}. \tag{2.12}$$

Assuming a classical dynamic description of the movement of the projectiles through the plasma, the latter expression can be written as:

$$Sp = -\frac{\vec{v}}{v} \cdot \vec{F}_{T-P}, \tag{2.13}$$

where $\vec{F}_{T-P}$ represents the decelerating force experienced by the ion due to its interaction with the plasma in a ds space region, as explained in the end of the previous Sect. 2.3.1.a (Eq. 2.11). Also, $\vec{v}$ is the velocity of the projectile before entering the ds region. A more detailed way of expressing Eq. 2.13, by using the theoretical context present in a previous section, includes the dependence on the coordinates and momenta of both the projectile and the plasma.

$$Sp\left(\vec{\mathbf{R}},\vec{\mathbf{P}},\{\vec{\mathbf{r}},\vec{\mathbf{p}}\},t\right)=\ \frac{\vec{v}(t)}{v(t)}\cdot\vec{F}_{T-P}\left(\vec{\mathbf{R}},\vec{\mathbf{P}},\{\vec{\mathbf{r}},\vec{\mathbf{p}}\},t\right), \tag{2.14}$$

where $\{\vec{\mathbf{r}}\}=\{\vec{S},\vec{s},\vec{\mathbf{s}}\}$ represents the coordinates of each particle of the plasma, and $\{\vec{\mathbf{p}}\}$ its associated momentum. Similarly, $\vec{\mathbf{R}}$ and $\vec{\mathbf{P}}$ are the coordinates and momenta of the projectile, respectively.

This expression provides the stopping of the projectile at a time "t", when it has a position $\vec{R}$, a velocity $\vec{v}$ (or momentum $\vec{P}$) and the plasma is in the state $\{\vec{\mathbf{r}},\vec{\mathbf{p}}\}$.

Our interest now is to express the stopping power as a magnitude where the plasma variables have been averaged, as discussed in the previous Sect. 2.3.1.a. Therefore, the stopping power in a t-instant, where the plasma parameters are averaged over $\{\vec{\mathbf{r}},\vec{\mathbf{p}}\}$, is:

$$\begin{aligned}Sp\left(\vec{\mathbf{R}},\vec{\mathbf{P}},t\right)=&\left\langle Sp\left(\vec{\mathbf{R}},\vec{\mathbf{P}},\{\vec{\mathbf{r}},\vec{\mathbf{p}}\},t\right)\right\rangle_{\{\vec{\mathbf{r}},\vec{\mathbf{p}}\}}\\ =&\frac{\vec{v}(t)}{v(t)}\cdot\left\langle\vec{F}_{T-P}\left(\vec{\mathbf{R}},\vec{\mathbf{P}},\{\vec{\mathbf{r}},\vec{\mathbf{p}}\},t\right)\right\rangle_{\{\vec{\mathbf{r}},\vec{\mathbf{p}}\}}.\end{aligned} \tag{2.15}$$

Here, $\vec{F}_{T-P}$ can be expressed in terms of the potential suffered by a projectile of the ion beam interacting with each plasma particle, as in Eq. 2.11. Then, we solve Eq. 2.15 by applying Eq. 2.10, finding the desired average over all the plasma:

$$\begin{aligned}&Sp\left(\vec{\mathbf{R}},\vec{\mathbf{P}},t\right)\\ &=\frac{\vec{v}(t)}{v(t)}\cdot\int_V d\vec{r}_1...d\vec{r}_n\int_0^\infty d\vec{p}_1...d\vec{p}_n\ f(\{\vec{\mathbf{r}},\vec{\mathbf{p}}\},t)\left(-\vec{\nabla}V_i(\vec{\mathbf{R}},\vec{\mathbf{P}},\{\vec{\mathbf{r}},\vec{\mathbf{p}}\},t)\right).\end{aligned} \tag{2.16}$$

In this sense, the proposal for a stopping model is reduced to the choice of how to define the interaction potential between the plasma particles and the projectile. After averaging over the plasma coordinates, the stopping is explicitly governed by the position and velocity of the projectiles at each instant $(\vec{\mathbf{R}}(t),\vec{\mathbf{P}}(t))$, so it is commonly expressed as $Sp(t)$. Moreover, it will have a parametric dependence on certain macroscopic parameters such as the free electron density, the atomic density, and the temperature of the plasma in the local ds region. This procedure is used to find the expressions of the stopping of the beam with the free electrons, bound electrons, and ions. In our model,

bound electrons are not considered, as the plasma is fully ionized. The free electrons and ion stopping are considered under a classical context.

A great number of stopping power models have been proposed in the last decades under different approximations, some of them of great utility to ICF modelling. The pioneering work of Bethe (1930), described the energy loss of charged particles (either relativistic or not) while travelling within matter. It accounted for all energy loss processes of the interaction by averaging over them. Numerous corrections and improvements have been applied to such model, depending on the considered conditions. Later on, the works of Bohm & Pines (1951); Pines & Bohm (1952) and Bohm & Pines (1953) introduced an approximation method for describing the dynamic linear electronic response, commonly known as Random Phase Approximation (RPA). In the RPA, electrons respond to the total electric potential, comprising both the external perturbing potential and a screening potential. The RPA model served as a foundation for subsequent models, such as the one presented by Maynard (1987), where the RPA approximation was applied to calculate the stopping of a non-relativistic ions by an electron fluid. More recently, the works of Peter (1991) and Peter & Meyer-ter Vehn (1991) (denoted PMV) proposed an electronic or nuclear stopping expression slowed by diverse material, based in the Bethe formula, within the classical statistic context of kinetic theory of gases. These works focused on the behaviour of ion projectiles with low velocity, which, as we show in Chapter 4, slow down drastically at the end of their penetration range. Afterwards, the stopping power of Li & Petrasso (1993a) and Li & Petrasso (1993b) (LP) was presented, becoming one of the most commonly used models in FI (e.g. Cayzac, 2013; Zou et al., 2016; Khatami & Khoshbinfar, 2020; Deng et al., 2021). The LP stopping power is able to consider the effects of large-angle scattering, small-angle binary collisions, collective plasma oscillation and it incorporates quantum effects, although all the previous are then adapted to classical formalism. The latter will be the model most frequently utilized in this thesis. At last, the model presented by Brown et al. (2005) (BPS) includes a rigorous treatment of a highly ionized dense plasma under the quantum mechanical theory and calculates the rate of energy loss of non-relativistic particles moving through it.

2.3.1.c Ion beam generation and characteristics

In the original proposal of FI the hot-spot was generated by ultra-relativistic electrons produced by the interaction of a powerful laser beam with the corona of the precompressed target (Tabak et al., 1994). Shortly after, rapid proton ignition was proposed (Roth et al., 2001), then heavier ions were considered too

(e.g. Hegelich et al., 2006). It is evident that demonstrating the feasibility of generating ion beams capable of meeting FI requirements is essential. Some of the most studied methods in this field are described below.

Maxwellian beams: Target Normal Sheath Acceleration

Discovered in the late 1990s, the ion-acceleration mechanism known as TNSA (short for Target Normal Sheath Acceleration) is probably the most studied one, both inside and outside the field of nuclear fusion (Fernandez et al., 2014; Roth & Schollmeier, 2017). This phenomenon occurs when a laser beam of high intensity (10^{19} - 10^{20} W/cm^2) is applied to a foil of solid matter, with a thickness of the order of micrometres. When the intense laser pulse interacts with the target material, it ionizes the atoms and creates a cloud of free electrons and plasma on the target surface, commonly referred to as the "sheath". As the electrons are liberated from the target material, they leave positively charged ions behind, causing the foil to become charged and preventing the electrons from dispersing.

The separation of charges within the plasma creates an electric field that exerts a force on the charged particles, causing them to accelerate away from the target surface. Thus, the sheath reflects part of the incident laser and also the particles of the foil inward. As a result of this reflection process, some charged particles inside the target are propelled forward with very high velocities, allowing them to reach higher energies compared to the initial thermal motion imparted solely by the laser or particle interaction. The high-energy particle beam generated by TNSA can consist of electrons or ions, and it is directed outward from the rear surface of the target. Moreover, in the area where the laser impacts the target, the gaps left by the accelerated electrons are occupied by a return current of cold electrons from the rest of the foil, which are heated by the laser and continue to replenish the sheath throughout the process duration. A schematic illustration of this process is shown in Fig. 2.8.

Experimental observations have revealed that the ion beams generated by TNSA follow an approximately Maxwellian energy distribution, so a temperature characterises them (Atzeni et al., 2002; Fernandez et al., 2014; Roth & Schollmeier, 2017; Zou et al., 2016). This implies that the kinetic energies of the ions have a wide variation, which in fast ignition requires the beam source to be installed close to the compressed fuel and often protected by a conical structure or other mechanisms. Otherwise, the temporal and spatial scattering that occurs during beam transport reduces the beam power, making ignition impossible (Atzeni et al., 2002; Fernandez et al., 2014). Other reports from literature have approximated the energy distributions as Gaussian-like, both experimentally (Afshari et al. (2020) and, according to Temporal (2006): Esirkepov et al.,

2002; Schwoerer et al., 2006; Hegelich et al., 2006) and in the simulation field (Tabak et al., 1994; Davis et al., 2011; Honrubia et al., 2009). Regarding ion beam focusing, the particle trajectory is, in principle, perpendicular to the back surface of the foil. Thus, using spherical cap-shaped foils enhances ion focusing the focusing. Any divergence from the beam trajectory could be corrected with the presence of a conical structure (Fernandez et al., 2014).

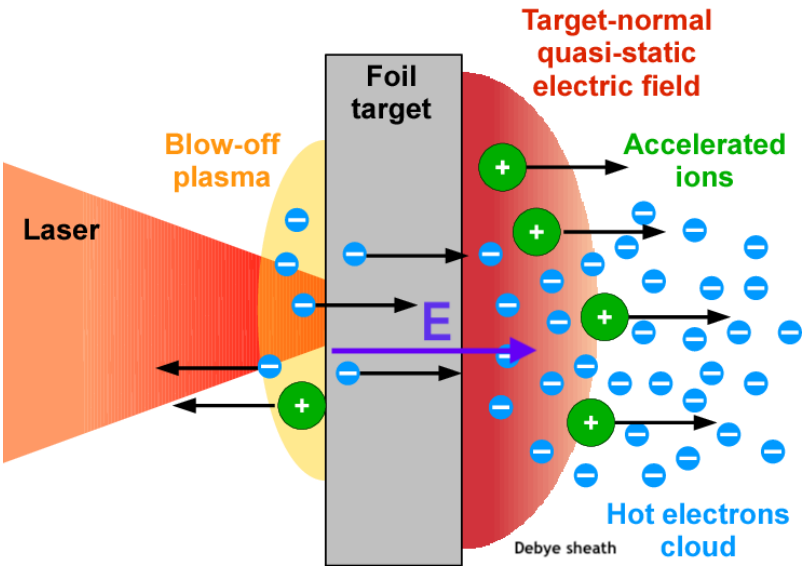

FIGURE 2.8— Illustrative example of TSNA scheme (Žáková, 2015).

Quasi-monoenergetic ions: Break Out Afterburner

A refinement approach of TSNA is the Breakout Afterburner (BOA), discovered through simulations by Yin et al. (2006). This approach involves two distinct phases of ion beam creation: an initial TNSA acceleration phase followed by an enhanced TNSA phase.

First, the dominant mechanism is the traditional TNSA explained in the section above. Then, the TNSA is strengthened with a more powerful pulse. Due to the thinness of the target, a large part of the electron population reach relativistic conditions for a short time. As a result, the plasma of the heated foil reaches relativistic induced transparency[7], so there are no cold electrons

[7]The frequency of a plasma ($\omega_P = (n_e e^2/m_e \epsilon_0)^{1/2}$) plays a role as a cut-off, where waves with lower frequencies than ω_P cannot propagate. In this context, a laser beam can penetrate a plasma up to a depth where the cut-off occurs, this is, where the frequency of the laser radiation (ω_L) becomes equal to the frequency of the plasma (in this case, the heated foil). However,

left in the target. The intense pressure of the laser pushes them in the direction of their propagation, resulting in a drift between ions and electrons. During this regime, the target becomes translucent to the radiation, allowing the laser to continue accelerating the electrons and consequently the ions, which have already separated from the foil. This mechanism is aptly named the Breakout Afterburner, as it bears resemblance to the afterburner systems found in some jet engines.

In Fig. 2.9 we show the phases considered in the BOA scheme, as explained above. As the projectiles are more directly accelerated by the laser pressure, the resulting ion beam resembles quasi-monoenergetic conditions. Thus, the ion-generating sheet can be placed farther away from the fuel, eliminating the complexity of cone-inserted capsules. Another remarkable feature of this mechanism is that, unlike TNSA, most of the laser energy is transmitted to the heavier ions in the foil.

Experimental generation of quasi-monoenergetic ion beams by BOA has been achieved at the Trident laser facility at Los Alamos National Laboratory (New Mexico, USA) (Jung et al., 2012, 2013a,b; Fernandez et al., 2014).

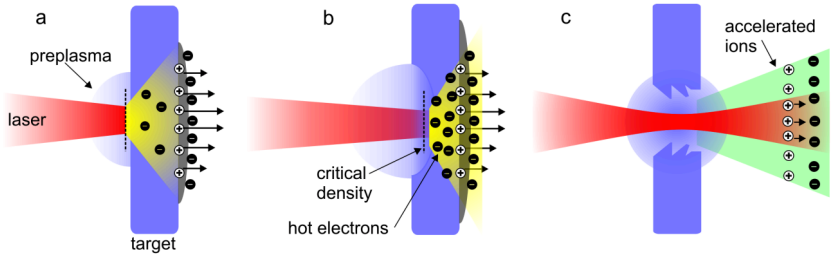

a) Target Normal Sheath Acceleration (TNSA) phase
b) Intermediate phase
c) Laser Breakout Afterburner (BOA) phase

FIGURE 2.9— Illustrative example of the phases that take place in the BOA scheme. Image taken from Roth et al. (2014).

when we consider interactions with intense laser pulses, the electrons can be accelerated to relativistic velocities, so their apparent mass increases by the Lorentz factor ($\gamma_e m_e$), and, consequently, the relativistic frequency of the plasma decreases as $\omega_P = (n_e e^2/\gamma_e m_e \epsilon_0)^{1/2}$. This means that, for a plasma with the same density, if the mean electron energy becomes relativistic, the plasma frequency is reduced and the medium becomes translucent, allowing previously cut-off radiation waves to propagate, which is known as transparent overdense regime (see, e.g. King et al., 2023).

Other methods of ion-beam generation

Apart from those described previously, there are other approaches that may allow the generation of ion beams with parameters suitable for fast ignition. The current status of these mechanisms, as well as those discussed above, can be found in the literature, for example, the review article by Fernandez et al. (2014) and the references therein.

- Ion Solitary Wave Acceleration (or ISWA, e.g. Jung et al. (2011)) also makes use of relativistically induced transparency, accelerating ions to high velocities by riding on solitary waves propagating through a plasma. Gaining energy by surfing on the wave crests creates quasi-monoenergetic ion beams.
- Radiation Pressure Acceleration - Light Sail (or RPA-LS, e.g. Liseikina & Macchi (2007)) transfers the moment from photons to a thin solid film, propelling its particles.
- Radiation Pressure Acceleration - Hole Boring (or RPA-HB, e.g. Macchi et al. (2005)) serves as a complementary mechanism. It uses intense laser pulses to create a tunnel through a plasma, allowing for efficient energy transfer and acceleration of ions along the tunnel axis.
- Collisionless Electrostatic Shock Acceleration (or CESA, e.g. Denavit (1992)) accelerates charged particles to high energies through the formation of electrostatic shocks in a plasma, without significant particle collisions playing a role in the acceleration mechanism. It has been described for opaque targets with certain critical densities.

Numerous questions remain unanswered about laser-plasma interaction processes at very high energy densities. The physics of the processes involved must be understood in greater depth to determine whether any of the above-mentioned mechanisms is possible to generate ion beams useful for fast ignition.

2.3.2 IFI approach: the heated plasma

For a detailed description of the heating process, first, due to an ion beam and then, and then, due to the posterior evolution of such plasma, acquaintance of the hydrodynamic and radiative transfer equations is required. This implies considering the equations that rule the conservation of energy, momentum and mass (given by Atzeni & Meyer-Ter-Vehn, 2004), and considering two fluids, electrons and ions. The simulations computed to solve such equations must be, at least, two-dimensional, to contemplate any possible asymmetry due to

hydrodynamic instabilities. However, as we detail in the next paragraphs, some considerations allow relaxing the demands when tackling this problem.

In situations where electromagnetic forces on individual plasma elements become as significant as hydrodynamic forces, Maxwell equations need to be incorporated into the equations of fluid mechanics to provide a comprehensive description of the phenomena under study. Additionally, the plasma must be treated as a mixture of electrons and ions, each with their corresponding fluid quantities. However, in many scenarios relevant to inertial confinement fusion (ICF), there is no significant charge separation, obviating the need to include the equations of electromagnetism in the modelling process. This condition is met when the Debye length (λ_{D}), a measure of the distance over which charged particles influence the electrical behaviour of a plasma, is much smaller than the free path of the electrons. This condition is generally fulfilled in FI conditions.

On the other hand, describing a plasma with fluid mechanics requires local thermodynamic equilibrium (LTE). In LTE conditions, a plasma exhibits high collisionality, rapid thermalization, homogeneity, and negligible radiative losses, allowing it to reach local equilibrium on a timescale adequate to the dynamics of the system. This can be validated by evaluating that the mean free path and the mean free time are smaller than the size and characteristic time of the problem being studied. Plasmas with low density or strong magnetic fields may not satisfy LTE conditions, such as optically thin plasmas or cases where the radiation emitted by the plasma can freely escape into vacuum. However, ICF plasmas commonly fulfil the LTE conditions due to their high densities and temperatures. Plasmas can be characterised by two temperatures: one for electrons and another for ions. Due to the significant difference in mass between the two (three orders of magnitude), ions are mainly responsible for the momentum transport, while electrons are primarily responsible for energy transport and conduction. In our case, ICF plasmas behave as a single fluid, with frequent collisions between its components leading to thermalization. Under this LTE conditions, ions and electrons are assumed to have the same temperature. The equilibrium between electrons and ions is assured when the plasma is not disturbed in the characteristic equilibrium time (τ_{eq}), such that there is no net energy exchange between both components. Throughout this work, the equilibrium time is mostly lower than the characteristic times associated to the projectiles of the beam, the hydrodynamic processes of the plasma or others. This allows the plasma to be described with a single temperature, since the components recover equilibrium faster in respect to the response from other interferences. This condition is explored further in Sect. 3.9.1.

Furthermore, when the nuclear fuel is compressed, generally by intense laser beams, for a brief period of time we find the plasma in an ideal confinement

equilibrium state. This is denoted as stagnated plasma and, moreover, the temperature and density fields can be approximated by uniforms distributions. At this point, the fuel has achieved a very high density but not enough temperature to initiate the nuclear fusion reactions. The time for which the stagnated state is maintained is given by confinement time, which is the ratio of the fuel sphere and the speed of sound $\tau_{\text{conf}} = R_{\text{F}}/c_{\text{s}}$, with $c_{\text{s}} = \sqrt{2k_B T/m_*}$, where m_* is the average mass of the fuel ions. This is the time available to generate a hot-spot in the plasma, with a time-sustained ignition and subsequent propagation throughout the plasma for the nuclear burn-up. In a typical experiment of a precompressed fuel with radius $R_{\text{F}} = 50$ μm and initial temperature of $T_0 = 1$ keV, the confinement time is $\tau_{\text{conf}} = 1.8 \cdot 10^{-10}$ seconds. This value is mainly larger than the characteristic time of internal processes of the plasma and beam interaction, as we present with more detail in Sect. 3.9.1.

Within the IFI scheme, during the stagnation phase the ion beam is applied to the fuel, creating a heated region after completing the interaction. Within this heated region, we study a zone of particular interest known as the "hot *spark*". If such *spark* is capable of beginning the ignition and posterior burning, we qualify it as "hot-spot". Ideally, this hot-spot should be as uniform and symmetric as possible in its temperature field, density distribution and location within the whole sphere, in order to achieve a burning that propagates symmetrically too. In the case of the standard ICF scheme, it is very important that the compression of the fuel is performed with a high spherical symmetry to minimise the occurrence of hydrodynamic instabilities. As a consequence, the hot-spot is mostly generated in the centre of the compressed nuclear fuel. However, in the IFI scheme, the requirements for compression with high spherical symmetry are relaxed, and situations where hot-spots occur at the edge or at intermediate points of the compressed nuclear fuel are also of interest. Nonetheless, a central hot-spot improves the performance, as it serves as an energy reservoir that can efficiently propagate energy to the surrounding fuel, minimize transport losses, and induce a symmetric explosion (Duderstadt & Moses, 1982; Gus'kov et al., 2014a). As we explain in Sect. 3.9, ion beams can create edge, intermediate and central hot-spots depending on the conditions of the beam.

In such modelling, we can consider two different scenarios for the core and the hot-spot (if achieved): an isobaric fuel, where the hot-spot has lower density, higher temperature and equal pressure than the rest of the sphere, or an isochoric fuel, where the hot-spot has equal density and higher temperature and pressure (see Fig. 2.10). In the direct drive ICF scheme, isobaric initial conditions are regarded as the standard configuration. This is due to their approximation of the conditions generated at the conclusion of the implosion of

the hollow shells driven and the shaped laser pulses. Conversely, in the ion fast ignition approach, the precompression is performed in such a way that both the density and temperature are uniform, so isochoric conditions are typically considered. Thus, in the IFI scenario, the heated region creates a higher inner pressure that continues to expand against the cold fuel.

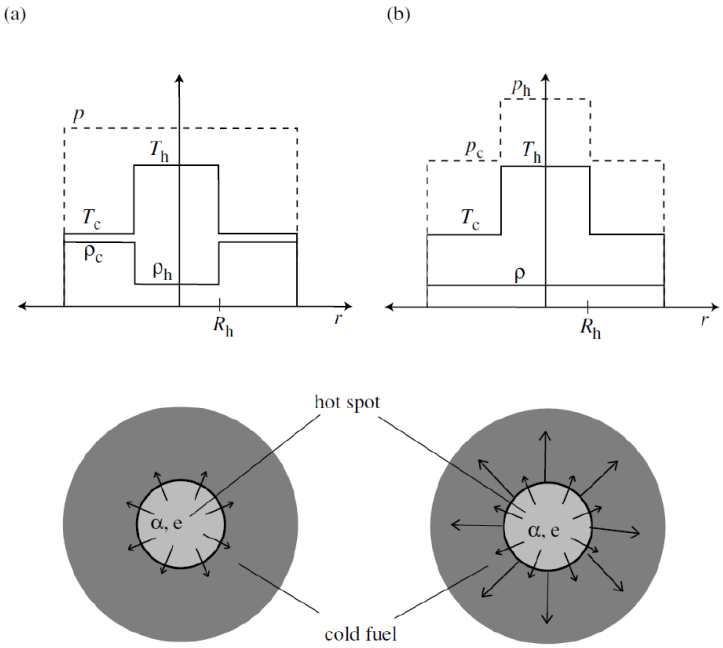

FIGURE 2.10— Schematic representation of the distribution of the fuel for a central *spark* in isobaric (a) and isochoric (b) scenarios. Source: Atzeni & Meyer-Ter-Vehn (2004).

Previous explanations point out how, for ICF plasmas, instead of performing highly complex simulations, other straightforward modelling can be applied. For example, there are zero-dimensional approximated models that allow describing appropriately some aspects of interest. This includes the generation of a small hot region by the ion beam (e.g. Gus'kov et al., 2010; Espinosa-Vivas et al., 2023), the early evolution of such a region, evaluating the nuclear ignition conditions for subsequent fuel burning (e.g. Atzeni & Meyer-Ter-Vehn, 2004; Gus'kov et al., 2011), or both simultaneously (e.g. Zou et al., 2016).

In particular, in this section, we focus on the zero-order criteria with which we can predict the posterior evolution of the plasma after the precompressed fuel is heated by the ion beam. These conditions have been well reported in the

literature, although they are still an important point of discussion (e.g. Fraley et al., 1974; Kidder, 1976; Atzeni & Meyer-Ter-Vehn, 2004; Tabak et al., 2006; Gus'kov et al., 2011; Gus' kov et al., 2017), but the scientific community accepts some considerations: the heated region can be characterised by the self-heating condition, the ignition condition and, if achieved, by the subsequent burning gain. In essence, the concepts presented below can be interpreted for both the isobaric case typical of the standard ICF and the isochoric case typical of the FI.

To begin with, let us present the self-heating condition as a simplified zero-order approach obtained by applying the energy conservation equation. It considers a spherical *spark*, determined by a temperature, a density and a radius, inscribed within a larger, cooler sphere of fuel. The rate of change in energy density of such region can be expressed as:

$$\frac{d\mathcal{E}(t)}{dt} = W_{\mathrm{fus,dep}}(t) - W_{\mathrm{mec}}(t) - W_{\mathrm{cond}}(t) - W_{\mathrm{rad}}(t), \tag{2.17}$$

where the W's terms are the power densities related to the fusion reactions that deposit energy in the heated volume ($W_{\mathrm{fus,dep}}$), the mechanical work (W_{mec}), the conduction (W_{cond}) and the radiation (W_{rad}) processes[8]. Note that the total power density released by the fusion reactions is obtained by the product of the reaction rate ($\langle\sigma_{\mathrm{fus}}v\rangle$) the energy released in a reaction (Q_{DT}) and the density of particles of the reactants, $W_{\mathrm{fus}} = n_{\mathrm{D}}n_{\mathrm{T}}\langle\sigma_{\mathrm{fus}}v\rangle Q_{\mathrm{DT}}$, where $Q_{\mathrm{DT}} = Q_\alpha + Q_{\mathrm{n}}$. Assuming that all the energy of the α-particles and neutrons remains within the fuel, we can consider what fraction of the energy associated to the α-particles (η_α) and neutrons (η_{n}) is deposited in the *spark* region, leading to: $W_{\mathrm{fus,dep}} = n_{\mathrm{D}}n_{\mathrm{T}}\langle\sigma_{\mathrm{fus}}v\rangle(\eta_\alpha Q_\alpha + \eta_{\mathrm{n}}Q_{\mathrm{n}})$. Conversely, the energy deposited in the cold plasma is calculated with $(1-\eta_\alpha)$ and $(1-\eta_{\mathrm{n}})$. In terms of W_{fus}, the expression is recovered taking $\eta_\alpha = 1$ and $\eta_{\mathrm{n}} = 1$, which is equivalent to considering just one volume where all the energy is deposited. In that case, if only α-particles or neutrons are considered, we use the expressions $W_{\mathrm{fus},\alpha}$ (with $\eta_\alpha = 1$ and $\eta_{\mathrm{n}} = 0$) or $W_{\mathrm{fus,n}}$ (with $\eta_\alpha = 0$ and $\eta_{\mathrm{n}} = 1$), respectively. Here, it is worth remaking that Eq. 2.17 describes the evolution of a selected *spark* volume, so only the energy deposited within it ($W_{\mathrm{fus,dep}}$) must be considered.

Making use of Eq. 2.17, we prove whether the hot *spark* can be defined as a viable hot-spot[9] and will continue the burning. This is done by evaluating

[8]The radiation power density contain various terms, but in the case of ICF plasmas, the dominant mechanism is the electron *bremsstrahlung*, this is, the radiation emitted by charged particles when they are decelerated or deflected by the electric field of other charged particles.

[9]In this section we avoid using the "*spark*" or "hs" subindex notation for simplicity purposes, but unless noted, the parameters refer to the hot-spot or a candidate *spark*.

whether the energy of the *spark* will increase after the beam interaction ($t = t_0$), with the values of ρ, R and T found at such instant:

$$W_{\mathrm{fus,dep}}(\rho, R, T) > W_{\mathrm{mec}}(\rho, R, T) + W_{\mathrm{cond}}(\rho, R, T) + W_{\mathrm{rad}}(\rho, R, T). \quad (2.18)$$

This is, the self-heating condition is fulfilled when the power generated by the fusion reactions is larger than the losses of the hydrodynamic processes immediately after the beam interaction has finished.

Secondly, we address the ignition condition, which is a less strict criterion than the self-heating. The ignition evaluates how the *spark* will evolve instants after the beam interaction, maybe reaching the hot-spot condition. Here, the key concept to consider is that the particles escaping from the *spark* heat the surrounding material, as well as the thermal conduction. Thereby, the neighbour material increases its temperature and, thus, the *spark* enlarges its mass and size through its environment, in respect to the initial hot region. This allows some *sparks* that initially do not meet the self-heating condition to evolve into successful hot-spots moments later.

For the purposes of defining the ignition condition, let us assume the propagation of the burning is happening and progressing towards the rest of cold plasma via conduction and energy liberated from the fusion. If the nuclear reactions release enough energy, the process replicates with increasing spherical waves of nuclear burning. The early stages of this expansion can be studied with a scalar model (Guskov et al., 1976; Atzeni & Caruso, 1984). This model estimates the evolution of the mass (M) and the internal energy (here expressed as the product of the energy density and the volume, $\mathcal{E}V$) of a spherical hot-spot surrounded by cold plasma. In respect to the self-heating (Eq. 2.18), now we are considering all the energy exchanged by the hot-spot that is deposited in the hot-spot itself and its surroundings, in a time such as $t+dt$. It is considered that the whole fuel sphere is at rest in the initial instant after the beam heating.

As the burning spreads, more and more fuel becomes part of the hot-spot, varying its internal energy. The majority of this power comes from α-particles and electrons from the hot-spot. Thus, the conservation of energy can be expressed as:

$$\frac{d(\mathcal{E}V)}{dt} = W_{\mathrm{fus},\alpha}V - W_{\mathrm{rad}}V - pSu, \quad (2.19)$$

where $W_{\mathrm{fus},\alpha}$ is the total power density associated to the α-particles from the fusion[10] created in the hot-spot, W_{rad} is the power density associated to the

[10]Strictly, the total fusion power density should be considered, including the neutron energy. However, the literature often neglects them, as the neutrons do not interact with the plasma and scape the fuel. In Eq. 2.18 its contribution could be neglected, too.

radiation, p is the pressure of the burning front of the hot-spot, S is its surface and u is the velocity of the burning front (dR/dt). The internal energy grows if the gain from fused α-particles is higher in respect to the losses due to radiation and pressure.

Then, as the heated surroundings become part of the burning region, the evolution of the hot-spot mass considers the energy of the α-particles deposited in the cold fuel, as well as the conduction losses. As a consequence, the mass accretion from the heated region is modelled by assuming that the escaping power must raise the specific energy of the cold material to the same internal energy of the rest of the hot-spot:

$$\frac{\mathcal{E}}{\rho}\frac{dM}{dt} = \left(W_{\mathrm{fus},\alpha}(1-\eta_\alpha) + W_{\mathrm{cond}}\right) V. \tag{2.20}$$

This is, the energy associated to α-particles and conduction that escapes the hot-spot is the responsible for increasing the value of the specific internal energy up to a certain $\mathcal{E}$-value for the increasing accretion rate dM/dt. The energy of the cold plasma is neglected, as it is significantly lower than $\mathcal{E}$.

In this context, we can express u as the velocity behind a shock wave, by using the equation of state for an ideal gas ($\gamma = 5/3$):

$$u = \left(\frac{3}{4}\Gamma_{\mathrm{B}} T \frac{\rho}{\rho_{\mathrm{c}}}\right), \tag{2.21}$$

where $\Gamma_B = \bar{R}/A_{\mathrm{DT}}$ is the gas constant, ρ_{c} is the density of the cold plasma, ρ and T are the temperature and density[11] of the hot-spot.

We can determine the characteristic hydrodynamic time, associated to the ignition, as $\tau^* = R/u_{\mathrm{sm}}$ and making use of definition from Eq. 2.21:

$$\tau^* = \frac{R}{\sqrt{\mathcal{E}/2\rho}}\left(\frac{\rho_{\mathrm{c}}}{\rho}\right) = \frac{2R}{(3\Gamma_{\mathrm{B}}T)^{1/2}}\left(\frac{\rho_{\mathrm{c}}}{\rho}\right). \tag{2.22}$$

With the hydrodynamic time of the ignition, we can express the terms of gain and loss in a dimensionless form:

$$K_\alpha = \frac{W_{\mathrm{fus},\alpha}\tau^*}{\mathcal{E}}; \quad K_{\mathrm{rad}} = \frac{W_{\mathrm{rad}}\tau^*}{\mathcal{E}}; \quad K_{\mathrm{cond}} = \frac{W_{\mathrm{cond}}\tau^*}{\mathcal{E}}. \tag{2.23}$$

These are a representation of the ratio of the energy density gained or lost in a τ^* time and the energy density of the hot-spot. Making use of these terms, we can rewrite Eqs. 2.19 and 2.20 in a dimensionless sort:

[11] In the case of an isochoric plasma the density is uniform, si $\rho = \rho_{\mathrm{c}}$.

$$\frac{\tau^*}{T}\frac{dT}{dt} = K_\alpha - K_{\rm rad} - K_{\rm cond} - 2, \tag{2.24}$$

$$\frac{\tau^*}{\rho}\frac{d\rho}{dt} = K_\alpha(1-\eta_\alpha) + K_{\rm cond} - 3. \tag{2.25}$$

Here, it is worth highlighting how the K_α term provides a measure of the progress of the ignition. The ratio between the energy produced in the characteristic time (τ^*) and the energy of the burning region needs to be a growing function, at least at the earliest stages after the ignition.

Thus, if we time-differentiate K_α using Eqs. 2.24, 2.25 and 2.22, as well as considering $m \approx 2$ for a temperature range of 7-20 keV (Atzeni & Meyer-Ter-Vehn, 2004), we find that:

$$\frac{\tau^*}{K_\alpha}\frac{dK_\alpha}{dt} = \frac{1}{2}(K_\alpha - K_{\rm rad} - 3). \tag{2.26}$$

This indicates that K_α will continue to increase if the expression within the parentheses is positive and the fuel will eventually ignite if the condition $(K_\alpha - K_{\rm rad})_{t=0} > 3$ is met. The evaluation is performed at the first instant after the beam interaction, so we denote now τ_0^*, calculated as $R\sqrt{2\rho/\mathcal{E}_0}$, where $\mathcal{E}_0 = 3\rho\Gamma_B T$ is energy per mass unit, considering the temperature of the initial *spark*. This, if expressed making use of Eq. 2.23, is written as:

$$(W_{{\rm fus},\alpha} - W_{\rm rad})\,\tau_0^* > 3\mathcal{E}_0, \tag{2.27}$$

which corresponds to the ignition condition we referred in previous Sect. 2.3.2, and that we will revisit in Sect. 3.6 of the model chapter.

To illustrate the behaviour of the self-heating and ignition conditions, Fig. 2.11 displays some results in the ($\rho R_{\rm hs}^*$, $T_{\rm hs}^*$)-space[12]. Solutions of the self-heating expression (Eq. 2.18) for $t = t_0$ are represented as a grey region. A procedure for calculating this will be explained in detail in Sect. 3.6. Then, the evolution of *sparks* with different initial conditions in the ($\rho R_{\rm hs}^*$, $T_{\rm hs}^*$)-space are shown, superimposed with the self-heating region as a grey zone. For each *spark*, the origin point is marked with a dot and a capital letter, accompanied by a line with arrows that shows the consequent progress. This serves as a graphic display of those cases that fulfil the ignition condition or do not. The *sparks* that evolve into the grey region of self-heating will become hot-spots and sustain the

[12]This notation includes "$*$" to indicate that $T_{\rm hs}^*$ represents the mass-averaged temperature of the initial hot region and that $pR_{\rm hs}^*$ is related to the region such that the temperature is $T > min(4\ keV; T_{\rm hs}^*/2)$.

burning, are marked with black dots and solid lines. Notice how, with time, they increase in size ($\rho R^*_{\rm hs}$) and temperature ($T^*_{\rm hs}$). Conversely, those dots representing cases where the evolution cools down and shrink will not achieve ignition are marked as hollow dots with dotted lines. The evolution of these *sparks* or hot-spots has been computed through numerical one-dimensional simulations under isochoric conditions (Atzeni & Meyer-Ter-Vehn, 2004). We can define the ignition curve for a given configuration as the boundary separating the regions of initial conditions that result in target ignition from those leading to target cooling. In Sect. 3.7 we address both the self-heating and the ignition threshold solutions using our modelling.

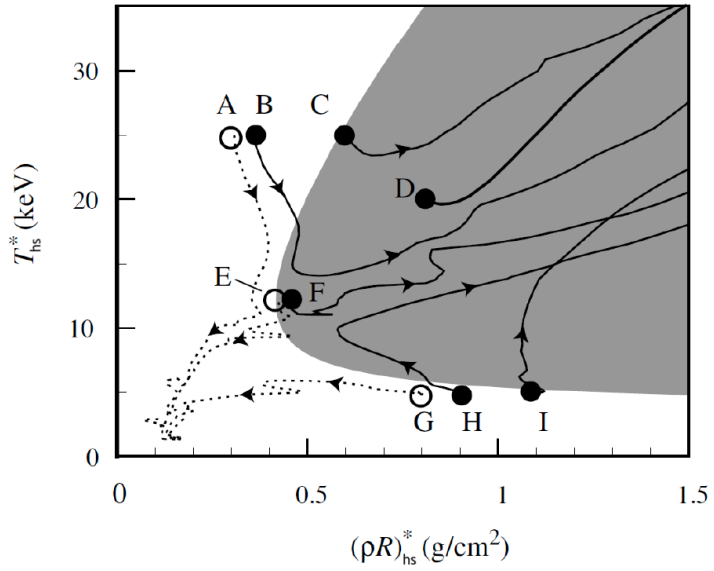

FIGURE 2.11— Representation in the (ρR, T) space of the self-heating region (grey area) and the simulation of the temporal evolution of different hot-spots (denoted with a capital letter). Hollow dots with dashed lines represent cases where the ignition is never achieved and black dots with solid lines represent the cases where the evolution leads to ignition. In both cases, the dots mark the initial instant. Source: Atzeni & Meyer-Ter-Vehn (2004).

If the heated plasma fulfils the conditions to achieve the burning, it is worth calculating the efficiency or fractional burn-up, which is the ratio between the total number of fusion reactions and the number of DT pairs initially present in the volume: $\Phi = N_{\rm fus}/N^{(0)}_{\rm DT}$, with $N^{(0)}_{\rm DT} = n_{\rm DT}V/2$. Then, this ratio is utilized to calculate the burning gain, which compares the thermonuclear energy released and the initial target energy $G_{\rm burn} = E_{\rm fus}/E_{\rm T}$. The energy of the target is

calculated according to the energy employed for the target compression and the energy expended on the ignitor formation.

2.3.3 State of the art of FI simulations

Within the world of fast ignition nuclear fusion, simulations play a crucial role in predicting the outcomes and estimating the requirements for future reactors. Our thesis is situated within this context, particularly focusing on computing the deposition of ion beam energy in the plasma fuel and its preliminary gain results. Before presenting our model and results, it is essential to discuss other types of simulations found in the literature.

Simulating the entire FI process as a whole is discouraged, as the spatial and temporal scales of the different stages (precompression, beam interaction, burning, etc) are very dissimilar, spanning orders of magnitude. Commonly, these processes are separated into different stages and simulated separately using methods suitable for each one (Fernandez et al., 2014).

On the one hand, research on the necessary conditions of the particle beam for fast ignition has been ongoing for some time. Initially, theoretical studies predicted the minimum energy necessary for the ignition under isochoric conditions (Atzeni, 1999; Atzeni & Meyer-Ter-Vehn, 2004):

$$E_{\text{ig}} = \frac{72}{(\rho[100\ \text{g/cm}^3])^2}\ \text{kJ}. \tag{2.28}$$

Additionally, one of the first numerical studies investigating these requirements was carried out by Atzeni (1999). That work assumes a highly simplified two-dimensional model (for an illustrative scheme, see Fig. 3.3) where the compressed fuel is a sphere of uniform density in a vacuum. The beam is perfectly collimated, cylindrical, mono-energetic, with uniform radial and temporal intensity distributions and a uniform energy deposition. Notably, the study does not specify the type of particles used in the beam, so the conclusions are, in principle, valid for both electrons and ions. This investigation provided expressions for the minimum values of energy, power and beam intensity to achieve ignition, as shown by the following equations:

$$E_{\text{ig}} = 140 \left(\frac{\rho}{100\ \text{g/cm}^3} \right)^{-1.85}\ \text{kJ}, \tag{2.29}$$

$$W_{\text{ig}} = 2.6 \cdot 10^{15} \left(\frac{\rho}{100\ \text{g/cm}^3} \right)^{-1}\ \text{W}, \tag{2.30}$$

$$I_{\mathrm{ig}} = 2.4 \cdot 10^{19} \left(\frac{\rho}{100\ \mathrm{g/cm^3}} \right)^{0.95} \ \mathrm{W/cm^2}. \tag{2.31}$$

This approach, however, has the disadvantage of omitting the details of the interaction between the particle beam and the target, which reduces its accuracy. We also note how the numerical expression does not completely match the theoretical one.

Shortly after the proposal of the fast ignition with protons (Roth et al., 2001), a similar model to the previous one was applied to it, including the transport of the beam particles (Atzeni et al., 2002). In this case, the time of flight of the beam particles between the source and the fuel was taken into account by assuming an exponential-type for the particle energy distribution. A correction to the ignition criterion given by the equations above was obtained by introducing adjustment factors, functions of the equivalent temperature of the protons. It is interesting to note that in this analysis the minimum ignition energy scales as $E_{\mathrm{ig}} \propto \rho^{-1}$, in contrast with the previous monoenergetic case with constant power of the previous model.

Later on, Honrubia et al. (2009), among others, studied the case of rapid ignition with heavier quasi-monoenergetic beams (of carbon ions), considering some spread. Here, more realistic configurations of the compressed fuel and ion energy deposition were performed. The minimum ignition energy was found to be dependent on the average kinetic energy of the ions (E_0). Under optimal conditions, ignition could be achieved with beam energies of around 9.5 kJ (for a DT density of 500 g/cm^3).

In subsequent studies, the use of monoenergetic ions of different species was considered again (Hegelich et al., 2006; Honrubia et al., 2014), and the minimum ignition energy was found to be almost independent of the type of ion. However, the kinetic energy attained increased with the atomic number of the species in question, following a scaling given approximately by $E_0 \propto Z^2$. For TSNA scenarios, the ignition by ion beams with Maxwellian distributions was also investigated (Honrubia & Murakami, 2015), where a more detailed energy deposition model, based on the Fokker-Planck equation, was introduced, and the effect of ion beam divergence was evaluated. The model of energy deposition slightly increased the ignition energy, but without substantial change. However, the beam divergence did, triggering the required beam energy well above acceptable values for angles greater than $10^\circ - 15^\circ$, showing the importance of effective focusing of the ion beams in FI. In Fig. 2.12, we display some exemplary results from the work of Honrubia et al. (2014), such as the initial fuel density distribution, the minimum ignition energy for different beam

species, and the 2D simulation of the energy deposition of the beam.

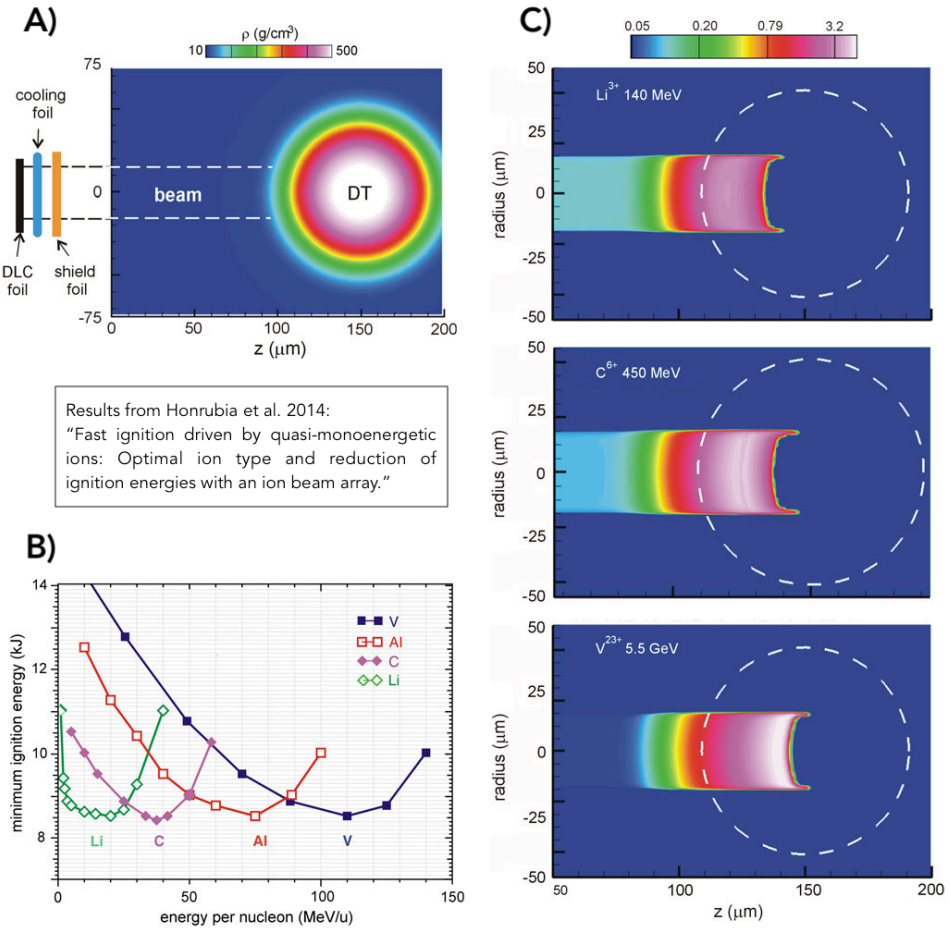

FIGURE 2.12— Results from Honrubia et al. (2014). A) Density map of the fuel configuration considered in that work. Perfectly collimated beam along the distance $d = 5$ mm from the ion source to the simulation box. B) Minimum ignition energies of the target shown in panel "A" heated by quasi-monoenergetic lithium, carbon, aluminium and vanadium ions as a function of the mean kinetic energy per nucleon. The energy spread $\sigma_E = 10\%$ and the beam diameter is 30 μm in all cases. C) Energy density in units of 10^{11} J/cm^3 deposited in the target of panel "A" by 8.5 kJ quasi-monoenergetic beams of 140 MeV lithium ions, of 450 MeV carbon ions and of 5.5 GeV vanadium ions. The dashed curves show the initial position of the density contour $\rho = 250$ g/cm3.

Progressively, different types of simulations have emerged, each tailored to the specific objectives of the study. Some aim for higher accuracy by incorpo-

rating multiple physical processes, while others opt for simpler approaches to reduce computational costs. Various beam and stopping expressions have been studied, along with plasmas under different conditions.

A well known author in this sense is S. Yu. Gus'kov, who has extensively studied both beam deposition and subsequent gain processes using the power density processes of the plasma (see Eq. 2.17 and expressions from Sect. 3.8). The beams considered in these studies are often monoenergetic, with the heated plasma parameters varying along with the ion beam characteristics and the features of its slowing down (e.g. Gus'kov et al., 2010; Gasparyan et al., 2013; Gus'kov et al., 2014a). The plasma under consideration can be pure DT, doped, or non-cryogenic, to take into account the ablator impurities or other pellet configurations (e.g. Gus'kov et al., 2015; Gus'kov & Sherman, 2016). A particularity of some of these works is that, unlike the works of Atzeni and Honrubia (e.g. Atzeni, 1999; Atzeni & Meyer-Ter-Vehn, 2004; Honrubia et al., 2009, 2014), when studying the gain of the already heated plasma, they do not considered the beam applied to generate such region. Instead, they systematically examine how different plasma characteristics lead to varying gains (Gus'kov et al., 2011).

Zou et al. (2016) present a distinct approach, focusing on the evolution of plasma temperature. Their study incorporates both beam interaction and hydrodynamic processes simultaneously, albeit without spatial distribution. They consider a beam consisting of protons with a Maxwellian energy distribution and investigate the plasma behaviour in the presence of impurities.

Our approach to IFI takes ideas from some of these works, as detailed in the following section. We divided our analysis into two main parts: the beam-plasma interaction process and the subsequent preliminary evolution of the plasma. The beam-plasma interaction is simulated in one dimension over time, while the preliminary plasma evolution is studied as a zero-dimensional model to assess ignition feasibility and predict potential burning gain. Our framework allows for the consideration of plasma fuels of different size, density, initial temperature and composition, as well as beams of different charge, energy, flux, and monoenergetic or quasi-monoenergetic characteristics. Our main objective is to conduct a systematic analysis in which we connect the beam characteristics with the conditions offered by the plasma after the interaction, as explained in the next section.

2.4 Motivation, objectives and thesis outline

Although in Europe and Asia the MCF approach has been taken as the main path towards achieving nuclear fusion, exploring alternative fusion concepts

like fast ignition is essential to gather a complete perspective on the future of possible nuclear reactors, aiming for enhanced performance and feasibility.

In this context, we explore the potential of ion fast ignition scheme by making a systematic and multiparametric study through simulations of an ion beam-fuel system, in different scenarios of interest for the IFI approach. Consequently, the main goal of this work is to establish the relationship between the characteristics of a plasma heated within the IFI context, and the ion beam used in such experiment. We contemplate a large range of values of interest, where the fuel is a deuterium-tritium plasma in equimolar concentration, which can be modelled for different temperatures, densities, radii and include impurities at different concentrations. Then, we consider different types of fast ion beams, either monoenergetic or quasi-monoenergetic (determined by an energy spread), for different ionic species, beam radii, energy of the projectiles and surface particle density (or flux). With the methodology we establish and our simulations, we provide results of the generated hot-spot and the efficiency of the subsequent nuclear burning, thus, relating the parameters of the plasma and the applied beam. Meanwhile, many authors analyse these components separately or focus on specific cases. Our goal is to comprehensively integrate these concepts and expand the studied framework. Our approach provides a more compact and integral vision of the energy deposition due to the beam and its implications, exploring thoroughly the parameter space and detailing those outlines of interest. We emphasize how simulations offer significant advantages by providing insights into beam and plasma dynamics, predicting its performance, improving its design, as well as the conditions of the target. All of these, without the considerable economic costs and logistical challenges associated with experimental testing.

To do so, we have developed a physical and computational one-dimensional model to simulate the ion beam-plasma interaction and evaluate the preliminar potential of the heated plasma for achieving the nuclear fusion burning. For the different scenarios we consider, we calculate the temperature field obtained during the interaction ($T(x,t)$), until the beam has deposited all of its energy. With this distribution of temperatures, we obtain the resulting properties of the heated plasma, such as the range, the maximum temperature, and the temperature at the beginning of the plasma across a wide range of conditions, among others. Then, from this simulation set, we determine the parameter space of the beam where ignition and self-heating are achieved and a hot-spot is formed. We present results describing the threshold conditions to achieve such hot-spot and study its main characteristics, including mean temperature, size and location within the sphere. Then, we estimate the potential evolution of the plasma after the heating, that is, for those cases that achieve the hot-spot condition,

we calculate the burning gain and the beam-plasma coupling efficiency. Furthermore, we identify the ion beam parameters that create hot-spots at the edge or the centre of the given plasma, depending on its conditions. Through this analysis, we aim to achieve a broad representation of the parameter space of the experiment, both for the initial conditions of the plasma and the beam characteristics.

Our simulations span a wide range of ion beam and plasma conditions. Among them, but not limited to, we select certain known parameters of interest in IFI studies, as outlined below. On the one hand, we consider pure DT or doped (Be, Li, Al or Cu at various concentrations) fuels, with plasma spheres of radii R_{F}=40-60 μm, initial temperature of T_0=0.5-5 keV and densities of ρ = 300-700 g/cm^3 (exemplary taken from Gus'kov et al., 2010; Gus'kov et al., 2014b; Honrubia et al., 2014; Nezam et al., 2020). Our modelling can handle variable density scenarios, including the consideration of the fuel corona if necessary.

On the other hand, for the ion beams, we select three characteristic IFI nuclear species: protons (p^+), carbon (C^{6+}) and vanadium (V^{23+}), with different radii of the beam r_{b}=10-20 μm (e.g. Atzeni, 1999; Gasparyan et al., 2013; Honrubia et al., 2014; Honrubia & Murakami, 2015; Zou et al., 2016). For each of these cases, we explore the parameter space of the ion projectile energies and beam surface particle density (or flux), denoted by E_0 and σ, respectively. We designed our computational approach to efficiently calculate arrays with varying values of flux and ion energy. We are also able to study monoenergetic ion beams and quasi-monoenergetic beams under different configurations. Our modelling considers the quasi-monoenergetic located at the edge of the plasma or at a "d" distance, approximated with a Gaussian energy distribution.

Our primary analysis prioritizes the ideal scenario of a pure DT plasma without corona, paired with a monoenergetic beam. This experiment is considered as a reference case, such that, then, we study independently the effect of considering a corona, including dopants in the fuel or applying a quasi-monoenergetic beam. By doing so, we are able to evaluate the influence of each scenario separately and compare them with the ideal case.

We pay special attention to hot-spots with a length similar to twice the radius of the beam, and positioned at the middle of the plasma sphere. This configuration assures a hot-spot volume with a geometry as similar to a sphere as possible, that also optimizes a posterior symmetrical explosion, as already stated in Sect. 2.3.2. For instance, a typical case addressed in the literature and in this work considers the radii of the fuel sphere and the beam to be of 15 μm and 50 μm, respectively. This kind of configuration has been previously examined by (Honrubia & Murakami, 2015), and identified as an optimal setup

within the framework of the ion fast ignition scheme. Then, our interest focus on those central hot-spots with maximum temperature located in the middle of the plasma (50 μm) with a length of 30 μm. By following this approach, we can provide the beam characteristics that create such hot-spot, along with its gain and temperature. The values selected in this parameter space are based on previous literature, although we extend the ranges of the analysis. In this way, we capture any potentially interesting results or conditions that may become technologically feasible in the future.

In a few words, the core objective of this work is to present a broad study of the IFI interaction under different experimental conditions. By doing so, we establish a clear connection between the characteristics of the beam applied and the resulting plasma state. This serves of great utility: when formulating an experiment we return the prediction of the resulting plasma, or, on the contrary, if targeting for the creation of a particular kind of hot-spot, we provide the necessary input parameters. To the best of our knowledge, this approach has not been extensively explored in previous literature.

Henceforth, this thesis is organised as follows. First, as already explained in above, a general overview of the current status of nuclear fusion has been performed. Then, in Chapter 3 we present our modelling to perform the simulations we aim to study. In Chapters 4, 5, 6, and 7 we apply our model to derive and discuss the results found under a wide range of key conditions. At last, in Chapter 8, we summarise the manuscript, state the future research lines and present our conclusions.

3

Model of the ion beam interaction with the precompressed plasma (in the context of the ion fast ignition scheme)

As explained in the introduction, in a nuclear reactor operated by ion fast ignition (IFI), the configuration involves a chamber that houses a target made up of a small spherical pellet containing fusion fuel, such as deuterium and tritium. The nuclear fuel is generally enveloped by an ablator capsule that serves as a container and also improves the energy absorption process in the heating and compression processes. An ablator is usually made of plastic (polystyrene or other hydrocarbons) or metal foams (ranging from very light elements to high-z elements, for example, from beryllium to gold). Furthermore, the use of light metal DT hydrides such as Li_2DT, $Li_2BeD_2T_2$, $Li_2Be_2D_3T_3$, NT_3BD_3 as non-cryogenic solid fuels have been proposed for inertial confinement fusion. In a similar way to the ICF scheme, in the first phase, high-energy lasers or particle beams impact the external layers of the target (ablator), causing its implosion. This consists of a rapid compression of the pellet to an optimal point, where a plasma is obtained, formed by a very dense and hot region (core) surrounded by a much less dense layer of plasma (corona). In the case of the IFI, this optimal point is the core, found in a state of very high density, the one required for the initiation of ignition and subsequent nuclear burning, and in a state of stagnation equilibrium, where the dynamic processes of the constituents of

the plasma are frozen. However, in the precompressed state, the temperature necessary to initiate an efficient ignition process of nuclear reactions has not yet been reached. In a second phase, an energetic beam of fast ions will be used to heat a small region of the core and create a hot-spot. The implosion could drive some of the ablator material inward of the compressed fuel, introducing impurities in the plasma. In general, these impurities (or dopants) increase the beam energy required for the plasma heating and decrease the nuclear gain. Therefore, we will explore different fractions of Be, Li, C, Al and Au as typical impurities to the DT plasma.

Following the compression, a separate high-intensity, ultra-short energetic, and fast particle beam is focused on the already-compressed core during the ignition phase to achieve the conditions necessary for nuclear fusion reactions. These ion beams are generally monocomponents made up of fully ionized ions, ranging from low to high nuclear charge. In this work, our focus is on particle beams, commonly composed of stripped ions such as protons (p^+), carbon (C^{6+}) or vanadium (V^{23+}). As mentioned in the previous chapter, within the IFI approach, one of the main open problems is the generation of ion beams appropriated to this scheme. A promising candidate are quasi-monoenergetic beams, in particular, those generated from a Maxwellian or Gaussian-like energy distribution, In this context, monoenergetic ion beams are considered as an ideal scenario. Therefore, and although infeasible in practice, in this work we pay special attention to understanding the interaction of perfectly monoenergetic beams. They serve as a benchmark for comparing and contrasting with the subsequent study of quasi-monoenergetic beams.

3.1 Plasma description

After the precompression phase of the small pellet, the fuel reaches the maximum condensation before the ion beam interaction. Following spherical symmetry for the fuel, its fields for the initial temperature ($T(r, t = 0)$) and density ($\rho(r, t = 0)$) are often described with two parts: the corona and the core plasmas. The corona presents low but increasing density and temperature, while the core, the highly compressed central region, is in a stagnation phase with approximately constant temperature and density, both higher than in the corona plasma. This is illustrated in Fig. 3.1, representing the precompressed plasma fuel.

Regarding the density, a possible way to describe its profile can be adapted from Fuentes (2018), as:

$$\rho(r) = max\left(\rho_{\max} e^{-\ln(\rho_{\max}/\rho_{\text{corona}})(r/R_{\text{core}})^{k_\rho}}, \rho_{\text{corona}}\right) \text{ g/cm}^3, \tag{3.1}$$

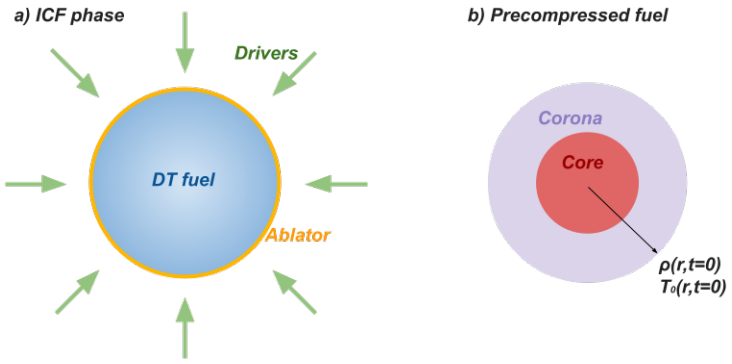

FIGURE 3.1— Scheme of the precompressed plasma fuel. We show its two distinctive parts, the corona and the core, as well as the beams that performed the compression with red arrows.

where $\rho_{\max}$ is the maximum density (corresponding to the core centre), ρ_{corona} is the density of the corona, r is the distance from the centre, R_{core} is the radius at which the density decreases to the corona density, and k_ρ is a coefficient that adjusts the steepness of the profile.

For instance, Fig. 3.2 represents the density profile of a plasma with $\rho_{\max} = 500$ g/cm^3, $\rho_{\text{corona}} = 10$ g/cm^3, $R_{\text{core}} = 70$ μm, and $k_\rho = 14$. We can clearly distinguish three regions: the corona region with a constant low density ($70 < r < 170$ μm), an almost isochoric part of the core ($0 < r < 50$ μm), which would correspond to R_{F}, and between both, a transitional part of the core with variable density ($50 < r < 70$ μm). In an optimal precompressed scenario, the surrounding corona should be as thin and transparent as possible. Thus, the transitional part of the core should be steep and narrow, this is, the larger possible k_ρ, leaving a virtually isochoric core-target.

In this work, we predominantly focus on studying targets under ideal circumstances. We simplify the model by disregarding the corona contribution and assuming a homogeneous spherical core with a radius (R_{F}), uniform initial temperature ($T(r, t = 0) = T_0$), also referred to as the cold plasma temperature (T_{c}), and uniform density, which remains practically constant, this is, as an isochoric plasma ($\rho(r, t) = \rho$). Thus, the fuel has an associated volume (V) and mass (M). Additionally, we consider the heat capacity at constant volume (C_{V}) as fixed (Gasparyan et al., 2013), due to the process being isochoric. Lastly, due to the high temperatures of the fuel, we consider a fully ionized plasma.

The base composition of the plasma is a mixture of deuterium and tritium, which we consider to be in equal proportion ($n_{\text{D}} = n_{\text{T}}$, $n_{\text{D}} + n_{\text{T}} = n_{\text{DT}}$). Then,

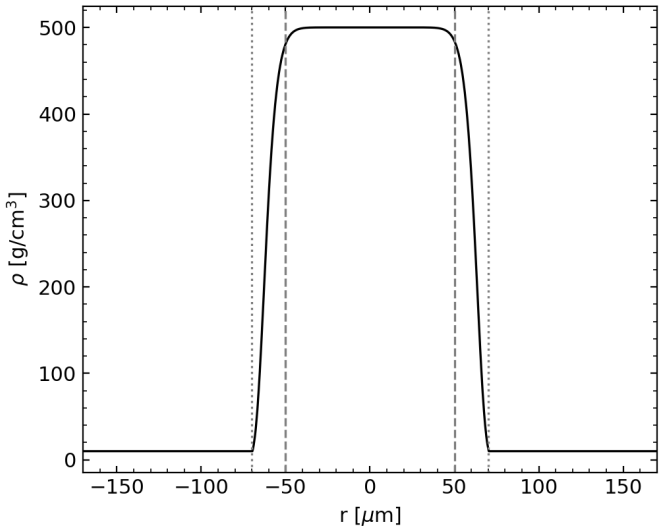

FIGURE 3.2— Density profile of a plasma fuel with $\rho_{\max} = 500$ g/cm^3, $\rho_{\text{corona}} = 10$ g/cm^3, $R_{\text{core}} = 70$ μm and $k_\rho = 14$.

the mean values of the DT atomic and mass number are $Z_{\text{DT}} = 0.5(Z_{\text{D}} + Z_{\text{T}})$, $A_{\text{DT}} = 0.5(A_{\text{D}} + A_{\text{T}})$ and the mean quadratic atomic number is given by $(Z_{\text{DT}})^2 = 0.5(Z_{\text{D}}^2 + Z_{\text{T}}^2)$. The atomic mass is $m_{DT} = A_{\text{DT}} m_{\text{n}}$ and the matter density is calculated as $\rho_{\text{DT}} = n_{\text{DT}} m_{\text{DT}} / N_{\text{A}}$, where N_{A} is the Avogadro constant. Assuming the DT plasma behaves as an ideal gas, we can define the heat capacity of a pure plasma as $C_{\text{V(DT)}} = 3K_{\text{B}}/m_{\text{DT}}N_{\text{A}}$, where K_{B} is the Boltzmann constant. Consequently, we can express the energy of the deuterium-tritium compound as $E_{\text{DT}} = \rho_{\text{DT}} V C_{\text{V(DT)}} T$.

As explained before, it is possible to find traces of impurities due to detached components from the ablator material in the Deuterium-Tritium (DT) plasma fuel. Hence, it is a primal interest to analyse the influence of the dopants in this scheme. We describe a doped plasma by considering a fraction of impurities relative to the pure DT plasma. Thus, the dopant concentration or abundance with respect to the DT is described as:

$$\xi = \frac{n_{\text{i(dop)}}}{n_{\text{i(DT)}}} = \frac{n_{\text{e(Dop)}} Z_{\text{dop}}^{-1}}{n_{\text{e(DT)}} Z_{\text{DT}}^{-1}}, \tag{3.2}$$

where n_{e} is the free electron density and n_{i} is the ion density.

In the case of doped DT plasmas, it is useful to define the mean values of the atomic mass and number (A_*, Z_*, and (Z_*^2)) of a doped DT plasma as follows:

$$A_* = \left(A_{\mathrm{DT}} + \xi A_{\mathrm{dop}}\right)/(1+\xi) \tag{3.3}$$

$$Z_* = \left(Z_{\mathrm{DT}} + \xi Z_{\mathrm{dop}}\right)/(1+\xi) \tag{3.4}$$

$$(Z_*^2) = \left(Z_{\mathrm{DT}}^2 + \xi Z_{\mathrm{dop}}^2\right)/(1+\xi). \tag{3.5}$$

where Z_{dop}, A_{dop} and $(Z_{\mathrm{dop}})^2$ are the atomic, mass and mean quadratic atomic numbers of the dopant, respectively.

Also, we can calculate the atomic weight of the mixture, considering the presence of free electrons:

$$m_* = (m_{\mathrm{DT}} + m_{\mathrm{dop}}) + (m_{\mathrm{DT,e}} + m_{\mathrm{dop,e}}) = A_* m_{\mathrm{n}} + Z_* m_{\mathrm{e}}. \tag{3.6}$$

So, after some straightforward calculations, now we can write the density, the heat capacity and the energy of the doped DT plasma as:

$$\rho = \rho_{\mathrm{DT}}(1+\xi)\frac{m_*}{m_{\mathrm{DT}}}, \tag{3.7}$$

$$C_{\mathrm{V}} = C_{\mathrm{V(DT)}}\frac{(1+Z_*)}{2}\frac{m_{\mathrm{DT}}}{m_*}, \tag{3.8}$$

$$E = \rho V C_{\mathrm{V}} T = E_{\mathrm{DT}}(1+\xi)\frac{(1+Z_*)}{2}. \tag{3.9}$$

Moreover, another way to indicate the quantity of dopants present in a plasma is as a fraction of the total, a method commonly used by authors such as Gus'kov et al. (2011); Gus'kov et al. (2015) and Gus'kov & Sherman (2016):

$$1 = X_{\mathrm{DT}} + X_{\mathrm{dop}}. \tag{3.10}$$

Then, for a mixture of DT in equal proportion ($n_{\mathrm{D}} = n_{\mathrm{T}} :\ X_{\mathrm{DT}} = 2X_{\mathrm{D}} = 2X_{\mathrm{T}}$) and a single dopant, we can write the relation between ξ and X_{dop} or X_{DT} as:

$$X_{\mathrm{dop}} = \frac{\xi}{1+\xi}; \quad X_{\mathrm{DT}} = \frac{1}{1+\xi} \tag{3.11}$$

$$\xi = \frac{X_{\mathrm{dop}}}{1-X_{\mathrm{dop}}} = \frac{1}{X_{\mathrm{DT}}} - 1. \tag{3.12}$$

3.2 Beam-plasma interaction description: power balance equation, slowing down and heating

The power balance equation that governs the change in energy of the plasma per unit volume ($\mathcal{E}$) is given by:

$$\frac{\partial \mathcal{E}(\vec{r},t)}{\partial t} + \vec{v}(\vec{r},t) \cdot \vec{\nabla}\mathcal{E}(\vec{r},t) = W_{\mathrm{d,beam}}(\vec{r},t) + W_{\mathrm{proc}}(\vec{r},t), \tag{3.13}$$

where $\mathcal{E}$ is the energy density of the plasma, $\vec{v}$ is the velocity, $W_{\mathrm{d,beam}}$ is the power density deposited by the beam, and W_{proc} is the power density of the internal processes of the plasma, including fusion, mechanical, conduction, and radiation processes.

As an ideal gas, the energy per volume of the plasma can be expressed as

$$\mathcal{E}(\vec{r},t) = \rho\, C_{\mathrm{V}} T(\vec{r},t), \tag{3.14}$$

with isochoric and homogeneous density and heat capacity.

Taking into account that we are interested in fuels at the stagnation state, the plasma can be considered at rest ($\vec{v} = 0$) and the convection term neglected. Consequently, Eq. 3.13 combined with Eq. 3.14, can be expressed as:

$$\rho\, C_{\mathrm{V}}\, \frac{dT(\vec{r},t)}{dt} = W_{\mathrm{d,beam}}(\vec{r},t) + W_{\mathrm{proc}}(\vec{r},t). \tag{3.15}$$

In our plasma heating model, we assume that the duration of the ion beam (τ_{beam}) is considered short enough in comparison with the hydrodynamic time and the characteristic time of each internal plasma process ($\tau_{\mathrm{beam}} < \tau_{\mathrm{hyd}}$ and $\tau_{\mathrm{beam}} < \tau_{\mathrm{proc}}$). This assumption allows us to neglect energy changes due to conduction, mechanical work, radiation, or fusion during the interaction time between the plasma and the beam, leading to $W_{\mathrm{proc}} \approx 0$. In Sect. 3.9.1 we present a more precise comparison to stablish the safe ranges of our modelling.

Furthermore, we consider that the ion beam enters the plasma sphere in a radial direction. If the projectile has sufficient kinetic energy or mass, or both, it can be considered that it travels along a straight line trajectory. On the contrary, for lower energies, the projectile shows a Brownian motion with stochastically changing momentum, resulting in transversal and longitudinal fluctuations known as spreading and straggling, respectively. In this work, the beam energy is assumed to be high enough to disregard such fluctuations, allowing us to treat the movement of the projectiles across the plasma as straight, simplifying the problem to one dimension. Thus, from now on, we use the x-coordinate to study the region of interest heated by the beam, replacing the $\vec{r}$ coordinates. Hence, the beam-target interaction can be described as one-dimensional (Beltran et al., 2020). To illustrate this concept, Fig. 3.3 represents the scheme of the interaction[1].

[1]The term "bin" from such image will be defined later on.

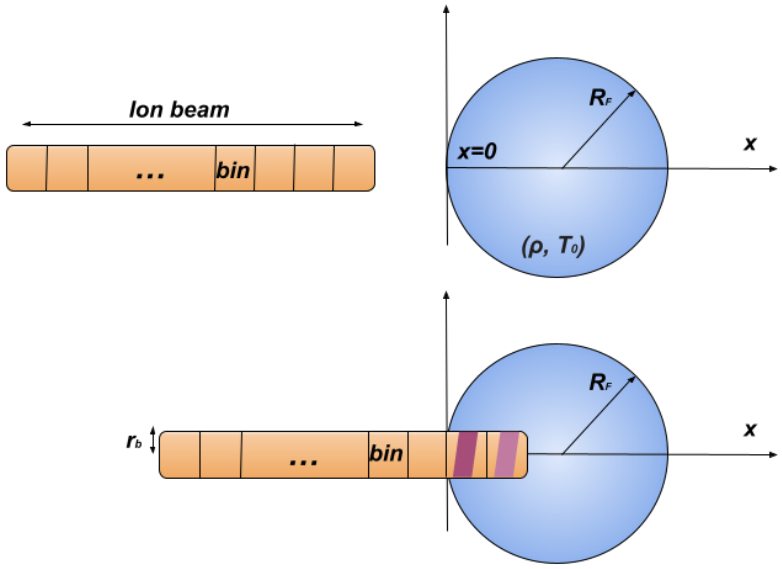

FIGURE 3.3— Scheme of the IFI set-up. We show the precompressed DT fuel sphere and the ion beam discretised into bins (see Sect. 3.12) for the numerical simulation of the interaction.

According to these considerations, we can rewrite Eq. 3.15 as the temperature field variation during the interaction:

$$\frac{dT(x,t)}{dt} = \frac{1}{\rho\, C_{\mathrm{V}}} W_{\mathrm{d,beam}}(x,t;\rho,T(x,t)), \tag{3.16}$$

where $x \in [0, 2R_{\mathrm{F}}]$ and $t \in [0, \tau_{\mathrm{beam}}]$. In this scenario, $W_{\mathrm{d,beam}}$ denotes the energy deposited by the ion beam at (x,t), per unit time and length.

3.3 Ion beam description

Consequently, it is necessary to define the characteristics of the ion beam and to establish how the beam deposits energy in the plasma. In this work, we consider the ion beams as perfectly collimated, fast, non-dispersive, cylindrical (with a circular section), axial (respect to the centre of the spherical precompressed plasma) and with homogeneous ion spatial distribution. The beam is composed of N_{p} fully stripped point-like ions with charge Z_{b} and mass number A_{b} (or m_{b}, as mass). Each ion-projectile has an average initial kinetic energy of $\bar{E}_0$ and, therefore, the total energy of the beam can be expressed as $E_{\mathrm{b}} = N_{\mathrm{p}}\bar{E}_0$. Finally, the beam is characterized by a radius (r_{b}) of its circular cross-section,

a surface particle density or flux[2] (σ), and an ion beam duration time (τ_{beam}). The flux is defined as $\sigma = N_{\text{p}}/(\pi r_{\text{b}}^2)$, this is, the surface particle density of the cross-section of our cylindrical beam, calculated as the number of ions N_{p} that go through a surface of $S_{\text{b}} = \pi r_{\text{b}}^2$. Due to the symmetry, the beam creates a heated cylindrical region $T(x,t)$, of length L_{h} and radius r_{b}, with a radial direction within the fuel sphere.

3.3.1 Monoenergetic ion beams

In monoenergetic ion beams, all ion-projectiles have the same kinetic energy E_0 (so $\bar{E}_0 = E_0$), and the power density deposited ($W_{\text{d,beam}}$) can be expressed as

$$W_{\text{d,beam}} = I \cdot Sp\left(E(x(t')), T(x,t), \rho\right). \tag{3.17}$$

Here, the intensity (I) of the beam is the number of ion-projectiles that go through the plasma per transverse area and unit time. For a constant intensity (time-independent) and homogeneous ion-projectile spatial distribution, it can be expressed as $I = \sigma/\tau_{\text{beam}}$.

Conversely, $Sp(E(x(t'), T(x,t), \rho)$ denotes the stopping power, which represents the energy deposited by one projectile in the plasma, per length unit and at each instant of time. $E(x(t'))$ is the kinetic energy of the particles travelling in the plasma with temperature $T(x,t)$, and is determined assuming a classical dynamic of the particles in the plasma, by means of the following expression:

$$\frac{dE(x(t'))}{dx} = -Sp\ \left(x; E(x(t')), T(x,t), \rho\right), \tag{3.18}$$

which describes the slowing down of the projectiles due to the particles of the plasma during the time of fly (τ_{fly}) as the ion travels in the fuel until it stops. Here, $t' \in [0, \tau_{\text{fly}}]$ is used to represent the time in which a projectile travels through the plasma, while $t \in [0, \tau_{\text{beam}}]$ represents the time of the whole beam interaction. Thus, in this work, a time of flight smaller than the time of the beam is assumed. Hence, Eq. 3.18 is solved for a selected time t, for an ion travelling along the plasma with $x = x(t')$, until it stops, where t are the instants of time during the slowing down of the ion in the interval $[t, t + \tau_{\text{fly}}]$. Implicitly, this modelling implies that the beams are generated at the edge of the plasma during this τ_{beam} time.

As stated at the beginning of this section, the initial and boundary conditions are given by $T(x,0) = T_0$ keV for any $x \in [0, 2R_{\text{F}}]$, and $E(x=0) = E_0$ for any $t \in [0, \tau_{\text{beam}}]$. In this work, the energy deposition and heating of the

[2]We acknowledge that "flux" is sometimes described as the flow rate per unit area, but throughout this work, it refers to the number of particles per area unit.

plasma are calculated in our model by solving Eq. 3.16 and 3.18 in a coupled way, driven directly by the stopping power. Thus, Equation 3.16 can be expressed in its integral form as:

$$T(x, \tau_{\text{beam}}) \ = T(x, 0) \ + \frac{I}{\rho \ C_{\text{V}}} \int_0^{\tau_{\text{beam}}} Sp\,(x; E(x), T(x,t), \rho) \ dt. \tag{3.19}$$

It is worth noting that, under the assumption that $\tau_{\text{fly}} < \tau_{\text{beam}} < \tau_{\text{hyd;proc}}$ and $W_{\text{d,beam}} > W_{\text{proc}}$, the solutions of Eq. 3.19 are explicitly independent of the beam time and the solutions depend exclusively on (σ, E_0). This is addressed in the next Sect. 3.12, where we describe the numerical procedure followed to tackle this problem.

3.3.2 Quasi-monoenergetic ion beams

In addition to considering the ideal case of a monoenergetic ion beam, this work extends the studies by modelling quasi-monoenergetic ion beams. We consider normalised Gaussian particle energy distribution function (F), widely used in the literature (Temporal, 2006; Honrubia et al., 2009; Gus'kov et al., 2014a, 2015), characterized by the energy variance (σ_{E}) and the initial mean energy ($\bar{E}_0$):

$$F(E_0, \bar{E}_0, \sigma_{\text{E}}) = \frac{e^{-(E_0 - \bar{E}_0)^2 / 2\sigma_{\text{E}}^2}}{\sqrt{2\pi}\sigma_{\text{E}}}, \tag{3.20}$$

where the variance also allows defining the energy spread of the beam as $\delta E = \sigma_{\text{E}} / \bar{E}_0$.

Note that the remaining conditions for both the beam and the plasma remain unchanged. The only difference lies in considering a beam whose energy is distributed as shown in Eq. 3.20. In this manner, the energy distribution function provides the number of ions of the beam per energy value. This means that in any section of this thesis involving a quasi-monoenergetic beam, there is no single energy as in the monoenergetic case, but rather a range of energies, which we denote $\mathfrak{E}_0$, such as $E_0 \in \mathfrak{E}_0$. We consider the projectiles within an interval given by $\mathfrak{E}_0 = [\bar{E}_0 - 3\sigma_{\text{E}}, \bar{E}_0 + 3\sigma_{\text{E}}]$, where "3" is an arbitrary parameter we multiply to σ_{E}, to extend the studied energy interval to the tails of the Gaussian distribution[3].

In this work, we consider two quasi-monoenergetic Gaussian beams, one generated at the edge of the precompressed fuel (G1) and one generated at a distance "d" of the edge (G2).

[3]Since the Gaussian function is infinite in extent, this restriction should avoid unreasonable large values and also assure that there are no negative energy values ($E_0 > 0$).

3.3.2.a G1: Gaussian beam at the edge of the plasma

For a non-monoenergetic beam situated at the beginning of the plasma, it is necessary to account for the different energies of the beam when simulating the interaction. The dependencies of the energy deposited by the beam are now represented as $W_{\mathrm{d,beam}}(x, t, \rho, T(x,t); \bar{E}_0, \sigma_{\mathrm{E}})$. In contrast to Eq. 3.17, the energy deposited by the beam $W_{\mathrm{d,beam}}$ is now calculated as an integral over the different initial energies E_0:

$$W_{\mathrm{d,beam}} = I \int_0^{\infty} F(E_0, \bar{E}_0, \sigma_{\mathrm{E}})\, Sp\left(x; E(x(t'); E_0), T(x,t), \rho\right) dE_0, \tag{3.21}$$

where, again, the intensity is constant and is given by $I = \sigma/\tau_{\mathrm{beam}}$. In this case, the slowing down of the projectiles varies depending on their initial energy $E_0 \in \mathfrak{E}_0$, so we explicitly state the dependence.

Following the explanations in Sect. 3.2, simulating the beam-plasma interaction requires computing simultaneously not only Eq. 3.16 and Eq. 3.18, but also Eq. 3.21:

$$\begin{aligned} T(x, \tau_{\mathrm{beam}}) &= T(x,0) \\ &+ \frac{I}{\rho\, C_{\mathrm{V}}} \int_0^{\tau_{\mathrm{beam}}} \left(\int_0^{\infty} F(E_0, \bar{E}_0, \sigma_{\mathrm{E}})\; Sp\left(x; E(x(t'); E_0), T(x,t), \rho\right)\; dE_0 \right) dt. \end{aligned} \tag{3.22}$$

Note that at each spatial position, the total stopping is calculated as the sum of the energy deposited by projectiles with different initial energies, which is then integrated over time to calculate the temperature.

Under the same assumptions for the characteristic times and the power densities, the solutions of Eq. 3.22 are, again, explicitly independent of the beam time and depend exclusively on $(\sigma, \bar{E}_0, \delta_{\mathrm{E}})$.

3.3.2.b G2: Gaussian beam separated from the plasma

When the quasi-monoenergetic beam is separated by a distance "d" from the plasma, those ions with higher energy from $\mathfrak{E}_0$ reach the edge of the fuel sphere earlier, depending on the distribution $F(E_0, \bar{E}_0, \sigma_{\mathrm{E}})$. Now, the intensity has a time and energy dependency, so it is no longer constant, in contrast to the monoenergetic or G1 cases.

In this case, a convenient form to express the power density deposited by the beam in the plasma is given by:

$$W_{\mathrm{d,beam}}(t) = \frac{\sigma P(t) Sp\left(E(x(t')), T(x,t), \rho\right)}{N_{\mathrm{p}} E_0^{\dagger}}, \tag{3.23}$$

where $E_0^\dagger$ is the energy of each projectile entering the edge of the plasma at an instant t, and $P(t)$ is the power of the beam at the edge of the fuel, derived considering the Gaussian energy distribution and the source-plasma distance (Temporal, 2006; Honrubia et al., 2009), and can be expressed as:

$$P(t) = \frac{1}{\sqrt{2\pi}} \frac{d^4 m_\mathrm{b}^2}{2t^5 \sigma_\mathrm{E}} e^{-\left[\frac{d^2 m_\mathrm{b}/2t^2 + \bar{E}_0}{\sqrt{2}\sigma_\mathrm{E}}\right]^2}. \tag{3.24}$$

Here, it is assumed that the projectiles travel at constant velocity from the source to the edge of the plasma. Therefore, the energy of each projectile entering the plasma at an instant t is calculated as $E_0^\dagger = \frac{1}{2} m_\mathrm{b} \frac{d^2}{t^2}$. Then, the characteristic time for the beam duration[4] can be estimated as $\tau_\mathrm{beam} \approx t_\mathrm{max} - t_\mathrm{min} = \sqrt{\frac{m_\mathrm{b} d^2}{2}} \left(\frac{1}{min(\mathfrak{E}_0)}^{1/2} - \frac{1}{max(\mathfrak{E}_0)}^{1/2} \right)$. Now, simulating the beam plasma interaction requires computing Eq. 3.16 and Eq. 3.18, but taking into account Eq. 3.24. Taking this into account, and after doing some straightforward calculations, the temperature field at the end of the interaction can be expressed as:

$$T(x, \tau_\mathrm{beam}) \; = T(x,0) \; + \frac{\sigma}{\rho \, C_\mathrm{V} N_\mathrm{p}} \int_0^{\tau_\mathrm{beam}} \frac{P(t) \; Sp(x; E(x), T(x,t))}{E_0^\dagger(t)} \, dt. \tag{3.25}$$

3.4 Stopping power model

The stopping power used in Eqs. 3.16 and 3.18 is given by the sum of contributions from each plasma component (Mehlhorn, 1980, 1981; Khatami & Khoshbinfar, 2020), taking into account the electron and the stripped ions fields. In the case of a pure DT plasma, the contributions come from the deuterium and tritium ions, along with the free electrons they lost. If any impurity is present, it is necessary to take into account the contributions of the dopant free electrons as $n_\mathrm{e} = n_\mathrm{e(DT)} + n_\mathrm{e(Dop)}$ and the stripped dopant ions.

$$Sp = \sum_i Sp_\mathrm{i} = Sp_\mathrm{e(D,T,dop)} + Sp_\mathrm{D} + Sp_\mathrm{T} + \sum_\mathrm{dop} Sp_\mathrm{(dop)}. \tag{3.26}$$

Here, subscript "i" denotes the plasma field considered, which contributions can be: the free electrons (e), the deuterium nuclei (D), the tritium nuclei (T) or any dopant (dop), if present. We denote m_i, n_i and Z_i as the mass, particle

[4]We note that, in the monoenergetic and the G1 cases, the beam is arranged at the edge of the fuel, so the beam time reflects the duration of the interaction within the plasma. In comparison, in the G2 case, the beam time is mostly described by the time required for the projectiles to travel the distance between the source and the fuel, so, in this case, the interaction time within the plasma is negligible in comparison.

density and charge of the "i" plasma component (D, T, electrons or dopants). On the other hand, the projectile particles are represented by atomic number Z_b and atomic mass m_b.

Concerning the stopping power, our analysis incorporates two widely employed models: the Li & Petrasso (1993a) (referred to as LP) and the Peter (1991) and Meyer-ter-Vehn (referred to as PMV), already introduced in Sect. 2.3.1. Both models share some terms, such as follows. The ratio $X_\mathrm{i} = v/v_{\mathrm{th,i}}$ between the velocity of the projectiles ($v = 2 \cdot E(x(t'))/m$) and the thermal velocity of the plasma ($v_{\mathrm{th,i}} = \sqrt{2K_\mathrm{B}T/m_\mathrm{i}}$), being K_B the Boltzmann constant. The term "erf" is the error function. We remind that e is the electron charge and ϵ_0 is the vacuum permittivity. At last, the Coulomb logarithm[5] ($\ln(\Lambda)$) term corresponds to the ratio between the Debye length (λ_D) and the impact parameter for a minimum collision distance, both for electrons and ions, ($p_{\mathrm{min_i}}$). This logarithm serves as a metric for estimating the importance of small-angle collisions large-angle scattering:

$$\ln(\Lambda)_\mathrm{i} = \ln(\lambda_{\mathrm{D_i}}/p_{\mathrm{min_i}}), \tag{3.27}$$

where,

$$\lambda_{\mathrm{D_i}} = max\left(\sqrt{\frac{4\pi\epsilon_0 K_\mathrm{B}\sqrt{T^2 + \mathcal{X}\cdot\epsilon_\mathrm{F}^2}}{4\pi(Z_\mathrm{i}e)^2 n_\mathrm{i}}}, 2\right)$$

$$p_{\mathrm{min_i}} = \sqrt{\left(\frac{Z_\mathrm{i}Z_\mathrm{b}e^2}{4\pi\epsilon_0 m_{\mathrm{r_i}} u_\mathrm{i}^2}\right)^2 + \mathcal{X}\cdot\left(\frac{\hbar}{2m_{\mathrm{r_i}}u_\mathrm{i}}\right)^2}.$$

Here, $\mathcal{X} = 1$ for the electron field and $\mathcal{X} = 0$ for the ion field. The relative mass is $m_\mathrm{r} = (m_\mathrm{i}\cdot m_\mathrm{b})/(m_\mathrm{i} + m_\mathrm{b})$, the relative velocity is $u \approx \sqrt{v^2 + v_{\mathrm{th,i}}^2}$ and the Fermi energy is $\epsilon_\mathrm{F} = 0.3646(n_\mathrm{e}[\mathrm{cm}^{-3}]/(10^{21}))^{2/3}$ eV.

In Sect. 4.1 we display some results of both PMV and LP models, as well as a comparison with the results of other authors.

3.4.1 Li-Petrasso

The Li & Petrasso (1993a) model (referred to as LP) stands as a well-established approach for assessing the behaviour of charged particles as they traverse a

[5] We have found certain differences through the literature (e.g. Li & Petrasso, 1993a; Zou et al., 2016; Deng et al., 2021). On the one hand, the thermal velocity of the plasma is often described as one dimensional ($v_{\mathrm{th,i}} = \sqrt{2K_\mathrm{B}T/m_\mathrm{i}}$), instead of three-dimensional. The term associated with $\mathcal{X}$ is also often neglected.

fusion plasma environment (Zou et al., 2016; Khatami & Khoshbinfar, 2020; Deng et al., 2021). The underpinning of the LP stopping formalism is derived from the Fokker-Planck equation and relies on an expansion of the collision operator based on the inverse of the Coulomb logarithm (Li & Petrasso, 1993b). The LP stopping power accounts for large-angle scattering, small-angle binary collisions, collective plasma oscillations, and the necessary quantum effects. These factors are subsequently adjusted to fit within a classical formalism. Its applicability is consistent for Coulomb logarithm values greater than or equal to 2, a criterion met by the experiments examined within this study. Thereby, the stopping power of the projectiles travelling through a fully ionized plasma of DT is given by the widely used expression:

$$Sp_{\mathrm{i}} = \frac{Z_{\mathrm{b}}^2 Z_{\mathrm{i}}^2 e^4 n_{\mathrm{i}}}{4\pi\epsilon_0^2 m_{\mathrm{i}} v^2} \left(G_{\mathrm{LP}}(X_{\mathrm{i}}) \cdot \ln(\Lambda)_{\mathrm{i}} + \Theta(X_{\mathrm{i}}) \cdot \ln(1.123 X_{\mathrm{i}}) \right) \tag{3.28}$$

with

$$\begin{aligned} G_{\mathrm{LP}}(X_{\mathrm{i}}) = &- \left(1 + \frac{m_i}{m_{\mathrm{b}}}\right) \frac{2}{\sqrt{\pi}} X_{\mathrm{i}} e^{-X_{\mathrm{i}}^2} \\ &+ \left(1 + \frac{m_i}{m_{\mathrm{b}}} \frac{1}{\ln(\Lambda)_{\mathrm{i}}}\right) \mathrm{erf}\left(X_{\mathrm{i}}\right). \end{aligned} \tag{3.29}$$

Here, Θ is the step function, with a value of 0 for $X_{\mathrm{i}}^2 \leq 1$ and a value of 1 for $X_{\mathrm{i}}^2 > 1$. Throughout this work, we use the LP model in our simulations, unless specifically noted.

3.4.2 Peter and Meyer-ter-Vehn

The Peter and Meyer-ter-Vehn (Peter, 1991) model was developed in a classical statistical context, within the framework of kinetic theory. Here, we present the analytical approximation of the PMV model, which is valid when $Z_{\mathrm{b}}/(n_{\mathrm{i}}\lambda_{D_{\mathrm{i}}}^3) < 1$, as shown below:

$$Sp_{\mathrm{i}} = \frac{Z_{\mathrm{b}}^2 Z_{\mathrm{i}}^2 e^4 n_{\mathrm{i}}}{4\pi\epsilon_0^2 m_{\mathrm{i}} v^2} \cdot \left(G_{\mathrm{PMV}}(X_{\mathrm{i}}) \cdot \ln(\Lambda) + H(X_{\mathrm{i}}) \cdot \ln(X_{\mathrm{i}}) \right), \tag{3.30}$$

with:

$$G_{\mathrm{PMV}}(X_{\mathrm{i}}) = -\sqrt{\frac{2}{\pi}} \cdot X_{\mathrm{i}} \cdot e^{-\frac{X_{\mathrm{i}}^2}{2}} + \mathrm{erf}\left(\frac{X_{\mathrm{i}}}{\sqrt{2}}\right)$$

$$H(X_{\mathrm{i}}) = \frac{-X_{\mathrm{i}}^3 \cdot e^{-\frac{X_{\mathrm{i}}^2}{2}}}{3\sqrt{2\pi}} + \frac{X_{\mathrm{i}}^4}{X_{\mathrm{i}}^4 + 12}.$$

3.5 Characteristic parameters of the heated region

After the ion beam interaction, the heated region of the plasma is completely characterized by its temperature field ($T(x) = T(x, \tau_{\rm beam})$), obtained from Eq. 3.19. For example, in Fig. 3.4 we have depicted three temperature distributions of a heated plasma (T_0=1 keV, ρ=500 g/cm^3) obtained after the interaction with an ion beam of C^{6+} (σ=2.9·10^{10} cm^{-2}) at three different kinetic energies: E_0=125, E_0=400 and E_0=675 MeV. In this figure, we also highlight several relevant characteristic parameters of the heated region, such as the temperature at the edge of the plasma ($T_{\rm x=0} = T(x = 0)$), the plasma initial temperature (T_0), the maximum temperature ($T_{\rm max}$) and its associated position ($x_{\rm T_{max}}$). Additionally, the total heated length or range ($L_{\rm h}$) is defined as follows[6]:

$$L_{\rm h} = \int_{E_0}^{0} \frac{dE}{-Sp(x, E(x); T(x))} dx. \tag{3.31}$$

Then, the mean temperature of the heated region is calculated from the distribution of temperatures:

$$T_{\rm h} = \frac{1}{L_{\rm h}} \int_{L_{\rm h}} T(x) dx. \tag{3.32}$$

As the beam is focused symmetrically in the centre of the spherical fuel, the heated region is a cylinder-alike volume of $V_{\rm h} = \pi r_{\rm b}^2 L_{\rm h}$ with radial symmetry in the temperature. Note that the energetic variation of the heated region must be equal to the energy of the beam, $\Delta E_{\rm h} = E_{\rm b}$, this is, $\rho\, C_{\rm V}(T_{\rm h} - T_0)V_{\rm h} = N_{\rm p} E_0$. Therefore, the temperature of the heated region can be expressed in terms of the initial parameters of the experiment as:

$$T_{\rm h} = T_0 + \frac{\sigma E_0}{\rho\, C_{\rm V} L_{\rm h}}. \tag{3.33}$$

This equation is also valid for the quasi-monoenergetic cases by considering the mean energy, $\bar{E}_0$. In addition, this equation includes the length of the

[6]This expression considers a monoenergetic beam. In the G1 case of a quasi-monoenergetic beam, the formula also applies, but integrates from the projectile with maximum energy ($max(\mathfrak{E}_0)$) to zero. In the G2 case, the final length of the heated region depends on the energy distribution. It is obtained after calculating the energy deposition of the projectiles according to their initial energy taken from the distribution $\mathfrak{E}_0$, whilst the heating is taking place and determining how far they reach. Among the depths obtained for each energy, the overall maximum range is selected. Regardless of the type of beam, numerically we calculate the range by evaluating the temperature, starting from the edge where the beam enters and continuing until the last value such that $T(x) > T_0$, that is, before returning to the cold plasma.

heated region, so it can be considered as a constraint on the quantities T_h and L_h. The relationship between the heated region and the experimental conditions of both the beam and the plasma can described by the quantity $(T_\mathrm{h} - T_0)L_\mathrm{h} = \Delta T_\mathrm{h} L_\mathrm{h} = \sigma E_0/(\rho\, C_\mathrm{V})$.

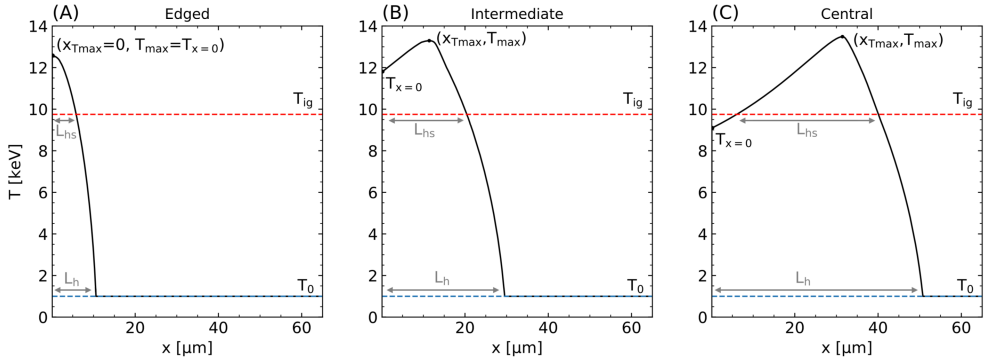

FIGURE 3.4— Spatial distribution of temperatures achieved after the interaction of a C^{6+} beam (σ=2.9·10^{10} cm^{-2}) with a DT plasma of T_0=1 keV and density ρ=500 g/cm^3, (A) for an edge hot-spot (E_0=125 MeV), (B) an intermediate hot-spot (E_0=400 MeV), and (C) a central hot-spot (E_0=675 MeV).

3.6 Self-heating and ignition gains

Our interest lies in examining the conditions for attaining self-heating, ignition, and subsequent combustion of the stagnated fuel. After the interaction with the beam, the internal processes of the plasma govern the evolution within the heated zone. In-depth investigations into the ignition process require sophisticated 2D or 3D radiative-hydrodynamic numerical simulations to accurately depict the spatial and temporal evolution of a heated region. However, many interesting features of the early evolution of the heated plasma are described by a zero-dimensional power balance model, as already advanced in Sect. 2.3.2. Considering the energetic processes of Eq. 3.15 in a zero-dimensional approximation, after the beam interaction has ended ($W_\mathrm{d,beam} = 0$), the temperature variation is written as:

$$\frac{dT(t)}{dt} = \frac{1}{\rho\, C_\mathrm{V}} \left(W_\mathrm{fus,dep}(t) - W_\mathrm{mec}(t) - W_\mathrm{cond}(t) - W_\mathrm{rad}(t)\right). \tag{3.34}$$

Here, the power density terms are: the electron heat conduction (W_cond), the electron radiation emission (W_rad), the mechanical work (W_mec) and the

fusion reactions deposited in the evaluated volume ($W_{\mathrm{fus,dep}}$). The expressions for every power density are presented in the following Sect. 3.8.

From Eq. 3.34, analysed after the beam interaction, we obtain the self-heating condition of any heated region. This condition is fulfilled if there is a positive variation on the temperature ($dT(t)/dt \geq 0$), that is, if the gain term $W_{\mathrm{fus,dep}}$ is greater than the power density loss terms $W_{\mathrm{loss}} = W_{\mathrm{mec}} + W_{\mathrm{cond}} + W_{\mathrm{rad}}$ (Gus'kov et al., 2011; Atzeni & Meyer-Ter-Vehn, 2004). This criterion can be expressed through the self-heating gain, defined as:

$$G_{\mathrm{sh}} = \frac{W_{\mathrm{fus,dep}}(\rho, R, T)}{W_{\mathrm{loss}}(\rho, R, T)}, \tag{3.35}$$

where the condition is fulfilled for a region characterized by (ρ, R, T) when $G_{\mathrm{sh}}(\rho, R, T) \geq 1$. The minimum of the self-heating curve $(R_{\mathrm{sh,min}}, T_{\mathrm{sh,min}})$ points out the threshold temperature for the ignition criterion ($T_{\mathrm{sh,min}} = T_{\mathrm{ig}}$). This ignition temperature is also displayed in Fig. 3.4, to indicate which region of the heated plasma is above it.

On the other hand, the zero-order approximation can also describe the early time evolution in temperature and volume of the heated region (Atzeni & Meyer-Ter-Vehn, 2004). From such modelling, a criterion that assures a sustained increment of the temperature over time is obtained, guaranteeing a posterior burning of the precompressed DT fuel. That is, given a region of interest (or *spark*), we can evaluate its capacity to accrete mass and eventually raise its temperature. The reasoning that leads to this criterion is explained in Sect. 2.3.2. Roughly, it is required that the energy density gained, normalised by the energy density of the hot-spot, grows over time. This change is governed by the emission of radiation and α-particles from the heated region, which are absorbed by the surroundings, enlarging the heated region itself. It can be expressed through the ignition gain:

$$G_{\mathrm{ig}} = \frac{\left(W_{\mathrm{fus},\alpha}(\rho, R, T) - W_{\mathrm{rad}}(\rho, R, T)\right) \tau_0^*}{3\mathcal{E}_0} \tag{3.36}$$

and the criterion is fulfilled when $G_{\mathrm{ig}}(\rho, R, T) \geq 1$. Here, $\tau_0^* = R\sqrt{2\rho/\mathcal{E}_0}$ is a characteristic ignition time (lower than compression time), $W_{\mathrm{fus},\alpha}$ refers to the total energy yielded by α-particles (see Sect. 3.8), $\mathcal{E}_0 = 3\rho\Gamma_B T$ is energy per mass unit, which is obtained from the temperature of the hot-spot to evaluate. We assume the plasma as an ideal gas, with $\Gamma_B = \bar{R}/A_{\mathrm{DT}}$ ($\bar{R}$ is the molar gas constant).

Both gains allow characterizing a heated region with the (ρ, R, T) parameters. In particular, $G_{\mathrm{sh}} = 1$ and $G_{\mathrm{ig}} = 1$ are thresholds for cases where the condition is achieved or not.

We note that the presence of impurities in a DT plasma modifies the density of the plasma and the power densities of the internal processes, thereby changing the ignition and self-heating conditions with respect to the pure case. If a dopant is introduced in the fuel it is necessary to consider the element and its concentration, so previous Eqs. 3.35 and 3.36 have an implicit dependence such as $G_{\rm sh}(\rho, R, T; Z_{\rm I}, \xi)$ and $G_{\rm ig}(\rho, R, T; Z_{\rm I}, \xi)$. Thereafter, in next Sect. 3.7 (Figs. 3.5 and 3.6) we illustrate the plasma $(\rho R, T)$-space and we determine the set of parameters that achieve the conditions presented in this section under different circumstances.

Notably, these criteria (through Eqs. 3.35 and 3.36) can also be considered in the parameter space (σ, E_0) of the beam, which fulfil the conditions $G_{\rm sh}(Z_{\rm b}, E_0, \sigma) \geq 1$ and $G_{\rm ig}(Z_{\rm b}, E_0, \sigma) \geq 1$, for a given plasma ($\rho$,$T_0$). This type of relation between the characteristics of the beam and the heated plasma is one of the main goals of this thesis.

3.7 Solutions of $G_{\rm sh}$ and $G_{\rm ig}$ in the $(\rho R, T)$-space

According to Eqs. 3.35 and 3.36 we can retrieve the (ρ, R, T)-space of the plasma and identify the parameter set that fulfils these conditions across various scenarios. After some manipulations, these equations can be retrieved in the $(\rho R, T, [\rho])$-space, with a weak dependence on the density of the plasma ($[\rho]$). For instance, in Fig. 3.5 we consider a pure DT plasma and display the solutions of $G_{\rm sh} = 1$ (dashed line) and $G_{\rm ig} = 1$ (solid line) in this space, considering a pure DT plasma. The region above each curve fulfils the self-heating and ignition criteria, respectively.

We mark the minimum of the self-heating curve with a vertical dashed line. This line matches the threshold temperature ($T_{\rm sh,min} = T_{\rm ig}$) used for the ignition criterion. We highlight with a coloured region those cases above the ignition curve that also fulfil $T > T_{\rm ig}$. This corresponds to the scenarios where we find a successful formation of the hot-spot, given a set of $(\rho R, T)$ plasma values. In following Sect. 3.9, we explain with more detail our definition for a hot-spot and, in particular, how we determine it from the distribution of temperatures generated by the beam. The blank region with $T > T_{\rm ig}$, but below the ignition curve, corresponds to those *sparks* that are not able to reach burning. The colour gradient represents the burning gains achieved for each ρR-T pair, which we will explain later, in Sect. 3.11.

For this pure DT scenario, the minimum areal density of the self-heating curve is $\rho R_{\rm sh,min} \approx 0.4$ g/cm^2. For this value, the self-heating curve has semi-flat behaviour between 8 and 12 keV, which are common values found in the literature to establish a temperature threshold for the ignition. In our case,

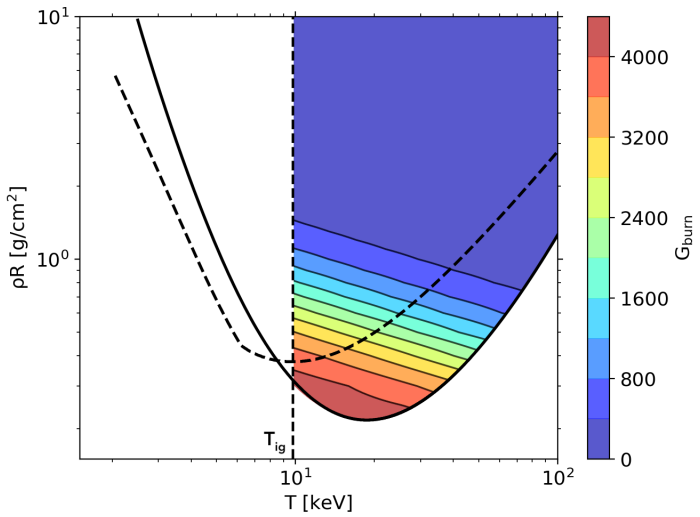

FIGURE 3.5— Ignition and self-heating diagram (ρR, T) of a pure DT plasma at ρ=500 g/cm^3. The solid line represents the solutions for $G_{\rm ig} = 1$, while the dashed line show the solutions for $G_{\rm sh} = 1$. Ignition temperature $T_{\rm ig}$ is shown as a vertical dashed line. The coloured area corresponds to those (ρR, T) where the hot-spot conditions are fulfilled. The colour gradient represents the burning gain for such conditions (presented below, in Sect. 3.11), considering a plasma sphere of $R_{\rm F}$=50 μm and density of ρ=500 g/cm^3.

we select the value that matches the exact minimum of $G_{\rm sh} = 1$, which is $T_{\rm sh,min} = T_{\rm ig} \approx 10$ keV. For temperatures lower than $T_{\rm ig} \approx 10$ keV, there are fulfilling solutions above the self-heating and ignition curves. However, when the plasma is that cold, the fusion power is not high enough (see Figs. 3.7 and 3.8) and the hot-spots would be unnecessary large and not that efficient. In fact, the most interesting region is that above the ignition curve but below the self-heating curve, this is at low values of ρR and temperatures above the threshold, but as close to $T_{\rm sh,min}$ as possible. In this zone, the propagation of the combustion will occur, while the plasma requirements are minimal (the required hot-spot is small and not very hot), also ensuring maximum values of the burning gain. It is worth mentioning, the minimum energy associated to those points, beginning with the self-heating. Although $\rho R_{\rm sh,min}$ and $T_{\rm sh,min}$ remain almost constant with the plasma density, in this case it does influence the result of the energy, finding $E_{\rm sh,min} = 2530$ J for $\rho = 300$ g/cm^2, $E_{\rm sh,min} = 955$ J for $\rho = 500$ g/cm^2 and $E_{\rm sh,min} = 522$ J for $\rho = 700$ g/cm^2. Similarly, for the ignition curve we find the minimum at, approximately, 0.22 g/cm^2 and 18 keV, which corresponds to minimum ignition energies of $E_{\rm ig,min} = 1010$, 360 and 180 J, for each respective density.

As another example, in Fig. 3.6 we have depicted the self-heating curve for a DT plasma including impurities of Be, C, Al and Cu at different concentrations, obtained from the condition $G_{\rm sh}(\rho R, T, Z_{\rm I}, \xi) = 1$. As explained above, for a given self-heating curve, the plasma parameters that fulfil the self-heating criterion are those located above the curve. The figure shows that the shape of the figure has a minimum $(\rho R_{\rm sh,min}(Z_{\rm I}, \xi), T_{\rm ig}(Z_{\rm I}, \xi))$. As the concentration of the impurity increases, the value of the minimum is shifted to higher values of the areal density and temperature, which implies that the set of values of $(\rho R_{\rm sh}(Z_{\rm I}, \xi), T_{\rm ig}(Z_{\rm I}, \xi))$ is reduced.

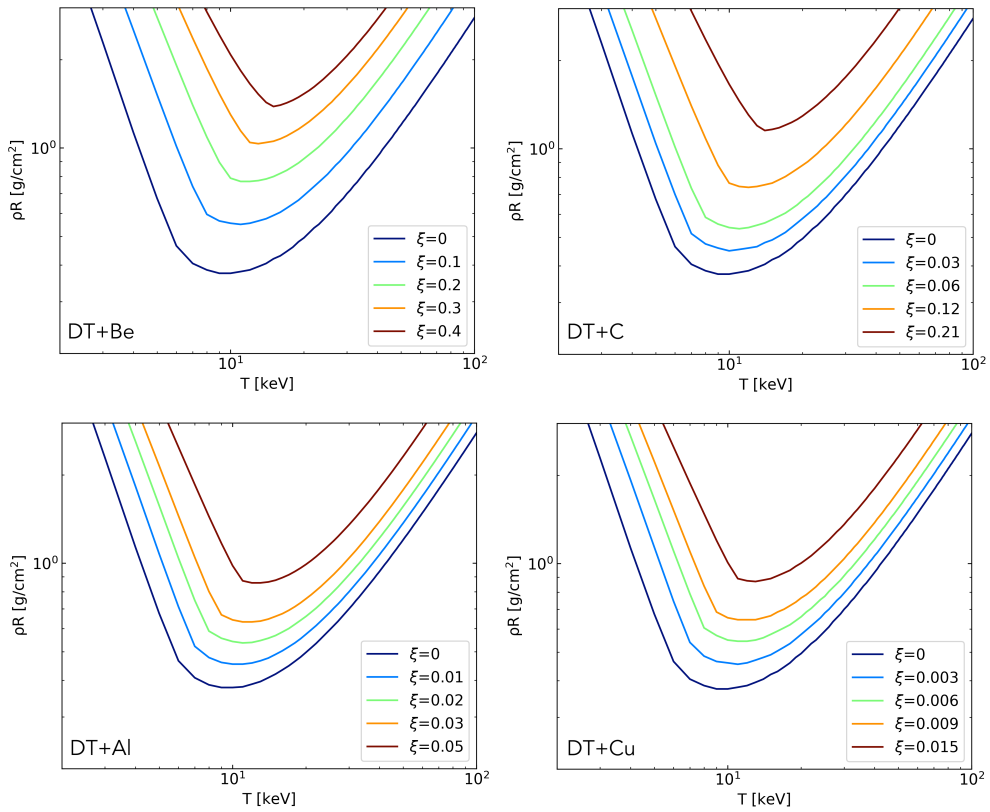

FIGURE 3.6— Self-heating diagrams $(\rho R, T)$ of a DT plasma ($\rho_{\rm DT}$=500 g/cm^3) doped with B, C, Al and Cu at different fractions.

For instance, for the pure DT plasma (as in Fig. 3.5) the minimum are $\rho R_{\rm sh,min}(Z_{\rm I}, \xi) \approx 0.4$ g/cm^2 and $T_{\rm ig}(Z_{\rm I}, \xi) \approx 10$ keV. Meanwhile, for a plasma doped with Be, the values of these parameters for $\xi = 0.3$ are 1 g/cm^2 and 13 keV, and for $\xi = 0.4$ are 1.4 g/cm^2 and 15 keV. The figure also shows that

the effect of the impurity is more pronounced as its atomic number increases. For a concentration of about $\xi \approx 0.2$ of a beryllium or carbon impurity, the values of $R_{\mathrm{sh,min}}(Z_{\mathrm{I}}, \xi)$ and $T_{\mathrm{ig}}(Z_{\mathrm{I}}, \xi)$ are 0.8 g/cm^2 and 11 keV for Be and 1.2 g/cm^2 and 14 keV for C. Although not represented, we have found that, even for a much lower concentration of Cu ($\xi = 0.015$), the values obtained for the minimum are 0.9 g/cm^2 and 13 keV, which are of the same order as those obtained for Be and C at $\xi = 0.2$. In general, we have found that the ignition curve moves towards regions of higher areal density and temperature with heavier dopants or higher concentrations.

3.8 Power densities

In order to evaluate the self-heating and ignition gains, in this section we present the power density terms. Unless noted, expressions use the SI units. Hereafter, k is the Coulomb constant, h is the Planck constant, c is the speed of light, and $\ln(\Lambda)$ is the Coulomb logarithm defined in Eq. 3.27, T and R are the temperature and the radius of the studied plasma region, respectively.

3.8.1 Nuclear fusion energy deposition

In the case of a DT precompressed fuel, the heating associated with the fusion energy deposition is determined by the rate of the DT reactions and the energy[7] transferred by the α-particles and neutrons to the plasma:

$$W_{\mathrm{fus,dep}} = n_{\mathrm{D}} n_{\mathrm{T}} \langle \sigma_{\mathrm{fus}} v \rangle (\eta_\alpha E_\alpha + \eta_{\mathrm{n}} E_{\mathrm{n}}) \quad [\mathrm{MeV/cm^3 s}]. \tag{3.37}$$

Here, it is worth noting that after performing some straightforward transformation (see Sect. 3.1) $n_{\mathrm{D}} n_{\mathrm{T}}$ is equivalent to $\rho N_{\mathrm{A}}/(2(1+\xi)m_*)$, to express the dependency with the material density (ρ).

Then, $E_\alpha = 3.52$ MeV and $E_{\mathrm{n}} = 14.06$ MeV are the initial energies, while η_α and η_{n} are the energy fractions for the α-particles or the neutrons, respectively. The fusion reaction rate is $\langle \sigma_{\mathrm{fus}} v \rangle$, which is calculated using the model proposed by Bosch & Hale (1992). This model, as expressed in Atzeni & Meyer-Ter-Vehn (2004), is written as:

$$\langle \sigma_{\mathrm{fus}} v \rangle = C_1 \zeta^{-5/6} \phi^2 \exp(-3\zeta^{1/3}\phi) \quad [\mathrm{cm^3/s}]. \tag{3.38}$$

Here, the temperature is expressed in keV

$$\zeta = 1 - \frac{C_2 T + C_4 T^2 + C_6 T^3}{1 + C_3 T + C_5 T^2 + C_7 T^3} \tag{3.39}$$

$$\phi = C_0 / T^{1/3} \tag{3.40}$$

[7] Previously noted Q, in Chapter 2.

The reaction fit of the DT fusion process ($D+T \rightarrow \alpha+n$) is valid in the range of temperatures 0.2-100 keV with an error of $< 0.25\%$, with the coefficients:

C_0 [keV$^{1/3}$]	$C_1 \cdot 10^{16}$ [cm^3/s]	$C_2 \cdot 10^3$ [keV^{-1}]	$C_3 \cdot 10^3$ [keV^{-1}]	$C_4 \cdot 10^3$ [keV^{-2}]	$C_5 \cdot 10^3$ [keV^{-2}]	$C_6 \cdot 10^3$ [keV^{-3}]	$C_7 \cdot 10^3$ [keV^{-3}]
6.6610	643.41	15.136	75.189	4.6064	13.500	-0.10675	0.01366

The energy fraction transferred by the α-particles to the studied volume of radius R can be calculated approximately using the expression from Gus'kov et al. (2011):

$$\eta_\alpha = \begin{cases} \frac{3}{2}\frac{R}{\lambda_\alpha} - \frac{1}{2}\left(\frac{R}{\lambda_\alpha}\right)^2 & R \leq \lambda_\alpha \\ 1 & R > \lambda_\alpha \end{cases} \tag{3.41}$$

where, in SI units

$$\lambda_\alpha = \frac{3(T \cdot K_\mathrm{B})^{3/2} E_\alpha^{1/2} m_\alpha^{1/2} m_\mathrm{n} A_*}{4\pi^{1/2} \ln(\Lambda_{\alpha\mathrm{e}}) m_\mathrm{e}^{1/2} e_\alpha^2 e^2 \rho\ Z_* \cdot k^2} \quad [m], \tag{3.42}$$

where m_n and m_α are the mass of the neutrons and α-particles, respectively. The Coulomb logarithm considers the interaction between α-particles and the free electrons.

At last, the energy fraction deposited in the plasma by the neutrons accounts for only the elastic collisions, because the cross-sections for inelastic scattering of neutrons by low-Z nuclei is significantly lower than those for elastic interactions (Atzeni & Meyer-Ter-Vehn, 2004). The energy fraction transferred by neutrons can be deduced, under certain approximations, as:

$$\eta_\mathrm{n} \approx \left[0.12 + 0.6\frac{A_\mathrm{dop} \cdot \xi}{(1 + A_\mathrm{dop})^2}\right] \cdot \frac{\rho R\ [\mathrm{g/cm^2}]}{A_*(1+\xi)}. \tag{3.43}$$

In Eq. 3.36, we denote $W_{\mathrm{fus},\alpha}(T, R)$ to denote the total energy carried out by the α-particles ($\eta_\alpha = 1$), neglecting the neutron contribution of the fusion ($\eta_\mathrm{n} = 0$).

3.8.2 Radiation loss

The energy losses for plasma self-radiation, W_rad, described by the emissivity of a fully ionized plasma (Zel'dovich & Raizer, 2001), are given by

$$W_\mathrm{rad} = \delta_\mathrm{r} \cdot \frac{32\pi}{3}\sqrt{\frac{2\pi K_\mathrm{B} T}{3m_\mathrm{e}}} \cdot \frac{Z_*(Z_*^2) e^6 \rho^2}{m_\mathrm{e} m_\mathrm{n}^2 A_*^2 c^3 h} \cdot k^3 \quad [\mathrm{J/m^3 s}]. \tag{3.44}$$

Here, $\delta_{\rm r}$ represents the fraction of thermal radiation energy lost from the volume of plasma, accounting for the absorption of the absorption of intrinsic radiation from the plasma. The value of $\delta_{\rm r}$ can be obtained with high accuracy (errors lower than 2%) as Gus'kov & Sherman (2016) described

$$\delta_{\rm r} = \left[1 + 1.56 \sqrt{\frac{R[\rm cm]}{\lambda_{\rm T}[\rm cm]}} \right]^{-1}, \tag{3.45}$$

where $\lambda_{\rm T}$ is the range of thermal photons with energy $h\nu = K_{\rm B}T$

$$\lambda_{\rm T} = 3.53 \frac{T^{7/2} A_*^2}{\rho^2 A_{\rm DT}^2 (Z_*^2) Z_*} \quad [\rm cm]. \tag{3.46}$$

3.8.3 Conduction loss

The energy losses related to electron heat conduction are given by Spitzer (1962)

$$W_{\rm cond} = 3k_0 \frac{T}{R^2} \quad [\rm J/m^3 s], \tag{3.47}$$

where k_0 is the electron thermal conductivity,

$$k_0 = 9.45 \left(\frac{2}{\pi} \right)^{\frac{3}{2}} \cdot \frac{K_{\rm B}(K_{\rm B}T)^{5/2} 0.472}{m_{\rm e}^{1/2} e^4 \ln(\Lambda_{\rm ee})(Z_* + 4) k^2} \quad [\rm J/K\ m\ s]. \tag{3.48}$$

Again, the previously presented Coulomb logarithm was used, considering only the free electron interactions in this case.

3.8.4 Mechanical work loss

The specific thermal losses of a spherical ignitor due to the work associated with the pressure force, $W_{\rm mec}$ are given by Gus'kov & Sherman (2016):

$$W_{\rm mec} = 3\beta \frac{\rho}{R} \left(T \cdot (\gamma - 1) C_{\rm V} \right)^{3/2} \quad [\rm J/m^3 s], \tag{3.49}$$

with $\beta = [2/(1+\gamma)]^{1/2}$, where the adiabatic exponent $\gamma = 5/3$ for a monoatomic gas with 3 degrees of freedom.

3.9 Definition and characterization of the hot-spot

Within the heated range, we consider a region of special interest named the hot-spot (hs), which, if found, assures the posterior burning of the fuel. A hot-spot necessarily fulfils: $T_{\rm hs} \geq T_{\rm ig}$ and a pair $(R_{\rm hs}, T_{\rm hs})$ such that the ignition gain is $G_{\rm ig} \geq 1$ (using Eq. 3.36).

The procedure we follow to detect any hot-spot in our heated plasma is:

1. Using the self-heating criterion we calculate the threshold temperature for the ignition ($T_{\mathrm{sh,min}} = T_{\mathrm{ig}}$), which is found associated with the minimum areal density ($\rho R_{\mathrm{sh,min}}$) obtained when solving $W_{\mathrm{fus,dep}}/W_{\mathrm{loss}} = 1$ for a given plasma (Eq. 3.35). This is illustrated below, in Sect. 3.7.

2. From the distribution of temperatures $T(x)$ calculated with Eq. 3.16 and 3.18, we search for points with temperature over the ignition temperature $T(x) > T_{\mathrm{ig}}$. If existent, such region is classified as "*spark*", as a candidate to be a hot-spot. We define a length for the *spark* (L_{spark}) and the mean temperature of such region as:

$$T_{\mathrm{spark}} = \frac{1}{L_{\mathrm{spark}}} \int_{L_{\mathrm{spark}}} T(x)dx. \tag{3.50}$$

3. Then, as the power terms from Eq. 3.34 assume spherical geometry, we need to calculate a radius R_{spark} associated with our *spark* (or candidate hot-spot). To do so, we take into account the actual 3D geometry of the problem. After the beam heating, we find a cylinder with a radius equal to beam radius r_{b} and a length of L_{spark}. Then, we approximate our cylindrical *spark* as a homogeneous and spherical one, considering that both geometries share the same volume (V_{spark}). Thus, we calculate the radius R_{spark} of the sphere associated with our cylindrical *spark* as $R_{\mathrm{spark}} = (\frac{3}{4}\, r_{\mathrm{b}}^2\, L_{\mathrm{spark}})^{1/3}$.

4. Once calculated the set $(R_{\mathrm{spark}}, T_{\mathrm{spark}})$ we evaluate if $G_{\mathrm{ig}}(R_{\mathrm{spark}}, T_{\mathrm{spark}}) > 1$, to confirm that such *spark* is, or will be, an actual hot-spot capable of burning the fuel. In affirmative case, we abandon the "spark" notation and use "hs" for hot-spot.

Figure 3.4 also exemplifies the hot-spots found within the different spatial distribution of temperatures. Depending on the characteristics of the beam, we find three different lengths of the hot-spot (L_{hs}), which are associated with a mean hot-spot temperature (T_{hs}, calculated using Eq. 3.50). Moreover, depending on the location of the hot-spot, they can be classified as edge, intermediate and central hot-spots. Intermediate and central hot-spots occur when the projectiles lose most of their energy immediately before the particles come to rest. This is due to the cross-section of the interacting projectiles increasing as their energy decreases. As it shown in Sect. 3.4, the energy lost by the projectiles decreases inversely with the square of their velocity. In such situation, a maximum of the stopping power appears away from the initial position, which is denoted as the Bragg peak. Conversely, the edge hot-spot (panel A) is found

when the maximum temperature is reached at the beginning of the plasma; that is, found when $T_{\mathrm{x=0}} = T_{\max}$ and $x_{\mathrm{Tmax}} = 0$. The intermediate hot-spot (panel B) is found when the maximum temperature is reached away from the beginning of the plasma, but the temperatures in the edge still fulfil the ignition criterion ($T_{\mathrm{x=0}} \geq T_{\mathrm{ig}}$ and $x_{\mathrm{Tmax}} \neq 0$). Finally, the central hot-spot (panel C) is found when all the points with temperatures above the ignition criterion are away from the edge in a well-localized region, that is, $T_{\mathrm{x=0}} < T_{\mathrm{ig}}$ and $x_{\mathrm{Tmax}} \neq 0$. It is worth noting that the terminology "central" is associated with the idea of finding the hot-spot away from the edge ($T_{\mathrm{x=0}} < T_{\mathrm{ig}}$), but it is not related to finding the hot-spot exactly in the centre of the fuel sphere.

We are also interested in the energy variation of the hot-spot with respect to the cold plasma: $\Delta E_{\mathrm{hs}} = \rho C_{\mathrm{V}}(T_{\mathrm{hs}} - T_0)V_{\mathrm{hs}}$. This quantity is important in order to measure how much energy from the beam is deposited in the region able to initiate the burning; in other words, the hot-spot. Thus, the coupling is defined as the ratio between the hot-spot energy and the beam energy $\Delta E_{\mathrm{hs}}/E_{\mathrm{b}}$.

3.9.1 Evaluation of the power densities and the characteristic times

Once the parameters that characterise the hot-spot have been presented, we can address the significance of the power densities and the characteristic times associated to the processes of the system. To begin with, we can calculate the power density values from the previous expressions of Sect. 3.8, given a temperature (T_{hs}) and a radius (R_{hs}). As an example of the behaviour of such processes, in Fig. 3.7 we fix the radius of the hot-spot to $R_{\mathrm{hs}} = 15$ μm and calculate the power density values at different temperatures, considering a pure DT fuel with density $\rho = 500$ g/cm^3.

Our simulations consider that the plasma processes are negligible during the interaction, either because their times are slower than the beam time or their power densities are lower compared to the power density of the beam ($W_{\mathrm{d,beam}}$). More precisely, $W_{\mathrm{d,beam}}$ should be larger than the addition of the internal processes of gain and loss ($W_{\mathrm{fus,dep}} - W_{\mathrm{loss}}$). As can be seen in the figure, for temperatures below 5 keV the contribution of the processes is very small and, moreover, the energy contribution of the fusion processes cancels out with the rest of the processes. Then, for increasing temperatures, the fusion gain wins over the power losses. For example, in the case of Fig. 3.8, for a density of $\rho = 500$ g/cm^3, a hot-spot of temperature $T_{\mathrm{hs}} = 15$ keV and a radius of $R_{\mathrm{hs}} = 15$ μm, the hot spot has a net power density of $W_{\mathrm{fus,dep}} - W_{\mathrm{loss}} = 3.1 \cdot 10^{23}$ J/cm^{3}s. In contrast, the associated beam that creates such hot-spot have a power of $W_{\mathrm{d,beam}} \approx 3.5 \cdot 10^{23}$ J/cm^{3}s for proton projectiles, $8 \cdot 10^{23}$ J/cm^{3}s for carbon and $1.6 \cdot 10^{24}$ J/cm^{3}s for vanadium. In the typical temperature range in which

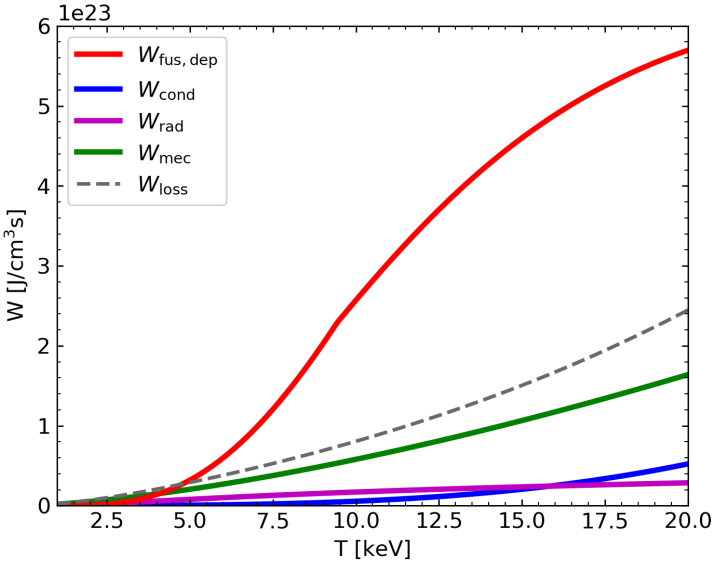

FIGURE 3.7— Contribution of the different power density terms as a function of the temperature in a pure DT plasma of density $\rho_{DT} = 500$ g/cm^3, with radius of 15 μm.

the beam would act, 1-20 keV, we find that the power of our beam is higher than that of the processes. However, depending on the experimental characteristics, the processes might become significant for the hot-spot simulation.

We propose another example understand better the behaviour of power densities. In this case, we chose another matter density value ($\rho_{DT} = 300$ g/cm^3) and extend the temperature range to see a more general behaviour. We represent these terms for both a pure and a doped plasma with beryllium at a concentration of $\xi = 0.1$. The results found are comparable to those of Zou et al. (2016) (figure 5-c). With this figure we explore higher temperatures, thus, we can qualitatively identify how, above a certain temperature, the losses overcome the fusion gain, making self-heating impossible. Besides, with respect to the pure case, the presence of an impurity increases the fusion power density but also raises the losses due to radiation and mechanical work more quickly. As we will show in Chapter 6, when a dopant is introduced in the plasma, to reach the same hot-spot conditions as in a pure DT case, the requirements of the beam are higher.

To further assure the validity of our modelling, it is also necessary to inspect the characteristic times of the system. Besides inspecting the relevance of the power densities, checking the characteristic times in each moment serves to

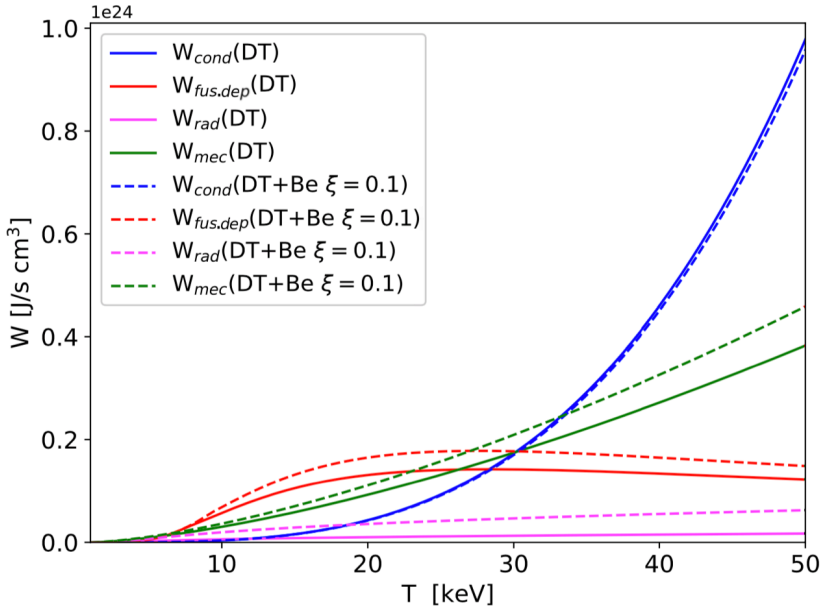

FIGURE 3.8— Contribution of the different power density terms as a function of the temperature in a pure DT plasma ($\rho_{\mathrm{DT}} = 300$ g/cm^3) and a doped DT plasma ($\rho_{\mathrm{DT+Be}(\xi=0.1)} = 408.2$ g/cm^3), both with radius of 15 μm.

evaluate the validity of our modelling. To begin with, the characteristic times associated to the processes inside the hot-spot of the plasma can be calculated as the quotient between the energy of the studied region and the power density of the process of interest ($W_{\mathrm{fus,dep}}$, W_{rad}, W_{mec}, W_{cond}):

$$\tau_{\mathrm{proc}} = \frac{\mathcal{E}_{\mathrm{hs}}}{W_{\mathrm{proc}}(T_{\mathrm{hs}}, R_{\mathrm{hs}})} \tag{3.51}$$

where the energy density can be calculated as $\mathcal{E} = \rho C_{\mathrm{V}} T_{\mathrm{hs}}$. These characteristic times give us information about the rate of energy change in the hot-spot due to each corresponding process.

On the other hand, another time worth inspecting is the hydrodynamic time of the hot-spot, which allows us to estimate the time in which the hot-spot mass remains confined and, therefore, there are no convective mechanisms, as our approximation implies. The hydrodynamic characteristic time is obtained as:

$$\tau_{\mathrm{hyd}} = \frac{R_{\mathrm{hs}}}{2c_s}\sqrt{\frac{R_{\mathrm{F}}}{R_{\mathrm{hs}}}} \tag{3.52}$$

with $c_s = \sqrt{2k_BT/m_*}$, where m_* is the average mass of the fuel ions.

In Fig. 3.9 we show the characteristic time of the hydrodynamic and plasma processes. Again, we select a hot-spot radius of $R_{hs} = 15$ μm and perform the study in a typical range of temperatures ($T_{hs} = 1 - 20$ keV), with a density of $\rho = 500$ g/cm^3. The characteristic time associated to conduction presents the larger values, except for higher temperatures. Meanwhile, the faster time is the one associated to the deposition of fusion energy in the hot-spot, except for lower temperatures. The rest of processes falls within these two characteristic times. It is worth noting that at low temperatures the power density of the processes is very short, so even if the characteristic time is large the process is negligible. We take $\tau_{fus,dep}$ as representative of the processes, given that it gives the lowest time values. Operating with ion beams associated to times shorter than the fusion time, ensures the confinement of the hot-spot and that there is no appreciable contribution of the internal processes during the beam-plasma interaction.

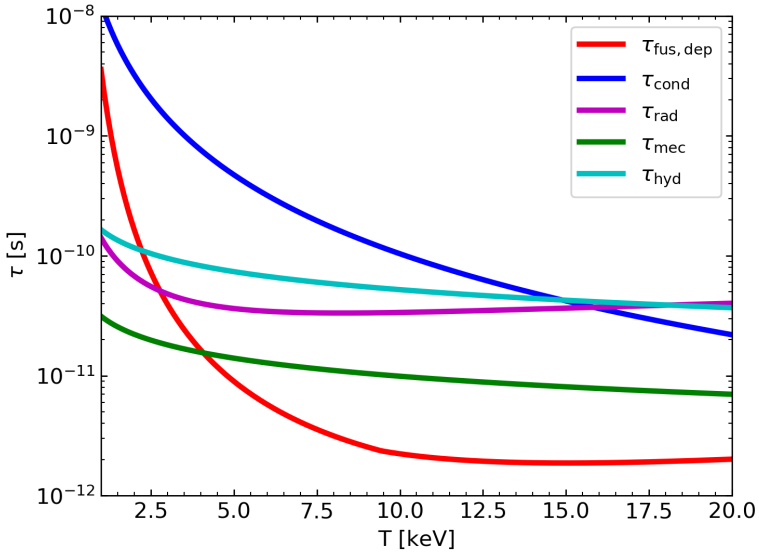

FIGURE 3.9— Characteristic times associated to the internal and hydrodynamic processes of the plasma, as a function of the temperature. We consider a pure DT plasma of density $\rho_{DT} = 500$ g/cm^3, with radius of 15 μm.

After studying the times associated to the characteristic times of the processes, it is necessary to inspect its relation with the other mechanisms taking place in the system. On the one hand, any process happening in the plasma needs to be shorter time than the confinement time ($\tau_{conf} = \frac{R_F}{c_s}$), where the

precompressed fuel is in the stagnation phase. On the other hand, for our modelling to be correct, the time of the processes needs to be longer than the time of the beam interaction. In the monoenergetic and G1 case, we take as a reference the flight time of the projectiles to perform such comparison ($\tau_{\rm fly} \in \tau_{\rm beam}$). The G2 case will be studied with more detail in Chapter 7. We estimate an averaged flight time[8] of a projectile travelling through the plasma as:

$$\tau_{\rm fly} = L_{\rm h} \sqrt{\frac{2m_{\rm b}}{E_0}}. \tag{3.53}$$

At last, the time necessary for achieving thermodynamic equilibrium must be faster than all of the above. This is a necessary condition to consider a sole temperature for the components of the plasma. This time can be calculated as (Atzeni & Meyer-Ter-Vehn, 2004):

$$\tau_{\rm eq} = \frac{0.99 \cdot 10^{13} A_* T_{\rm hs}^{3/2}}{n Z_*^2 \ln(\Lambda_{\rm ee})}. \tag{3.54}$$

Ideally, the situation to accomplish would be $\tau_{\rm conf} > \tau_{\rm hyd;proc} \gtrsim \tau_{\rm fus,dep} > \tau_{\rm beam} > \tau_{\rm fly} > \tau_{\rm eq}$. Consequently, in Fig. 3.10, we present a representative example of this comparison, which can be extended to other simulations in this work. We chose the same plasma conditions as in Fig. 3.9, with a sphere of radius $R_{\rm F} = 50$ μm, while for $\tau_{\rm fly}$ we chose a carbon ion beam and select the set conditions that returned the shortest and longest projectile times, considering the values of (σ, E_0) within the range of our simulations. Again, we represent the time against the temperature of the hot-spot for a fixed radius. We have found the variation with $R_{\rm hs}$ to be less relevant when studying the characteristic times.

As expected, we find the confinement time above the rest, so any activity taking place in the plasma has enough time to operate. The range of low temperatures where $\tau_{\rm fus,dep}$ (representative of the rest of processes) is above $\tau_{\rm conf}$ can be omitted, as the power density at such conditions is negligible. Any other internal process found above $\tau_{\rm conf}$ in this range of low temperatures can be neglected too, following a similar reasoning regarding the processes not operating at such low power levels. The hydrodynamic time associated to the hot-spot is also below the confinement time, assuring its mass keeps confined. The flight times of the projectiles, from its minimum to its maximum durations, are in general below the fusion time, fulfilling the condition we imposed in

[8] This expression has been validated with Atzeni & Meyer-Ter-Vehn (2004) calculation for the projectile time: $\tau_{\rm proj} = \frac{42 T^{3/2} 10^{12}}{\rho ln(\Lambda_{\rm i})}$ $[ps]$.

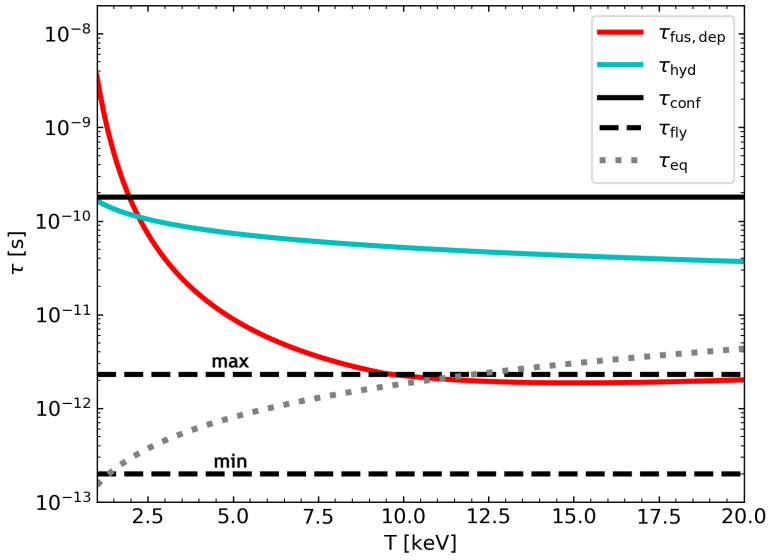

FIGURE 3.10— Characteristic times that describe our system as a function of the temperature, namely: fusion deposition in the hot-spot, hydrodynamic time of the hot-spot, confinement time of the fuel sphere, flight time of the projectiles of the beam (minimum and maximum) and equilibrium time of the plasma. We consider a pure DT plasma of density $\rho_{DT} = 500$ g/cm^3, with radius of 15 μm.

Sect 3.2. We find that, after 10 keV, some of the maximum τ_{fly} values might be in the same order of magnitude or slightly above the fusion time. This result is to be expected, given that the DT fuel is able to fuse in 10-20 keV. In such conditions, considering the internal processes taking place in the plasma would improve the quality of the simulations. Alternatively, we can argue that the beam interaction often dominates over the power density of the internal process, as we explained above with $W_{d,beam}$. Nonetheless, it is of our interest to separate the beam interaction and the rest of mechanisms that take place in the plasma, so we assume this approximation.

Ultimately, we find the equilibrium time mostly between the minimum and maximum τ_{fly} values. For temperatures higher than 10 keV we find τ_{eq} in the same order of magnitude or slightly above $\tau_{fus,dep}$ and the maximum value of τ_{fly}. In these conditions, the equilibrium condition might wave, specially when sharing the same duration as the flight time of the projectiles. However, in the literature, considering a sole temperature is still a valid approximation in the first instants of the ignition (Gauthier et al., 2013; Gasparyan et al., 2013; Gus'kov et al., 2014b; Zou et al., 2016, e.g.).

3.10 Analytical model for the temperature field

In this work, we have also developed an analytical approximated model to determine the temperature field of pure DT plasmas heated by monoenergetic ion beams, as introduced by Espinosa-Vivas et al. (2023). For this purpose we have approximately solved the equations of the heating model, this is, Eqs. 3.16 and 3.18. We make three basic considerations: the dynamic of the ion projectiles in the plasma is sufficiently well described by the stopping with plasma electrons (at high projectile energies) and with plasma ions (at low projectile energies); the ions travel always travel in a plasma with uniform temperature; and the ion beam heats the plasma very fast. These points require addressing the relationship between the ion energy and the plasma temperature. If the velocity of the beam ions is above the thermal velocity of the plasma electrons, then the stopping power increases as the ion energy decreases when travelling through the plasma. The opposite behaviour is found in the case of an ion with a velocity below the electron thermal velocity. The limit in which the energy of the travelling ions matches the thermal velocity of the plasma electrons can be calculated as $E_{\mathrm{se(MeV)}} \approx 1.85 A_* T_{\mathrm{h(keV)}}$, where T_{h} is the mean temperature of the plasma after the heating (Gus'kov et al., 2010). This is commonly referred to as thermal threshold. Then, considering the asymptotic behaviour of the energy due to the stopping with plasma electrons (Li & Petrasso, 1993a), and taking as a reference the thermal threshold energy ($E_{\mathrm{se,e}}$), we have an expression for the stopping power given as:

$$Sp(E) \propto \begin{cases} E^{1/2} & \text{if } E < E_{\mathrm{se,e}} \\ E^{-1} & \text{if } E \geq E_{\mathrm{se,e}}. \end{cases} \tag{3.55}$$

If we assume that the ions consistently traverse a plasma with a uniform temperature, after some manipulations, we derive that, for a specific time, $Sp(x,t)\alpha \left(1 - \frac{x - x_{\mathrm{Tmax}}}{\lambda}\right)$ for $E < E_{\mathrm{se,e}}$ and $\left(1 - \zeta \frac{x - x_{\mathrm{Tmax}}}{\lambda}\right)^{-1/2}$ for $E \geq E_{\mathrm{se,e}}$. Here, λ is the length between x_{Tmax} and the position where the heated region ends (L_{h}). The value of ζ is calculated as $\zeta = (1 - \delta^2)$, with $\delta = E_{\mathrm{se,e}}/E_0$. We need to address how, during the heating process, the temperature of the plasma is not uniform. To do so, we assume that at any time the ions travel through a plasma of constant temperature approximated by the average of the heated region at any given time, $\langle T(x,t) \rangle$. Thus, previous Eq. 3.55 is now written as:

$$Sp(x,t) \propto \begin{cases} \left(1 - \frac{x - x_{\mathrm{Tmax}}}{\lambda}\right)^{a_1} & \text{if } E < E_{\mathrm{se,e}} \\ \left(1 - \zeta \frac{x}{x_{\mathrm{Tmax}}}\right)^{-a_2} & \text{if } E \geq E_{\mathrm{se,e}}, \end{cases} \tag{3.56}$$

where a_1 and a_2 are parameters to fit. The fitting parameters introduced in this manner are linked to the impact of the real non-uniformity of the temperature in the plasma, resulting from progressive heating by the ions of the beam.

Substituting Eq. 3.56 into Eq. 3.17 and assuming a very fast deposition of the energy in the plasma (the intensity has a delta-behaviour $I(t) \approx \sigma\delta(t - \tau_{\mathrm{beam}})$), then, once the beam-plasma interaction has ended, we find an analytical expression for the temperature field created (Espinosa-Vivas et al., 2023):

$$T(x) = \begin{cases} T_0 + (T_{\max} - T_0) \cdot \left(1 - \frac{x - x_{\mathrm{Tmax}}}{\lambda}\right)^{a_1} \\ \qquad \text{if } \lambda + x_{\mathrm{Tmax}} > x > x_{\mathrm{Tmax}} \\ T_{\mathrm{x=0}} + \varepsilon(T_{\max} - T_{\mathrm{x=0}}) \cdot \\ \quad \left(1 - \left(1 - \zeta \frac{x}{x_{\mathrm{Tmax}}}\right)^{-a_2}\right) \\ \qquad \text{if } x_{\mathrm{Tmax}} > x > 0, \end{cases} \tag{3.57}$$

where the boundary conditions are given as $T(x = 0) = T_{\mathrm{x=0}}$ and $T(x_{\mathrm{Tmax}} + \lambda) = T_0$, with $\varepsilon = -\delta^{2a_2}/(1 - \delta^{2a_2})$. The cases in which $a_2 \neq 0$ are associated with intermediate or central hot-spots, while for edge hot-spots $a_2 = 0$. The latter is equivalent to finding $x_{\mathrm{Tmax}} = 0$ and $\lambda = L_{\mathrm{h}}$.

The analytical model of Eq. 3.57 presents another way of addressing the final state of the plasma after the beam interaction. It describes the final temperature of the plasma with an explicit expression, which might ease understanding of its behaviour. Additionally, employing Eq. 3.57 saves computational resources instead of performing the entire numerical simulation.

As foreseen in Espinosa-Vivas et al. (2023), from the analytical model of the temperature field (Eq. 3.57) both the hot-spot temperature and length can be approximated as:

$$T_{\mathrm{hs}} = T_0 + \left(\frac{1}{1 + a_1}\right)(T_{\max} - T_0)\left(\frac{1 - s^{(1+a_1)/a_1}}{1 - s^{1/a_1}}\right), \tag{3.58}$$

with $s = (T_{\mathrm{ig}} - T_0)/(T_{\max} - T_0)$, and

$$L_{\mathrm{hs}} = x_{\mathrm{Tmax}} \cdot f + \lambda\left(1 - \left[\frac{T_{\mathrm{ig}} - T_0}{T_{\max} - T_0}\right]^{1/a_1}\right), \tag{3.59}$$

where f equals 0 for edge hot-spots, 1 for intermediate hot-spots and is given by with $f = 1 - (1/\zeta)\left(1 - \left[1 - \frac{T_{\mathrm{ig}} - T_{\mathrm{x=0}}}{\varepsilon(T_{\max} - T_{\mathrm{x=0}})}\right]^{1/a_2}\right)$ for central hot-spots.

We demonstrate the potential of the model presented in this section with the test results shown in Fig. 3.11. We consider a pure DT plasma of density

$\rho = 300$ g/cm^3 and initial temperature $T_0 = 1$ keV, heated with a vanadium beam with flux of $\sigma = 1.1 \cdot 10^{19}$ cm^{-2} and three different kinetic energies $E_0 = 2000$, 4000 and 7000 MeV. The coloured lines represent the simulation of our numerical model, while the dashed black lines show our analytic model after fitting the free parameters a_1 and a_2. Moreover, the dotted black lines show the results of the analytic model of Gus' kov et al. (2009), which only estimates the decrease in temperature from $T_{\max}$ to T_0, considering a value of $a_1 = 0.4$.

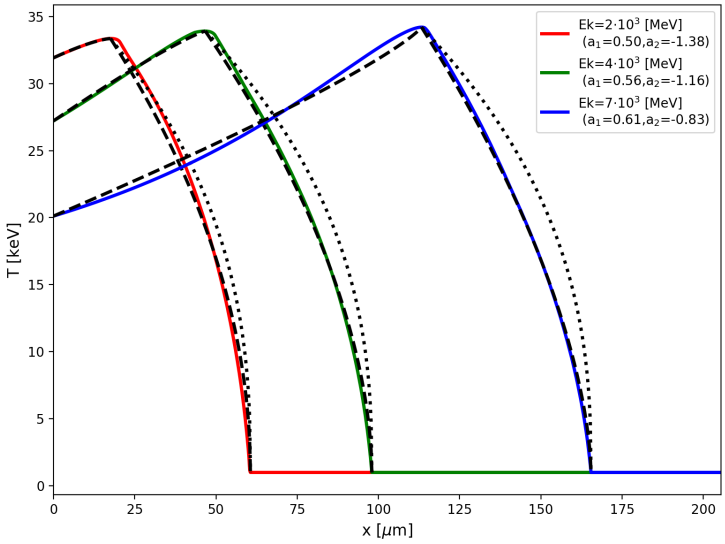

FIGURE 3.11— Comparison of the distribution of temperatures obtained with our numerical model and those of the analytic model after fitting the free parameters a_1 and a_2. The plasma has a density of $\rho = 300$ g/cm^3 and an initial temperature of $T_0 = 1$ keV, heated by a monoenergetic vanadium beam with a flux $\sigma = 1.1 \cdot 10^{19}$ cm^{-2}, at different initial energies.

It is found that our analytic model properly follows the numerical results more accurately than the approximation of Gus' kov et al. (2009). Moreover, our analytic model is able to reproduce central hot-spot temperature distributions, while Gus' kov et al. (2009) only described the temperature distribution from its maximum to the final range. Thus, depending on the expected distribution of temperatures, we can foresee values for (a_1, a_2) and avoid simulating the whole interaction, if it were necessary. In Sect. 4.5, we analyse further the results obtained with the analytical model and compare them with the numerical model.

3.11 Burning gain

When the values of $T_{\rm hs}$ and $R_{\rm hs}$ are known, it is possible to obtain the self-heating or ignition efficiencies for any given hot-spot. Additionally, the last gain analysed is the burning gain, $G_{\rm burn}$, which is related to the subsequent combustion of the whole precompressed fuel. It measures the efficiency of the nuclear fusion energy produced by the burning of a spherical DT fuel of radius $R_{\rm F}$. This is defined as:

$$G_{\rm burn} = \frac{E_{\rm fus}}{(E_{\rm hs} + E_{\rm c})}, \tag{3.60}$$

where $E_{\rm hs}$ is the energy of the hot-spot, $E_{\rm c}$ is the energy of the cold region and $E_{\rm fus}$ is the total fusion energy liberated during the burning of the whole fuel. The fusion energy is calculated as the integral over the burning time of the sphere volume: $E_{\rm fus} = \int_{\tau_{\rm total}} \left(\int_V W_{\rm fus}\, dV\right) dt$, with the total power density being $W_{\rm fus} = n_{\rm D} n_{\rm T} \langle \sigma_{\rm fus} v \rangle\, Q_{\rm DT}$.

As explained in Sect. 2.3.2, a complete evaluation of this gain would require precise hydrodynamic simulations. Alternatively, in this work, we have used an analytical expression for the burning gain of a uniformly precompressed fuel ignited by a small hot-spot immersed in a larger sphere of colder fuel (Fraley et al., 1974; Kidder, 1976), which is widely used in ion fast ignition theory (Atzeni & Meyer-Ter-Vehn, 2004; Gus'kov et al., 2011). This is an accurate approach with respect to hydrodynamic simulations, for $\rho R_{\rm F} \gtrapprox 1 - 1.5$ g/cm^2 (Fraley et al., 1974; Atzeni & Tabak, 2005), a criterion that is mostly fulfilled in the present work: for the reference case of $\rho = 500$ g/cm^3 and $R_{\rm F} = 50$ μm, we obtain $\rho R_{\rm F} = 2.5$ g/cm^2. Then, for a density of $\rho = 300$ g/cm^3 we find $\rho R_{\rm F} = 1.5$ g/cm^2 and for $\rho = 700$ g/cm^3 we find $\rho R_{\rm F} = 3.5$ g/cm^2. Among our studied cases, the worst scenario in relation to that condition would be $\rho = 300$ g/cm^3 and $R_{\rm F} = 40$ μm, where we retrieve $\rho R_{\rm F} = 1.2$ g/cm^2, which is in the order of threshold value.

At last, the burning gain is expressed as:

$$G_{\rm burn} = \frac{G_0 (\rho R_{\rm F})^3}{(\rho R_{\rm hs})^3 + ((\rho R_{\rm F})^3 - (\rho R_{\rm hs})^3)\, \frac{T_*}{T_{\rm hs}}}. \tag{3.61}$$

The temperature T_* refers to the cold fuel temperature T_0 in the case of a Maxwellian plasma and $T_* = 2\epsilon_{\rm F} Z_*/5(1 + Z_*)$ in the case of a degenerate gas, which is, in general, the case of this work. Then, the gain of a homogeneous plasma is:

$$G_0 = \frac{\epsilon_r g}{3 T_{\rm hs}(1 + Z_*)(1 + \xi)}, \tag{3.62}$$

while the energy released in one fusion reaction is $\epsilon_r = 17.6$ MeV. At last, the burn-up factor is

$$g = \frac{\rho R_{\rm F} \cdot \frac{A_{\rm DT}}{A_*(1+\xi)}}{\rho R_{\rm F} \cdot \frac{A_{\rm DT}}{A_*(1+\xi)} + H_{\rm B} \cdot \kappa}, \tag{3.63}$$

where $\kappa = 1$ if $\xi < 3/(Z_{\rm dop}+1)$ and $\kappa = \left(\frac{(1+Z_{\rm dop})(1+Z_*)}{4\cdot(1-X_{\rm dop})(1+Z_{\rm dop}+Z_{\rm DT}(1+Z_{\rm dop}))}\right)^2$ if $\xi \geq 3/(Z_{\rm dop}+1)$. At last, $H_{\rm B} = 7.25\sqrt{(1+Z_*)/A_*}$.

An example of the burning gains achieved in the (ρR-T)-space was shown previously, in Fig. 3.5. As $G_{\rm burn}$ depends on the radius of the sphere, we take as an example a plasma of $R_{\rm F}$=50 μm. The colour gradient represented there, shows the maximum values of the burning gain close to the bottom of the ignition curve, meaning that the optimal hot-spots are those that are able to burn the whole sphere with the minimum size and temperature necessary to reach ignition. In the chapters with results, this is found again, but in terms of the parameters of the beam that create these hot-spots.

Previous works, such us Gus'kov et al. (2011); Gus'kov et al. (2014b, 2015) and Gus'kov & Sherman (2016), have analysed the self-heating, the ignition and the burning gains in the (ρ, R, T)-space of a pure and doped plasma. Nonetheless, in this work, we widen these studies by performing an extensive analysis in the beam parameter space of (σ, E_0). This is, we retrieve the radius and temperature of the hot-spot depending on the beam applied, $R_{\rm hs}(\sigma, E_0)$ and $T_{\rm hs}(\sigma, E_0)$, and introduce them in the burning gain expression to obtain $G_{\rm burn}(\sigma, E_0) = G_{\rm burn}\left(R_{\rm hs}(\sigma, E_0), T_{\rm hs}(\sigma, E_0)\right)$. With this course of action, we provide the particular characteristics of the beam that reach certain plasma temperature, hot-spot length and gain, instead of just addressing the plasma conditions through R and T. We extend the analysis by considering different beam species and radii, as well as different plasma initial conditions $(\rho, T_0, R_{\rm F}, Z_*, \xi)$. With our simulations, we are able to determine relevant properties of the heated region, the hot-spot, and its corresponding gains.

3.12 Numerical model

The differential equations 3.16 and 3.18, are solved using numerical methods, so it is necessary to present a discrete form of these expressions.

The stopping power governs the variation of the kinetic energy of the beam per length unit (Eq. 3.18). Therefore, it depends on the velocity of the projectile, in each position and instant, as well as the temperature of the plasma. This one-dimensional problem is discretised into a set of $N_{\rm x}$ nodes, where the step is $\Delta x = 2R_{\rm F}/N_{\rm x}$ and the mesh is given by $x_{\rm n} = n \cdot \Delta x$. Eq. 3.18 can be expressed in the Euler method formalism as:

$$E_{\mathrm{n}+1} = E_{\mathrm{n}} - Sp_{\mathrm{n}} \cdot \Delta x. \tag{3.64}$$

Taking into account that the stopping power is defined positive, it reduces the kinetic energy (E) of the ions in each n^{th} point of the mesh, expressed in Sect. 3.2 through $x(t')$. The calculation is performed for every projectile until it has lost all its energy ($E_{\mathrm{n}} = 0$), which coincides with the range.

Equation 3.64 describes the deceleration of a single projectile for an instant t, in which it suffers the energy loss in a given plasma state. Then, solving Eq. 3.16 requires the presence of an index that indicates the instant of time t, which we denote m. Following these ideas, Eq. 3.64 is expressed for the m^{th} instant (or projectile) that enters the n^{th} node of the plasma as:

$$E_{n+1,m} = E_{n,m} - Sp_{n,m} \cdot \Delta x. \tag{3.65}$$

Although this equation is written in the Euler method formalism, it will be solved using a Runge-Kutta method. Here, it is important to highlight the dependence of the stopping power on the kinetic energy of the projectile and the temperature of the plasma: $Sp_{n,m} = Sp\,(E_{n,m}, T_{n,m})$.

At each time step, m, Eq. 3.65 is solved for every n, in such a way that the stopping power determines the heating of the plasma, and thus, the value of the temperature. Therefore, the temperature field is updated applying the Euler method as:

$$T_{n,m+1} = T_{n,m} + \frac{I}{\rho\, C_V} Sp_{n,m}\, \Delta t. \tag{3.66}$$

Here, Δt should be calculated as a partition of the beam duration $\tau_{\mathrm{beam}}/N_{\mathrm{t}}$, where N_{t} is a selected number of temporal nodes. However, we assume the beam duration τ_{beam} to be unknown, so in our numerical calculations, we apply a change to the integrated variable t to perform the computation. We do so by redefining $I \cdot dt$ as db, which corresponds to a partition of the flux, (σ/N_{b}), where N_{b} is an arbitrary number of nodes we choose. This requires the intensity to be constant[9], but allows eliminating the τ_{beam} parameter in solving the set of equations (Beltran et al., 2020). In a discrete description, this change is expressed as:

$$\Delta b = I \Delta t = \frac{\sigma}{N_{\mathrm{b}}}, \tag{3.67}$$

which transforms Eq. 3.66 into:

$$T_{n,m+1} = T_{n,m} + \frac{1}{\rho\, C_V} Sp_{n,m}\, \Delta b, \tag{3.68}$$

[9]This is the procedure applied in most parts of this work. Later we address the modelling for other cases. Exceptions are mentioned when necessary throughout the document.

where Δb is a partition of the beam flux, we denote "*bin*". By these means, the ion beam flux is considered split into $N_\mathrm{b} = \tau_\mathrm{beam}/\Delta t$ uniform bins that are successively passed through the plasma. Each bin is composed of the same fraction of ions, which move together through the plasma at the same time, as Fig. 3.3 shows. This change from time to bin-dependence is very useful, because it allows tackling the problem without explicitly treating the time and the particle flux (Gasparyan et al., 2013). Ultimately, Eq. 3.68 governs our computations, describing the change in the plasma temperature due to m^{th} bin in the n^{th} spatial node. Numerically, the boundary and initial conditions are such that for every m-time at $n = 0$, we have the initial energy of the projectiles as $E_{0,m} = E_0$. Then, for every n-node at the first instant $m = 0$, the temperature of the plasma is $T_{n,0} = T_0$.

The previous numerical description is given for the ideal case of uniform temperature conditions and a monoenergetic beam. During our work, we have addressed situations that do not consider these approximations. In the first case, although not shown in the results of this thesis, implementing a non-uniform initial temperature mesh is straightforward. It is done by assigning the proper temperature $T_{0,n} = T(x, t = 0)$ value for each n-node of the spatial mesh at $m = 0$. In the second case, implementing the two quasi-monoenergetic scenarios we presented in Sect. 3.3, requires further examination. For this calculation, the energy distribution is discretised in an array with a number of partitions (N_E), so $\mathfrak{E}_0 = [E_{0;0}...E_{0;N_\mathrm{E}}]$, where $E_{0;0} = \bar{E}_0 - 3\sigma_\mathrm{E}$ and $E_{0;N_\mathrm{E}} = \bar{E}_0 + 3\sigma_\mathrm{E}$. As explained in Sect. 3.3.2, "3" is an arbitrary parameter we choose to assure reaching outmost energies of the distribution. Consequently, the energy step is calculated as $\Delta E = (E_{0;N_\mathrm{E}} - E_{0;0})/N_\mathrm{E}$.

In the case of G1, with a quasi-monoenergetic beam located at the edge of the plasma, each bin has an internal distribution of energies. To ease the explanation, let us say that each bin is subdivided into sub-bins of projectiles with different energy. As the bins travel, the sub-bins with different energy behave differently; for instance, the slower projectiles stop earlier and the more energetic reach further. Therefore, it is necessary to study the energy decrease of each sub-bin, at each position and instant. This implies that Eq. 3.65 is now written with a new subindex dependence (l), representing the energetic sub-bin under examination. Thus, now the problem involves three loops that solve:

$$E_{n+1,m,l} = E_{n,m,l} - sp_{n,m,l} \cdot \Delta x, \tag{3.69}$$

where we denote the stopping with lowercase (sp) to remark it is the stopping of a certain energetic sub-bin. Then, at each instant and position, we sum the total deposited energy by each energetic sub-bin and calculate the total

increase in the temperature at each position, according to Eq. 3.68, before the next bin enters the plasma: $Sp_{n,m} = \sum_{l=0}^{N_\mathrm{E}} F_l \, sp_{n,m,l} \, \Delta E$, with F_l being the energy distribution from Eq. 3.20. Aside from the integration over the different projectile energies, the procedure remains the same as explained in Sect. 3.12.

In the case of G2, with a quasi-monoenergetic beam separated by a distance "d" from the edge of the fuel, it is not necessary to solve a third loop nor use an extra subindex. This is because the energy of the projectiles that reach the edge of the plasma can be ordered according to the distance they must travel to reach the edge. However, in this context, it is necessary to abandon the bin notation and work directly with the time of fly of the projectiles from the source to the edge of the plasma (τ_beam). This is calculated as the time difference between the most and less energetic projectiles: $\tau_\mathrm{beam} \approx t_\mathrm{max} - t_\mathrm{min} = \sqrt{\frac{m_\mathrm{b} d^2}{2}} \left(\frac{1}{E_{0;0}}^{1/2} - \frac{1}{E_{0;N_\mathrm{E}}}^{1/2} \right)$. Then, we calculate the temporal discretisation as $\Delta t = \tau_\mathrm{beam}/N_\mathrm{t}$ and the discretised time as $t = t_\mathrm{min} + m\Delta t$. Therefore, and as mentioned above, the initial energy at each instant of time is not the same and is given by $E^\dagger_{0,m} = (m_\mathrm{b} d^2)/(2t^2)$, where we keep the m notation for the temporal variable. At last, previous Eq. 3.68 is changed to:

$$T_{n,m+1} = T_{n,m} + \frac{\sigma}{\rho \, C_V} \frac{P_m \, Sp_{m,n}}{E^\dagger_{0,m}} \, \Delta t, \tag{3.70}$$

where the computational model operates by directly integrating over the beam time instead of dividing the beam into bins. Here, it is worth noting that we have found Eq. 3.70 to be independent of the distance. Given the definitions of all terms, and after some straightforward manipulations, we demonstrated that "d" is cancelled out during in the calculation.

In our simulations, the number of nodes of the spatial and temporal meshes ($N_\mathrm{x}, N_\mathrm{b}, [N_\mathrm{E}]$) plays a crucial role in determining the validity of our results. The results get finer by increasing the number of nodes, but this comes at the cost of computational resources and time. We have performed various experiments to determine which number of nodes is appropriate for a trustful calculation. We calculate the mean relative error of the kinetic energy and temperature as the difference between the solution values of a given mesh and those of a mesh with twice the number of nodes, i.e.: $\langle |E[2N_\mathrm{x}] - E[N_\mathrm{x}]| \, / \, E[N_\mathrm{x}] \rangle$ and $\langle |T[2N_\mathrm{b}] - T[N_\mathrm{b}]| \, / \, T[N_\mathrm{b}] \rangle$.

In Fig. 3.12 the mean relative error of the kinetic energy and the temperature are shown as a function of the number of nodes, for both spatial and temporal (bins) discretisations. As expected, the error decreases with the number of nodes. However, it shows that the kinetic energy error is consistently higher than the temperature error. In this sense, selecting a Runge-Kutta method for

solving the kinetic energy equation is a better option, as adopting an Euler method would result in even greater expected errors. We have found that this behaviour can be attributed to the fact that changes in kinetic energy exhibit steeper slopes compared to those in temperature.

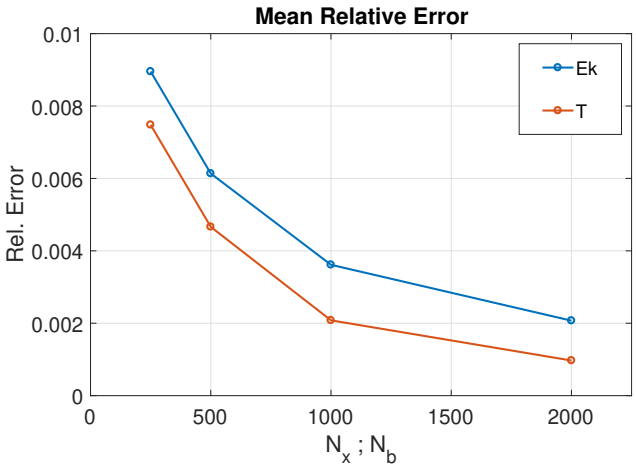

FIGURE 3.12— Mean relative error of the kinetic energy and temperature solutions when duplicating the number of nodes in both spatial (N_x) and beam (N_b) discretisations. Experiment with a DT plasma at 1 keV and $\rho = 300$ g/cm^3, with a proton beam of $E_0 = 3$ MeV and $\sigma = 1.56 \cdot 10^{21}$ cm^{-2}.

In Fig. 3.13 the spatial distribution of the final temperature is shown, with different discretisations of the beam (N_b). This allows observing how the temporal discretisation of the temperature equation affects the outcome. Taking only one bin is equivalent to considering the beam entering as a whole into the plasma, in this case, forming one major peak. When three bins are used, the temperature distribution has three smaller peaks, one for each bin. It is found that as the number of bins increases, the solution converges, thus simulating the progressive entrance of the beam into the plasma. However, an insufficient number of bins leads to oscillations in the solution, resulting in a peak for each bin. If the refinement of the beam discretisation lacks precision, it fails to simulate the beam smoothly, instead resembling separate projectiles. Additionally, the range and the maximum temperature results of the beam interaction are different if the number of bins is insufficient.

Our numerical simulations consider a uniform discretisation of the spatial and temporal grids, where, in most cases, the number of mesh nodes are $N_\mathrm{x} = 2048$ and $N_\mathrm{x} = 1024$. When a quasi-monoenergetic beam is considered, our simulations indicate that $N_\mathrm{E} \gtrsim 32$ leads to a convergence in the results. In our

simulations, we often use a value of $N_{\mathrm{E}} = 64$ energetic nodes.

We need to highlight here that, throughout this work, the simulation procedure explained above is computed systematically for large arrays with diverse values of flux (σ) and projectile energy (E_0). We recall that our primary aim is to systematically present results of the heated plasma in the (σ, E_0)-space. In such cases, we calculate 100×100 arrays with every combination of the selected (σ, E_0)-values, and then obtain key features of the heated region and the hot-spot.

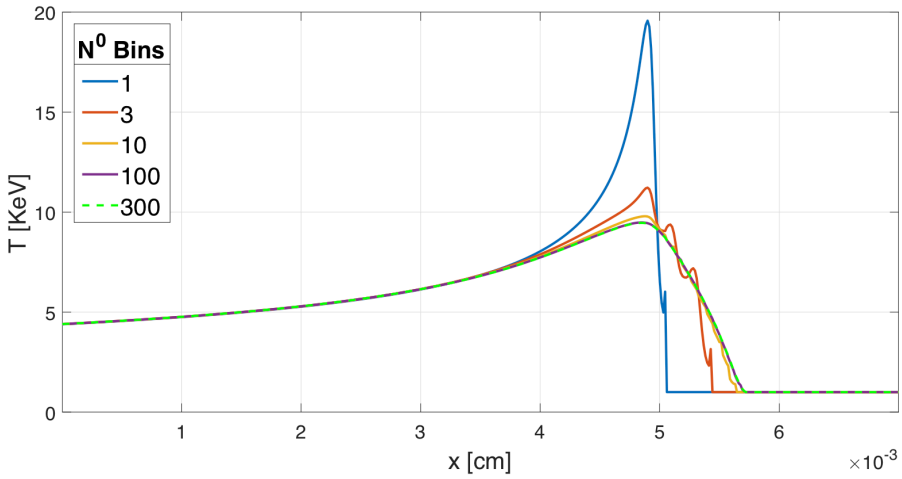

FIGURE 3.13— Spatial distribution of the temperature of the plasma when the beam has been discretised in different numbers of bins. Experiment with a DT plasma of $\rho = 300$ g/cm^3 at 1 keV and a vanadium beam with $E_0 = 5100$ MeV and $\sigma = 1.22 \cdot 10^{18}$ cm^{-2}

Another problem we solve in this work consists of determining the values of ρR and T that make $G_{\mathrm{sh}} = 1$ and $G_{\mathrm{ig}} = 1$, respectively. As presented in Sect. 3.6, these criteria assure the self-heating or ignition of the hot-spot, so it is crucial to calculate the threshold values of each case. For searching the solution of $G_{\mathrm{hs}}(\rho R, T) = 1$ and $G_{\mathrm{ig}}(\rho R, T) = 1$ we apply an iterative method in which we compute both gains for every temperature of interest and then find the ρR value that solves the equation. This is, given a temperature T_j we calculate $W_{i,j} = W_{\mathrm{fus,dep}}(T_j, \rho R) - (W_{\mathrm{mec}}(T_j) + W_{\mathrm{cond}}(T_j, \rho R) + W_{\mathrm{rad}}(T_j, \rho R))$ and compare it with its previous step $W_{i-1,j}$. If the product of both is lower than zero ($W_{i,j} \cdot W_{i-1,j} \leq 0$), a solution has been found. Then, we move to the next temperature T_{j+1}. We note that the self-heating and ignition curves shift towards different regions of the $(\rho R, T)$-space depending on the plasma considered, as we demonstrate in Fig. 3.6 when dopants are included. Therefore,

properly selecting the range of study for T_j and ρR is mandatory. We recommend initially performing a rough exploration of the parameter space to find the initial and final values ($[T_0, T_f]$ and $[\rho R_0, \rho R_f]$) for finely tuning the actual search. We remind that solving $G_{\rm hs}(\rho R, T) = 1$ and $G_{\rm ig}(\rho R, T) = 1$ is crucial for determining the hot-spot. The characteristics of the hot-spot, such as $T_{\rm hs}$, $L_{\rm hs}$, $R_{\rm hs}$ or $G_{\rm burn}$, are only calculated if there is a temperature such that $T > T_{\rm ig}$ (obtained after determining the self-heating curve) and $G_{\rm ig}(\rho R_{\rm hs}, T_{\rm hs}) > 1$.

In the next Chapters 4, 5, 6 and 7 we perform different experiments using typical values from the literature for both the plasma and the beam (see, for instance, Atzeni, 1999; Atzeni & Meyer-Ter-Vehn, 2004; Gus'kov et al., 2010; Gasparyan et al., 2013; Gus'kov et al., 2014b,a; Honrubia et al., 2014; Honrubia & Murakami, 2015; Zou et al., 2016; Nezam et al., 2020). The plasma is described as a compressed sphere of DT fuel with radii of $R_{\rm F}$=40, 50 or 60 μm at stagnation state. If impurities are considered, the chosen elements are beryllium (Be), carbon (C), aluminium (Al), and copper (Cu). Mostly, the distributions for the initial temperature and density are homogeneous, selecting T_0=0.5, 1 or 5 keV and ρ = 300, 500 or 700 g/cm^3, respectively, although for some experiments we examine a plasma of variable density. Then, for the beam we consider fast ions such as protons (p^+), carbon (C^{6+}) and vanadium (V^{23+}), with three different radii $r_{\rm b}$=10, 15 or 20 μm. The beam can be either monoenergetic or quasi-monoenergetic (with a Gaussian energy distribution of energy spread: δE = 5, 10 or 15%, according to Hegelich et al. 2011), located at the edge of the plasma or separated a certain "d" distance. Regarding the energy of the beam ($E_{\rm b} = S_{\rm b}\sigma E_0$), we focus our study on the cases of interest for the ion fast ignition scheme. Therefore, we perform a parametric search in the (σ, E_0)-ranges, where a hot-spot is generated inside the heated region. We take as a reference case a pure plasma without corona and a monoenergetic beam. Accordingly, and unless noted otherwise when performing a different experiment, the initial and boundary conditions of the plasma are given by ($T(x,0) = T_0, \rho(x,t) = \rho$), and for the ion beams are given by ($\sigma(0,t) = \sigma, E(0,t) = E_0$).

4

Preliminary results of the beam-plasma interaction

With the simulations presented in this chapter we aim to describe the most basic behaviours of the beam plasma interaction and, moreover, to validate our simulations, both numerical and analytic model. Then, we search for the ranges of interest in the (σ, E_0)-space of the ion fast ignition scheme, where a hot-spot is generated inside the heated region. A wide variety of conditions are chosen for this preliminary study, using typical values from the literature for both the plasma and the beam (see, for instance, Gus'kov et al., 2010; Gasparyan et al., 2013; Honrubia et al., 2014; Gus'kov et al., 2014a; Zou et al., 2016; Espinosa-Vivas et al., 2023).

4.1 Stopping power analysis

The core calculation when solving Eqs. 3.16 and 3.18 is the stopping power model. The discussion over which stopping model should be used for ion projectiles travelling in dense and hot plasmas is still open debate. It has been proven that the different models (as presented in Sect. 2.3.1.b: RPA, PMV, LP, BPS...) provide distinct results, specially for projectiles with low energy and in the order of the thermal velocity of the plasma electrons.

Therefore, to begin with, we inspect the implementation of the two stopping power expressions considered in this work, as presented in Sect. 3.4, the PMV and LP models. Also, in order to have confidence in our results, we validate them with previous literature. To do so, we evaluate the stopping power of free electrons and ions by examining the slowing down of proton projectiles in a fully ionized DT plasma. The matter density and temperature are set at

$\rho = 300$ g/cm^3 and $T_0 = 1$ keV, respectively. Additionally, we consider the DT plasma mixture with dopant elements such as aluminium and copper, where the dopant percentage relative to the DT abundance is set at $\xi = 0.005$.

Figure 4.1 illustrates the ion stopping (left) and the electron stopping (right) for the LP model (solid lines), the PMV model (dashed lines), and the one utilized in Zou et al. (2016) (figure 1) (dotted line). We note that Zou et al. (2016) also uses the LP stopping model, although with some modifications in respect to ours.

First, it is evident that the ion and free electron stopping power of protons increases when the DT mixture contains a dopant, with a higher rate of increase observed as the atomic number of the dopant rises. The maximum value of ion stopping occurs at low proton energies, while for free electron stopping, it is attained at higher energies. In both cases, at energies corresponding to the thermal velocities of the ions ($v_{\mathrm{th,ions}}$) and the free electrons ($v_{\mathrm{th,e}}$), corresponding to each thermal threshold energy ($E_{\mathrm{se,ions}}$ and $E_{\mathrm{se,e}}$). On the other hand, the comparison reveals that both models exhibit qualitatively similar behaviour, although the LP model shows better agreement with the reference than the PMV model. In the case of the electron stopping, the PMV model overestimates the slowing down, while the LP model almost matches the results of Zou et al. (2016). In the case of the ion stopping power, the PMV model underestimates the results, while our LP model tends to overestimate the solutions, especially at very low energies. As said above, these differences are deemed acceptable considering that the PMV and both LP stopping power models involve differing approximations. Moreover, we can despise these differences taking into account that the electron field is the main responsible for the interaction (see the total stopping in Fig. 4.2), while the ions just contribute to the final breaking point of the projectiles, when they have low energy. Considering that throughout this work we mainly use the LP model, correctly validated with Zou et al. (2016) for the electron stopping, we can assert safety in our results.

For a further understanding of the behaviour of the stopping model, in Fig. 4.2 we show the total LP stopping of proton, carbon and vanadium ions in a range of energies from $E \approx 10^{-3}$ to 10^4 MeV (10^2 MeV for protons). We consider a pure DT plasma with density of $\rho = 500$ g/cm^3 and two temperatures, 1 and 5 keV, represented with solid and dashed lines, respectively. We note how the ion species operate in different range of energies. For each beam, at low energies, we find the stopping due to the ion field of the plasma, responsible for the final break of the projectiles. Meanwhile, at intermediate energies we find the central peak associated to the electron field, which dominates the slowing down of the projectiles along their trajectory. In comparison with Fig. 4.1, we find that a higher density returns larger values of the stopping, due to an increase

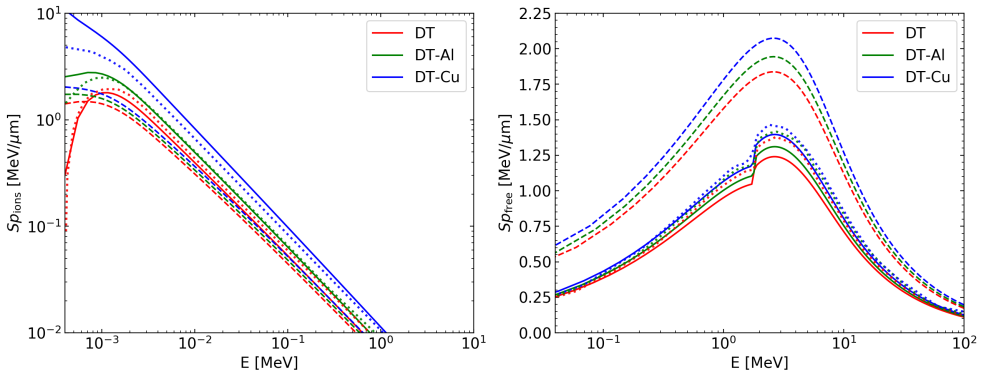

FIGURE 4.1— Stopping Power for ions (left) and electrons (right) when applying proton projectiles. Both experiments calculated for a DT plasma at 1 keV temperature, $\rho = 300$ g/cm^3 and with a dopant portion in respect to the DT of $\xi = 0.005$, for different kinds of dopants. Solid lines correspond to our results with the LP, dashed ones to the PMV model, and dotted lines to those of Zou et al. (2016) (figure 1).

in the number of free electrons that make the plasma more opaque. Also, we observe how increasing the temperature displaces the maximum values to higher energies and diminishes the stopping effect, due to the increased thermal velocities of the plasma particles and reduced collision cross-sections. This creates a more transparent medium in which the projectiles can travel further. When comparing the ion species, we find that heavier projectiles return larger stopping values. This explains why the flux requirements for high-Z beams are lower, as shown in Sect. 4.7.

Next, we assess the spatial solutions for the energy loss by solving Eq. 3.18. Considering a DT plasma at $\rho = 300$ g/cm^3, Fig. 4.3 illustrates the stopping power as a function of spatial position (x) for a fully ionized carbon ion with an initial energy of $E_0 = 440$ MeV entering the plasma at various temperatures. The plot displays the stopping power calculated by the LP model (solid line), the PMV model (dashed line), alongside the analytical model computed in Gus'kov et al. (2010) (figure 1, dotted line). While the results exhibit some numerical disparities, they demonstrate a consistent functional behaviour. These discrepancies arise from differences in the stopping power expressions utilized by our model and those employed by the authors of the reference. For instance, we find the PMV model to return shorter ranges in respect to the other two models. For low plasma temperatures, such as 1 keV, we find the characteristic Bragg peak due to the projectiles slowing down in the electron field. Then, for higher temperatures this peak flattens, as the stopping power decreases. On

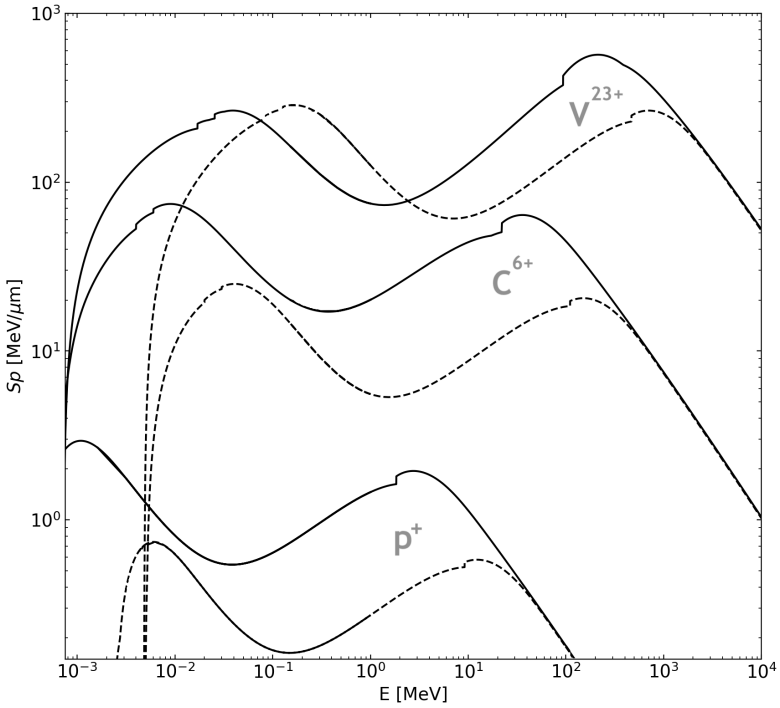

FIGURE 4.2— Stopping Power in respect to the energy of the ion projectiles. We consider a pure DT plasma with $\rho = 500$ g/cm^3, at $T = 1$ keV (solid lines) and $T = 5$ keV (dashed lines).

the other hand, a notable difference is the distinct final peak observed for 5 and 10 keV, which is attributable to the inclusion of ion stopping power in our model but not in Gus'kov et al. (2010). Furthermore, these peaks manifest towards the end of each curve due to the higher values of ion stopping power at lower projectile velocities, as shown in previous Fig. 4.1. In this figure, we can also observe how increasing the temperature makes the plasma more transparent, allowing the projectiles to travel further within the fuel.

4.2 Penetration range of a projectile

As another preliminary result of the model proposed in Sect. 3.2, we calculate the stopping of a sole particle within plasmas of different density and temperature. This way we address the most basic behaviour of particles travelling through the material, in this case, considering the LP stopping model. Thus, we show the penetration range in ρL_{h} units against a varying plasma temper-

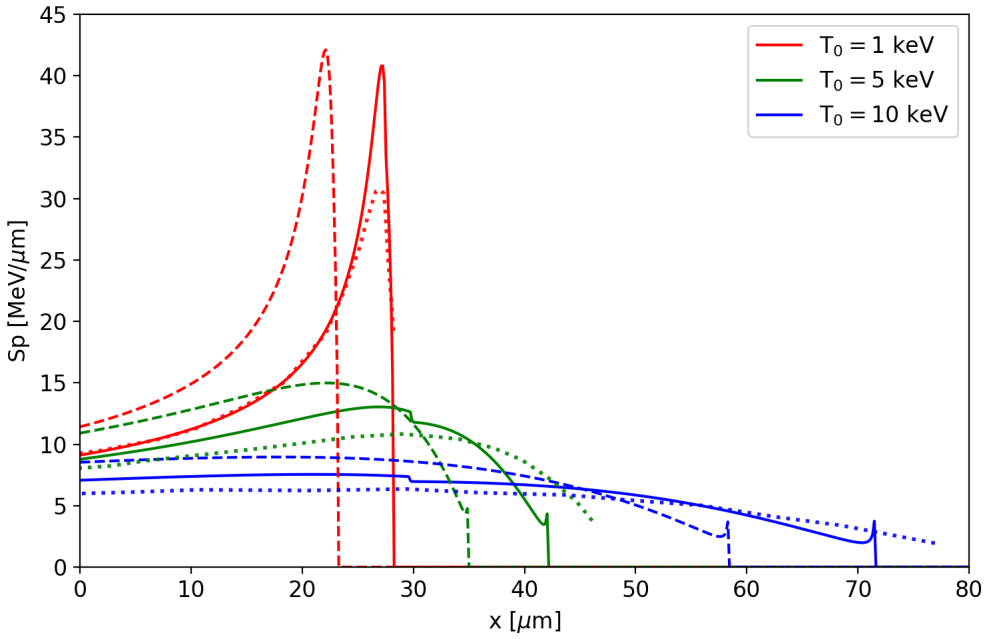

FIGURE 4.3— Stopping power of a carbon ion as it deepens in the plasma. The projectile has an energy of $E_0 = 440$ MeV and enters a DT plasma with $\rho = 300$ g/cm^3 and a T of 1, 5, and 10 keV. Solid and dashed lines correspond to our results (LP and PMV models, respectively) and dotted ones to those of Gus'kov et al. (2010) (figure 1).

ature in Fig. 4.4 and against the plasma density in Fig. 4.5. Both figures are calculated for different beam species and projectile energies.

In Fig. 4.4 we show the penetration range for three ion species (p^+, C^{6+}, V^{23+}) with an increasing plasma temperature at a density of $\rho = 500$ g/cm^2. For each ion charge we show three projectile energies, respectively solid, dashed and dotted lines: in red E_0=7.5, 27.5 and 47.5 MeV for protons, in blue E_0=450, 600 and 750 MeV for carbon and in green E_0=5500, 6500 and 7500 MeV for vanadium. As expected, for every beam specie, increasing the projectile energy allows further penetration range. We find a quasi-constant behaviour for lower temperatures, where the penetration range does not increase significantly up to a certain temperature threshold that depends mostly on the beam specie and ion energy. For protons such temperature is ~ 2 keV, for carbon is about ~ 5 keV and for vanadium is ~ 10 keV. The constant behaviour is more apparent when the beam specie or the energy are increased. For instance, protons at 7.5 MeV do not present a constant behaviour, while at 47.5 MeV they do, with

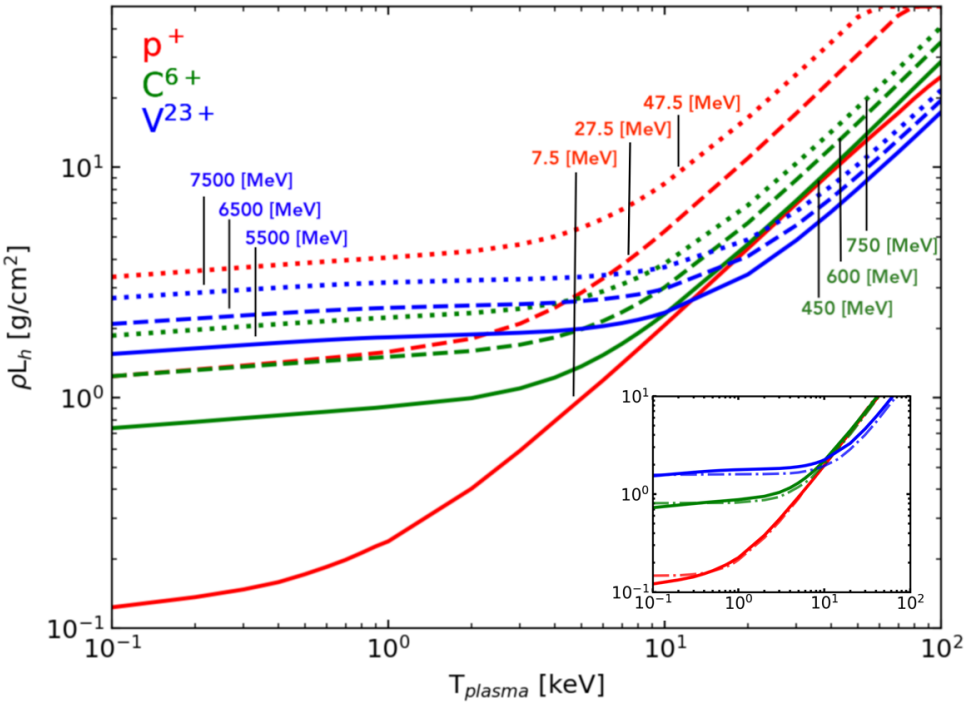

FIGURE 4.4— Penetration range of a monoenergetic ion in DT at 500 g/cm^3 as a function of the plasma temperature. The projectiles are p^+ in red (solid E_0=7.5 MeV, dashed E_0=27.5 MeV, dotted E_0=47.5 MeV), C^{6+} in green (solid E_0=450 MeV, dashed E_0=600 MeV, dotted E_0=750 MeV) and V^{23+} in blue (solid E_0=5500 MeV, dashed E_0=6500 MeV, dotted E_0=7500 MeV). The embedded image show the results obtained by Honrubia et al. (2014) (as dash-dotted lines) for p^+ at E_0=7.5 MeV, for C^{6+} at E_0=450 MeV and for V^{23+} at E_0=5500 MeV, compared to the same cases calculated in our work with the LP model (as solid lines) for a plasma at $\rho = 300$ g/cm^3.

$\rho L_\mathrm{h} \approx 3.3$ g/cm^2, up to 3 keV. On the contrary, a vanadium ion with energy of $E_0 = 5.5$ GeV, returns an approximately constant range of $\rho L_\mathrm{h} \approx 1.5$ g/cm^2 up to 10 keV. For temperatures larger than this threshold the penetration range increases exponentially, this is, the plasma becomes more transparent to the projectiles. If during the whole heating process the ions enter into an increasingly hotter plasma, but reach the same range, then the energy deposition will be localised. This characteristic is a desirable feature for an efficient deposition of the energy in a particular region. For example, for a monoenergetic beam of heavy ions, such as vanadium, we see that energy can be deposited during the whole heating process in a certain region of the plasma. Specifically, during the

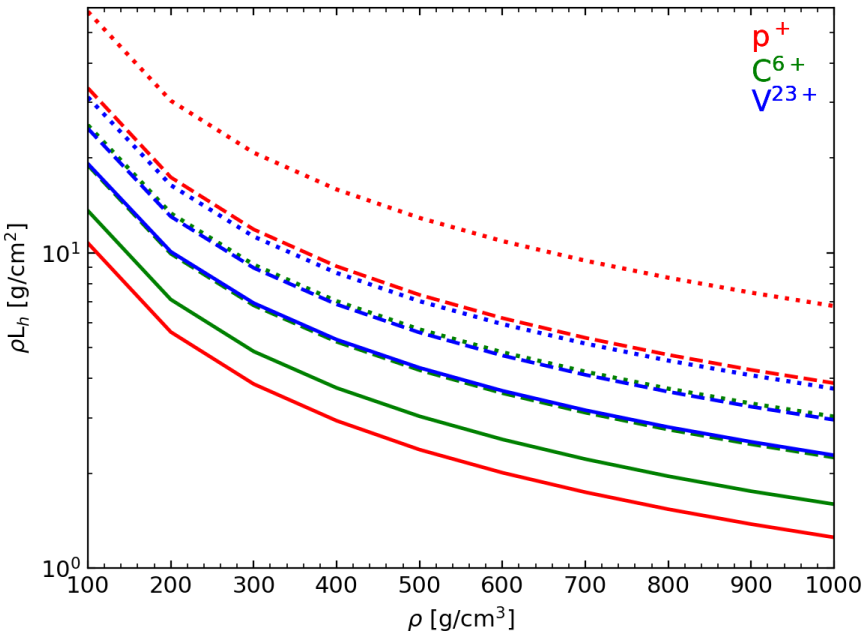

FIGURE 4.5— Penetration range of a monoenergetic ion in DT at $T_0 = 1$ keV as a function of the plasma density. The projectiles and energies are the same as stated in the Fig. 4.4.

heating process that takes the plasma from 0.1 keV to the ignition temperature of about 10 keV. On the other hand, in the case of a non-monoenergetic beam of light ions, the most energetic ions travel through the plasma first, followed by slower ions. By finely tuning the experiment, it is possible to follow a heating process in which the plasma interacts first with high-energy ions and, then, as the plasma warms up, with lower-energy ions, in order to deposit the energy of all the ions, regardless of their energy, in the same region of the plasma. At last, it is worth noting that the curves in Fig. 4.4 establish, for a given ion energy, constraints on the range of the heated region of the plasma. In particular, the minimum range associated with each energy.

Additionally, within Fig. 4.4 there is an inset image of the results obtained by Honrubia et al. (2014), which uses a more elaborated stopping power model. The projectiles selected are p^+ at E_0=7.5 MeV, C^{6+} at E_0=450 MeV and V^{23+} at E_0=5500 MeV, interacting with a plasma at $\rho = 300$ g/cm^3. We represent our results with solid lines and the ones from the literature with dash-dotted lines. In this range of temperatures, we find a good agreement between both results for the different energies proposed, finding an average error around 2%

and maximum error of 10%. This serves as a validation of our calculations, where the differences come from the stopping model applied.

Then, in Fig. 4.5, we show the penetration range for the same cases as in Fig. 4.4, but with an increasing plasma density. The penetration range descends with the density and, again, the higher the projectile energy, the further the penetration range.

4.3 Temperature field validation

Besides proving the stopping power model, it is necessary to address the evolution of the plasma as the projectiles pass through, which is calculated by solving Eq. 3.16. After the beam-plasma interaction, the temperature field is the foundation of the posterior results we present in this thesis. A systematic description of the heated region and the hot-spot under different conditions is only possible if we know the distribution of temperatures. Therefore, in this section, we present a set of experiments that allow us to exhibit and validate the results of our model.

To do so, in Figs. 4.6 and 4.7 we depict the plasma temperature as a function of the distance multiplied by the density (ρx), at the final instant of the beam. Choosing a DT plasma of $\rho = 300$ g/cm^3 and $T_0 = 1$ keV, we present our results with the LP and the PMV models (solid and dashed lines, respectively), juxtaposed with those from figures 1 and 4 of Gus'kov et al. (2014a)[1] (dotted lines).

In Fig. 4.6, we consider three carbon ion beams with ($E_0 = 120$ MeV; $\sigma = 7.8 \cdot 10^{19}$ cm^{-2}), ($E_0 = 160$ MeV; $\sigma = 5.9 \cdot 10^{19}$ cm^{-2}) and ($E_0 = 200$ MeV; $\sigma = 4.7 \cdot 10^{19}$ cm^{-2}). The heated plasma presents a typical result of an edge hot-spot case, with higher temperature values in the initial region of the sphere. Our simulations overestimate the maximum temperature and underestimate the total range in respect to the solutions of Gus'kov et al. (2014a). We note that the LP model is closer to the reference than the PMV model.

Similarly, in Fig. 4.7 we show the spatial distribution of temperature when a carbon ion beam with an initial kinetic energy of $E_0 = 1800$ MeV enters the plasma at flux values of $3.5 \cdot 10^{18}$, $1.4 \cdot 10^{19}$ and $2.8 \cdot 10^{19}$ cm^{-2}. In contrast to the previous scenario, for the three fluxes, the plasma reaches its maximum temperature afar from the edge of the plasma, as in a central hot-spot case. In this case, the maximum temperature is found at $\rho x \approx 8$ g/cm^2 for the PMV stopping model and at $\rho x \approx 10.5$ g/cm^2 for LP and the reference results (Gus'kov et al., 2014a). This shows how the most significant deceleration of the projectiles occurs in the central region, indicating a greater energy loss by the

[1]This author often uses its own stopping model, presented in Gus' kov et al. (2009)

projectile and subsequently a higher plasma temperatures. Here, it is worth highlighting that the position of the maximum temperature, does not change with the flux, this is, only depends on the energy of the beam. This behaviour aligns with our results from Chapter 5. Inspecting further this figure, we find the ranges resulting of the LP model to agree closely with the reference, while the PMV model returns shorter depths. Then, in respect to the maximum temperatures, the LP model is slightly superior compared to the reference, while the PMV stopping overestimates its value.

Both Figs. 4.6 and 4.7, show some discrepancies between the reference results and both our models. Again, this is due to the utilization of different stopping power models, despite, in general, the behaviour is shared overall. Between the PMV and the LP models, the latter agrees better with all the literature results we have checked, so it will be selected for most experiments of this thesis.

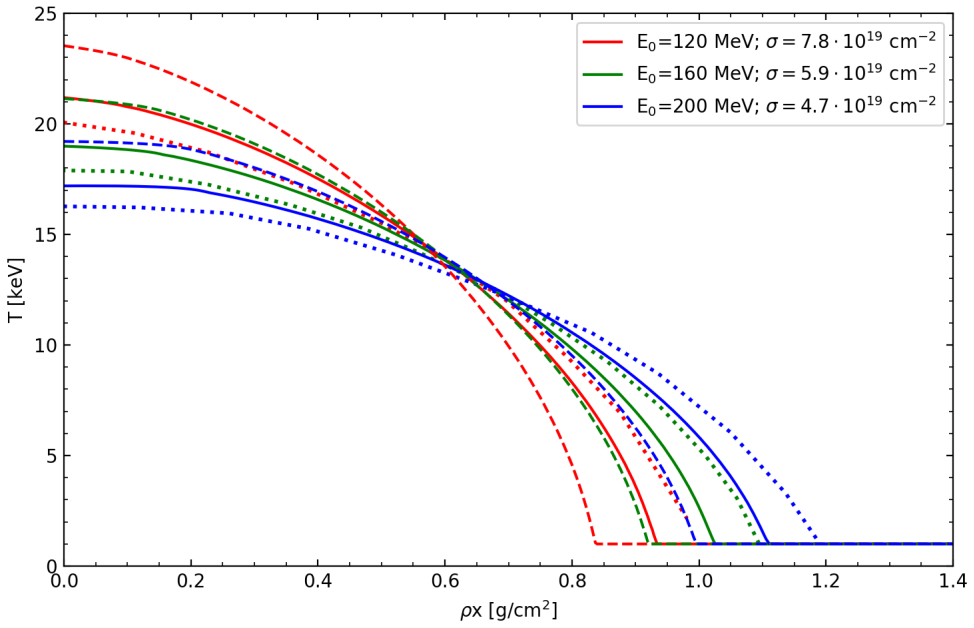

FIGURE 4.6— Temperature distribution of a DT plasma of $\rho = 300$ g/cm^3 and $T_0 = 1$ keV after heating with carbon ion beams of ($E_0 = 120$ MeV, $\sigma = 7.8 \cdot 10^{19}$ cm^{-2}), ($E_0 = 160$ MeV, $\sigma = 5.9 \cdot 10^{19}$ cm^{-2}) and ($E_0 = 200$ MeV, $\sigma = 4.7 \cdot 10^{19}$ cm^{-2}). Solid and dashed lines correspond to our results (LP and PMV models, respectively) and dotted ones to Gus'kov et al. (2014a) (figure 1).

After selecting the stopping LP model, we perform another validation of

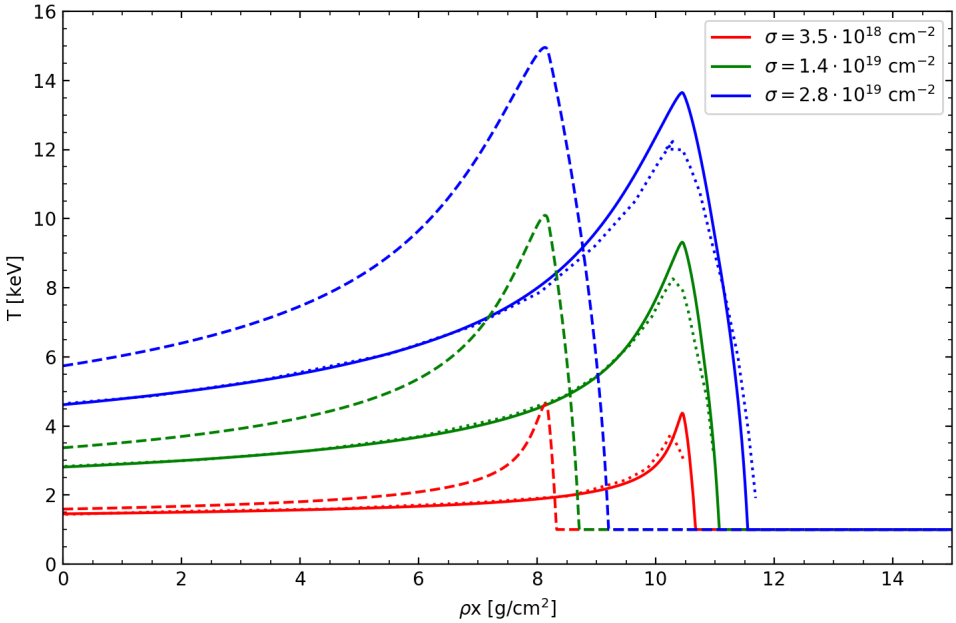

FIGURE 4.7— Temperature distribution of the same plasma of Fig. 4.6 considering a carbon ion beam of energy $E_0 = 1800$ MeV at various specific flux values $\sigma = 3.5 \cdot 10^{18}$, $1.4 \cdot 10^{19}$ and $2.8 \cdot 10^{19}$ cm^{-2}. Solid and dashed lines correspond to our results (LP and PMV models, respectively) and dotted ones to Gus'kov et al. (2014a) (figure 4).

our simulations through Fig. 4.8, comparing with the solutions of Gus'kov et al. (2014a) (figure 5). Once more, the plasma conditions are as in Fig. 4.6, but with a vanadium beam of 5100 MeV. In this case, we perform the experiment of heating the plasma considering the whole beam enters instantaneously, this is, as one bin and without temporal evolution. Such beam has a flux of $\sigma = 1.2 \cdot 10^{18}$ cm^{-2}. Additionally, we simulate the same beam but discretized into bins considering the same flux of $1.2 \cdot 10^{18}$ cm^{-2} and another one of $2.4 \cdot 10^{18}$ cm^{-2}. As in Fig. 4.7 we find central hot-spots, which in the case of just one bin, return a sharper and more localised temperature distribution, with a shorter range. For one bin, there is a disagreement in the range found with our model and that of Gus'kov et al. (2014a), while the maximum temperatures are more alike. On the contrary, after discretising the beam, the results agree more in range, but our model overestimates the maximum temperatures. As explained before, it is expected to find such differences due to the different approximations of each model. As the results follow a similar behaviour within the confidence

ranges, we are confident to lean on the LP model for most of the calculations of this work. We remind that the LP is a well established model, accounting for quantum corrections, large-angle scattering, small-angle binary collisions and collective plasma oscillations.

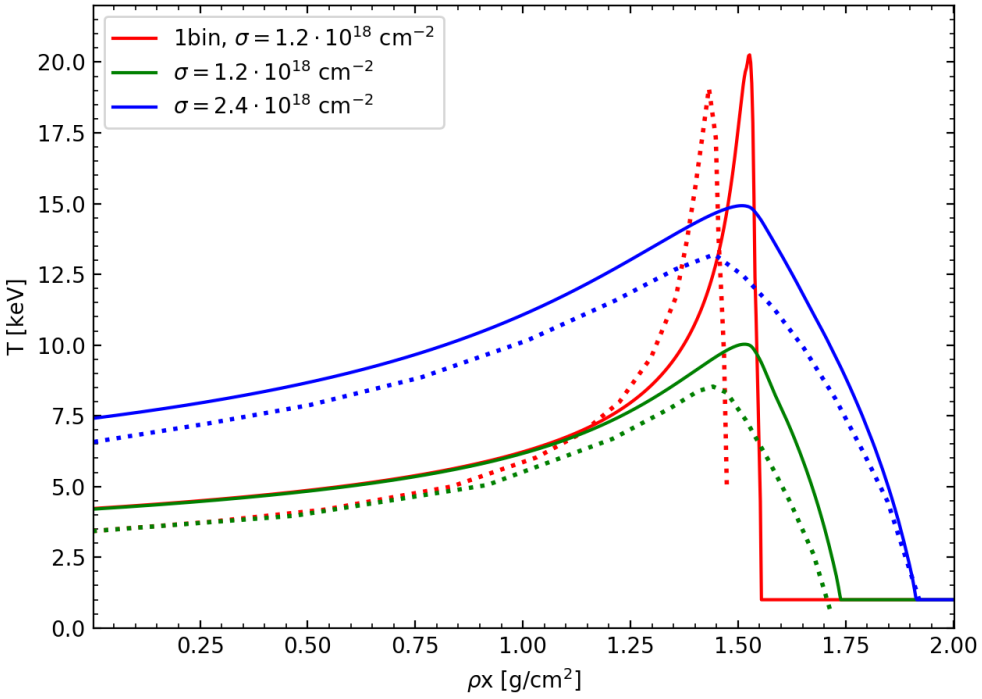

FIGURE 4.8— Temperature distribution of the same plasma of Fig. 4.6 considering a vanadium ion beam of energy $E_0 = 5100$ MeV considering the beam as a whole (1 bin) with $1.2 \cdot 10^{18}$ cm^{-2}, then a partitioned beam with $1.2 \cdot 10^{18}$ cm^{-2} and another $2.4 \cdot 10^{18}$ cm^{-2}. Solid lines correspond to our results (LP) and dashed ones to the ones of Gus'kov et al. (2014a) (figure 5).

A final and more complete validation experiment is shown in Fig. 4.9, comparing with the solutions of Gus'kov et al. (2015) (figure 4), in this case, considering a doped plasma and also a quasi-monoenergetic ion beam. The plasma has a density of $\rho_{\mathrm{DT}} = 300$ g/cm^3 with beryllium ($\xi = 0.4925$) at $T_0 = 1$ keV. The beam considered has a Gaussian energy distribution starting at the edge of the sphere with $\bar{E}_0 = 11.5$ GeV, an energy variance of $\sigma_{\mathrm{E}} = 0$, 1 and 2 GeV, as well as a flux of $\sigma = 7.1 \cdot 10^{18}$ cm^{-2}. Note how increasing the energy spread, expands the total range but lower the maximum temperatures. Again, aside

from some differences in the maximum temperature and the range between our calculations (solid lines) and the ones from Gus'kov et al. (2015) (dotted), this test allows us to validate the implementation of both the doped plasma expressions and the quasi-monoenergetic model.

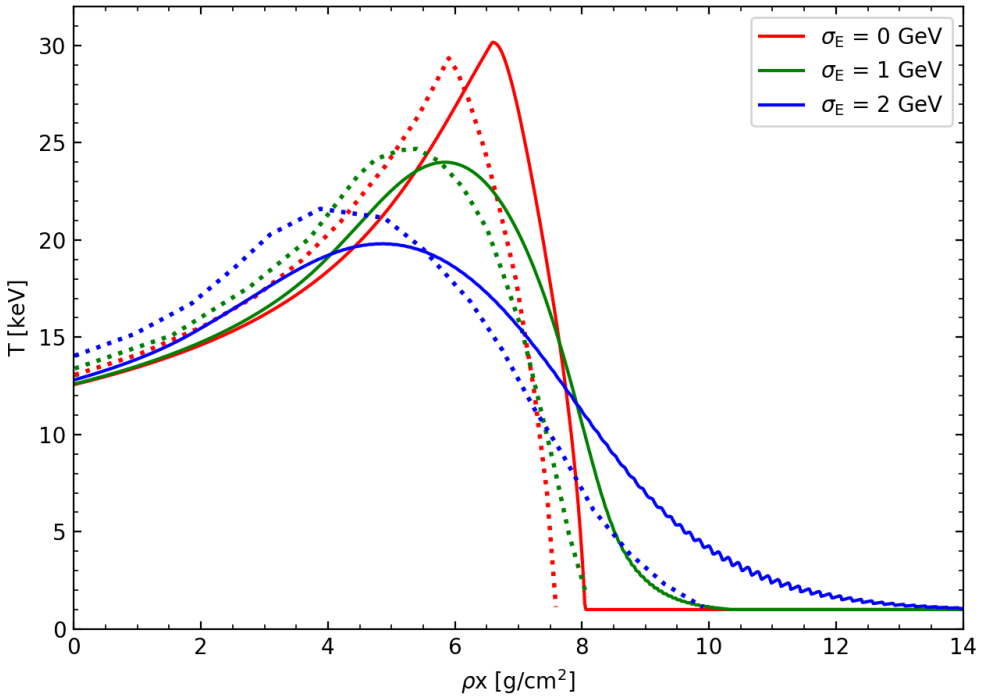

FIGURE 4.9— Temperature distribution of a plasma doped with beryllium ($\xi = 0.4925$) at $T_0 = 1$ keV and $\rho_{DT} = 300$ g/cm^3. The beam a vanadium ion beam of energy $E_0 = 5100$ MeV considering the beam as a whole (1 bin) with $1.2 \cdot 10^{18}$ cm^{-2}, then a partitioned beam with $1.2 \cdot 10^{18}$ cm^{-2} and another $2.4 \cdot 10^{18}$ cm^{-2}. The beam considered has a Gaussian energy distribution with $\bar{E}_0 = 11.5$ GeV, an energy spread of $\sigma_E = 0$, 1 and 2 GeV, and a flux of $\sigma = 7.1 \cdot 10^{18}$ cm^{-2}. Solid lines correspond to our results (LP) and dotted ones to those of Gus'kov et al. (2015) (figure 4).

4.4 Spatial-temporal study of the beam-plasma interaction

Depending on the precompression process, the plasma can be found in different densities and temperatures at the stagnation state. Then, the heating of a plasma in the fast ignition approach entails nonlinear processes. Hence, both factors play a significant role in the slowing of the projectiles.

Thus, with Figs. 4.11 and 4.10 we perform a thorough analysis to complete the examination of the beam-plasma interaction. In this experiment, we consider a proton beam with a pure DT plasma using typical FI conditions[2] (e.g. Gus'kov et al., 2010; Gasparyan et al., 2013): the beam has an initial kinetic energy of $E_0 = 3$ MeV and a flux of $\sigma = 1.6 \cdot 10^{21}$ cm^2. Both figures are a compound of subplot panels distributed as three rows and two columns. Row panels represent, respectively, the kinetic energy of the projectiles, the stopping power and the heating process. These parameters are shown as a function of the distance in the first column and as a function of time (by means of the bins that enter the plasma) in the second column. In the left column, the spatial distribution is shown for two different "instants" associated to the first and last bin (out of $N_\mathrm{b} \approx 2048$) that passes through the plasma. In the right column, the evolution of the plasma is studied at two particular points, corresponding to the edge of the sphere ($x = 0$) and half of its radius ($x = R_\mathrm{F}/2$). We remind that the time evolution of the calculation, which involves the slowing down of projectiles and the heating of the plasma, has been solved according to Eq. 3.68. In such equation, it was possible to change the time intervals (Δt) to particle bins (Δb) as partitions of the flux. This is only possible with the approximations taken in our model, such as neglecting the internal power densities of the plasma during the interaction. In Fig. 4.11 the results are shown for different densities ($\rho = 200$ and 500 g/cm^3) with a fixed initial temperature ($T_0 = 1$ keV), while in Fig. 4.10 the density is fixed ($\rho = 300$ g/cm^3) for different initial temperatures ($T_0 = 0.5$ and 1.5 keV). The results presented here are revisions taken from our previous work Rodríguez-Beltrán (2018).

Figures 4.10 and 4.11 offer substantial insights into the general behaviour of the plasma and the beam. For this analysis, it is important to remind that, as the temperature of the plasma increases due to the interaction, it becomes more transparent, reducing the stopping power and increasing the ion penetration depth. This was already addressed in Sect. 4.1 and demonstrated with Fig. 4.4.

To begin with, we address the general behaviour we find throughout the six panels of both figures, without taking into account the initial temperature or density. In panel A, it is shown how the kinetic energy descends for all bins as the projectile is slowed down. The first bins reach shorter ranges within the still cold plasma. As a function of time, in panel B, the kinetic energy is almost constant for the beginning of the plasma, as a proton beam creates an edge heated region (see panel E) and $x = 0$ will be the most heated and transparent

[2]For these experiments, we used the PMV model. Although it presents numerical differences compared to the reference LP model, the functional behaviour is similar, which is the interest in for this section.

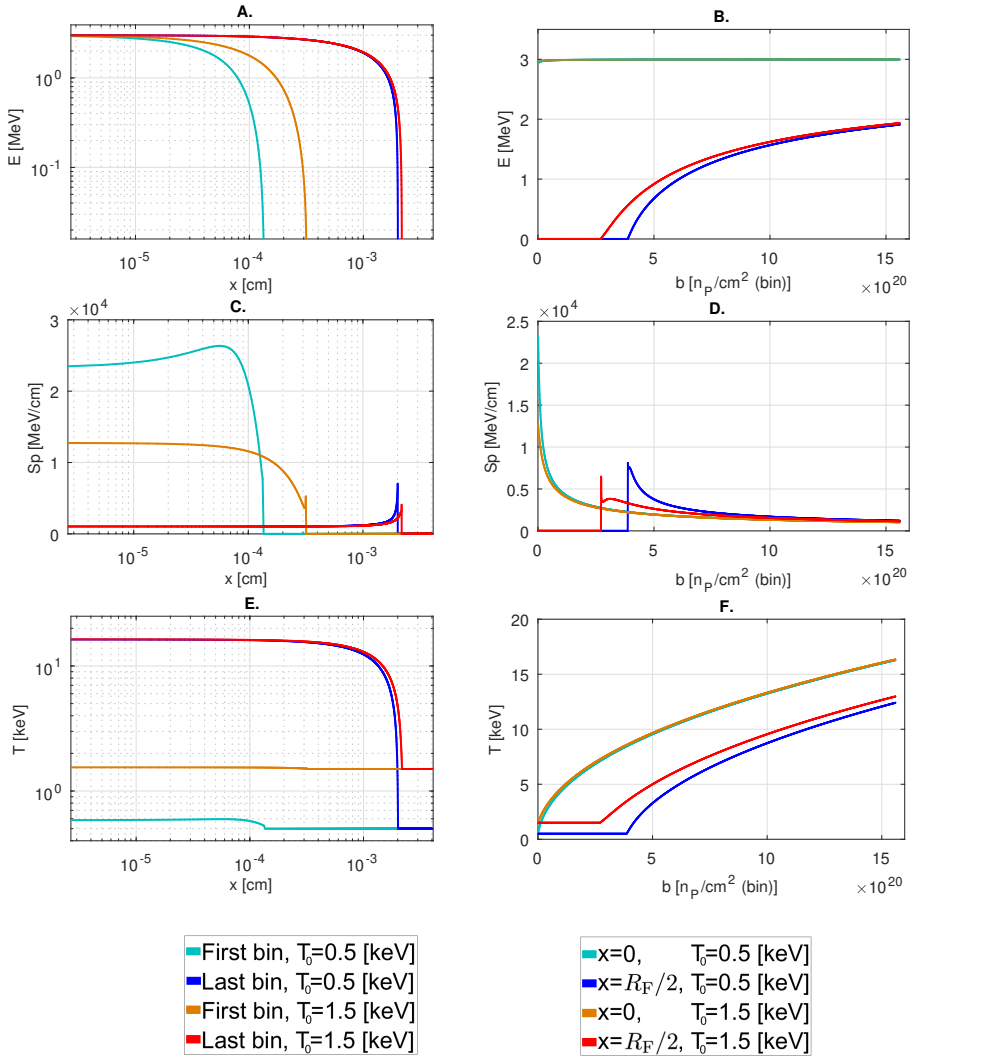

FIGURE 4.10— Experiments with a DT plasma at $\rho = 300$ g/cm^3 and different initial temperatures ($T_0 = 0.5$ and 1 keV), using a proton beam partitioned in $N_\mathrm{b} \approx 2048$ bins, with an initial kinetic energy of $E_0 = 3$ MeV and $\sigma = 1.6 \cdot 10^{21}$ cm^2 (Rodríguez-Beltrán, 2018).

point. Meanwhile, for $x = R_\mathrm{F}/2$ the energy stars ascending (due to the plasma becoming more transparent), but only after the projectiles have been able to dig to such range. In panel C, it is shown the stopping power as a function of the distance. We observe its value quasi-constant up to the final points of the penetration, where, in general, it augments before finally dropping to zero.

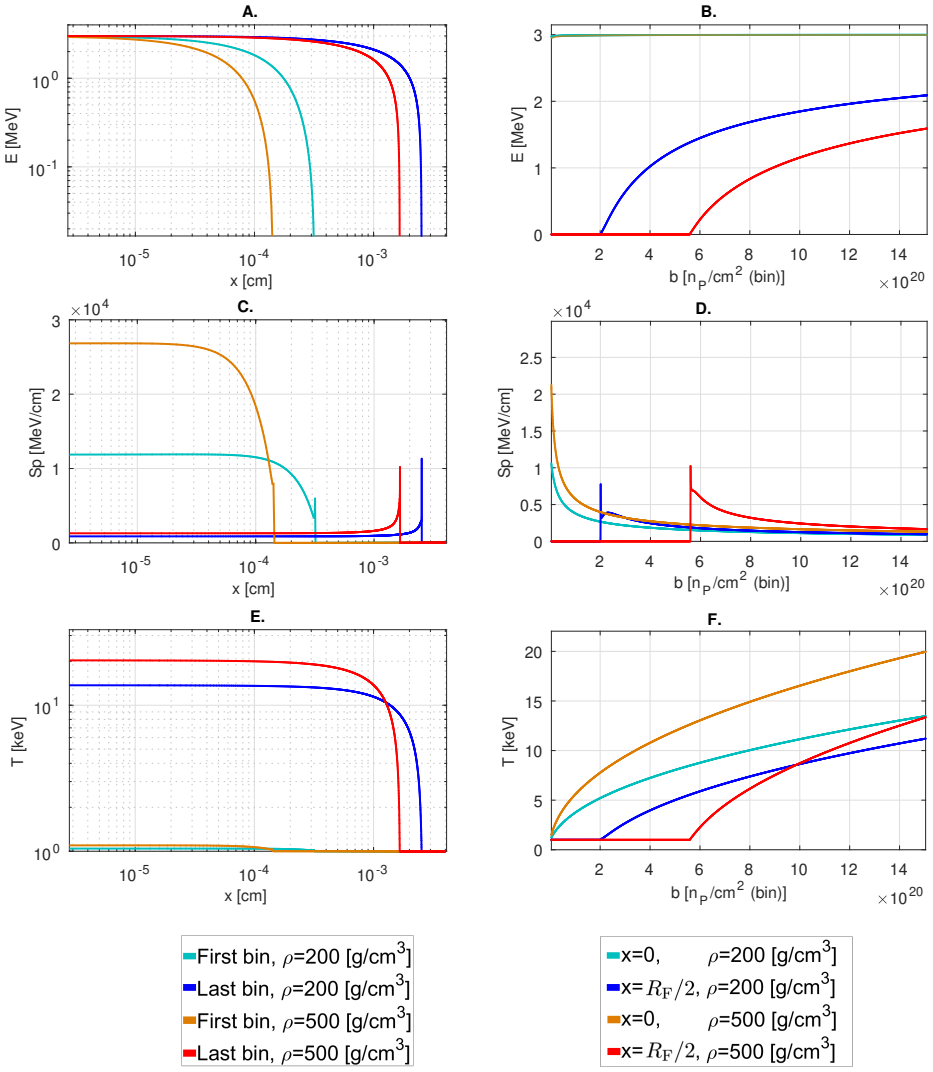

FIGURE 4.11— Experiments with a deuterium-tritium plasma at $T_0 = 1$ keV and different densities ($\rho = 200$ and 500 g/cm^3, using a proton beam partitioned in $N_\mathrm{b} \approx 2048$ bins, with an initial kinetic energy of $E_0 = 3$ MeV and $\sigma = 1.6 \cdot 10^{21}$ cm^2 (Rodríguez-Beltrán, 2018).

These peaks most likely correspond to the moment where the energy of the projectiles resonates with the field of particles of the plasma. Then, in panel D, it is shown how the stopping descends with time, as the plasma heats-up. Panel E shows an edge temperature distribution, typical of proton beams, while panel F shows its increase of temperature over time.

Once the general behaviour is described, we can address the dependence with the initial temperature and density. On the one hand, when considering a higher and a lower initial temperature, as in Fig. 4.10, we observe certain interesting behaviours. In panel A, the difference in range is significant for the first bin, while, after the whole beam interaction, they reach a similar depth because the plasma has been already heated. This is also observed in panel B, where for $x = 0$ and $x = R_{\mathrm{F}}/2$ the temperature of both T_0 cases, converges at the last bins. In panel C, we find how the coldest ($T_0 = 0.5$ keV) plasma has a larger stopping, although its value also converges at the final instants, as panel D shows. The stopping decreases over time, due to the plasma heating. At last, panel E shows an apparently small increment in temperature for the first bin, being this increase higher in the colder plasma. The colder plasma undergoes changes more drastically at the beginning of the interaction, but once the whole beam enters, regardless of the initial temperature, a similar final distribution of temperatures is obtained, as panel F also shows.

On the other hand, varying the density of the plasma is more influential than varying the initial temperature, as we demonstrate in Fig. 4.11. A denser fuel reduces the range of the beam and increases the stopping, thus, creating a hotter plasma. We can state that changing the density is more significative for the final temperature distribution.

4.5 Results of the analytic model

Considering the analytical model presented in Sect. 3.10, we illustrate its potential with the exemplary results of Fig. 4.12. We compare the temperature fields derived from our numerical simulations and analytical approximations across various beam parameter values. The analytical results are obtained after fitting the free parameters (a_1, a_2) in respect to the numerical calculations. The plasma has a density of $\rho = 300$ g/cm^3 and initial temperature of $T_0 = 1$ keV, heated by monoenergetic carbon beams of various energies and fluxes (values are shown in the images). Additionally, when a central hot-spot is found, we display those values that are constant (L_{hs}, T_{hs} and T_{max}) within the figures.

After obtaining the temperature distributions from the simulations and the analytical model, we retrieve the parameters associated to the heated region and the hot-spot (T_{hs}, L_{hs}, L_{h}, etc) for both cases, with the intention of comparing the quality of the analytic model in respect to the numerical solution. Throughout the range of beam parameters investigated in this study, the average relative errors between the analytical fittings and numerical simulations consistently remain below 1%, specially for the central and intermediate cases. It is observed that they tend to be higher for edge hot-spots compared to cen-

tral and intermediate cases, with maximum values generally below 7% and 3%, respectively. As these average relative errors are small enough, we can confirm the close resemblance between the properties obtained through the analytical formula and those from numerical simulations, as shown in Espinosa-Vivas et al. (2023).

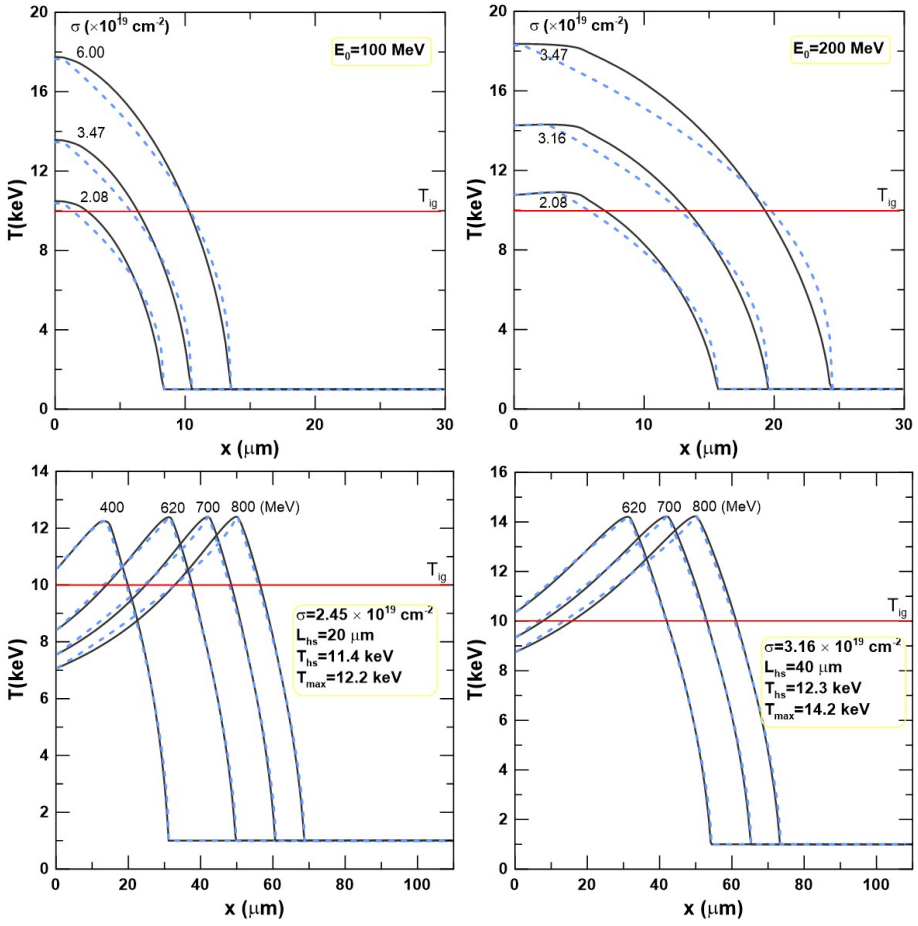

FIGURE 4.12— Comparison of the spatial temperature distributions in a DT plasma ($\rho = 300$ g/cm^3, $T_0 = 1$ keV) heated by monoenergetic carbon beams obtained with our numerical model (solid line) and those provided fitted according to the analytic model of Sect. 3.10 (dotted lines). Espinosa-Vivas et al. (2023).

Table 4.1 presents the fitting parameters for low ion energies across various beam fluxes. Edge plasmas typically manifest for particle energies below 200 MeV, as indicated in Fig. 4.12. Consequently, only the first expression of Eq. 3.57 is utilized in such hot-spots. Edge hot-spots are denoted with $a_2 = 0$

in the table. Conversely, cases associated with $a_2 \neq 0$ are indicative of intermediate or central hot-spots. In Table 4.2, we provide the fitting parameters for medium and high energy per ion values, with three fluxes of the beam. From such table, we find central hot-spots for the energy levels of 400 and 500 MeV if the flux is lower than $\sigma \lesssim 2.4 \cdot 10^{19}$ cm^{-2} and $\sigma \lesssim 2.8 \cdot 10^{19}$ cm^{-2}, respectively. The cases with energies of 620, 700, and 800 MeV are central hot-spots, the rest are intermediate hot-spots.

E_0 [MeV]	100		150		200	
σ [10^{19} cm^{-2}]	a_1	a_2	a_1	a_2	a_1	a_2
2.00	0.436	0	0.444	−1.630	0.506	−1.681
2.59	0.443	0	0.443	0	0.467	−1.678
3.16	0.445	0	0.430	0	0.480	−1.663
3.47	0.442	0	0.431	0	0.454	−1.679
5.58	0.441	0	0.425	0	0.425	0
6.00	0.436	0	0.424	0	0.423	0

TABLE 4.1— Values for the fitting parameters of the analytical model, a_1 and a_2, at the range of low initial energies (E_0), for different values of the flux (σ). Espinosa-Vivas et al. (2023).

σ [10^{19} cm^{-2}]	2.45		2.76		3.16	
E_0 [MeV]	a_1	a_2	a_1	a_2	a_1	a_2
400	0.570	−1.190	0.569	−1.338	0.553	−1.464
500	0.644	−1.095	0.616	−1.100	0.581	−1.114
620	0.640	−0.924	0.636	−0.969	0.641	−1.028
700	0.643	−0.828	0.629	−0.874	0.634	−0.900
800	0.623	−0.745	0.629	−0.790	0.639	−0.825

TABLE 4.2— Values for the fitting parameters of the analytical model, a_1 and a_2, at the range of high initial energies (E_0), for different values of the flux (σ). Espinosa-Vivas et al. (2023).

Upon examination of the tables, we note that a_1 variations are not very drastic in respect to the beam parameters, both for edge and central hot-spots, with values hovering around 0.4 and 0.64, respectively. Meanwhile, for a_2, the fitting parameter ranges from -1.7 to -0.8, moving from intermediate to central hot-spots, respectively. We find that, at least for the carbon beams presented here, when the parameter fulfils $0 > a_2 > -1$ we find a central hot-spot and, when $a_2 < -1$ the temperature distribution corresponds to an intermediate hot-spot.

In the central case, the numerical simulations suggest as a reasonable approximation to assume that the energy deposited by the ion beam in the hot-spot predominantly distributes around the region where $T_{\max}$ is reached, being $L_{\rm hs} \approx 2\lambda$ approximately constant[3], a result that was already highlighted by Gus'kov et al. (2010).

Consequently, the calculation of $T_{\rm hs}$ and $L_{\rm hs}$ for both edge and central hot-spots may rely solely on the part of the analytical expression dependent on a_1, which exhibits a weak dependence on the beam parameters, as discussed earlier. With this understanding, the calculation of the hot-spots characteristics can be approximated with Eqs. 3.58 and 3.59. However, despite the possibility of utilizing the same analytical expression for both types of hot-spots, the behaviour of $T_{\max}$, differ between them. As mentioned earlier, a_1 may almost remain constant in both cases, albeit it tends to be higher for central hot-spots compared to edge hot-spots (see Table 4.1 and Table 4.2). As for $T_{\max}$ and λ, simulations reveal that it increases with σ and E_0 for edge cases, whereas for central hot-spots, it increases with σ but remains relatively constant with E_0, as depicted in Fig. 4.12.

In conclusion, if the free parameters are known, we can extract key properties of the hot-spot without performing the whole numerical simulation. Thus, we could directly predict the gain of the plasma implementing the solutions of $T_{\rm hs}$ and $L_{\rm hs}$ in Eqs. 3.35, 3.36 and 3.61, saving computational resources and time if necessary.

4.6 Validation of the hot-spot gain

After analysing and verifying the temperature distribution by the ion beam interaction, it is necessary addressing the gains presented in Chapter 3. From the field of temperatures, we determine the hot-spot, that is, the spark-region able to ignite. This region is evaluated through the self-heating, the ignition and the burning gains.

In Fig. 4.13 we compare our results for $G_{\rm ig} = 1$ and $G_{\rm sh} = 1$ with the calculations of Atzeni & Meyer-Ter-Vehn (2004) (figure 4.4) and Gus'kov et al. (2011) (figure 2), respectively, and we can observe a good agreement with our calculations. However, some differences can be commented. Above the threshold of 10 keV, we find our results for ignition to be less restrictive with ρR than the reference, while the self-heating is slightly more limiting. Nevertheless, we find sufficient agreement to validate our established criteria.

Then, in Fig. 4.14 we corroborate our results for the burn-up factor (g) and

[3]We remind that λ is the length between $x_{\rm Tmax}$ and the position where the heated region ends ($L_{\rm h}$).

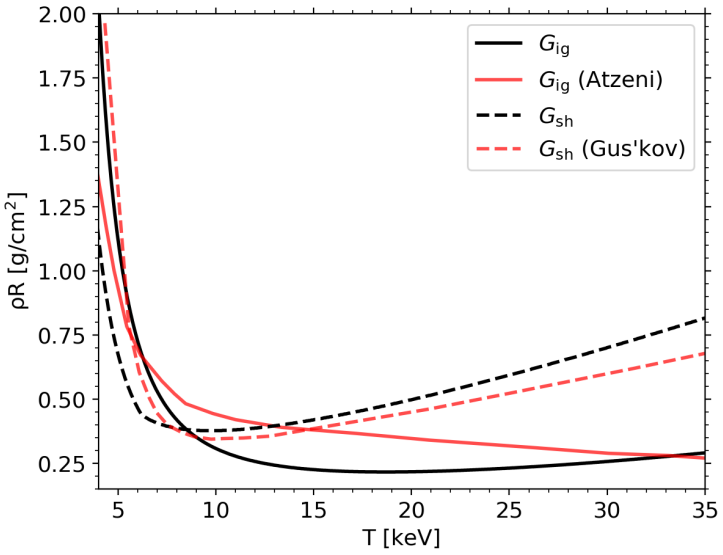

FIGURE 4.13— Ignition and self-heating results in the $(\rho R, T)$-space for a pure DT plasma at ρ=500 g/cm^3. Solid lines correspond to $G_{\rm ig} = 1$, while dashed lines show $G_{\rm sh} = 1$. Our results are displayed in black in comparison to those of Atzeni & Meyer-Ter-Vehn (2004) and Gus'kov et al. (2011) as red lines.

the gain of a homogeneous plasma (G_0), which are the core ingredients of the burning gain calculations we present throughout this thesis. We consider a pure and doped DT plasmas with different impurity fractions ($X_{\rm dop} = 1/(1+\xi)$) and dopants, with a plasma at $T = 15$ keV and $\rho R_{\rm F,DT} = 3$ g/cm^2. According to Eq. 3.63, in the regime of moderate impurity presence, our results match those of Gus'kov et al. (2011) (figures 4 and 5), then for high impurity percentages, we overestimate the burning gain. Throughout this work, in most cases, we do not tackle large impurity levels. Subsequently, the burning gain ($G_{\rm burn}$) values found in this thesis are in the order of various reference results (Gus'kov et al., 2011; Gus'kov et al., 2014b, 2015). For instance, when comparing with table 2 from Gus'kov et al. (2011) we find that our results are similar, with a relative error between 1-3%, but slightly overestimated, as shown in Table 4.3.

4.7 Determination of the (σ, E_0)-space parameter of the ion beam

A key aspect of this work is the determination of an appropriate space parameter for the energy of the ions and the beam flux (σ, E_0). Thus, for each plasma condition and ion beam, we have approximated the (σ, E_0)-values that provide hot-spots with insightful potential. That is, a region inside the heated plasma

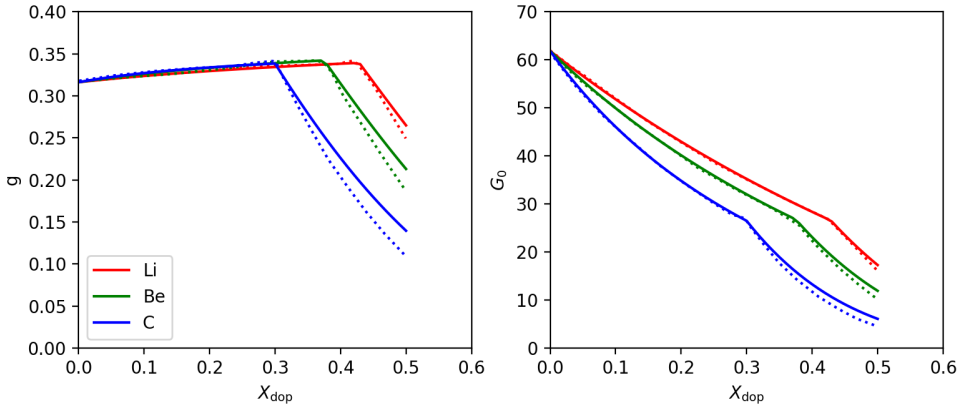

FIGURE 4.14— burn-up factor (g) and gain of a homogeneous plasma (G_0) as a function of the impurity fraction for three different dopants (lithium, beryllium and carbon) considering a plasma at $T = 15$ keV and $\rho R_{\rm DT} = 3$ g/cm^2. Solid lines correspond to our results and dotted ones to those of Gus'kov et al. (2011) (figures 4 and 5).

	$G_{\rm burn}$					
	$\rho R_{\rm F} = 4$		$\rho R_{\rm F} = 6$		$\rho R_{\rm F} = 8$	
ρ [g/cm^3]	Ours	Ref	Ours	Ref	Ours	Ref
300	284	280	949	940	1796	1770
500	269	260	829	820	1459	1430
700	257	250	747	740	1254	1220
1000	243	230	659	650	1056	1050

TABLE 4.3— Burning gain results considering a DT plasma doped with beryllium ($\xi = 0.5$), a hot-spot at $T_{\rm hs} = 20$ keV and $\rho R_{\rm hs} = 1.5$ g/cm^2. For every areal density (in g/cm^2 units), we show first our results and then those of Gus'kov et al. (2011) (table 2).

with average temperature higher than the ignition temperature ($T_{\rm hs}(\sigma, E_0) \geq T_{\rm ig}$), length lower than the diameter of the fuel sphere ($L_{\rm h}(\sigma, E_0) < 2R_{\rm F}$) and such as the ignition gain $G_{\rm ig}(T_{\rm hs}, R_{\rm hs}; E_0, \sigma) \geq 1$, where $R_{\rm hs}$ is derived from $L_{\rm hs}$ as shown in the Sect. 3.9. The parameter space is explored by calculating the beam-plasma interaction for each pair (σ, E_0), in arrays of 100×100 cases, and extracting the key features of the heated region and the hot-spot.

As an example, Fig. 4.15 depicts the isolines in the (σ, E_0)-space of the ignition gain $G_{\rm ig} = 1$ and the length of the heated region $L_{\rm h}$=100 μm, corresponding to twice the radius of a fuel sphere of $R_{\rm F}$=50 μm. In that figure, we also show the isolines for $T_{\rm hs}$=20 keV. The initial temperature is T_0=1 keV and carbon ion beams are applied, with a radius of $r_{\rm b}$=15 μm. As we know that

the density is more influential in the resulting heated region (see Fig. 4.11), we represent three cases, 300, 500 and 700 g/cm^3. Every (σ, E_0) value above the isoline of $G_{\rm ig} = 1$ ensures the hot-spot creation. This region is limited by the points below the contour of $L_{\rm h}$=100 μm, corresponding to the largest possible heated region within such sphere.

Consequently, for any experiment, the limits of our space of interest are determined as follows. The lower limit, $\sigma_{\rm min,ig}$, is fixed by the lower flux value for $G_{\rm ig} = 1$. The corresponding upper limit, $E_{0\,\rm max}$, is found where the isoline of $L_{\rm h} = 2R_{\rm F}$ intersects the $G_{\rm ig} = 1$ line. Then, $\sigma_{\rm max}$ was selected such as the isoline of $T_{\rm hs} \approx 20$ keV intersects with the line $L_{\rm h} = 2R_{\rm F}$. Such reference temperature is selected to assure we are working in an interval of temperatures where the equilibrium time and the internal processes time are adequate in respect to the beam interaction (see Fig. 3.9), as well as the power density of the internal processes against the one for the beam. Moreover, we have found that for such high temperature the burning gain results are not of interest in the IFI context, as we will show in the next chapters. In any case, for larger temperatures the general behaviour is similar and can be predicted following the results presented in the current work. At last, $E_{0\,\rm min,ig}$ is obtained as the lowest possible value for the selected $\sigma_{\rm max}$ with $G_{\rm ig} > 1$.

This procedure was applied to every beam specie and radius, to every plasma density and initial temperature. Although not explicitly presented in this thesis, the (σ, E_0)-ranges of study for various dopants and concentrations have been calculated, too. We can advance that for doped plasmas, the space of study narrows as the impurities are heavier or in higher concentrations. The ignition conditions are more restrictive, as it is shown in Chapter 6.

As an example, in Tables 4.4 and 4.5 we list the ranges of our study $(\sigma_{\rm min,ig}, \sigma_{\rm max}, E_{0\,\rm min,ig}, E_{0\,\rm max})$ for a beam of $r_{\rm b}$=15 μm and a pure DT plasma of T_0=1 keV. We show $E_{0\,\rm max}$ and $\sigma_{\rm max}$ depending on the density, as we found a significant change. On the other hand, the results keep approximately stable when changing either the beam radius or the initial temperature. As shown in Figs. 4.10 and 4.11 the initial temperature does not influence drastically the final distribution of temperatures, while the density does. In respect to the beam radius, it is necessary for calculating $G_{\rm ig}$, but its effect is minor in comparison to the value of the density. In these tables, we observe how the values $\sigma_{\rm min,ig}$ decrease with the beam charge, while the $E_{0\,\rm max}$ values increases. We have found that, in general, for a pure DT plasma, even though the outcome might vary depending on the exact characteristics of the experiment, the results we have presented serve as a representative approximation of the limits of $G_{\rm ig} = 1$ in the (σ, E_0)-space.

When following the isoline of $G_{\rm ig} = 1$, we find that the hot-spot tempera-

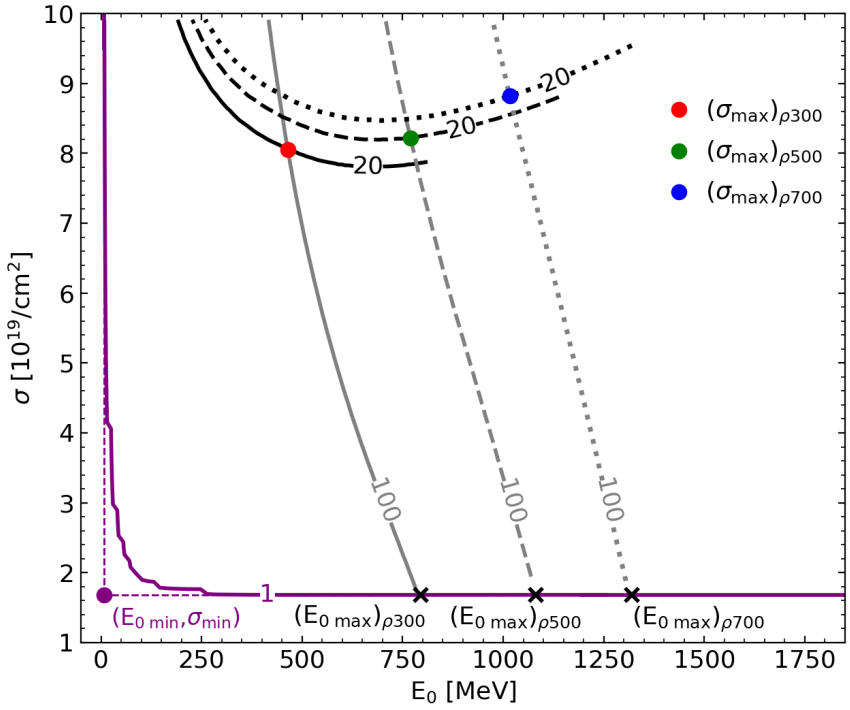

FIGURE 4.15— Isolines in the (σ, E_0) parameter space: ignition gain $G_{\rm ig} = 1$ (purple line), length of the heated plasma $L_{\rm h}$=100 μm (grey lines) and hot-spot temperature of $T_{\rm hs}$=20 keV. Plasma densities are $\rho = 300$ (solid), $\rho = 500$ (dashed) and ρ=700 g/cm^3 (dotted). We use C^{6+} beam of radius $r_{\rm b}$=15 μm.

tures range from $T_{\rm hs} \approx 10$ keV at high energies to 12.5 keV if low projectile energies are considered. Then, the areal density oscillates around $\rho R_{\rm hs} \approx 0.25-0.35$ depending on the experiment. We can relate these values with the ignition and self-heating curves shown in Fig. 3.5. We find that the heated plasmas associated to the different (σ, E_0) through the $G_{\rm ig} = 1$ isoline correspond to a region on the $(\rho R, T)$-space found approximately below the minimum of the self-heating curve and on the right of $T_{\rm ig}$. Additionally, this region matches the highest burning gain values available, indicating that an optimal beam requires finely tuning its (σ, E_0)-parameters, in order to get closer to the $G_{\rm ig} = 1$ isoline, as it is shown in the following chapters. Moreover, we provide which beam energies are required to reach the $G_{\rm ig} = 1$ isoline at every (σ, E_0)-case. We have found that beam energy ranges from $E_{\rm b} \approx 20$ kJ for highly energetic projectiles and low fluxes, to $E_{\rm b} \approx 1$ kJ for high fluxes. Similarly, the specific

energy density ($\sigma \cdot E_0$) goes from 3 GJ/cm^2 to 0.15 GJ/cm^2, respectively. These results agree with previous literature, being in the same order of works such as Gus'kov et al. (2014b) and Honrubia et al. (2014). For these conditions, the beam should operate in a characteristic time of $\tau_{\text{beam}} \approx 10^{-11} - 10^{-12}$ seconds, in order to approximately fulfil the conditions of this work in respect to the internal times of the plasma.

IC	$E_{0\,\text{min,ig}}$	$E_{0\,\text{max}}(\rho_{300})$	$E_{0\,\text{max}}(\rho_{500})$	$E_{0\,\text{max}}(\rho_{700})$
p^+	0.2	26.1	41.1	52.4
C^{6+}	7.3	792.9	$1.10 \cdot 10^3$	$1.30 \cdot 10^3$
V^{23+}	60.9	$7.10 \cdot 10^3$	$9.40 \cdot 10^3$	$1.10 \cdot 10^4$

TABLE 4.4— Energy ranges (MeV) of the parameter space to study, considering a plasma with initial temperature of T_0=1 keV and beam radius r_b=15 μm. IC denotes the charge of the ions in the beam; $E_{0\,\text{min,ig}}$ is the minimum projectile energy to achieve the ignition criterion; $E_{0\,\text{max}}$ denotes the maximum projectile energy when L_h=100 μm, which is plotted for plasma densities ρ=300, 500 and 700 g/cm^3.

IC	$\sigma_{\text{min,ig}}$	$\sigma_{\text{max}}(\rho_{300})$	$\sigma_{\text{max}}(\rho_{500})$	$\sigma_{\text{max}}(\rho_{700})$
p^+	$5.70 \cdot 10^{20}$	$4.50 \cdot 10^{21}$	$3.60 \cdot 10^{21}$	$3.40 \cdot 10^{21}$
C^{6+}	$1.60 \cdot 10^{19}$	$8.10 \cdot 10^{19}$	$8.20 \cdot 10^{19}$	$8.80 \cdot 10^{19}$
V^{23+}	$1.30 \cdot 10^{18}$	$6.50 \cdot 10^{18}$	$7.90 \cdot 10^{18}$	$9.20 \cdot 10^{18}$

TABLE 4.5— Flux ranges (1/cm^2) of the parameter space to study, considering a plasma with initial temperature of T_0=1 keV and beam radius r_b=15 μm. IC denotes the charge of the ions in the beam; $\sigma_{\text{min,ig}}$ represents the minimum beam flux needed to achieve the ignition criterion; σ_{max} denotes the maximum beam flux when T_hs=20 keV, which is depicted for plasma densities ρ=300, 500 and 700 g/cm^3.

In summary, with this chapter we have verified our numerical and analytic models in respect to previous results from the literature, aside from reasonable numerical differences. Then, the general behaviour of the interaction was acknowledged, as well as a procedure for selecting the range of beam characteristics where a hot-spot is generated inside the heated region. These previous points are key for continuing our evaluation on a broader variety of scenarios, as the following chapters gather.

5

Simulation and analysis of the beam-plasma interaction of monoenergetic ion beams with pure DT fuels

In the previous chapter, we presented preliminary results of our model. This allowed us to compare and validate our solutions with those obtained by other authors. Another key result was the determination of the (σ, E_0)-range where a hot-spot is generated. Illustrative, in Sect. 4.7 we presented the ranges of study for monoenergetic beams (p^+, C^{6+}, V^{23+}) interacting with a pure DT plasma. This allows focusing our simulations and analysis on situations of interest in the field of inertial fusion and, in particular, on the ion fast ignition scheme. In the current chapter, we focus on monoenergetic ion beams interacting with a pure DT fuel. We consider plasmas with different densities (from 300 to 700 g/cm^2) and initial temperatures (from 0.5 to 5 keV). Thus, we proceed to the systematic simulation of the spatial distribution of the temperatures after the beam interaction. From this temperature field, we extract the fundamental parameters of the heated plasma and the corresponding hot-spot. The length and temperature from the latter allow us to evaluate where ignition is achieved, the burning gain values or the coupling parameters between the beam and the plasma.

In this chapter, we start our systematic study by considering that the beam is generated at the edge of the plasma. This is an idealised situation, but presents the advantage that the corona plasma does not influence the interaction

process, thus, characterising the heating by exclusively considering the beam and the precompressed core. Some experimental arrangements were already predicted to come close to this consideration (e.g. Kodama et al., 2001; Betti & Zhou, 2005). Also, when considering the scheme where a cone is embedded in the plasma, the beam can be targeted to reach the uniform density of the core. Then, towards the end of this chapter, we include the presence of a corona, to examine its influence and evaluate how necessary is to consider its presence. In that context, it is important to consider the distance at which the ion beam is generated from the plasma edge.

The particular cases we chose to show in this chapter are representative of general behaviours encountered throughout our simulations.

5.1 Length and temperature distributions in the (σ, E_0)-space

We present key results of the heated plasma and the hot-spot after the beam-plasma interaction, such as its characteristic lengths and temperatures in the region of the (σ, E_0)-space where the ignition is achieved. Representative simulations were performed for a DT plasma of density ρ=500 g/cm^3, T_0=1 keV and R_F=50 μm. The beams selected are p^+, C^{6+} and V^{23+}. Thus, in the left column of Fig. 5.1 we show the isolines associated to the hot-spot lengths L_hs, the ranges L_h and the positions of the maximum temperatures x_Tmax, for the (σ, E_0) beam parameters. In the right column of Fig. 5.1 we depict the isolines of hot-spot mean temperatures T_hs, the maximum temperatures T_max and the temperatures at the edge of the plasma $T_\mathrm{x=0}$. With this set of parameters, we can characterise the beam-plasma interaction, knowing, for example, what beam energy is required to generate a hot-spot with a certain length or temperature, depending on the charge of the projectiles. This is done by retrieving the characteristic (σ, E_0)-values associated to the desired plasma conditions and then calculating $E_\mathrm{b} = \sigma E_0 \pi r_\mathrm{b}^2$. We can also calculate the energy deposited in the hot-spot or the energy of the whole heated region, as $\Delta E_\mathrm{hs} = \rho C_\mathrm{V}(T_\mathrm{hs} - T_0) L_\mathrm{hs} \pi r_\mathrm{b}^2$ and $E_\mathrm{h} = \rho C_\mathrm{V} T_\mathrm{h} L_\mathrm{h} \pi r_\mathrm{b}^2$, respectively. Moreover, from some of these parameters and the corresponding isoline maps, we can retrieve the burning gain (see Eq. 3.61), which is a key result in the IFI scheme. Alternatively, we can reconstruct the temperature field from the analytical model (see Eqs. 3.57, 3.58 and 3.59). This can be useful to start complex radiative-hydrodynamic simulations of the hot-spot evolution for the nuclear fuel burn-up, by selecting typical hot-spots of IFI.

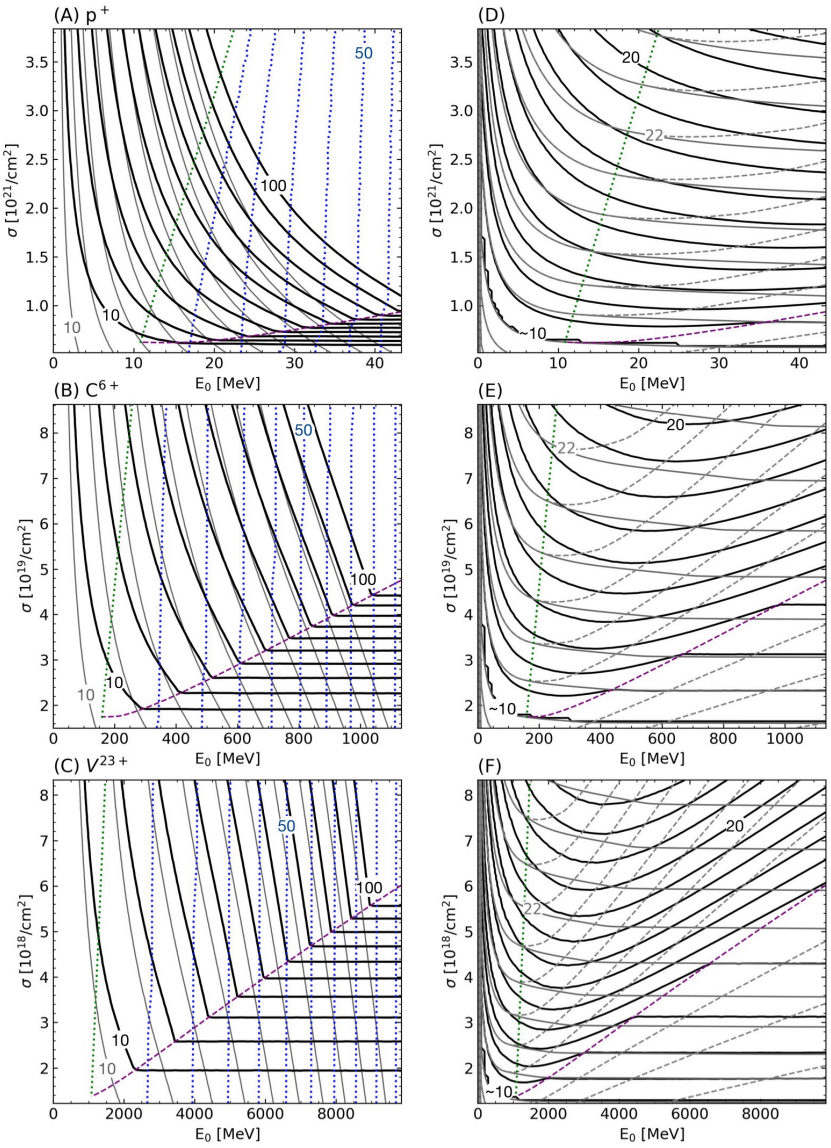

FIGURE 5.1— Results for a pure DT plasma of ρ=500 g/cm^3 and T_0=1 keV, for beams of p^+ (A and D panels), C^{6+} (B and E panels) and V^{23+} (C and F panels). Left: Isolines of $L_{\rm hs}$ (solid black line), $L_{\rm h}$ (solid grey line) and $x_{\rm Tmax}$ (dotted blue line); units are in μm and the spacing between lines is of 10 μm. Right: Isolines of $T_{\rm hs}$ (solid black line), $T_{\rm max}$ (solid grey line) and $T_{\rm x=0}$ (dashed grey line); units are in keV and the spacing between lines is of 1 keV for $T_{\rm hs}$ and in intervals of 2 keV for $T_{\rm max}$ and $T_{\rm x=0}$. The green solid lines ($x_{\rm Tmax}=0$) divide the (σ, E_0)-space in edge and intermediate hot-spot regions. The purple solid lines ($T_{\rm x=0}=T_{\rm ig}$) separate the intermediate and central hot-spot regions.

We can observe the (σ, E_0)-regions where we find an edge, intermediate or central hot-spot, as explained in Sect. 3.9. An edge hot-spot region is created when $x_{\mathrm{Tmax}} = 0$, that is, T_{max} is equal to $T_{\mathrm{x=0}}$. The threshold between the edge and the intermediate hot-spot regions is marked in both figures with a green dotted line. The central hot-spot region is found when $T_{\mathrm{x=0}} < T_{\mathrm{ig}}$ and matches those cases where L_{hs}, T_{hs} and T_{max} are constant with the kinetic energy for a given flux. The intermediate hot-spot region is in between the edge and the central hot-spot region, it corresponds to cases where $x_{\mathrm{Tmax}} \neq 0$ but $T_{\mathrm{x=0}} \geq T_{\mathrm{ig}}$. The threshold between the intermediate and the central hot-spot region is shown with a purple dashed line. We have included in the figure, for some cases, a zoom-in within the ranges of study obtained in Sect. 4.7, for the sake of a clearer representation.

Studying Fig. 5.1, we can detect certain differences for different ion compositions of the beams. The space of parameters where central hot-spot is achieved increases with the beam charge (Z_{b}). Thus, the steep of the lines that divide the edge, intermediate and central hot-spot regions rise with Z_{b}. Additionally, for the central hot-spot analysed in this work, the highest temperatures achieved by the hot-spot $(T_{\mathrm{hs}}, T_{\mathrm{max}})$ increase with the beam charge.

On the other hand, some common behaviours are observed for all the beams species considered. First, within the edge hot-spot region, the variables (L_{h}, L_{hs}, T_{hs}, $T_{\mathrm{x=0}} = T_{\mathrm{max}}$) present a similar shape. All of them increase with both flux and energy, even though the variation is more dependant with the energy.

Second, in the intermediate hot-spot region, the variables L_{h} and L_{hs} present the same behaviour as in the edge hot-spot region. Conversely, the temperature parameters behave differently: the isolines of $T_{\mathrm{x=0}}$ and T_{max} separate when entering the intermediate hot-spot region; $T_{\mathrm{x=0}}$ increases with the flux but decreases with the energy; T_{max} presents a trend towards a constant behaviour with the energy for a given flux; T_{hs} continues to increase with the energy and the flux, then, in a certain threshold, starts decreasing with the energy, but less drastically than $T_{\mathrm{x=0}}$.

Third, for central hot-spots it is detected that, for a given flux value, the region is delimited by an array of threshold points $(\sigma^*, E^*(\sigma^*))$ such that the hot-spots generated with $E_0 > E^*$ have the same values for L_{hs}, T_{hs} and T_{max}. In other words, for a given energy these parameters only increase with σ. For instance, with a vanadium beam, at $\sigma^* = 2.7{\cdot}10^{18}$ cm^{-2}, the constant behaviour occurs at $E^*(\sigma) \approx 3500$ MeV, finding that $L_{\mathrm{hs}} \approx 21$ μm, $T_{\mathrm{hs}} \approx 12.7$ keV and $T_{\mathrm{max}} \approx 15.5$ keV. Then, at higher a higher flux ($\sigma = 3.8 \cdot 10^{18}$ cm^{-2}) the threshold is found at $E^* \approx 5500$ MeV, and the same parameters ascend to $L_{\mathrm{hs}} \approx 42.6$ μm, $T_{\mathrm{hs}} \approx 13.9$ keV and $T_{\mathrm{max}} \approx 18.8$ keV. In other words, for energies higher than the threshold, E^*, we can also define a $\sigma^*_{L_{\mathrm{hs}}}$ value that correspond

to a length of the hot-spot, independently of the energy. Correspondingly, the energy threshold can be assigned to a value of $L_{\rm hs}$, this is $E^*_{L_{\rm hs}}$. On the contrary, in the central hot-spot region other magnitudes do not follow this constant behaviour, such as the position of the maximum temperature ($x_{\rm Tmax}$), the range ($L_{\rm h}$) and the temperature at the beginning of the plasma ($T_{\rm x=0}$), which do change with energy. We find that $L_{\rm h}$ and $x_{\rm Tmax}$ behaviour is the same as in edge and intermediate hot-spot regions. In particular, $x_{\rm Tmax}$ increases with E_0 and it is almost independent of σ. Therefore, in order to create a hot-spot in the centre of the fuel sphere, it is necessary to tune accurately the kinetic energy. For example, achieving $x_{\rm Tmax}$=$R_{\rm F}$=50 μm requires E_0=37$\sim$38 MeV for protons, E_0=800$\sim$820 MeV for carbon and $E_0 \approx$ 6600 MeV for vanadium.

We want to highlight the potential of the behaviour found in the (σ, E_0)-space. When following a particular $L_{\rm hs}$ isoline it is possible to reach the same length in different scenarios. For low energies and larger fluxes, the hot-spot is created at the edge of the plasma. Meanwhile, the same hot-spot length is obtained as a central hot-spot for low fluxes and higher energies. The isolines of the temperature of the hot-spot work in a similar way.

As an instance of the behaviour in the central hot-spot region, in Fig. 5.2 we represent the temperature field of a V^{23+} beam for σ=3.1$\cdot$ 10^{18} cm^{-2}, associated with values of $L_{\rm hs}$=30 μm, $T_{\rm hs}$=13 and $T_{\rm max}$=16.6 keV. If we select three different kinetic energies, E_0=5865, 6630 and 7300 MeV, we observe how they correspond to the positions of $x_{\rm Tmax}$=40, 50 and 60 μm and the ranges $L_{\rm h}$=50.5, 60.5 and 70 μm. This shows how these lengths increase with their respective energy values (also, their edge temperature decreases as $T_{\rm x=0}$=8, 7.3 and 6.8 keV), while the hot-spot parameters and $T_{\rm max}$ remain constant.

Then, in Fig. 5.3 we fix the energy at E_0=6630 MeV, where $x_{\rm Tmax} \approx$ 50 μm, for three different fluxes σ=2.6$\cdot$10^{18}, 3.1$\cdot$10^{18} and 3.5$\cdot$10^{18} cm^{-2}, matching $L_{\rm hs}$=20, 30 and 40 μm. As expected, the position of the maximum temperature is fixed at $x_{\rm Tmax} \approx$ 50 μm, the temperatures of interest increase with the flux: $T_{\rm hs}$=12.3, 13 and 13.3 keV, T_0=6.2, 7.3 and 8.2 keV and $T_{\rm max}$=15, 16.6 and 17.9 keV, respectively for every σ-value.

5.2 Length and temperature distributions in the (σ, E_0)-space varying plasma ρ and T_0

So far, the study has been performed for a fixed set of plasma initial conditions (ρ=500 g/cm^3 and T_0=1 keV). Now, we address the influence of different initial plasma temperatures and mass densities. We selected various cases to exemplify the dependence of the beam-plasma interaction. Hence, in Fig. 5.4 we consider three mass densities, ρ=300, 500 and 700 g/cm^3, for T_0=1 keV. Then, in Fig. 5.5,

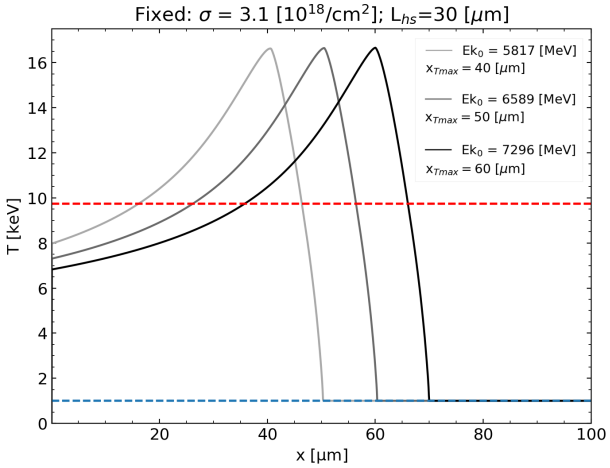

FIGURE 5.2— Spatial distribution of the plasma temperatures (ρ=500 g/cm^{-3}) after the interaction with a V^{23+} beam for a fixed σ=3.1·10^{18} cm^{-2} and three different kinetic energies E_0=5817, 6589 and 7296 MeV.

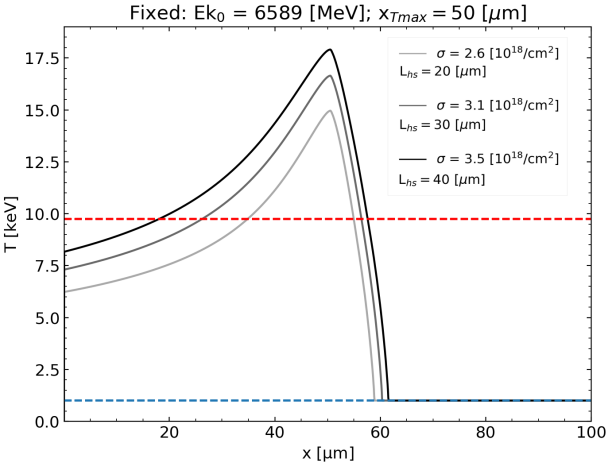

FIGURE 5.3— Same conditions as in Fig. 5.2 but considering a fixed E_0=6589 MeV and three different fluxes σ=2.6·10^{18}, 3.1·10^{18} and 3.5·10^{18} cm^{-2}.

we consider three values of plasma initial temperature, for a mass density of ρ=500 g/cm^3.

Through the current work, we focus on certain cases of interest related to typical experimental values. We select experiments with beam radii of r_b=10,

15 and 20 μm, combined with sphere radii of R_{F}=40, 50 and 60 μm (which are typical IFI values, as stated in Sect. 2.4). Then, for achieving a hot-spot whose cylindrical geometry resembles a sphere, we need $L_{\mathrm{hs}} \approx 2r_{\mathrm{b}}$, and, in order to achieve a central explosion, it is required that it is located in the middle of the plasma $x_{\mathrm{Tmax}} \approx R_{\mathrm{F}}$.

Hence, in Figs. 5.4 and 5.5 we show where L_{hs}=20, 30 and 40 μm are located. Additionally, we show x_{Tmax}=50 μm. Here, x_{Tmax}=40 and 60 μm are not included for the sake of clarity in the figure, but their related E_0 values are shown in Tables 5.1, 5.2 and 5.3. In Figs. 5.4 and 5.5, the values of T_{hs} corresponding to L_{hs}=20, 30 and 40 μm in the central hot-spot region have been included. In all figures, $x_{\mathrm{Tmax}} \approx 0$ is plotted, which divides the (σ, E_0)-space between edge and intermediate hot-spot. Furthermore, the lines corresponding to $T_{\mathrm{x=0}} = T_{\mathrm{ig}}$ are also depicted, which separate the intermediate and central hot-spots. This analysis is repeated for different beams: p^+, C^{6+} and V^{23+}.

On the one hand, Fig. 5.4 shows that, in the central hot-spot region, the denser the plasma, the more flux is necessary to achieve the same L_{hs}. Meanwhile, in the edge and intermediate hot-spot regions, when increasing the density, more projectile energy is required for achieving a similar hot-spot. For identical hot-spot lengths, the temperatures are slightly superior when increasing the plasma density. Also, it is found that more ion energy is needed to reach the same location for the maximum temperature, x_{Tmax}. In the particular case of the proton beam, x_{Tmax}=50 μm is never achieved in our region of study. Finally, changing the density does not affect significantly the position of the $x_{\mathrm{Tmax}} = 0$ and the $T_{\mathrm{x=0}} = T_{\mathrm{ig}}$ lines.

On the other hand, in Fig. 5.5, when increasing the initial temperature T_0, either less flux for central hot-spots or less projectile energy for edge-intermediate hot-spots is required for achieving the same lengths. For such L_{hs}, we find that the hot-spot temperature descends with the initial temperature. We find that the position of the maximum temperature, x_{Tmax}, does not depend significantly on the initial temperature. At last, changing the initial temperature changes the position of the $x_{\mathrm{Tmax}} = 0$ line and the $T_{\mathrm{x=0}} = T_{\mathrm{ig}}$ line. This is found more drastically for the T_0=5 keV case, where the edge hot-spot region is expanded and central hot-spots are harder to create. Such restriction on the central hot-spot region is due to the plasma being more transparent from the beginning. Finally, larger temperatures are obtained for heavier beam species, as can be seen in Fig. 5.5.

This analysis is completed with the Tables 5.1, 5.2 and 5.3. We select representative conditions desirable for a central and approximately symmetric combustion (see Sect. 2.3.2). On the one hand, we show the energy results at which $x_{\mathrm{Tmax}} \approx R_{\mathrm{F}}$, considering typical spheres such that $R_{\mathrm{F}} = 40$, 50 and

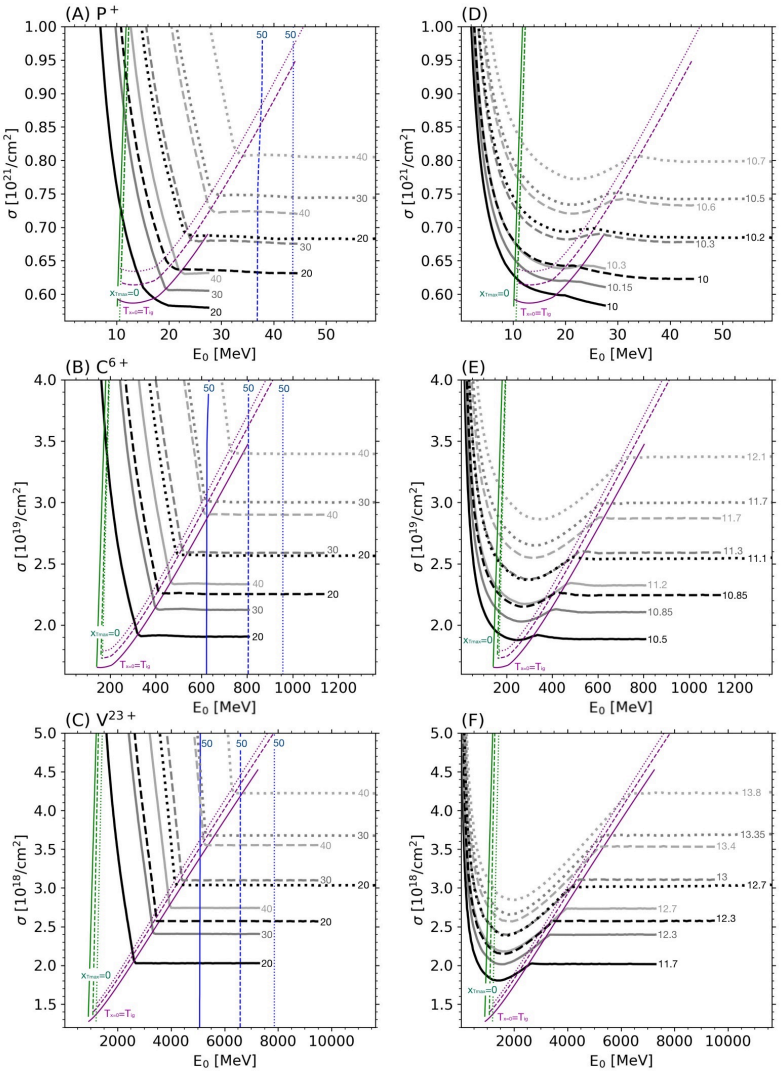

FIGURE 5.4— Isoline results for a pure DT plasma (T_0=1 keV) with densities of ρ=300 g/cm^3 (solid), ρ=500 g/cm^3 (dashed) and ρ=700 g/cm^3 (dotted). Beams of p^+ (panels A and D), C^{6+} (panels B and E) and V^{23+} (panels C and F) are considered. Left: Black, grey and light-grey colours represent the hot-spot lengths for $L_{\rm hs}$=20, 30 and 40 μm. Dotted blue lines represent $x_{\rm Tmax}$=50 μm. Right: Black, grey and light-grey colours represent the hot-spot temperatures ($T_{\rm hs}$) corresponding to $L_{\rm hs}$=20, 30 and 40 μm in the central hot-spot region, with all temperatures in keV. The green solid lines ($x_{\rm Tmax}=0$) divide the (σ, E_0)-space in edge and intermediate hot-spot regions. The purple solid lines ($T_{\rm x=0}=T_{\rm ig}$) separate the intermediate and central hot-spot regions.

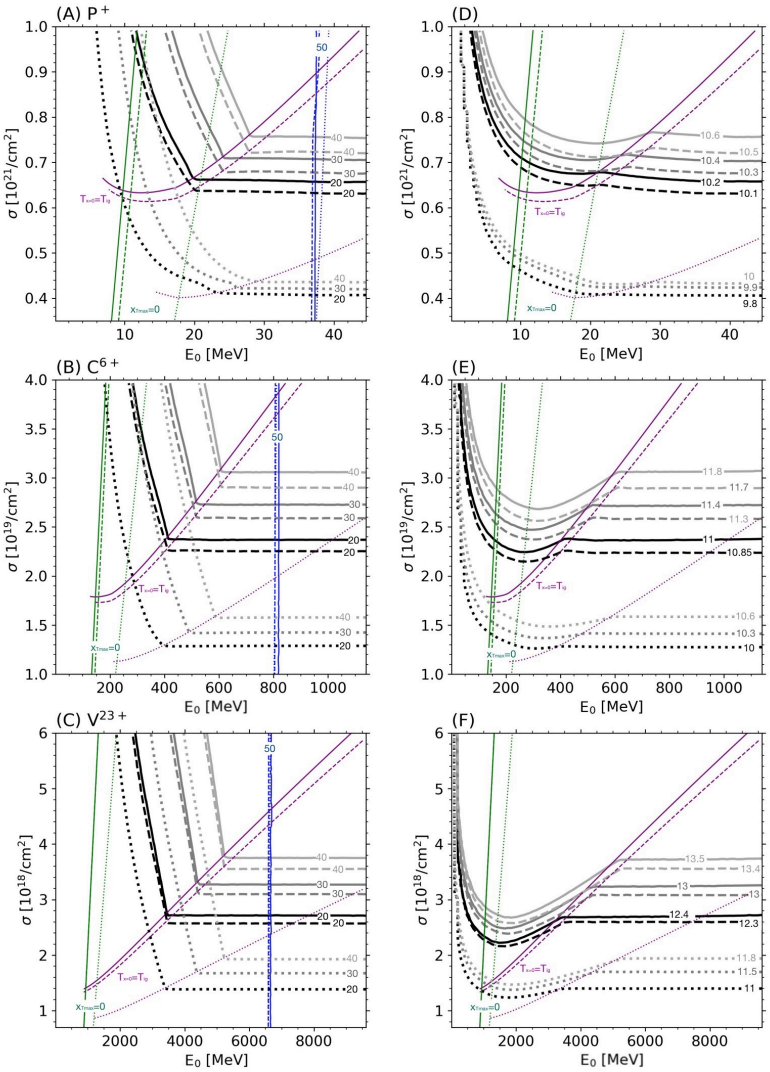

FIGURE 5.5— Isoline results for a pure DT plasma (ρ=500 g/cm^3) with initial temperature T_0 = 0.5 (solid), T_0 = 1 (dashed) and T_0=5 keV (dotted). Beams of p^+ (panels A and D), C^{6+} (panels B and E) and V^{23+} (panels C and F) are considered. Left: Black, grey and light-grey colours represent the hot-spot lengths for $L_{\rm hs}$=20, 30 and 40 μm. Dotted blue lines represent $x_{\rm Tmax}$=50 μm. Right: Black, grey and light-grey colours represent the hot-spot temperatures ($T_{\rm hs}$) corresponding to $L_{\rm hs}$=20, 30 and 40 μm in the central hot-spot region, with all temperatures in keV. The green solid lines ($x_{\rm Tmax}$ = 0) divide the (σ, E_0)-space in edge and intermediate hot-spot regions. The purple solid lines ($T_{\rm x=0}$ = $T_{\rm ig}$) separate the intermediate and central hot-spot regions.

60 μm. On the other hand, separately, we show the flux results at which $L_{\rm hs} \approx 2r_{\rm b}$ for central hot-spots, selecting $r_{\rm b} = 10$, 15 and 20 μm, this is, again, $L_{\rm hs} = 20$, 30 and 40 μm. For each hot-spot length, we append its temperature when the hot-spot is central. These solutions are calculated for our considered beams (p^+, C^{6+}, V^{23+}), plasma densities ($\rho = 300$, 500, 700 g/cm^3) and initial temperatures ($T_0 = 0.5$,1, 5 keV). When the solution is not available within our (σ, E_0)-ranges of study, the correspondent cell of the table is left unfilled.

This serves as a powerful tool to characterise experiments. For example, let us consider a fuel sphere of 60 μm, initially at $T_0 = 1$ keV and density 500 g/cm^3 interacting with a carbon beam of $r_{\rm b} = 15$ μm. It would be desirable to have a hot-spot length of $L_{\rm hs} = 30$ μm with a central hot-spot with its maximum located at $x_{\rm Tmax} = 60$ μm. Looking at the tables below, we can find the values of E_0 and σ at which such hot-spot is formed (in of this case, $E_0 = 890$ MeV and $\sigma = 2.6 \cdot 10^{19}$ cm^{-2}) and what temperature will it have ($T_{\rm hs} = 11.4$ keV). We can complement this kind of analysis with the results for the burning gain shown below in Sect. 5.3, to predict the outcome of the experiment.

Additionally, it is worth addressing other magnitudes associated to the results of these tables. In respect to the number of particles of the beam, the results depend on the radius of the beam ($N_{\rm p} = \sigma\pi r_{\rm b}^2$). For each beam specie, the minimum number of flux corresponds to ($r_{\rm b} = 10$ μm; $\rho = 300$ g/cm^3; $T_0 = 5$ keV; $L_{\rm hs} = 20$ μm) and the maximum to ($r_{\rm b} = 20$ μm; $\rho = 700$ g/cm^3; $T_0 = 0.5$ keV; $L_{\rm hs} = 40$ μm). In this range, we find that for protons, the number of particles is in the order of $N_{\rm p} \approx 1.25 \cdot 10^{15} - 1 \cdot 10^{16}$, for carbon is $N_{\rm p} \approx 3.45 \cdot 10^{13} - 4.5 \cdot 10^{14}$ and for vanadium is $N_{\rm p} \approx 3.45 \cdot 10^{12} - 5.7 \cdot 10^{13}$. Moreover, we can determine the energy of the beam of the cases presented above, considering the minimum and maximum energies of the tables, $x_{\rm Tmax} = 40$ and 60 μm, respectively. For protons, we find $E_{\rm b} \approx 5.2 - 80$ kJ, for carbon is $E_{\rm b} \approx 3 - 80$ kJ and for vanadium is $E_{\rm b} \approx 2.5 - 80$ kJ. Note how the minimum beam energy decreases with the charge, while the maximum remains approximately the same. In comparison, we can calculate the energy deposited in the hot-spot for each one of the previous experiments, considering $L_{\rm hs} = 20$ and 40 μm respectively, for the chosen minimum and maximum scenarios. For protons, we find $\Delta E_{\rm hs} \approx 1.04 - 42$ kJ, for carbon is $\Delta E_{\rm hs} \approx 1.1 - 48$ kJ and for vanadium is $\Delta E_{\rm hs} \approx 1.2 - 54$ kJ. With the previous results, we can evaluate how much energy of the beam is actually deposited in the hot-spot, by evaluating the coupling efficiency ($\Delta E_{\rm hs}/E_{\rm b}$). We find 20%-53% for protons, 37%-60% for carbon and 48%-68% for vanadium. Therefore, we want to highlight that, for a given set of plasma initial conditions and a beam radius, when creating a central hot-spot with the same $(L_{\rm hs}, x_{\rm Tmax})$-values, the coupling is higher for heavier-ions, such as vanadium.

Beam: p^+

ρ =300 g/cm^3; T$_0$=0.5 keV		
x_{Tmax}	E$_0$	
40	26.3	
50	-	
60	-	
L_{hs}	σ [10^{20}]	T_{hs}
20	6.0	10.0
30	6.3	10.3
40	6.6	10.8

ρ =300 g/cm^3; T$_0$=1 keV		
x_{Tmax}	E$_0$	
40	26.2	
50	-	
60	-	
L_{hs}	σ [10^{20}]	T_{hs}
20	5.8	10.0
30	6.0	10.2
40	6.3	10.3

ρ =300 g/cm^3; T$_0$=5 keV		
x_{Tmax}	E$_0$	
40	-	
50	-	
60	-	
L_{hs}	σ [10^{20}]	T_{hs}
20	4.0	9.8
30	4.2	9.9
40	4.4	10.0

ρ =500 g/cm^3; T$_0$=0.5 keV		
x_{Tmax}	E$_0$	
40	33.1	
50	37.2	
60	41.2	
L_{hs}	σ [10^{20}]	T_{hs}
20	6.8	10.2
30	7.1	10.4
40	7.6	10.6

ρ =500 g/cm^3; T$_0$=1 keV		
x_{Tmax}	E$_0$	
40	32.7	
50	36.9	
60	40.7	
L_{hs}	σ [10^{20}]	T_{hs}
20	6.4	10.1
30	6.8	10.3
40	7.3	10.5

ρ =500 g/cm^3; T$_0$=5 keV		
x_{Tmax}	E$_0$	
40	-	
50	-	
60	-	
L_{hs}	σ [10^{20}]	T_{hs}
20	4.2	9.8
30	4.3	9.9
40	4.4	10.0

ρ =700 g/cm^3; T$_0$=0.5 keV		
x_{Tmax}	E$_0$	
40	39.2	
50	44.5	
60	49.3	
L_{hs}	σ [10^{20}]	T_{hs}
20	7.2	10.3
30	7.8	10.6
40	8.5	10.9

ρ =700 g/cm^3; T$_0$=1 keV		
x_{Tmax}	E$_0$	
40	38.7	
50	43.7	
60	48.3	
L_{hs}	σ [10^{20}]	T_{hs}
20	6.8	10.2
30	7.5	10.5
40	8.1	10.7

ρ =700 g/cm^3; T$_0$=5 keV		
x_{Tmax}	E$_0$	
40	38.6	
50	43.6	
60	-	
L_{hs}	σ [10^{20}]	T_{hs}
20	4.3	10.1
30	4.5	10.3
40	4.7	10.4

TABLE 5.1— Numerical results of the heated plasma for a set of cases of interest, considering a proton beam for the interaction. The selected cases are the position of the maximum temperature such as x_{Tmax}=40, 50 or 60 μm and the length of the hot-spot such as L_{hs}=20, 30 or 40 μm. We provide results for each density (ρ=300, 500 and 700 g/cm^3) and initial temperatures of the plasma (T_0=0.5, 1, 5 keV). We present the beam requirements (σ, E_0) necessary for achieving a plasma under these conditions. We add the temperature associated to such hot-spot (T_{hs}).

Beam: C^{6+}

ρ =300 g/cm^3; T$_0$=0.5 keV		
x_{Tmax}	E$_0$	
40	554.2	
50	625.9	
60	692.2	
L_{hs}	σ [10^{19}]	T_{hs}
20	2.0	10.6
30	2.2	11.0
40	2.5	11.3

ρ =300 g/cm^3; T$_0$=1 keV		
x_{Tmax}	E$_0$	
40	553.2	
50	624.3	
60	687.7	
L_{hs}	σ [10^{19}]	T_{hs}
20	1.9	10.5
30	2.1	10.9
40	2.3	11.2

ρ =300 g/cm^3; T$_0$=5 keV		
x_{Tmax}	E$_0$	
40	552.3	
50	623.3	
60	687.6	
L_{hs}	σ [10^{19}]	T_{hs}
20	1.1	10.1
30	1.2	10.2
40	1.3	10.3

ρ =500 g/cm^3; T$_0$=0.5 keV		
x_{Tmax}	E$_0$	
40	722.3	
50	818.4	
60	903.8	
L_{hs}	σ [10^{19}]	T_{hs}
20	2.4	11.0
30	2.7	11.4
40	3.1	11.8

ρ =500 g/cm^3; T$_0$=1 keV		
x_{Tmax}	E$_0$	
40	711.5	
50	804.7	
60	890.0	
L_{hs}	σ [10^{19}]	T_{hs}
20	2.3	10.9
30	2.6	11.3
40	2.9	11.7

ρ =500 g/cm^3; T$_0$=5 keV		
x_{Tmax}	E$_0$	
40	711.2	
50	803.0	
60	887.1	
L_{hs}	σ [10^{19}]	T_{hs}
20	1.3	10.2
30	1.4	10.3
40	1.6	10.6

ρ =700 g/cm^3; T$_0$=0.5 keV		
x_{Tmax}	E$_0$	
40	859.4	
50	968.7	
60	1072.5	
L_{hs}	σ [10^{19}]	T_{hs}
20	2.7	11.3
30	3.2	11.8
40	3.6	12.3

ρ =700 g/cm^3; T$_0$=1 keV		
x_{Tmax}	E$_0$	
40	844.3	
50	956.3	
60	1057.6	
L_{hs}	σ [10^{19}]	T_{hs}
20	2.6	11.1
30	3.0	11.7
40	3.4	12.1

ρ =700 g/cm^3; T$_0$=5 keV		
x_{Tmax}	E$_0$	
40	840.9	
50	949.8	
60	1049.8	
L_{hs}	σ [10^{19}]	T_{hs}
20	1.4	10.3
30	1.6	10.6
40	1.8	10.9

TABLE 5.2— Same as Table 5.1, but considering a carbon beam for the interaction.

Beam: V^{23+}

ρ =300 g/cm^3; T$_0$=0.5 keV		
x_{Tmax}	E$_0$	
40	4497.6	
50	5098.7	
60	5648.4	
L_{hs}	σ [10^{18}]	T_{hs}
20	2.1	11.8
30	2.5	12.5
40	2.9	12.9

ρ =300 g/cm^3; T$_0$=1 keV		
x_{Tmax}	E$_0$	
40	4488.5	
50	5083.3	
60	5620.4	
L_{hs}	σ [10^{18}]	T_{hs}
20	2.0	11.7
30	2.4	12.3
40	2.7	12.7

ρ =300 g/cm^3; T$_0$=5 keV		
x_{Tmax}	E$_0$	
40	4481.8	
50	5080.4	
60	5618.0	
L_{hs}	σ [10^{18}]	T_{hs}
20	1.1	10.6
30	1.3	11.0
40	1.5	11.4

ρ =500 g/cm^3; T$_0$=0.5 keV		
x_{Tmax}	E$_0$	
40	5884.6	
50	6657.1	
60	7364.0	
L_{hs}	σ [10^{18}]	T_{hs}
20	2.7	12.4
30	3.3	13.0
40	3.8	13.5

ρ =500 g/cm^3; T$_0$=1 keV		
x_{Tmax}	E$_0$	
40	5862.6	
50	6624.0	
60	7310.6	
L_{hs}	σ [10^{18}]	T_{hs}
20	2.6	12.3
30	3.1	12.9
40	3.6	13.4

ρ =500 g/cm^3; T$_0$=5 keV		
x_{Tmax}	E$_0$	
40	5839.5	
50	6602.6	
60	7302.6	
L_{hs}	σ [10^{18}]	T_{hs}
20	1.4	11.0
30	1.7	11.5
40	1.9	11.8

ρ =700 g/cm^3; T$_0$=0.5 keV		
x_{Tmax}	E$_0$	
40	6988.8	
50	7900.3	
60	8739.6	
L_{hs}	σ [10^{18}]	T_{hs}
20	3.2	12.9
30	3.9	13.6
40	4.5	13.9

ρ =700 g/cm^3; T$_0$=1 keV		
x_{Tmax}	E$_0$	
40	6927.4	
50	7848.3	
60	8692.0	
L_{hs}	σ [10^{18}]	T_{hs}
20	3.0	12.7
30	3.7	13.4
40	4.2	13.8

ρ =700 g/cm^3; T$_0$=5 keV		
x_{Tmax}	E$_0$	
40	6915.2	
50	7822.0	
60	8653.3	
L_{hs}	σ [10^{18}]	T_{hs}
20	1.6	11.3
30	2.0	11.8
40	2.3	12.0

TABLE 5.3— Same as Table 5.1, but considering a vanadium beam for the interaction.

5.3 Burning gain and coupling results

After studying the characteristics of the resulting heated plasma and its hot-spot, we study the burning gain ($G_{\rm burn}$), as it is a fundamental parameter for a successful nuclear fusion. To do so, we apply Eq. 3.61, which, adapted for a pure plasma with homogeneous density, can be written as:

$$G_{\rm burn} = \frac{\rho R_{\rm F}}{\rho R_{\rm F} + H_{\rm B}} \cdot \frac{\epsilon_r}{6T_{\rm hs}} \cdot \frac{R_{\rm F}^3}{3L_{\rm hs}r_{\rm b}^2/4 + (R_{\rm F}^3 - 3L_{\rm hs}r_{\rm b}^2/4)\,\frac{T_*}{T_{\rm hs}}}, \tag{5.1}$$

where we have stated clear the dependence with the results of $L_{\rm hs}$ and $T_{\rm hs}$ that were presented above.

We present burning gain maps as a function of the energy of the projectiles and the flux of the beam. Then, we vary the rest of components of our parameter space: the beam specie and radius ($r_{\rm b}$), the plasma density (ρ), its initial temperature (T_0) and the fuel radius ($R_{\rm F}$). Burning gain colour maps are shown in Figs. 5.6, 5.7, 5.8, 5.9 and 5.10. These figures are limited by the ignition curve ($G_{\rm ig} = 1$) and the upper range ($L_{\rm h} < 2R_{\rm F}$). To provide a general perspective of how each parameter affects the burning gain, we have taken as a reference case a carbon beam C^{6+} of radius $r_{\rm b}$=15 μm and a plasma of density ρ=500 g/cm^3, initial temperature of T_0=1 keV and radius of $R_{\rm F}$=50 μm. Such case is represented in all central panels of each figure. On top and bottom of the reference panel, we alter one of the five parameters, leaving the rest fixed to the reference case. From Fig. 5.6 to Fig. 5.10, first one changes the species of the beam, second varies its radius, third the plasma density, fourth the initial temperature and fifth the radius of the fuel sphere. For a proper comparison between these five figures, we have fixed the colorbar from $G_{\rm burn} \approx 0$ to 5000, which are the minimum and maximum values found along the experiments.

Studying the dependence of the burning gain respect to the projectile energy and flux of the beam, we find a similar structure in all gain maps: the higher burning factors are found close to the ignition curve, where the hot-spot requires less energy to form, but still is able to return a successful combustion. This is found in small regions of low projectile energy or low beam flux, or both. For large projectile energies or beam fluxes, the burning gain descends drastically up to a blank region where the range is larger than $2R_{\rm F}$. Following the structures found in Fig. 5.1, we acknowledge regions of edge, intermediate and central hot-spots. Again, the last ones present constant behaviour with the energy of the projectiles. Burning gain depends on the radius and temperature of the hot-spot, so, as both are found to be constant (explained in Sect. 3.11), the gain is constant too.

Varying the rest of parameters, aside from the projectile energy and flux of the beam, allows comparing the burning gain efficiency for different experiment setups. Row per row, we find:

- For lighter beam species, not only is it difficult to find a central hot-spot, but the regions with high burning gain are smaller. Heavier beams present elevated burning gains in larger regions close to the isoline of $G_{\mathrm{ig}} = 1$.
- Smaller beam radii retrieve larger burning gains. For hot-spots of the same length and temperature, having a lower beam radius means achieving the burning of the whole sphere with a more compact hot-spot volume, which means employing less energy.
- Higher plasma densities provide considerable larger gains.
- Lower initial temperatures provide larger regions with higher gains, although is not a dominant parameter for changing the results.
- For hot-spots with same dimensions, reducing the size of the fuel sphere decreases the burning gain, as less material is burnt, accordingly to Eq. (3.61).

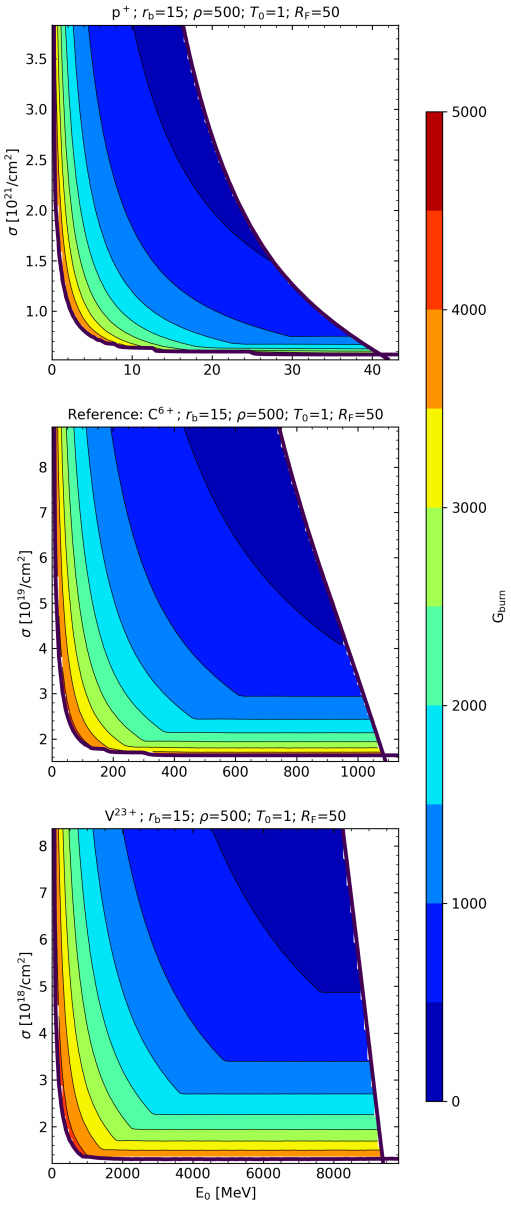

FIGURE 5.6— Burning gains in the (σ, E_0)-space. Central panel serves as reference case, using a carbon beam C^{6+} of radius r_b=15 μm and a plasma of density ρ=500 g/cm^3, initial temperature T_0=1 keV and radius R_F=50 μm. Top and bottom panels vary one parameter in respect to the reference case, leaving the rest fixed. In this case we change the beam type (p^+, C^{6+} and V^{23+}).

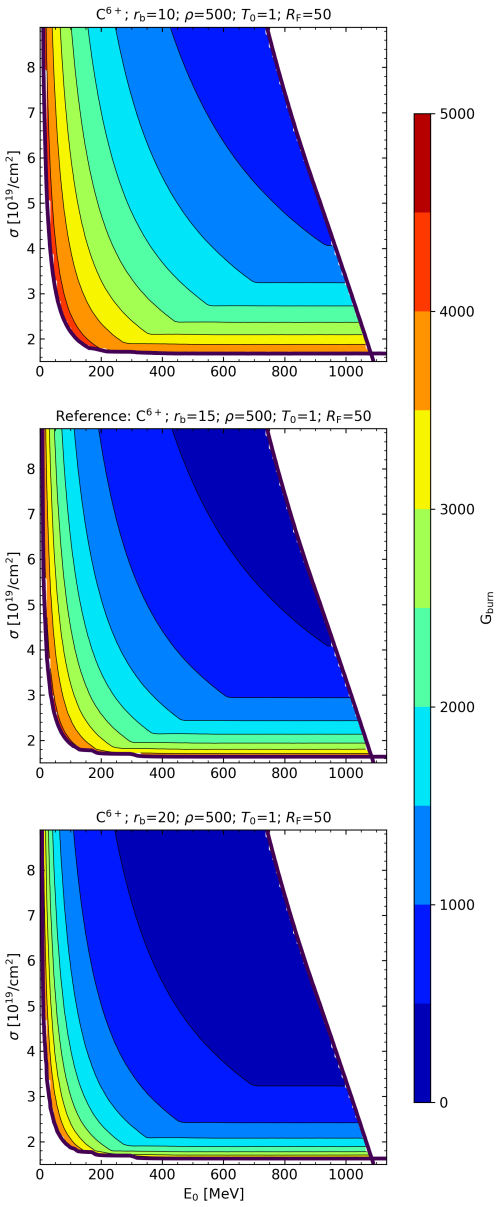

FIGURE 5.7— Similar to Fig. 5.6, but varying the beam radii (r_{b}=10, 15 and 20 μm) in respect to the central reference case.

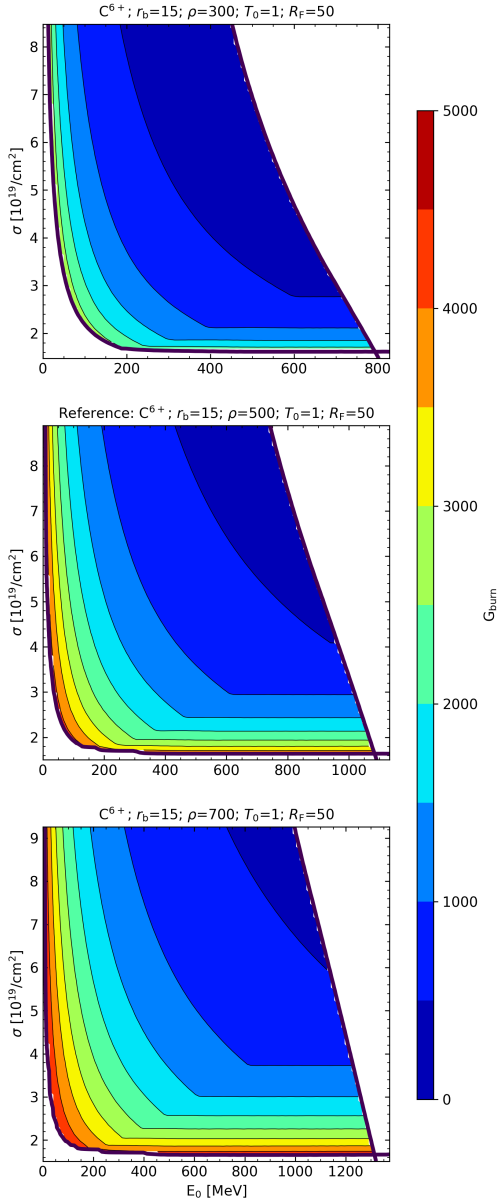

FIGURE 5.8— Similar to Fig. 5.6, but varying the plasma density ($\rho = 300$, 500 and 700 μm) in respect to the central reference case.

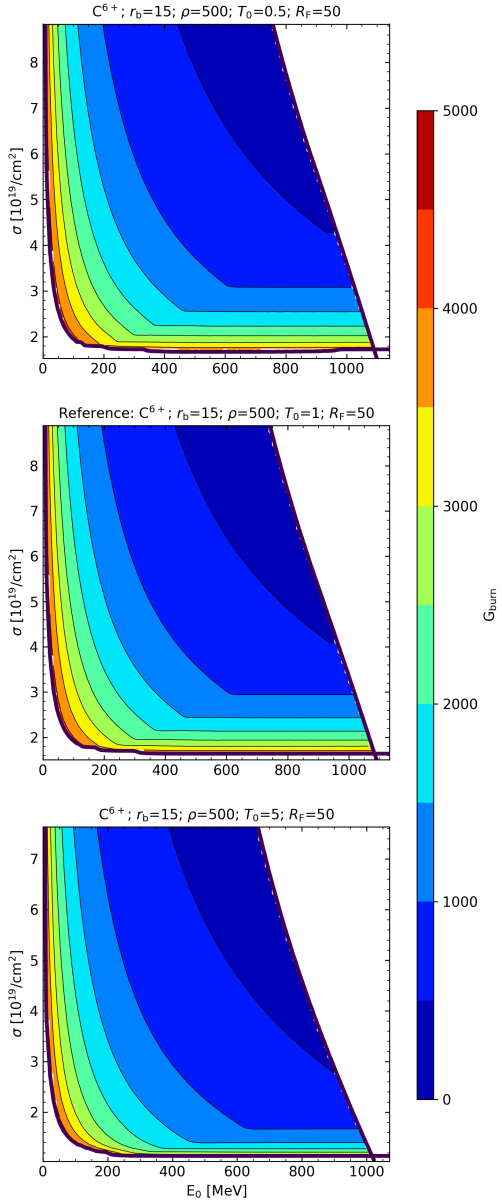

FIGURE 5.9— Similar to Fig. 5.6, but varying the plasma initial temperature ($T_0 = 0.5$, 1 and 5 keV) in respect to the central reference case.

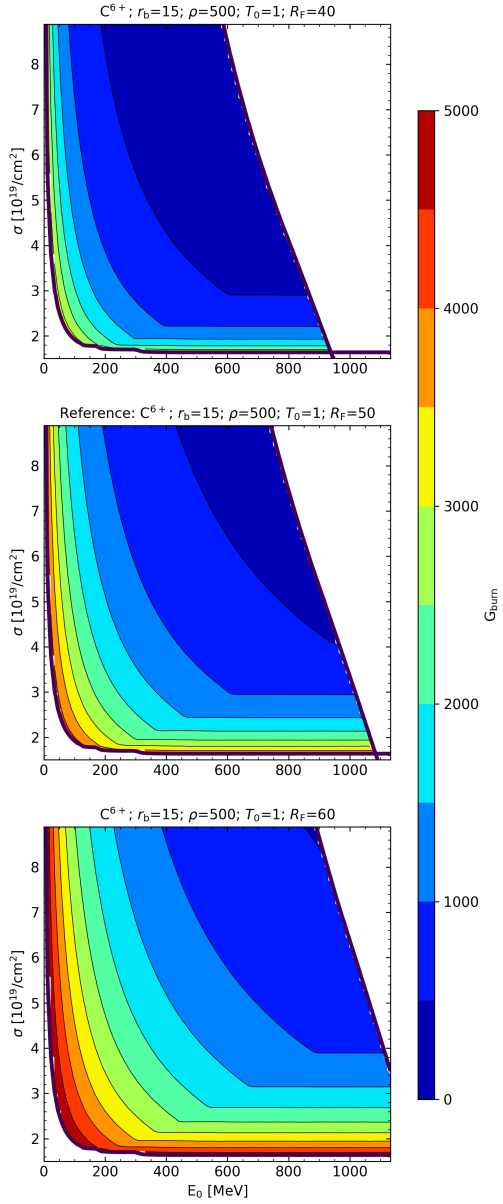

FIGURE 5.10— Similar to Fig. 5.6, but varying the fuel sphere radii (R_{F} = 40, 50 and 60 μm) in respect to the central reference case.

Following the results presented in Tables 5.1, 5.2 and 5.3, we calculate the burning gain values found at central hot-spots with lengths $L_{\rm hs}$ = 20, 30 and 40 μm, for a beam and plasma radii of 15 and 50 μm, respectively. For these experiments, we find the maximum gain values close to 2000 while minimum above 500. As in the burning figures displayed in this section, larger hot-spot lengths are located at higher fluxes and return lower gains. Then, these tables show how the burning gain increases with the density and lowers if the initial temperature does. When changing the ion charge, for the same hot-spot length, we find that heavier ions return lower burning gains. This might seem contradictory with the results of Fig. 5.6, in which we find larger regions with high gain values for high-Z beams. However, we note how interpreting the general distribution of results in the (σ, E_0)-space is not equivalent to checking the exact position of the $L_{\rm hs}$, which fall at different positions in respect to the gain maps.

Beam: p^+

ρ =300; T_0=0.5	
$L_{\rm hs}$	$G_{\rm burn}$
20	1615.3
30	1006.4
40	802.6

ρ =300; T_0=1	
$L_{\rm hs}$	$G_{\rm burn}$
20	1672.7
30	1120.7
40	867.2

ρ =300; T_0=5	
$L_{\rm hs}$	$G_{\rm burn}$
20	-
30	-
40	-

ρ =500; T_0=0.5	
$L_{\rm hs}$	$G_{\rm burn}$
20	1820.9
30	1368.4
40	1100.8

ρ =500; T_0=1	
$L_{\rm hs}$	$G_{\rm burn}$
20	1823.6
30	1387.4
40	1103.3

ρ =500; T_0=5	
$L_{\rm hs}$	$G_{\rm burn}$
20	2134.2
30	1712.2
40	1163.9

ρ =700; T_0=0.5	
$L_{\rm hs}$	$G_{\rm burn}$
20	2068.9
30	1608.0
40	1296.4

ρ =700; T_0=1	
$L_{\rm hs}$	$G_{\rm burn}$
20	2123.8
30	1618.5
40	1299.1

ρ =700; T_0=5	
$L_{\rm hs}$	$G_{\rm burn}$
20	2344.9
30	1932.6
40	1485.7

TABLE 5.4— Numerical results of the burning gain for the same set of cases of interest as in Table 5.1, this is, considering a proton beam for the interaction. The selected cases are lengths of the hot-spot such as $L_{\rm hs}$=20, 30 or 40 μm. We provide results for each density (ρ=300, 500 and 700 g/cm^3) and initial temperatures of the plasma (T_0=0.5, 1, 5 keV). Beam and fuel radii fixed at 15 and 50 μm, respectively

Beam: C^{6+}

ρ =300; T_0=0.5	
L_{hs}	G_{burn}
20	1342.2
30	974.1
40	754.9

ρ =300; T_0=1	
L_{hs}	G_{burn}
20	1355.4
30	984.9
40	761.8

ρ =300; T_0=5	
L_{hs}	G_{burn}
20	1453.4
30	1019.1
40	826.1

ρ =500; T_0=0.5	
L_{hs}	G_{burn}
20	1737.5
30	1289.6
40	1009.0

ρ =500; T_0=1	
L_{hs}	G_{burn}
20	1753.1
30	1297.1
40	1019.2

ρ =500; T_0=5	
L_{hs}	G_{burn}
20	1852.9
30	1384.2
40	1102.5

ρ =700; T_0=0.5	
L_{hs}	G_{burn}
20	1985.2
30	1491.5
40	1179.9

ρ =700; T_0=1	
L_{hs}	G_{burn}
20	1989.7
30	1497.7
40	1189.6

ρ =700; T_0=5	
L_{hs}	G_{burn}
20	2089.0
30	1598.0
40	1286.3

TABLE 5.5— Same as Table 5.4, but considering a carbon beam for the interaction.

Beam: V^{23+}

ρ =300; T_0=0.5	
L_{hs}	G_{burn}
20	1247.3
30	880.9
40	673.7

ρ =300; T_0=1	
L_{hs}	G_{burn}
20	1255.6
30	889.7
40	682.5

ρ =300; T_0=5	
L_{hs}	G_{burn}
20	1352.4
30	968.6
40	750.9

ρ =500; T_0=0.5	
L_{hs}	G_{burn}
20	1609.6
30	1163.9
40	906.2

ρ =500; T_0=1	
L_{hs}	G_{burn}
20	1610.9
30	1173.3
40	913.4

ρ =500; T_0=5	
L_{hs}	G_{burn}
20	1734.5
30	1286.6
40	1012.1

ρ =700; T_0=0.5	
L_{hs}	G_{burn}
20	1834.9
30	1356.2
40	1067.9

ρ =700; T_0=1	
L_{hs}	G_{burn}
20	1837.6
30	1362.9
40	1078.7

ρ =700; T_0=5	
L_{hs}	G_{burn}
20	1969.9
30	1491.7
40	1196.9

TABLE 5.6— Same as Table 5.4, but considering a vanadium beam for the interaction.

Besides from the burning gain it is worth quantifying the energy deposited in the hot-spot in respect to the energy introduced by the beam ($\Delta E_{hs}/E_b$), this is, the coupling (see Sect. 3.9). Low coupling values indicate that part of the energy

from the beam is lost in regions that do not create ignition. First, we address the energy of the beam and the energy deposited in the hot-spot independently. Thus, in Fig. 5.11 we show both magnitudes in separated columns of panels, for different ion charges. We remind that the energy of the beam is equivalent to the energy deposited in the whole heated region (in absence of a corona). Close to the ignition curve we find beam energies between $E_{\rm b} \gtrapprox 0$ and maximum values of 30, 20 and 10 kJ, for proton, carbon and vanadium ions, respectively. On the other hand, the hot-spot energies associated to the ignition curve are found in an interval between $\Delta E_{\rm hs} \gtrapprox 0$ and 5 kJ. These results are found within the interval deduced from Tables 5.1, 5.2 and 5.3[1]. The region close to the ignition curve is of great interest, as it represents those cases where minimum energy is invested to create a hot-spot that will burn the fuel, as was shown with the previous burning gain results. Then, the maximum values found for both $E_{\rm b}$ and $\Delta E_{\rm hs}$ correspond to 70, 75 and 80 kJ, when increasing the ion charge. The distribution of results in the (σ, E_0)-space is similar between $E_{\rm b}$ and $E_{\rm hs}$ for edge and intermediate hot-spots, although it varies when central hot-spots are created.

[1]We remind the results extracted from Tables 5.1, 5.2 and 5.3 considered a much diverse span of plasma conditions, therefore finding a wider range of $E_{\rm b}$ and $\Delta E_{\rm hs}$ results in the ignition curve.

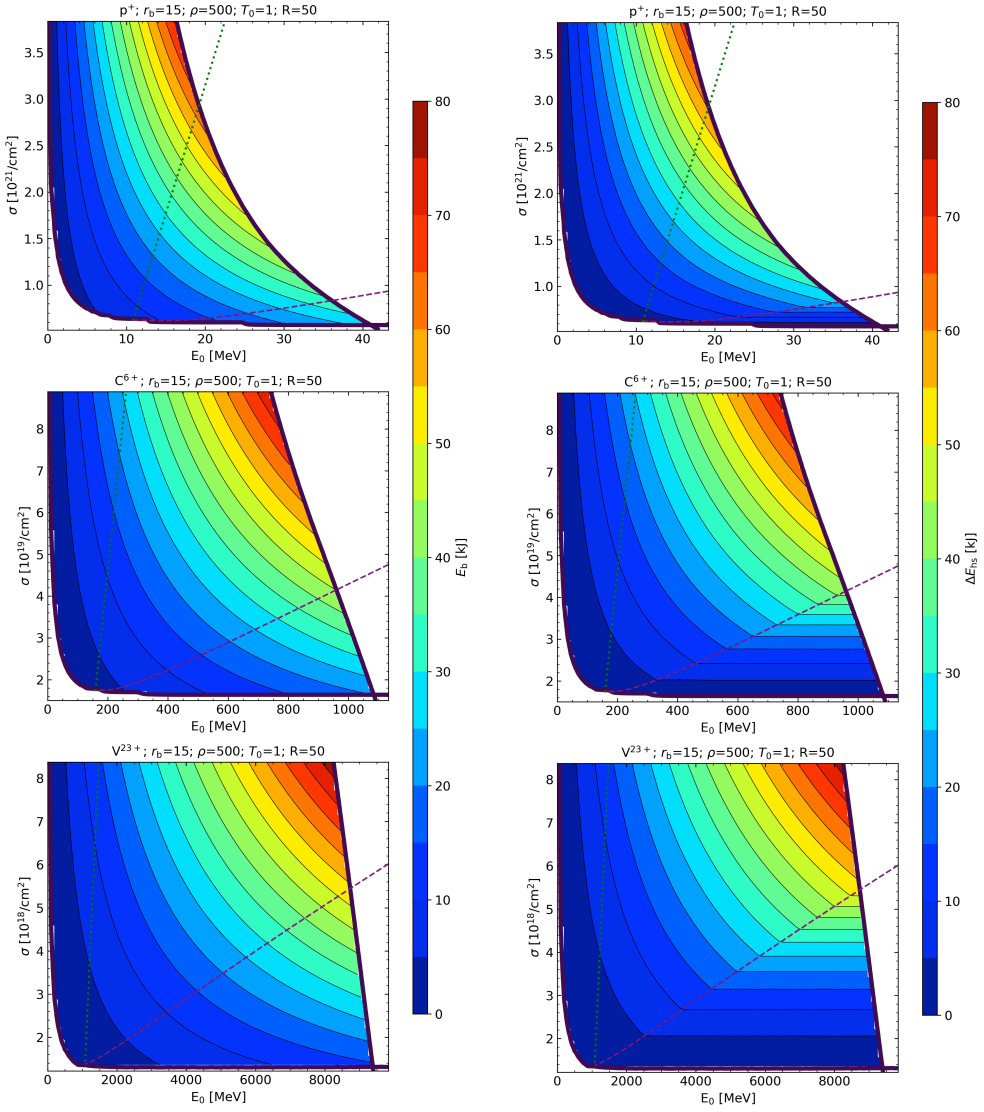

FIGURE 5.11— Energy of the beam (left column) and energy deposited in the hot-spot (right column) for different ions, in respect to the (σ, E_0)-space.

Then, in Fig. 5.12 we show an extended study of the coupling efficiency results. The central column serves as reference case, using a carbon beam, a plasma of density ρ=500 g/cm^3 and an initial temperature T_0=1 keV. Left and right columns are variations in respect to the reference case. Each row varies one of these three parameters while leaving the rest fixed, as the title of each panel indicates. The beam and fuel radii are not considered in this case, as the coupling is independent of them. Consequently, there is no need to limit the coloured map to $L_\mathrm{h} < 2R_\mathrm{F}$ either.

The general behaviour of the coupling in the (σ, E_0)-space is distinguishable in two zones. In the edge and intermediate hot-spot regions there is an increase mainly dominated by the flux and secondarily by the energy of the projectiles. In the central hot-spot region, we find a palette of increasing coupling efficiencies, mostly dependent on the beam flux. This change in the functional shape depends mainly on the charge of the ion beam. Higher beam species increase the central hot-spot region and reveal such palette of couplings. When varying the density or the initial temperature, the colormaps of the coupling does not change roughly. Although, in cases with same (σ, E_0)-values, we find:

- In the edge-intermediate hot-spot region, increasing the density decreases the coupling. In the central hot-spot region, it happens the opposite.
- When increasing the initial temperature of the plasma (T_0) the coupling increases in all regions.

The key result to address is that, for central hot-spots, the coupling does not reach the highest coupling values, as some energy of the beam is deposited in the beginning of the plasma in order to penetrate the fuel up to the centre, where the hot-spot appears.

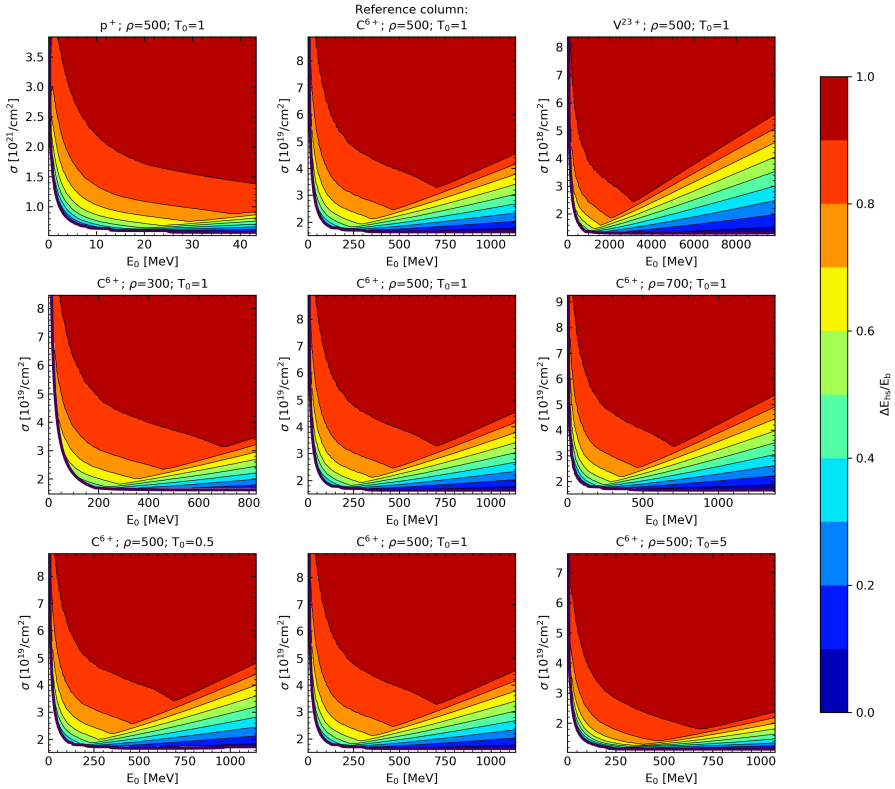

FIGURE 5.12— Coupling between the hot-spot and the beam energy ($\Delta E_{\rm hs}/E_{\rm b}$) for different beam-plasma conditions, in the (σ, E_0)-space. The central column serves as reference case (C^{6+}, ρ=500 g/cm^3, T_0=1 keV). Left and right columns are variations in respect to the reference case. Each row varies one of these parameters while leaving the rest fixed.

The lowest coupling is found near the ignition curve ($G_{\rm ig} = 1$), which is the region where the highest burning gain is located. Creating the spark in the centre of the fuel is advantageous for the FI, however, for central hot-spots the coupling efficiency never reaches its optimum value. A compromise between proper burning gain, the coupling efficiency and finding a central hot-spot must be taken. To address such problem, in Fig. 5.13 we represent the product between both parameters, $G_{\rm burn} \times (\Delta E_{\rm hs}/E_{\rm b})$, and we display the lines delimiting the edge and intermediate hot-spot regions (green dotted line) and the intermediate and central hot-spot regions (purple dashed line). For this example we take the same reference cases of Fig. 5.6, this is, proton, carbon and vanadium beams of radius $r_{\rm b}$=15 μm and a plasma of density ρ=500 g/cm^3, initial temperature T_0=1 keV and radius $R_{\rm F}$=50 μm.

We find the highest values for edge hot-spots (very short and not extremely hot), at high fluxes and low projectile energies. For central hot-spots, the results are more concerning, as the burning gain descends when increasing the flux and the coupling descends when augmenting the projectile energy. Heavier beams present more favourable results in larger regions of the studied space. Thus, an optimal trade-off between burning, coupling and finding a central hot-spot would appear, for example, when selecting a carbon ion beam, at $E_0 \approx 600$ MeV and $\sigma \approx 2.5 \cdot 10^{19}$ g/cm^2 ($G_{\rm burn} \times (\Delta E_{\rm hs}/E_{\rm b}) \approx 900$). In such point we find a balanced gain and coupling, with a hot-spot centred at 30 μm, with twice the length of the beam radius $L_{\rm hs} \approx 30$ μm (i.e. where assuming a sphere shape for the hot-spot is the better). At $E_0 \approx 800$ MeV we will find a similar hot-spot, but positioned exactly in the centre of the fuel sphere and with a lower coupling ($G_{\rm burn} \times (\Delta E_{\rm hs}/E_{\rm b}) \approx 700$).

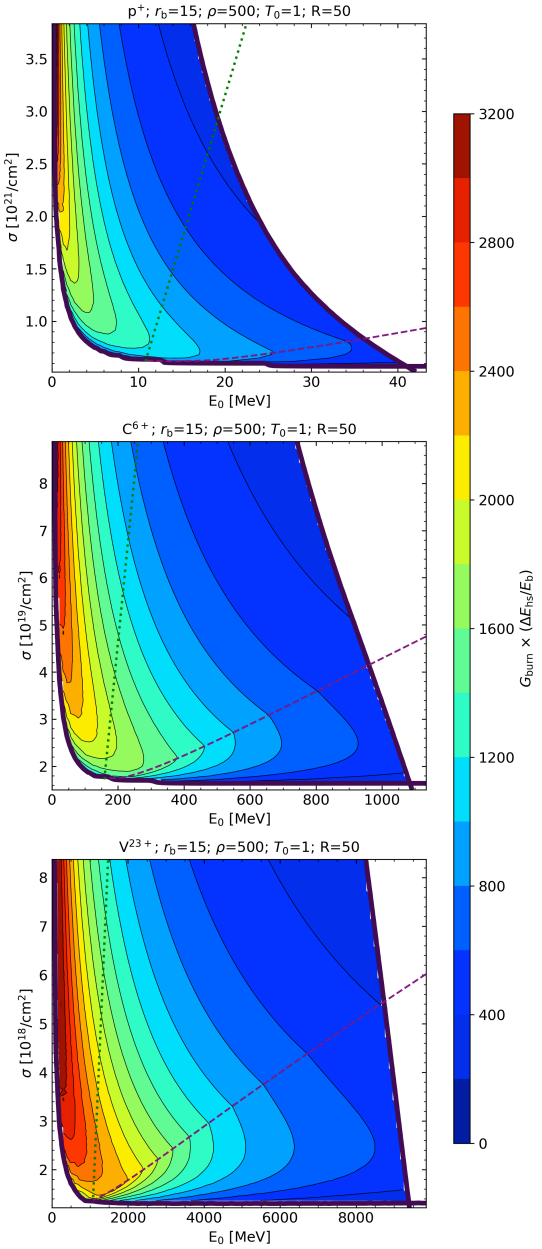

FIGURE 5.13— Product of the burning gain and coupling, $G_{\rm burn}\times(\Delta E_{\rm hs}/E_{\rm b})$ in the (σ, E_0)-space. We select p^+ (top), C^{6+} (middle) and V^{23+} (bottom) beams of radius $r_{\rm b}$=15 μm and a plasma of density ρ=500 g/cm^3, initial temperature T_0=1 keV and radius $R_{\rm F}$=50 μm.

5.4 Results with a fuel corona

In this section we perform a similar study to the one above, but considering a corona for the fuel sphere, in order to determine the differences with the only-core case. This implies the beam travels through a region of low density and its particles have a previous slowing down in the process, reaching the core with less energy compared to the non-corona scenario. The conditions of the experiment are the same as in Fig. 5.1, but, to exemplify the impact of the corona, we chose the spatial and density distribution of Fig. 3.2. That is, we consider a corona of low density ($\rho_{\mathrm{c}} = 10$ g/cm^3) covering 100 μm, followed by a corona-core transition region of 20 μm with variable density, and, at last, the *constant* part of the core with a diameter that measures approximately 100 μm, which corresponds to most of the experiments performed in the sections before, where $R_{\mathrm{F}} = 50$ μm.

First, we want to address the state of the core after being heated. To do so, in Fig. 5.14 we display the length and temperature results for proton, carbon and vanadium beams. These results are meant to be compared with those of Fig. 5.1. They are calculated in the same (σ, E_0)-range, for a better comparison with the non-corona case, and are displayed following the same linestyle to designate each parameter. The most remarkable result, in respect to the case without corona, is a displacement of all results to superior values of E_0. In other words, the general behaviour is the same, but, when considering the corona, the projectiles require more energy to achieve the same depth, so all the results are moved to higher energies. For instance, reaching $x_{\mathrm{Tmax}} = 50$ μm with a carbon beam needs about 800 MeV for the non-corona case and 900 MeV. A similar behaviour is found for L_{h} isolines, which move to higher energies. The shape of $T_{\mathrm{x=0}}$ isolines becomes narrower with the x-axis. This is due to the minimum energy necessary to reach ignition being higher and the $T_{\mathrm{x=0}} = T_{\mathrm{ig}}$ threshold (shown in purple) being steeper. On the other hand, once the central hot-spot region is reached, the results for L_{hs} and T_{hs} are the same with or without corona (constant in respect to E_0), as in our experiment considering a corona region does not change the dependency with the flux. Comparably, in the intermediate and central hot-spot regions, T_{max} presents a similar behaviour. In general, these results indicate that the same conditions for the heated plasma can be reached by finely tuning the proper beam conditions.

Secondly, Fig. 5.15 serves as an example to analyse the changes of $G_{\mathrm{ig}} = 1$, the (σ, E_0)-space where the ignition can take place, as well as G_{burn}, with and without corona (left and right columns, respectively). We select the same reference cases of Fig. 5.6 (i.e. proton, carbon and vanadium beams of $r_{\mathrm{b}} = 15$ μm, $\rho = 500$ g/cm^3, $T_0 = 1$ keV and $R_{\mathrm{F}} = 50$ μm). As expected, the

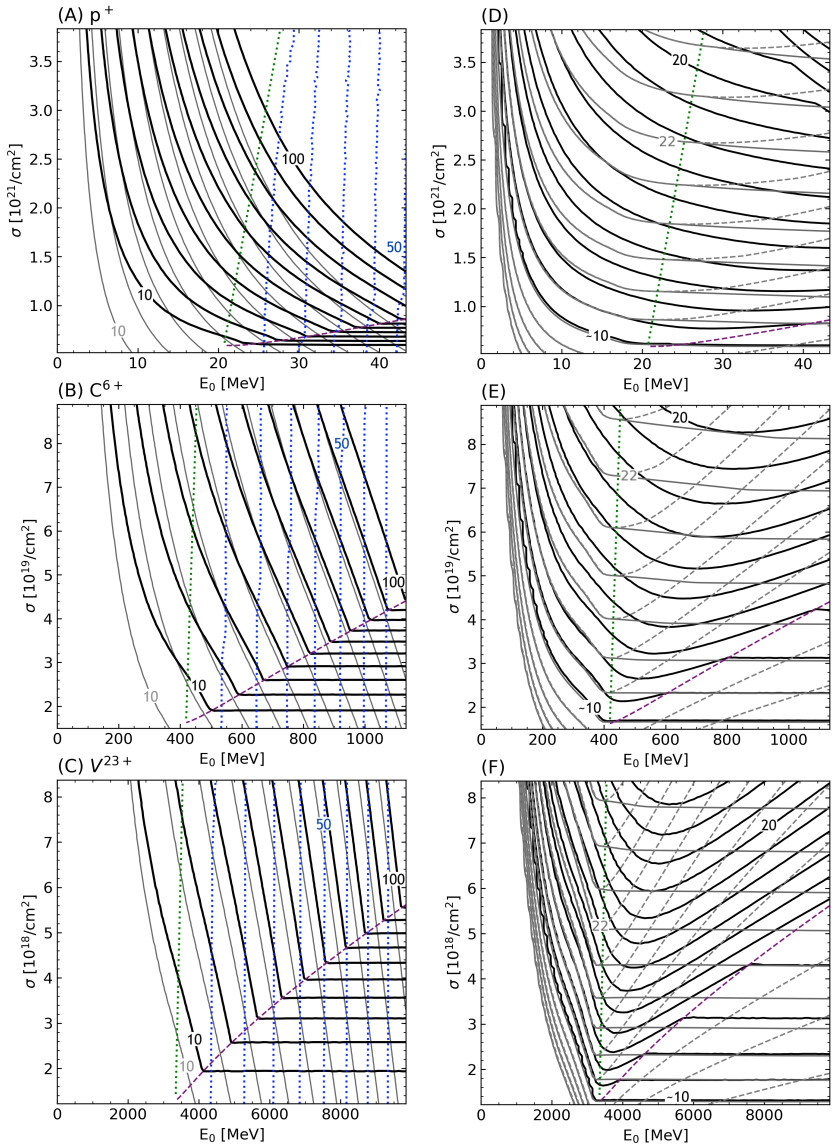

FIGURE 5.14— Results for the experiments of Fig. 5.1, but considering a corona of variable density. The linestyle of the isolines to designate each parameter is also the same to the one of that figure.

ignition threshold (as black thick line) has been displaced into higher energies, so the minimum projectile energy ($E_{0\,\mathrm{min,ig}}$) would require greater values. For example, when comparing with the minimum energy of the non-corona case (see

Table 4.4), for $\rho = 500$ g/cm^3, in the corona case we find $E_{0\,\mathrm{min,ig}} \approx 2.2$ MeV for protons, 100 MeV for carbon and 1365 MeV for vanadium. This implies the thresholds increase by a 1000%, 1270% and 21430%, respectively. Moreover, the vertical left limit we found in Fig. 5.15 is not as straight any more, so $E_{0\,\mathrm{min,ig}}$ is not completely representative of the range of study. We want to note that $E_{0\,\mathrm{max}}$ increases correspondingly and that $\sigma_{\mathrm{min,ig}}$ is the same as in the non-corona case. With regard to the burning gain, aside from the displacement of the results in the x-axis, the possible minimum and maximum values of G_{burn} are the same, from 0 to 4000, only more energy is required to reach the same G_{burn} values.

Thirdly, with Fig. 5.16 we exemplary compare the changes in the coupling ($\Delta E_{\mathrm{hs}}/\Delta E_{\mathrm{b}}$) with those of Fig. 5.12 (i.e. $\rho = 500$ g/cm^3, $T_0 = 1$ keV) for proton, carbon and vanadium beams. This is, the non-corona case (left column of panels) and the fuel considering a corona (right column of panels). As before, every result is displaced to high energy regions. However, in this case, the implications of considering the corona are more significant. In general, the coupling values are reduced and distributed differently. Lower couplings are more predominant in the edge hot-spot region and the shape of these contours is different. Now, each region is less rounded, constrained by an almost straight vertical line. The central hot-spot region is more similar to the non-corona shape, showing again the results as a palette of coupling values. These changes occur because a part of the beam energy is consistently lost in the corona. Beams that create edge hot-spots lose more energy in the corona, leading to the vertical palette of values found now for the coupling. Contrarily, for central hot-spots, the corona is more transparent for the beam, finding more alike results to those of the non-corona case. We want to highlight that, before, we explained that it was possible to obtain the same heated plasma conditions in the non-corona and corona cases by adjusting the beam characteristics (mainly the energy of the projectiles). However, the coupling does not follow this behaviour, being not that easily tunable. For example, in the corona case, reaching a coupling close to one ($\Delta E_{\mathrm{hs}}/E_{\mathrm{b}} \approx 1$) is often not possible in the studied ranges of (σ, E_0), in comparison to the non-corona fuel.

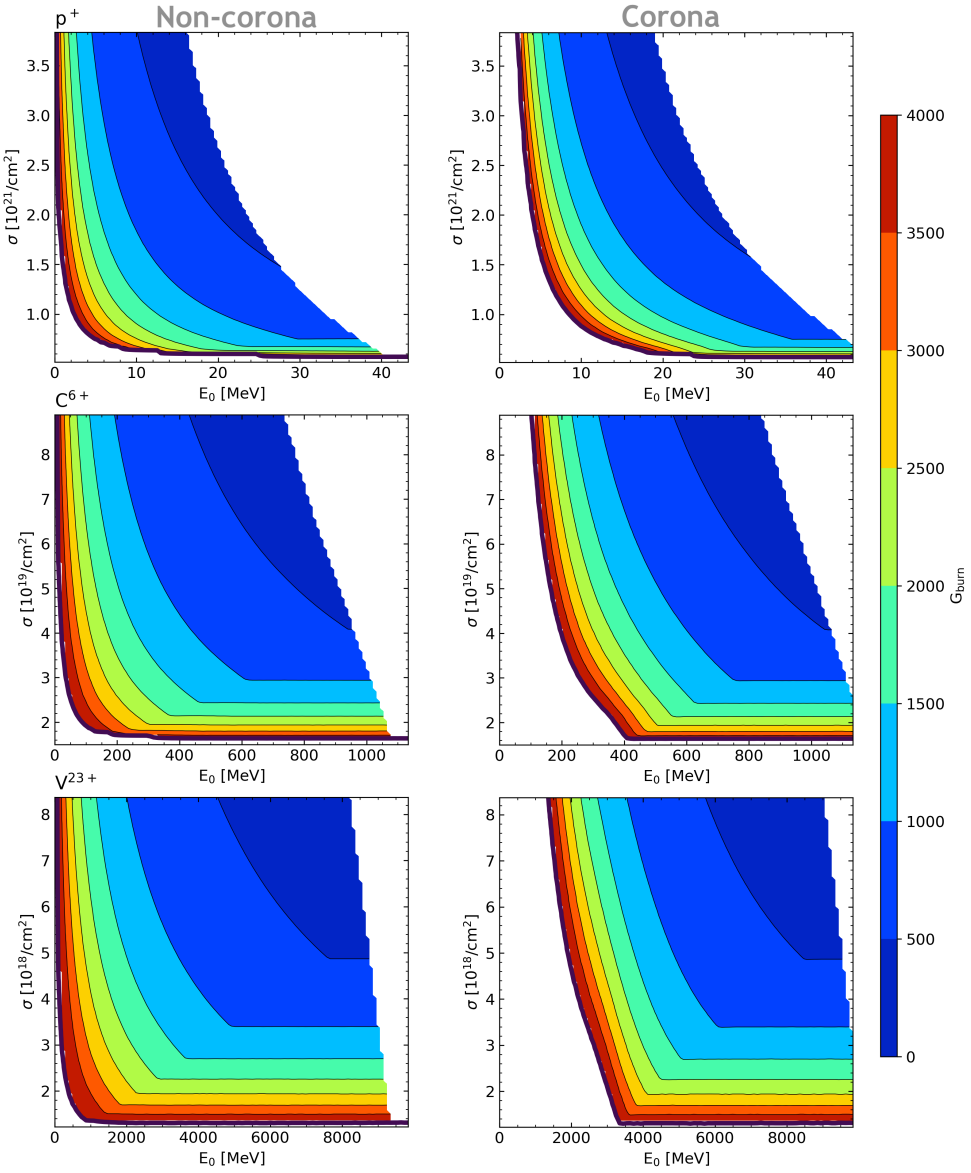

FIGURE 5.15— Burning gains in the (σ, E_0)-space. The experiments considered are the same as in Fig. 5.6 ($r_\mathrm{b} = 15$ μm, $\rho = 500$ g/cm^3, $T_0 = 1$ keV, $R_\mathrm{F} = 50$ μm) for proton (top row), carbon (middle row) and vanadium (bottom row) beams. The left column is used as the reference case without corona and the right columns do consider a corona.

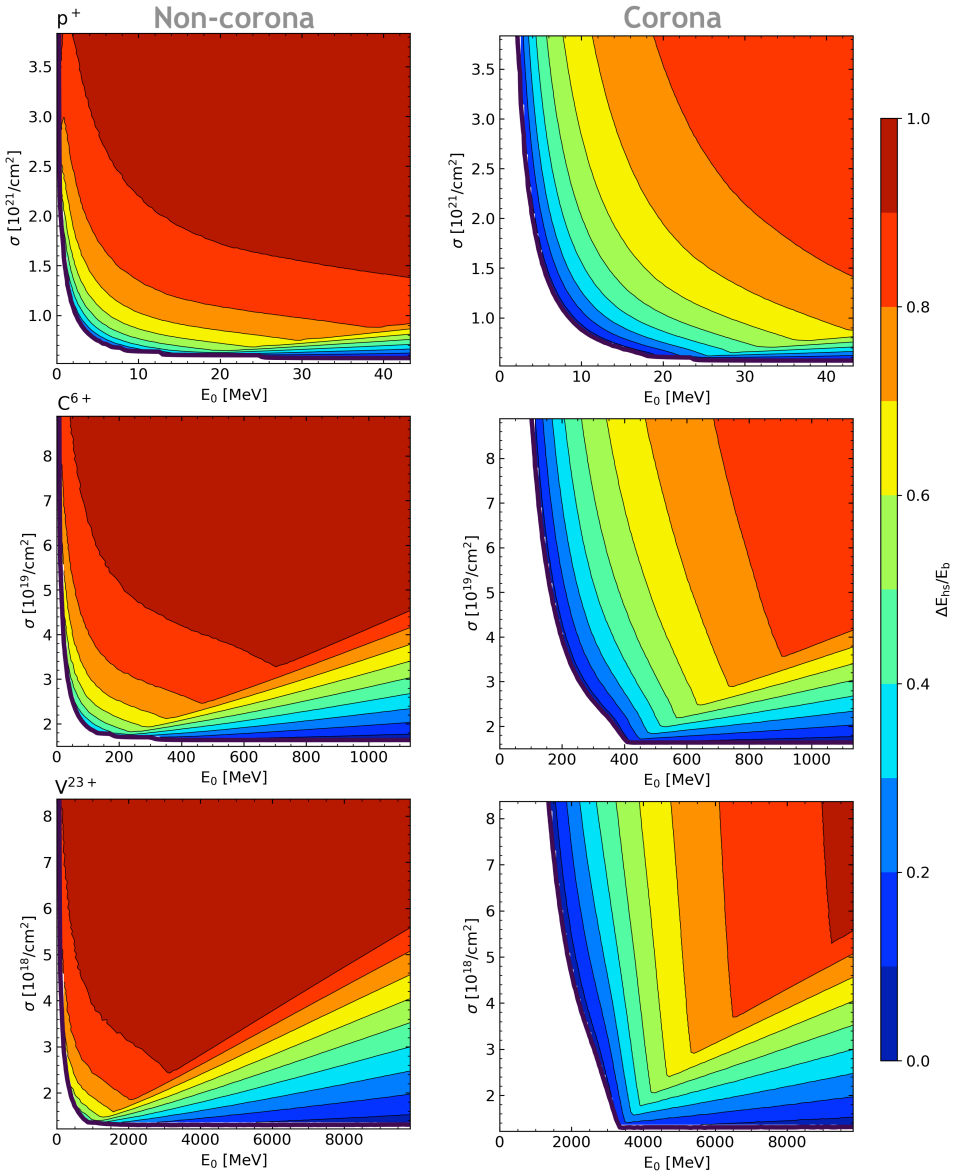

FIGURE 5.16— Coupling efficiency between the hot-spot and the beam energy in the (σ, E_0)-space. The experiment considered is the same as the central panel 5.12 ($\rho = 500$ g/cm^3, $T_0 = 1$ keV) for proton (top row), carbon (middle row) and vanadium (bottom row) beams. The left column is used as the reference case without corona and the right columns do consider a corona.

As a bottom line, we can say that results are similar but displaced to higher energies, except for the coupling values, that might be lower and located differently. Thus, in order to address the non-corona approximation, it is necessary to consider the change in projectile energies or to create an experiment where the beam source is as close to the core as possible.

6

Simulation and analysis of the beam-plasma interaction of monoenergetic ion beams with doped DT fuels

In this chapter, a huge number of numerical simulations were performed to study of the interaction between a fast monoenergetic ion beam and doped DT fuel. To exemplify the behaviour of a fuel that is not pure, we have chosen various ion beams and a plasma doped with fully ionized impurities (Be, C, Al and Cu) at different concentrations. As explained at the beginning of Chapter 3, during the compression process, traces of the ablator material get mixed with the DT fuel. Therefore, analysing the influence of the impurities on the characteristic parameters of the hot-spots generated in FI is key for a more realistic study. We present the results of the heated plasma and the hot-spot, the self-heating, the ignition curves, the burning gain and the coupling of such doped DT plasma. With the inclusion of different dopants and concentrations, the number of variables of our study is even larger. Thus, we narrow down the study by selecting a fast fully ionized monoenergetic proton, carbon and vanadium ion beams with radius $r_\mathrm{b} = 15$ μm and a representative plasma with $R_\mathrm{F} = 50$ μm, $\rho_\mathrm{DT} = 500$ g/cm^3 and $T_0 = 1$ keV. We left as free parameters the kind of impurity (Z_dop) and its concentration (ξ), as well as a wide range of values for the energy of the beam ions (E_0) and its flux (σ). As explained in Sect. 2.4, neither corona nor quasi-monoenergetic beams are considered, in order to evaluate separately the influence of dopants in respect to the pure DT

plasma case. We note that, to ease the comparison, in this chapter the limits $(\sigma_{\min}, \sigma_{\max}, E_{0\,\min})$ of the parameter space are often the same as in previous Chapter 5. We have extended $E_{0\,\max}$ to gather the range of $L_{\rm h} = 100$ μm and sometimes, if necessary, we apply a zoom-in for a clearer representation.

6.1 Length and temperature distributions in the (σ, E_0)-space

To fully understand the influence of dopants in the conditions of the plasma after the interaction, first we show some results associated with changes in length and temperature of the hot-spot. Following the ideas already presented in Sect. 2.4, we choose the hot-spot such that $L_{\rm hs} = 2r_{\rm b}$ and $x_{\rm Tmax} = R_{\rm F}$. As the beam and sphere radii are of 15 μm and 50 μm, respectively, in the top four panels of Figs. 6.1, 6.2 and 6.3 (each figure corresponds to a proton, carbon and vanadium beam) we have depicted the isolines of $L_{\rm hs} = 30$ μm and $x_{\rm Tmax} = 50$ μm in the (σ, E_0)-space, for a pure DT plasma ($\xi = 0$) and for the dopants selected at different concentrations. Then, in the bottom four panels, we show the temperatures associated to such lengths in the central hot-spot region for the same cases.

In the top four panels of Figs. 6.1, 6.2 and 6.3 we observe how, when the concentration is increased, both $L_{\rm hs} = 30$ and $x_{\rm Tmax} = 50$ μm displace towards higher energy and flux values, aligned to the pure DT isoline. This is mainly due to the increase of the slowing down of the ions of the beam exerted by free electrons and nuclei associated with impurities. Moreover, when adding a dopant, the density of the plasma increases, reducing all lengths, as demonstrated in Sects. 4.2 and 4.4.

A precise way of determining the change in the isoline positions can be done by inspecting the energy at which $x_{\rm Tmax} = 50$ μm is reached (as in the pure case, the lines are vertical) or by studying the point $(\sigma^*(Z_I, \xi), E_0^*(\sigma^*, Z_I, \xi))$, when the central hot-spot region is reached (see Sect. 5.1). For instance, $x_{\rm Tmax} = 50$ μm is found in a pure DT fuel at $E_0 \approx 800$ MeV, then, this value increases up to 1275 MeV for a Be doped fuel ($\xi = 0.4$). On the other hand, we find that $E_0^*(Z_I, \xi)$ and $\sigma^*(Z_I, \xi)$ increase with both the atomic number and the concentration of the impurity. As an example, for a pure plasma, we find $E_0^*(Z_I, \xi) \approx 500$ MeV and $\sigma^*(Z_I, \xi) \approx 2.5 \cdot 10^{19}$ cm^{-2}. When Be ($\xi = 0.2$) is introduced in the plasma, these values are shifted to $E_0^*(Z_I, \xi) \approx 1100$ MeV and $\sigma^*(Z_I, \xi) \approx 3.4 \cdot 10^{19}$ cm^{-2}, while if the impurity is carbon at a similar concentration, $E_0^*(Z_I, \xi) \approx 1225$ MeV and $\sigma^*(Z_I, \xi) \approx 4.4 \cdot 10^{19}$ cm^{-2}. For the case of Cu ($\xi = 0.015$), we obtain $E_0^*(Z_I, \xi) \approx 625$ MeV and $\sigma^*(Z_I, \xi) \approx 3.7 \cdot 10^{19}$ cm^{-2}. When a heavier dopant is considered, $(\sigma^*(Z_I, \xi), E_0^*(\sigma^*, Z_I, \xi))$-values of the same order are found for lower concentrations.

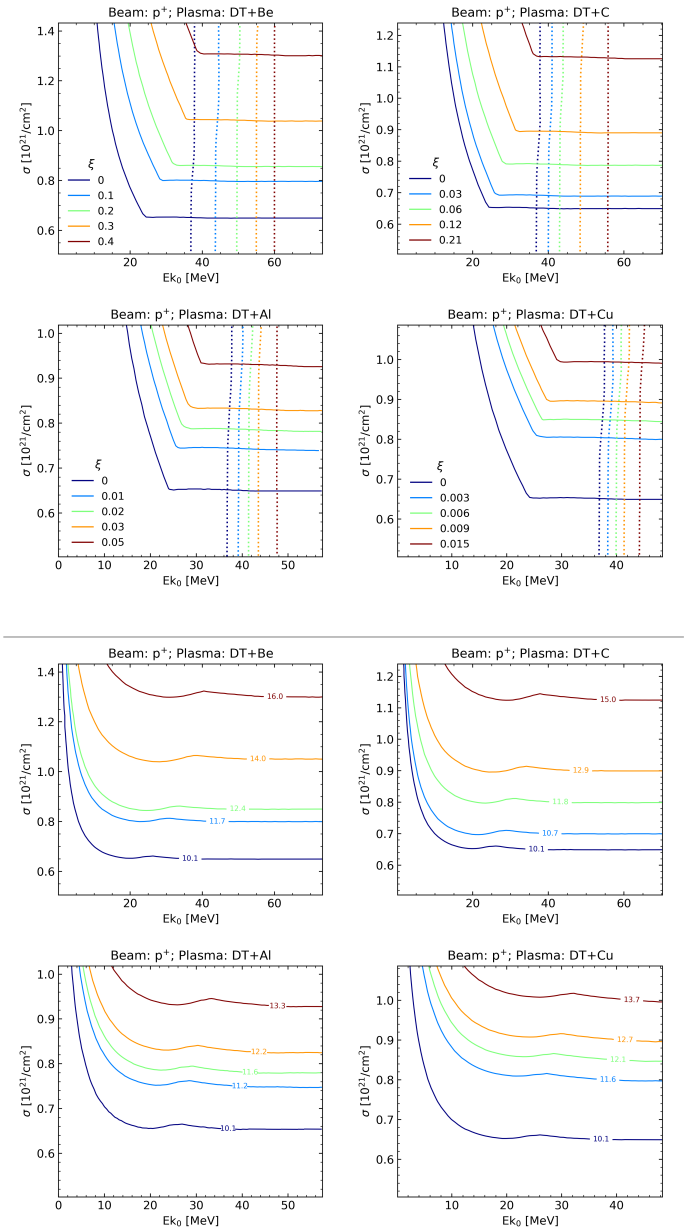

FIGURE 6.1— Isoline results retrieved after applying a proton beam to a DT plasma including four kinds of impurities at different concentrations: Be (top-left), C (top-right), Al (bottom-left) and Cu (bottom-right). Top four panels: solid lines represent a hot-spot length of $L_{\mathrm{hs}} = 30$ μm and dotted lines represent the position of the maximum temperature when is located at $x_{\mathrm{Tmax}} = 50$ μm. Bottom four panels: isolines of the hot-spot temperatures (T_{hs}) corresponding to lengths of $L_{\mathrm{hs}} = 30$ μm in the central hot-spot region.

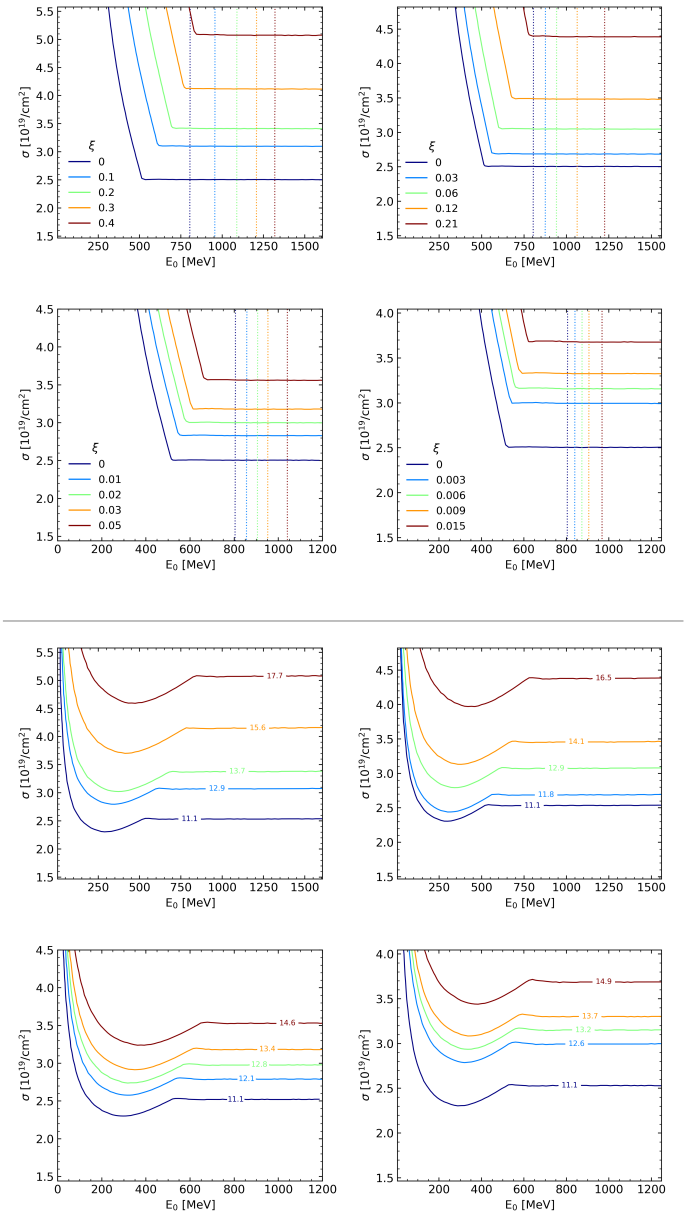

FIGURE 6.2— Same as in Fig. 6.1 but applying a carbon beam.

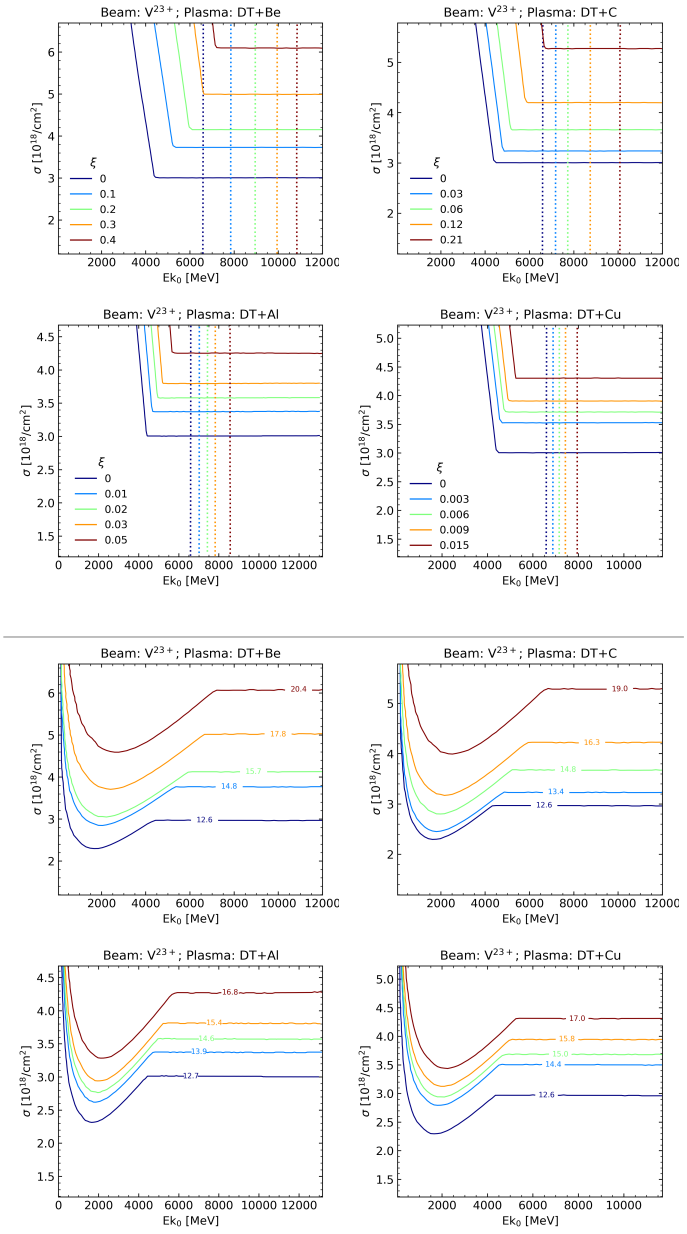

FIGURE 6.3— Same as in Fig. 6.1 but applying a vanadium beam.

Meanwhile, in the bottom four panels of Figs. 6.1, 6.2 and 6.3 we show the isolines of the hot-spot temperatures ($T_{\rm hs}$) associated to $L_{\rm hs} = 30$ μm when they are in the central hot-spot region. It is found that the hot-spots become hotter when either the atomic number or the concentration of the impurity increase. For example, in the pure case, $T_{\rm hs} = 11.1$ keV, while for beryllium doped fuel $T_{\rm hs} = 13.7$ keV for $\xi = 0.2$. For a similar concentration, a carbon dopant reaches a temperature of $T_{\rm hs} = 16.5$ keV. This increase in temperature could be anticipated according to the results of Sec. 4.4, as the density of the plasma increases when a dopant is introduced.

With all these experiments, we are able to provide the beam characteristics (σ, E_0) at which it is possible to generate a hot-spot with a length of 30 μm and located at the centre of the sphere ($x_{\rm Tmax} = 50$ μm), as well as its associated temperature, for different mixtures of the fuel. Later on, we also provide its associated burn gain and coupling values for some of these concentrations, by means of the systematic results of Sect. 6.3. If necessary, our modelling is capable of calculating this sort of results for any desired input parameters.

6.2 Ignition and self-heating threshold in the (σ, E_0)-space

After addressing the characteristics of the hot-spot, we study the threshold values of σ and E_0 at which self-heating and ignition can be reached. To do so, in Figs. 6.4, 6.5 and 6.6 we have plotted the self-heating curves ($G_{\rm sh}(\sigma, E_0, Z_I, \xi) = 1$) and ignition curves ($G_{\rm ig}(\sigma, E_0, Z_I, \xi) = 1$). Values of the (σ, E_0)-space above those curves fulfil their respective conditions. The colour code is the same as in Sect. 6.1.

As expected, for the ranges of medium and high energies, these curves have an almost constant value. This is due to $L_{\rm hs}$ and $T_{\rm hs}$ being constant with energy when the central hot-spot region is reached. For a DT pure plasma ($\xi = 0$), the minimum values of σ are very similar for self-heating and ignition curves ($\sigma_{\rm min,sh} \approx \sigma_{\rm min,ig} \approx 1.6{\cdot}10^{19}$ cm^{-2}) although some small differences are detected at low energies ($E_0 < 150$ MeV).

When an impurity is introduced in the DT fuel, the differences between self-heating and ignition curves becomes more relevant. Moreover, both curves are shifted to higher values of σ and E_0, which implies that the region of beam parameters in which the criterion are fulfilled is reduced. These behaviours are more pronounced as the atomic number and the concentration of the impurity increase. For example, for the case of Be, the value of $\sigma^*_{\rm sh}$ increases to $1.9 \cdot 10^{19}$ cm^{-2}, $2.1 \cdot 10^{19}$ cm^{-2} and $3.9 \cdot 10^{19}$ cm^{-2} when $\xi = 0.1$, 0.2 and 0.3, respectively. For the carbon doped case, the values are $2.2 \cdot 10^{19}$ and $3.3 \cdot 10^{19}$ cm^{-2}, when $\xi = 0.1$ and 0.2, respectively.

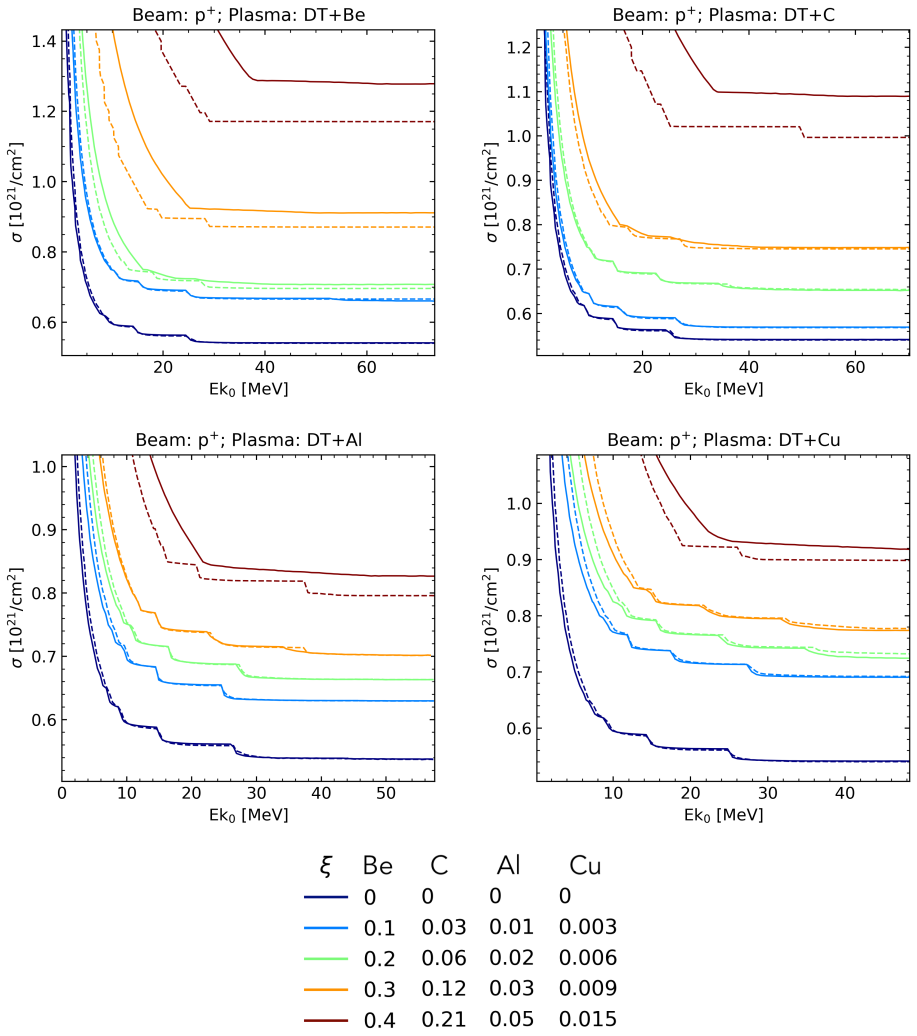

FIGURE 6.4— Isoline results retrieved after applying a proton beam to a DT plasma including four kinds of impurities at different concentrations: Be (top-left), C (top-right), Al (bottom-left) and Cu (bottom-right). Self-heating ($G_{\mathrm{sh}} = 1$) is represented as dashed lines and ignition curves ($G_{\mathrm{ig}} = 1$) is represented as solid lines. Each colour coincides with the concentrations shown at Fig. 3.6.

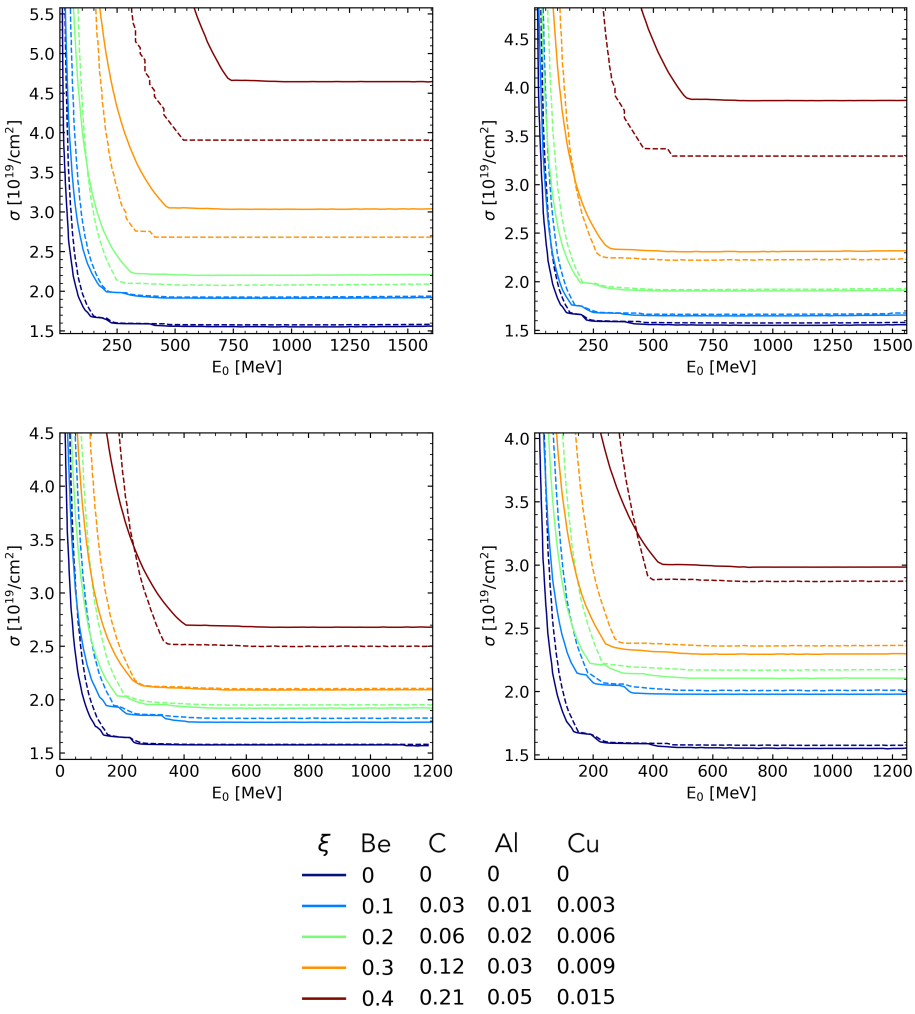

FIGURE 6.5— Same as in Fig. 6.4 but applying a carbon beam.

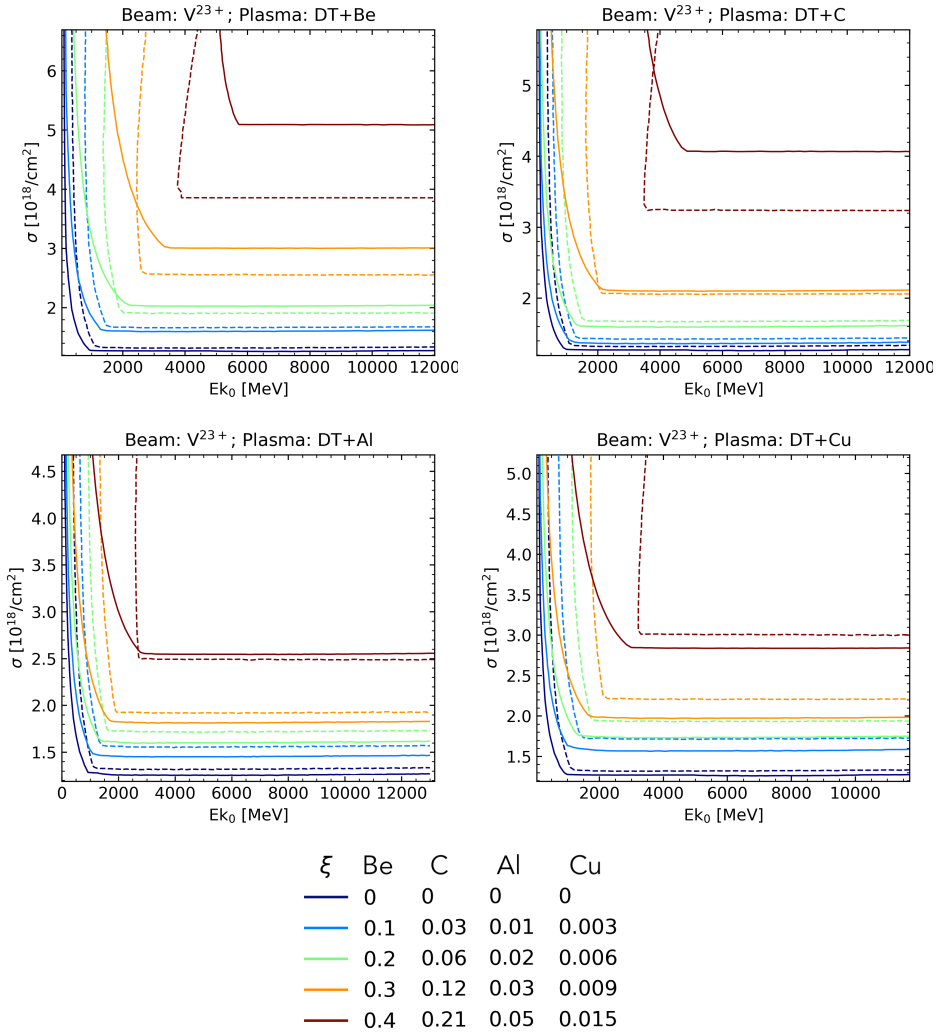

FIGURE 6.6— Same as in Fig. 6.4 but applying a vanadium beam.

We note that, at low values of ξ, the values of $\sigma_{\mathrm{min,ig}}$ are slightly lower than $\sigma_{\mathrm{min,sh}}$. However, the panels of Figs. 6.4, 6.5 and 6.6 show that, for every impurity, there is a certain concentration value ($\xi^*(Z_I)$) from which the self-heating curve is found below the ignition curve. In such cases, the self-heating criterion is less restrictive than the ignition criterion, in contradiction to the ideas stated in Sects. 2.3.2, 3.6 and 3.7. This means that the self-heating criterion does not ensure the ignition and, therefore, the posterior burning of the heated region. In that situation, the set of beam parameters included between both curves is not of interest. For Be, C, Al and Cu impurities, we have found that $\xi^*(Z_I)$ is around 0.15, 0.1, 0.035 and 0.01, respectively.

6.3 Burning gain and coupling results in the (σ, E_0)-space

Finally, we have analysed the influence of the impurities in the nuclear burn. Again, it is characterized by the burning gain parameter, G_{burn}, given by Eq. 3.61. This parameter also depends on the radius of the sphere ($R_{\mathrm{F}} = 50\ \mu$m), so we have restricted our analysis to cases in which the range of the ion is less than $L_{\mathrm{h}} = 100\ \mu$m. For higher lengths, the ion beam deposits energy outside the fuel, so this situation has not been considered in the present study.

In Figs. 6.7, 6.8 and 6.9 we depict the burning gains obtained for a pure DT plasma in comparison to the same plasma doped with Be, C, Al and Cu impurities at different concentrations. Each figure considers a different beam: p^+, C^{6+} and V^{23+}. In these figures, the thick black line at low σ represents the ignition curve ($\sigma_{\mathrm{min,ig}}(E_0, Z_I, \xi)$) which indicates that only above this curve does nuclear burn take place. The other thick black line showed in the figures represents the isoline of $L_{\mathrm{h}}(\sigma, E_0, Z_I, \xi) = 100\ \mu$m. As discussed previously, with Sects. 6.1 and 6.2, both the ignition curve and the $L_{\mathrm{h}} = 100\ \mu$m isolines are shifted toward higher values of σ and E_0 when impurities are introduced and their concentration is increased. As a consequence of the ignition requirements, the (σ, E_0)-space where burning can take place is reduced. More importantly, if the region where the burning is possible shrinks, the maximum burning gain values are restricted. When increasing the concentration of each impurity, we find that the same gains are found in almost the same (σ, E_0)-values, slightly displaced towards higher fluxes when the concentration is increased. Thus, when some of those values are no longer available to create a hot-spot that achieves ignition, the optimal values for G_{burn} are lost. These deductions are similar for all the dopants shown, at least for the selected concentrations. For example, Fig. 6.8 shows that G_{burn} reaches a maximum value around $G_{\mathrm{burn}} \approx 4000$ (or, from Eq. 3.60, $E_{\mathrm{fus}} \approx 4000 \cdot (E_{\mathrm{hs}} + E_{\mathrm{c}})$), while, for example, a carbon doped fuel this value is reduced to $G_{\mathrm{burn}} \lesssim 2400$ and $\lesssim 800$ when the concentration

is 0.06 and 0.21, respectively. Furthermore, the maximum values of the gains are obtained close to the ignition curves, where hot-spots have the lowest values of the areal density and temperature. This happens when the beams have either low flux or ion energy. On the other hand, we have observed that the maximum value of the burning gain is reduced as the atomic number of the impurity increases. For instance, for beryllium and carbon impurities at $\xi \approx 0.2$, the maximum value is $G_{\mathrm{burn}} \lesssim 1600$ and $\lesssim 800$, respectively.

Finally, in Figs. 6.10, 6.11 and 6.12, we present the results of the coupling $(\Delta E_{\mathrm{hs}}/E_{\mathrm{b}})$ for the same cases selected when presenting the results of the burning gain. Again, each figure corresponds to a different beam specie. For each impurity, when increasing the concentration, the same coupling results are displaced towards higher flux values and, again, the region of study is reduced. However, in this case the lower values of the coupling disappear, in favour of the energy deposition.

The coupling figures also serve to comment on how the edge and central hot-spot regions behave in the presence of dopants (see, for instance, Fig. 6.11). We find that, when introducing an impurity of increasing concentration, the size of the central hot-spot region grows. Although in our studied parameter space the available regions are restricted to higher (σ, E_0)-values, the impurities might ease finding central hot-spots.

With all the results of this chapter, we can reason that the presence of impurities is highly detrimental in the FI context. In comparison to a pure DT fuel, the requirements for the beam are stricter and the feasible burning gains are lower.

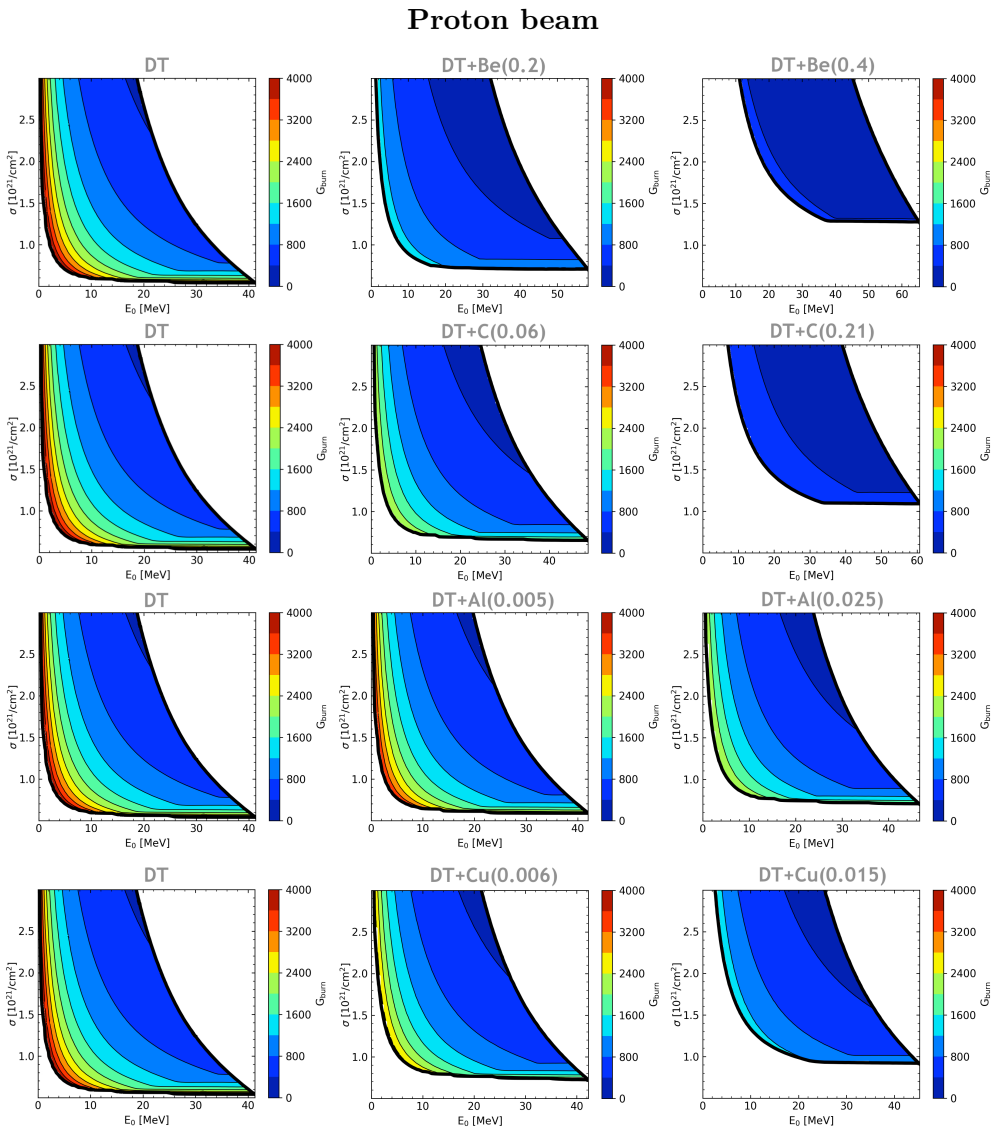

FIGURE 6.7— Burning gain of a pure DT plasma (left column) and including different impurities at different concentrations (central and right columns) when applying a proton beam.

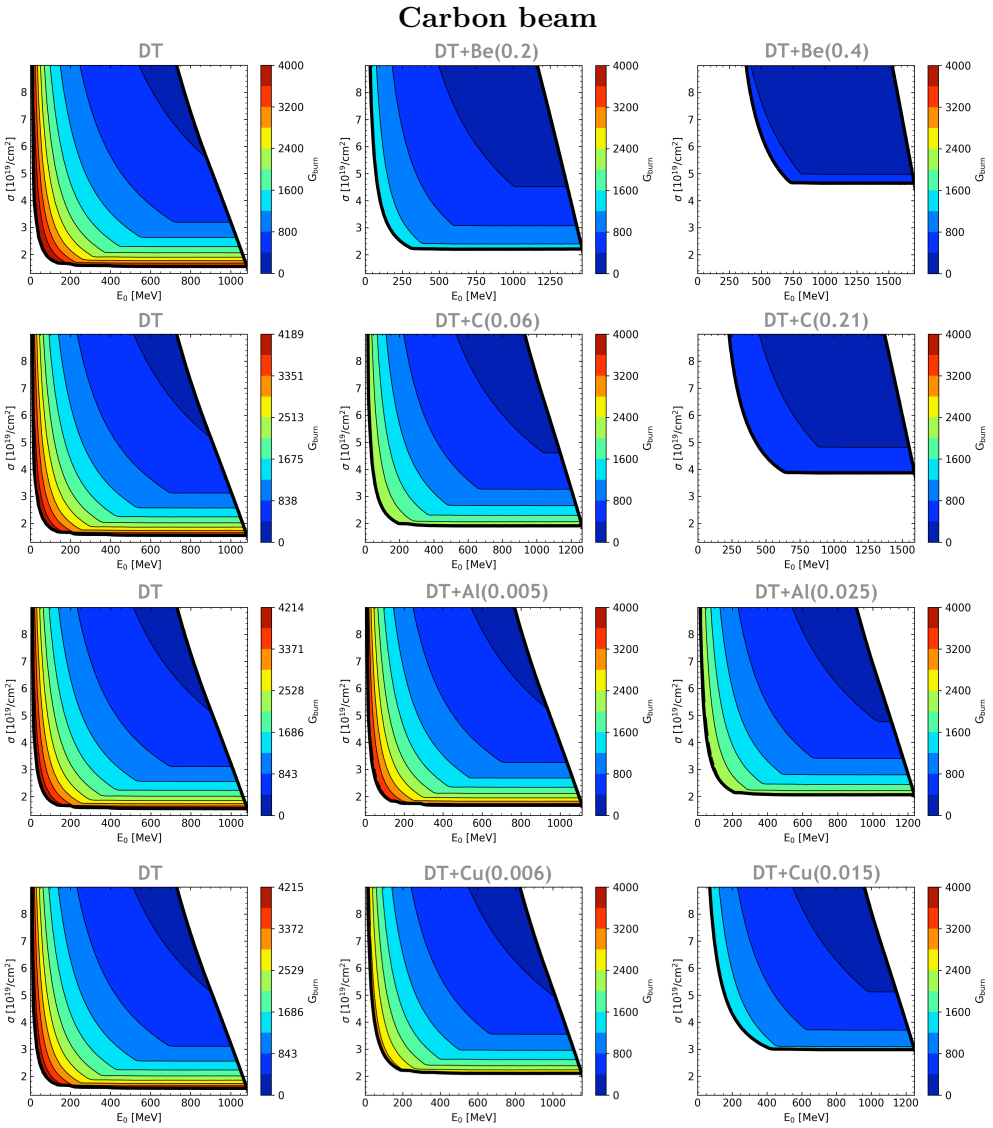

FIGURE 6.8— Similar to Fig. 6.7, but applying a carbon beam.

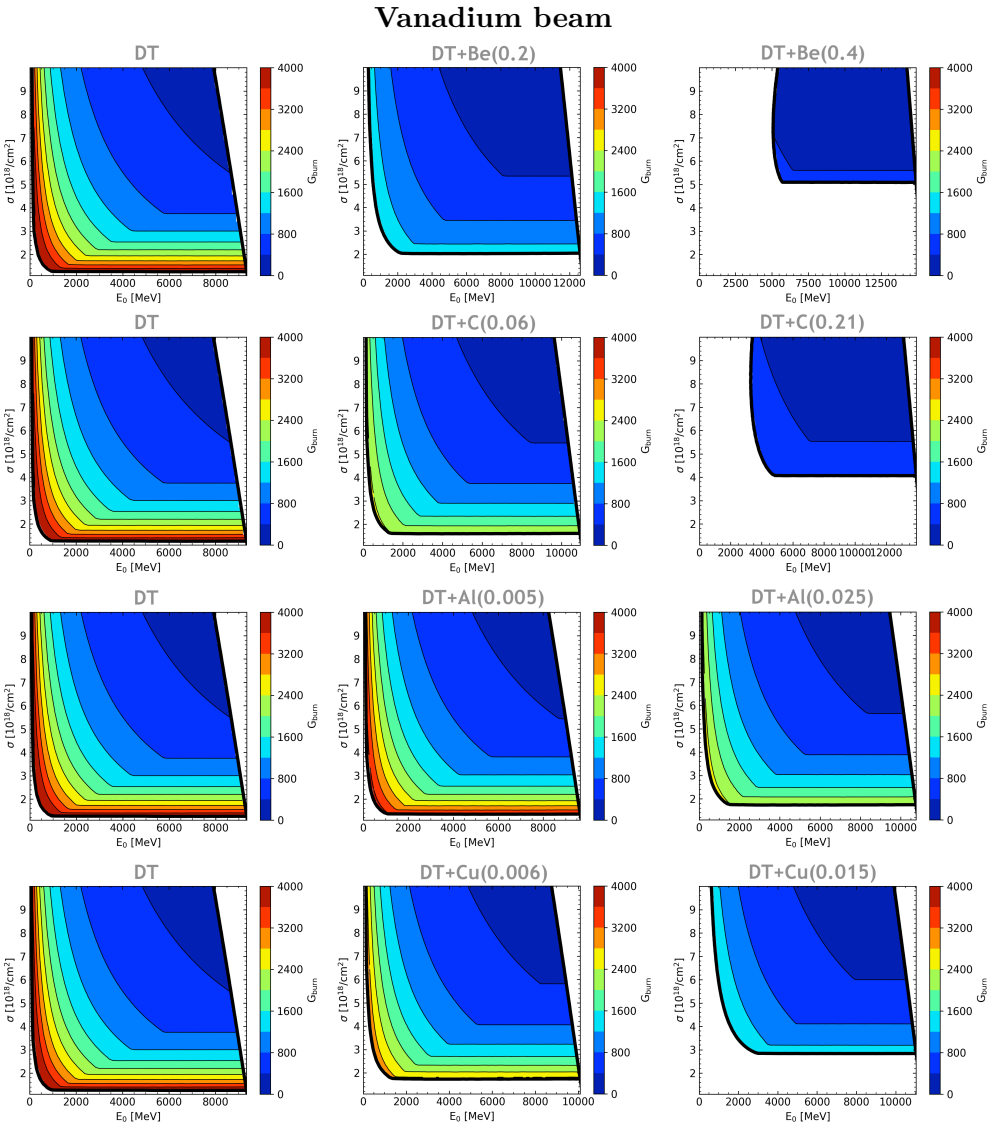

FIGURE 6.9— Similar to Fig. 6.7, but applying a vanadium beam.

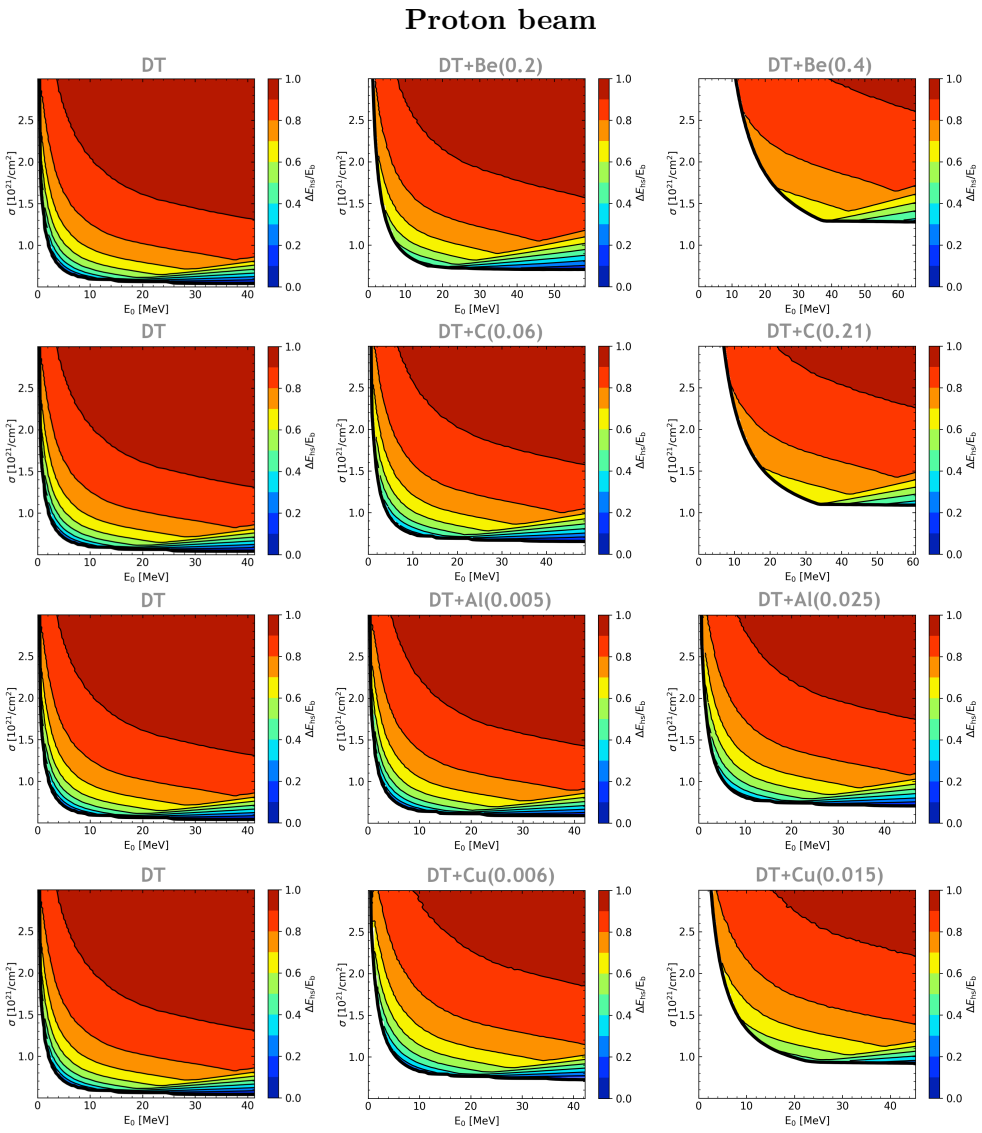

FIGURE 6.10— Coupling values of a pure DT plasma (left column) and including different impurities at different concentrations (central and right columns) when applying a proton beam.

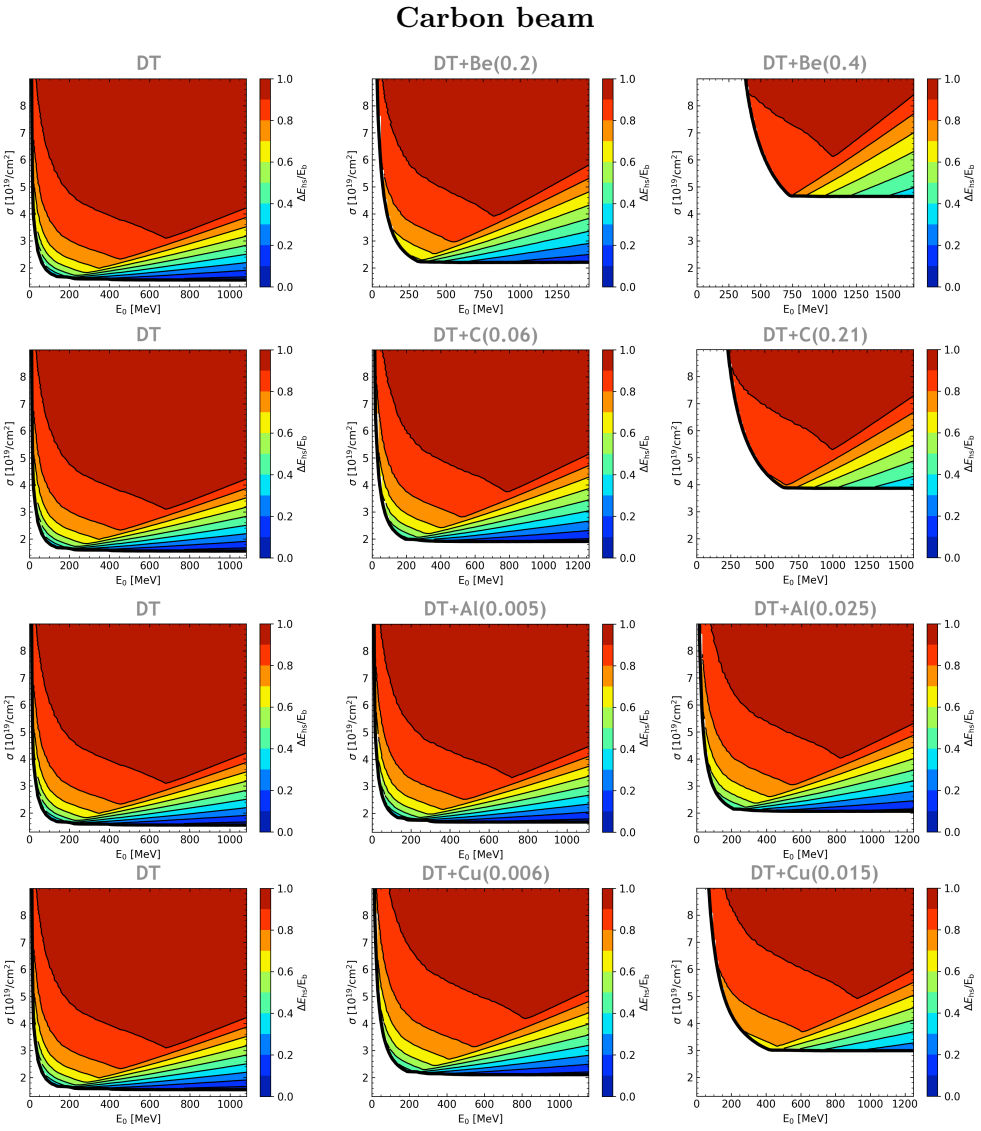

FIGURE 6.11— Similar to Fig. 6.10, but applying a carbon beam.

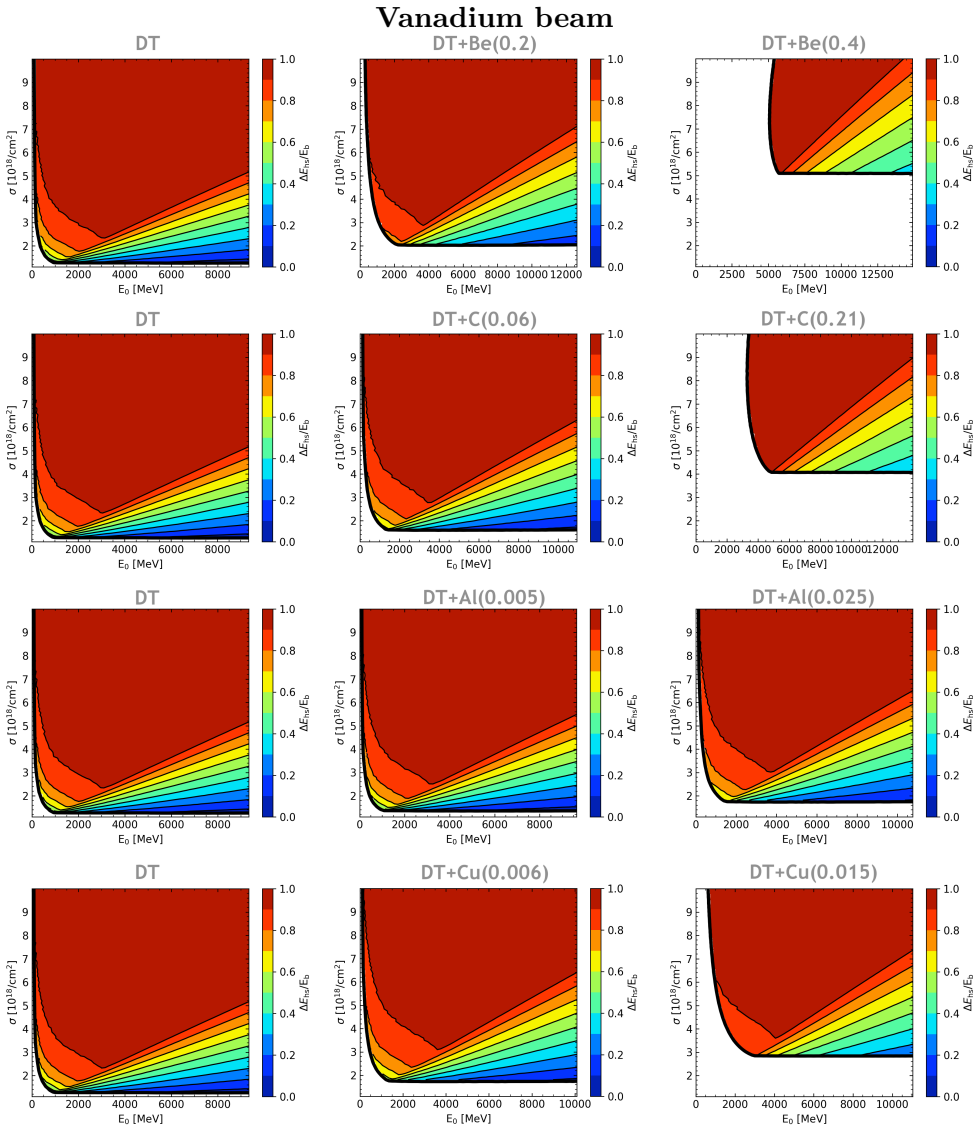

FIGURE 6.12— Similar to Fig. 6.10, but applying a vanadium beam.

7

Simulation and analysis of the beam-plasma interaction of quasi-monoenergetic Gaussian ion beams with pure DT fuels

This chapter delves into the interaction between quasi-monoenergetic beams and a pure DT plasma. We compare the results of a monoenergetic beam with two quasi-monoenergetic Gaussian beams. As explained in Sect. 3.3.2, one generated at the edge of the precompressed fuel (G1) and one generated at a distance "d" of the edge (G2 or time-dependent)[1]. We determine the ion beam parameters that fulfilled the self-heating and ignition criteria in each case, that is, in the $(\sigma, \bar{E}_0, \delta E)$-space. Then, we present the differences in the retrieved hot-spots and heated regions, as well as the burning gains of the thermonuclear fuel.

Although our simulations can be performed for a variety of experimental conditions, in this chapter we will only show exemplary results for a plasma of density $\rho = 500$ g/cm^3 and initial temperature $T_0 = 1$ keV, with different vanadium beams. These cases are representative of the general behaviour we have found through our modelling. The beam considered has a wide range of the parameters $(\sigma, \bar{E}_0, \delta E)$, as well as being located at the edge of the plasma or not (G1 or G2 cases). The energy spread values considered in our study corresponds

[1]We note that, when performing our numerical calculations, the results are ultimately independent of the distance, as explained in Sect. 3.12.

to quasi-monoenergetic Gaussian beams, that is, they were selected equal to or less than 15% ($\delta E \lesssim 0.15$, Hegelich et al., 2011). No corona or dopants are considered, to study the effect of considering a quasi-monoenergetic beam alone and contrast the results with the monoenergetic case.

7.1 Spatial-temporal results

To begin with, we analyse the changes in the stopping power when considering a Gaussian distribution for the energies of the beam. Thus, in Fig. 7.1, we show the stopping power of a bin entering the plasma at the end of the heating process. We consider a flux of $\sigma = 2.7 \cdot 10^{18}$ cm^{-2} (left) and $\sigma = 3.8 \cdot 10^{18}$ cm^{-2} (right), for mean initial energies given by $\bar{E}_0 = 4000$ and 7000 MeV. The energy spreads (δE) considered are 0% (monoenergetic), 5%, 10% and 15%, with no separation between the source and the target (G1, $d = 0$).

In the case of quasi-monoenergetic beams ($\delta E \neq 0\%$), the ions at each instant, t, enter the plasma with a variety of initial energies in a proportion established by the Gaussian energy distribution from Eq. 3.20. As a consequence, each ion[2] has their own evolution (or slowing down) through the plasma, suffering a different stopping. The stopping power showed in the figure ($Sp(x; \bar{E}_0, \delta E)$) corresponds to the accumulated stopping power over all the projectiles.

In Fig. 7.1 we see how the stopping of monoenergetic beams reaches its maximum value just before becoming zero, or equivalently, forming the Bragg peak just before the ions stop. As expected, for a given value of the flux, the length of the heated region (L_h) increases with the initial energy (E_0). Meanwhile, for quasi-monoenergetic beams, we see that the main effect of an energy spread is reducing or making disappear the Bragg peak. This is due to the ion projectiles not having the same energy, and so, its slowing is different and do not stop at the exact same range.

Secondly, in Fig. 7.2 we show the spatial temperature field achieved after heating the plasma with the same conditions of Fig. 7.1. For the selected conditions of the beam, we find central hot-spots for all the experiments. Similarly to the previous results, having a distribution of energies for the ion projectiles spreads the energy deposition. For instance, projectiles with energy over $\bar{E}_0$ will reach further than in the monoenergetic case. Conversely, as not all the projectiles deposit their energy at the same time and position, less temperature is reached. This justifies how, for quasi-monoenergetic beams with increasing dispersion, the temperatures achieved are lower, the position of the maximum temperature decreases, but the range of the final heated region is larger. There-

[2]Or "sub-bin", according to our computation, as explained in Sect. 3.12

fore, when the energy spread is higher, the hot-spots are cooler and closer to the edge of the plasma. This change is crucial when taking into account that reaching temperatures over the ignition threshold (T_{ig}) is a requisite for the burning of the fuel. This foresees the limitations of Gaussian or Maxwellian beams to achieve ignition against monoenergetic beams, as we will address later on, with Fig. 7.5.

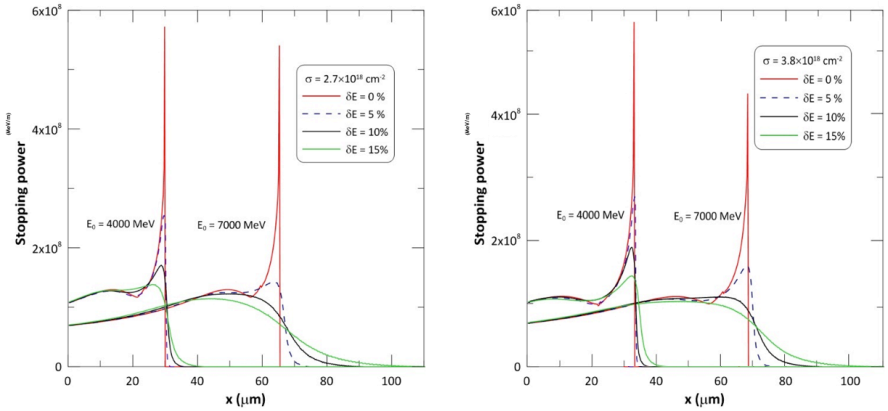

FIGURE 7.1— Stopping power [MeV/m] of the last bin as it deepens in the plasma. A quasi-monoenergetic Gaussian beam is considered (G1), located at the edge of the plasma, with vanadium projectiles of two energies ($\bar{E}_0 = 4000$ and 7000 MeV) and two fluxes ($\sigma = 2.7 \cdot 10^{18}$ cm^{-2} on the left and $\sigma = 3.8 \cdot 10^{18}$ cm^{-2} on the right). Plasma conditions are $T_0 = 1$ keV and $\rho = 500$ g/cm^3 (Gil et al., 2023).

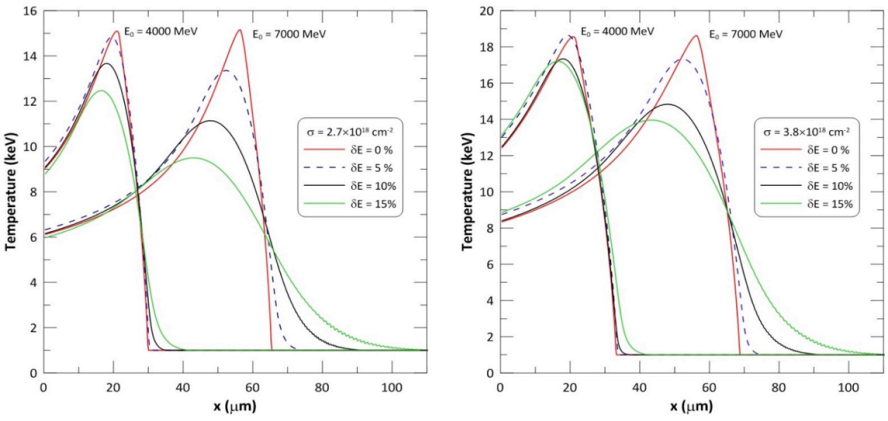

FIGURE 7.2— Temperature field after heating a plasma with a vanadium beam. The conditions considered are the same of Fig. 7.1 (Gil et al., 2023).

With Tables 7.1 and 7.2 we complement the information of Fig. 7.2 and present a more detailed view on the relevant properties of hot-spots generated by vanadium ion beams, considering various parameter values $(\sigma, \bar{E}_0, \delta E)$. Our discussion revolves around particle densities of $\sigma = 2.7 \cdot 10^{18}$ cm^{-2} (Table 7.1) and $\sigma = 3.8 \cdot 10^{18}$ cm^{-2} (Table 7.2), as these values correspond to hot-spot lengths on the order of 20 and 40 μm, respectively. These values are key, considering that typical values of the beam radii are in the order of $r_\mathrm{b} \approx$10 to 20 μm (Fernandez et al., 2014; Honrubia & Murakami, 2015), so we select beams that create hot-spots where $L_\mathrm{hs} \approx 2r_\mathrm{b}$, to ensure that the hot-spot volume can be approximated as a sphere as optimally as possible.

	$\delta E = 0\%$				$\delta E = 10\%$				$\delta E = 15\%$			
$\bar{E}_0$	L_hs	T_hs	x_Tmax	T_max	L_hs	T_hs	x_Tmax	T_max	L_hs	T_hs	x_Tmax	T_max
1000	5.8	13.5	0	14.9	5.8	13.5	0	14.9	5.8	13.4	0	14.9
4000	20.8	12.7	20.8	15.5	20.8	12.5	17.8	14.1	20.6	12.1	16.3	13.3
5500	20.8	12.7	38.2	15.5	20.4	11.8	32.4	12.7	18.3	11.1	29.5	11.6
7000	20.8	12.8	57.2	15.5	18.1	11.1	48.6	11.5	0	0	43.9	9.9
7500	20.8	12.8	63.4	15.5	16.3	10.8	53.7	11.1	0	0	48.3	9.6

TABLE 7.1— Values for the characteristic parameters of the heated plasma and the hot-spot for different values of the $(\bar{E}_0, \delta E)$, considering a fixed value of $\sigma = 2.7 \cdot 10^{18}$ cm^{-2}. The lengths are in μm, the temperatures in keV and the energies in MeV (Gil et al., 2023).

	$\delta E = 0\%$				$\delta E = 10\%$				$\delta E = 15\%$			
$\bar{E}_0$	L_hs	T_hs	x_Tmax	T_max	L_hs	T_hs	x_Tmax	T_max	L_hs	T_hs	x_Tmax	T_max
1000	7.5	15.3	0	17.9	7.5	15.3	0	17.9	7.5	15.3	0	17.9
4000	28.6	15.4	20.8	18.6	28.6	15.2	17.8	17.5	28.6	14.9	16.3	16.8
5500	42.6	14.1	38.2	18.8	42.6	13.5	32.9	16.3	42.5	13.1	29.7	15.1
7000	42.6	14.1	57.2	18.8	42.6	13.0	48.8	15.0	42.6	12.3	44.0	13.5
7500	42.6	14.1	63.2	18.8	42.6	12.9	53.7	14.6	42.5	12.0	48.5	13.1

TABLE 7.2— Similar to Table 7.1, but considering a beam with $\sigma = 3.8 \cdot 10^{18}$ cm^{-2} (Gil et al., 2023).

The numerical simulations reveal that, in both tables, for a given set of parameters $(\sigma, \bar{E}_0)$ of the beam, the hot-spot parameters $(L_\mathrm{hs}, T_\mathrm{hs}, T_\mathrm{max}, x_\mathrm{Tmax})$ generally decrease with an increase in the energy spread (δE) of the beam. From the results of Fig. 7.2 we know that the total range increases, as it is later demonstrated again, in Fig. 7.7. We note that the effect of δE is stronger with higher energies $(\bar{E}_0)$, specially for T_max and x_Tmax. It is interesting to compare the maximum temperature and its position for a quasi-monoenergetic

beam relative to the corresponding quantities of the monoenergetic one. For example, for $\sigma = 2.7 \cdot 10^{18}$ cm^{-2}, $\bar{E}_0 = 5500$ MeV and $\delta E = 10\%$ the changes in the maximum temperature and in its position are in the order of a 9% and 14%, respectively. And, when the energy spread increases to $\delta E = 15\%$, the changes obtained are the order of 26% and 23%, respectively. For $\sigma = 3.8 \cdot 10^{18}$ cm^{-2}, the same energy and $\delta E = 10\%$, the changes in the maximum temperature and its position are in the order of 13% and 15%, respectively. And, for energy spread of $\delta E = 15\%$, the changes are of the order of 20% and 23%, respectively. However, for low enough energies, the changes in parameters of the hot-spot are negligible or small. This can be observed in both tables, for instance with $\bar{E}_0 = 1000$ MeV and both fluxes, where the changes in the maximum temperature are less than 5% and in its positions are at the edge of the plasma.

As it was demonstrated in Chapter 5, for a monoenergetic beam, the characteristics of $L_{\rm hs}$, $T_{\rm hs}$, and $T_{\rm max}$ in central hot-spots remain approximately constant with energy. For instance, in Table 7.1, with $\sigma = 2.7 \cdot 10^{18}$ cm^{-2}, this happens at energies of 4000, 5500, 7000, and 7500 MeV. Then, when the flux increases, this behaviour persists but occurs at higher threshold energies and with elevated parameter values. This is shown in Table 7.2, in which central hot-spots are found only for 5500, 7000, and 7500 MeV, with a flux of $\sigma = 3.8 \cdot 10^{18}$ cm^{-2}. Hence, and as explained in Sect. 5.1, for monoenergetic beams there is a threshold energy ($E^*(\sigma^*)$) dependent on the flux, such that the hot-spots generated are central. From numerical simulations we can confirm that, for $\sigma = 2.7 \cdot 10^{18}$ cm^{-2}, this occurs for energies higher than a threshold energy of $E^*(\sigma^*) \approx 3500$ MeV, then, at higher a higher flux of $\sigma = 3.8 \cdot 10^{18}$ cm^{-2} at $E^* \approx 5500$ MeV. As it is seen in Tables 7.1 and 7.2, for values of the ion energy larger than E^*, in each respective case, the parameters $L_{\rm hs}$, $T_{\rm hs}$ and $T_{\rm max}$ keep constant.

On the contrary, this constant behaviour of central hot-spots tends to vanish when quasi-monoenergetic beams are considered. The differences with the monoenergetic case are more acute as the energy spread increases. For instance, the relative difference of the maximum temperature ($T_{\rm max}$) in the case ($\bar{E}_0 = 5500$ MeV,$\sigma = 2.7 \cdot 10^{18}$ cm^{-2}) is an 18% for $\delta E = 10\%$ and a 25% for $\delta E = 15\%$. Then, we observe that these changes are even larger when increasing the energies, as for instance, for ($\bar{E}_0 = 7500$ MeV,$\sigma = 2.7 \cdot 10^{18}$ cm^{-2},$\delta E = 15\%$) the relative difference is of 38% in comparison to the previous examples. At last, the effect is smoothed if the flux is increased, as the case of ($\bar{E}_0 = 7500$ MeV,$\sigma = 3.8 \cdot 10^{18}$ cm^{-2},$\delta E = 15\%$), finding a change of 20%, in respect to the previous cases. When studying the parameters associated to the hot-spot, we could argue that the results ($L_{\rm hs}, T_{\rm hs}$) do not change as drastically with δE. For instance, in the case of ($\bar{E}_0 = 5500$ MeV,$\sigma = 2.7 \cdot 10^{18}$ cm^{-2}),

when comparing the hot-spot temperature ($T_{\rm hs}$) with the monoenergetic beam, we find a 7% of relative difference for $\delta E = 10\%$ and a 12% for $\delta E = 15\%$, which are lower values in comparison to the ones found previously for $T_{\rm max}$. Eventually, the lowering of $L_{\rm hs}$ and $T_{\rm hs}$ leads to the non-formation or disappearance of the hot-spot. This is found in Table 7.1, for $\delta E = 15\%$, where the length and mean temperature values of the hot-spot at 7000 and 7500 MeV are zero, indicating the absence of points in the heated region with a temperature exceeding the ignition temperature ($T_{\rm max} \approx 10$ keV). At last, with regard to edge hot-spots, the values of $L_{\rm hs}$, $T_{\rm hs}$ and $T_{\rm max}$ increase slightly in respect to the monoenergetic case.

Furthermore, we note that the position of the maximum temperature in respect to the edge is also reduced when the energy spread is increased. However, one behaviour is shared with the monoenergetic case: as we found in Sect. 5.1, $x_{\rm Tmax}$ depends mostly on the initial energy of the ions and remains practically independent of the flux of the beam. This observation holds true for vanadium quasi-monoenergetic ion beams as well. This is easily noticeable when comparing any case of Table 7.1 ($\sigma = 2.7 \cdot 10^{18}$ cm^{-2}) with its analogue in Table 7.2 ($\sigma = 3.8 \cdot 10^{18}$ cm^{-2}).

Additionally, in Fig. 7.3 we illustrate a more detailed representation of the evolution of the plasma for different energy distributions of the beam. We show the time evolution of the temperature field during the heating process of the plasma by monoenergetic ($\delta E = 0\%$) and quasi-monoenergetic ($\delta E = 15\%$). For this analysis, we assume both beams have the same intensity (I), flux ($\sigma = 3.8 \cdot 10^{18}$ cm^{-2}) and energy (7000 MeV), and therefore, they have the same characteristic time ($\tau_{\rm beam} = \sigma / I$). It has been selected in several instants of the simulation, from $t_1 = 0.01\tau_{\rm beam}$ until $t_7 = \tau_{\rm beam}$. After the whole interaction, both beams are able to generate a hot-spot, although the monoenergetic reaches this conditions earlier, at $t_4 \approx 0.4\tau_{\rm beam}$, while the quasi-monoenergetic does at $t_6 \approx 0.8\tau_{\rm beam}$. At such instant ($t_6$), the hot-spot length associated with the monoenergetic beam is shorter than the one of the quasi-monoenergetic beam. However, as it can be seen in this figure or in Table 7.2 (for central hot-spot cases, with high $\bar{E}_0$), at the end of the heating process, both hot-spots do reach similar length values of $L_{\rm hs} \approx 43$ μm.

After this careful examination of a quasi-monoenergetic Gaussian beam located at the edge of the plasma ($d = 0$), it is also necessary to address the results found when the source is separated from the fuel. Thus, in Fig. 7.4 we show the spatial temperature field reached at the end of the heating process for different conditions of the beams. The plasma considered is the same as in Fig. 7.2, but in this case the beams have a flux of $\sigma \approx 3 \cdot 10^{18}$ cm^{-2}, with energies of $\bar{E}_0 \approx 5000$ and 6500 MeV and energy spreads of $\delta E = 0\%$ (monoenergetic),

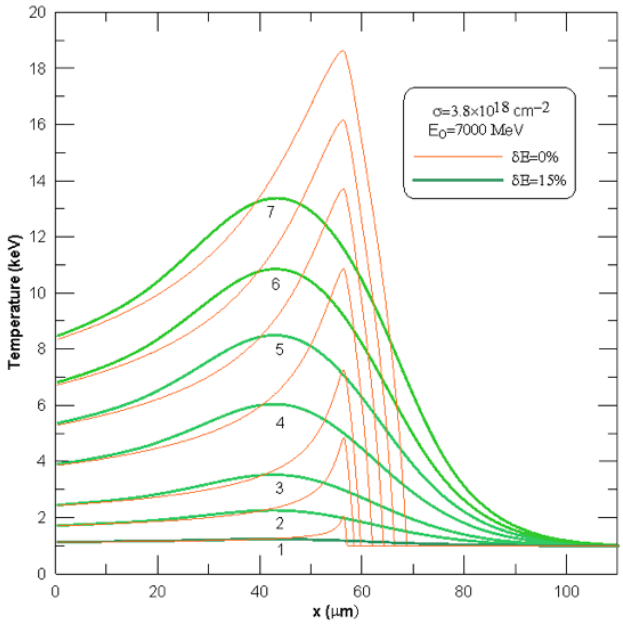

FIGURE 7.3— Time evolution of the temperature field of the heating process for seven instants of time ($t/\tau_{\rm beam}$=0.01, 0.1, 0.2, 0.4, 0.6, 0.8 and 1). Two vanadium beams are considered: monoenergetic and a Gaussian (δE = 15%) located at the edge of the plasma (G1), both with $\bar{E}_0 = 7000$ MeV and $\sigma = 3.8 \cdot 10^{18}$ cm^{-2}. The conditions of the plasma are the same of Fig. 7.1.

$\delta E = 10\%$ and $\delta E = 15\%$. Additionally, we consider the quasi-monoenergetic beams located at the edge of the plasma (G1) and another one at a distance "d" (G2).

We find that the resulting distributions of temperatures create central hot-spots. Again, we can see the main effects of the energy spread on the temperature field: the maximum temperature decreases, the position of the maximum temperature is displaced and the length of the heated region $L_{\rm h}$ increases. To further address these differences, we have inspected the results in the $(\sigma, \bar{E}_0)$-space and calculated the relative differences. Examples of these results are displayed in the following sections. Between the G1 and G2 cases, we find some similarities, as the maximum temperature and range, and a discrepancy in the position of $x_{\rm Tmax}$, being further from the edge in the G2 case. As we will show below, when comparing G1 and G2 scenarios in the $(\sigma, \bar{E}_0)$-space most of the results are nearly equivalent, including the hot-spot parameters. This is particularly relevant because the gains we study are determined by the radius and mean temperature of the hot-spot, so, between G1 and G2, those results will

be similar too.

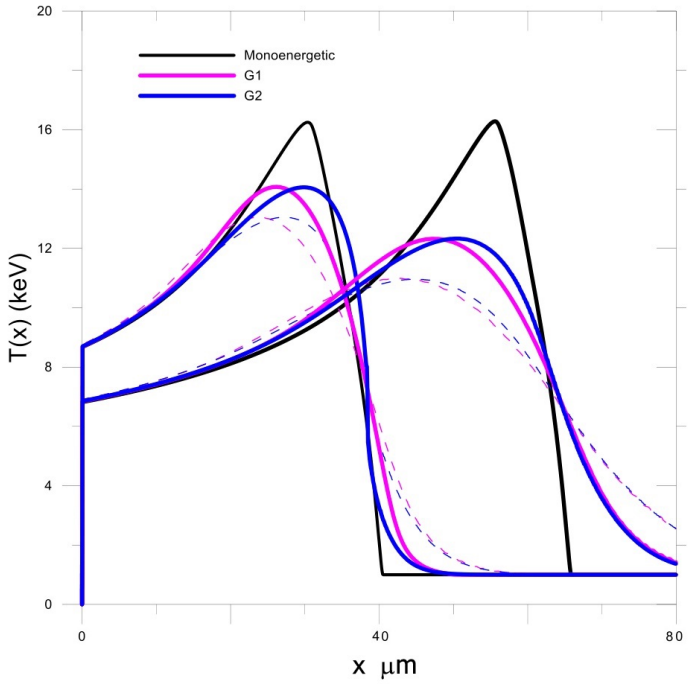

FIGURE 7.4— Temperature field after heating a plasma with a vanadium beam. The scenarios considered are: a monoenergetic beam, a quasi-monoenergetic beam located at the edge of the plasma (G1) and another one located at a "d" distance (G2). The conditions of the beam are $\bar{E}_0 \approx 5000$ and 6500 MeV and $\sigma \approx 3 \cdot 10^{18}$ cm^{-2}. For the quasi-monoenergetic beams, the energy spreads are $\delta E = 10\%$ (solid line), $\delta E = 15\%$ (dashed line). The plasma conditions are the same of Fig. 7.1.

7.2 Ignition threshold in the $(\sigma, \bar{E}_0)$-space

Hereafter, we detail the systematic results found in the $(\sigma, \bar{E}_0)$-space for a monoenergetic beam, a quasi-monoenergetic Gaussian beam found at the edge of the plasma (G1) and another one found at a "d"distance (G2). Both Gaussian beams have energy dispersions of $\delta E = 5$, 10 and 15%. To ease the comparison, the ranges of the $(\sigma, \bar{E}_0)$-space are the same of Chapter 5. If necessary, a zoom-in is applied to the σ-axis for better visibility.

First, we want to address the region within the $(\sigma, \bar{E}_0)$-space where the ignition is achieved. This is shown in Fig. 7.5, where we display the ignition curve ($G_{\text{ig}} = 1$) for the different type of beams. For each energy spread, the

two quasi-monoenergetic beams (G1 and G2) are represented together, because the ignition threshold of both are almost identical. As it is shown in Figs. 7.7 and 7.8, the hot-spot parameters of G1 and G2 are much alike, leading to similar ignition values. We can address how this parity appears, by taking into account that the only difference between G1 and G2 is the energy with which the projectiles enter the plasma. In the G1 case there is a Gaussian distribution for each bin, while in G2 the projectiles enter in an orderly manner, first the most energetic ones, that have travelled the separation distance the fastest and finally the slowest. However, ultimately, the same set of projectiles deposits energy in the plasma, leading to akin temperature distributions.

We remind that the area above the ignition curve correspond to those cases where the burning is possible. In comparison to the monoenergetic case, we find that both Gaussian beams fulfil the ignition conditions in a diminished $(\sigma, \bar{E}_0)$-area. We can see that the ignition curves shift toward higher values of the parameters σ and $\bar{E}_0$ when the energy spread increases. This is an indication of how the *spark* temperature and length are lower when considering a quasi-monoenergetic case, and thus, do not reach the ignition conditions for some $(\sigma, \bar{E}_0)$-cases, where a monoenergetic beam does.

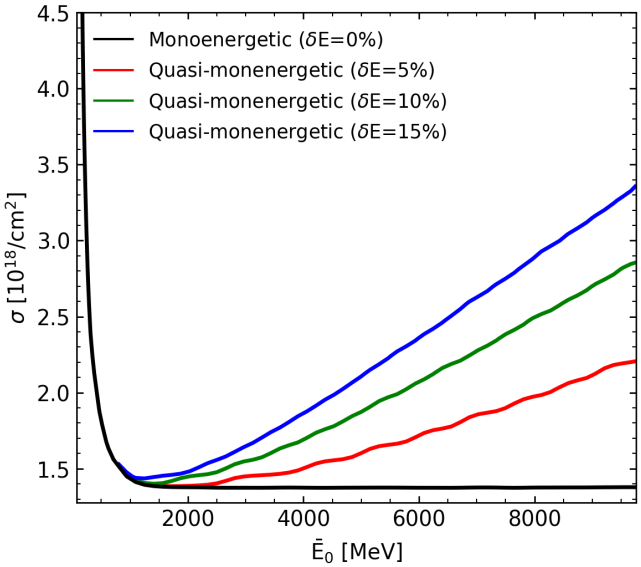

FIGURE 7.5— Ignition curve ($G_{\rm ig}(\sigma, \bar{E}_0, \delta E) = 1$) in the $(\sigma, \bar{E}_0)$-space, considering three types of vanadium ion beams and different energy spreads.

7.3 Length and temperature distributions in the $(\sigma, \bar{E}_0)$-space

After illustrating the space where the burning is possible, we proceed to show the state of the hot-spot and the heated region in the $(\sigma, \bar{E}_0)$-space. Before all else, in Fig. 7.6 we show the results for a monoenergetic beam. Although this information is repeated with the bottom panels of Fig. 5.1, we display it here again to ease the comparison with the rest of cases. Then, in Fig. 7.7 we show the analogue results for a quasi-monoenergetic beam at the edge of the plasma (G1) and in Fig. 7.8 we show the results for the same quasi-monoenergetic beams but separated from the fuel (G2). In both quasi-monoenergetic figures, three energy spreads are contemplated, $\delta E = 5\%$, 10% and 15%.

There, the isolines depicted in the $(\sigma, \bar{E}_0)$-space associated to lengths are displayed in the left panels and the isolines associated to temperatures in the right ones. In the left panel we show the range (L_h) as grey solid isolines, the length of the hot-spot (L_hs) as solid black lines and the position of the maximum temperature (x_Tmax) as blue dotted lines. For the isolines of L_h and L_hs we indicate the minor value (10 μm) and for x_Tmax we indicate the reference value of half the sphere (50 μm). The rest of the isolines are always displayed in intervals of 10 μm. In the right panel, we show the isolines associated to the temperature at the edge of the plasma ($T_\mathrm{x=0}$) as dashed grey lines, the temperature of the hot-spot (T_hs) as black solid lines and the maximum temperature (T_max) as solid grey lines. The minor value depicted of the isolines is 10 keV, and the rest of the isolines are displayed in intervals of 2 keV. As explained in Sect. 5.1, we indicate the threshold $(\sigma, \bar{E}_0)$-values where edge, intermediate and central hot-spots are found as dotted green and dashed purple lines, respectively. Edge hot-spots are found at very low energies (left of the green line), central is found in almost the entire range of $\bar{E}_0$ (at right and below of the purple line), then, the intermediate hot-spots are found between both regions.

In Sect. 5.1 we explained the general behaviour of the parameters in the monoenergetic case. In short, the length of the heated plasma (L_h) increases with both the energy of the projectiles and the flux, this is, increases with the energy of the beam ($E_\mathrm{b} = S_\mathrm{b}\sigma E_0$), although the dependence is stronger with E_0. For L_hs, the behaviour is similar in the edge and intermediate hot-spot regions, while in the central hot-spot region we find a constant value in respect to the energy. Similarly to L_hs, T_hs, the maximum temperatures (T_max) shows an almost constant behaviour in respect to the energy for intermediate and central hot-spots. At last, the solutions for x_Tmax are displayed with vertical lines, that is, the position of the maximum temperature mostly depends on E_0.

A general result of the G1 and G2 beams in respect to the monoenergetic beam is that the constant behaviour of central hot-spots in respect to E_0 is not

found any more. As before, we note that the effects of the Gaussian beam are more drastic when the energy spread is enlarged. Additionally, the lines that separate the edge, intermediate and central hot-spot regions approximately do not change in respect to the monoenergetic case.

On the one hand, when comparing the results of Fig. 7.7 (G1), with the monoenergetic case of Fig. 7.6, we find that, when an energy spread is applied, the same ranges ($L_{\rm h}$) require less energy. This was already advanced with Fig. 7.2 where we showed how the heated regions enlarged. For instance, in the monoenergetic case $L_{\rm h} = 100$ μm was found approximately at 8250$\sim$9500 MeV, while for an energy spread of $\delta E = 15\%$, the same isoline is more vertical and it is found $\sim$6700 MeV. With regard to the hot-spot length ($L_{\rm hs}$) we do not find drastic differences in the edge and intermediate hot-spot regions. However, as advanced before, in the central hot-spot region, we find how the constant behaviour shown in Fig. 7.6 disappears as the energy spread is increased. This is specially notable at low fluxes or once high enough energies are considered. In this sense, $L_{\rm hs}$ isolines are narrowed, moving towards higher fluxes for reaching the same value as in the monoenergetic scenario. We also find that the position of the maximum temperature requires higher energies with a Gaussian beam, for instance, $x_{\rm Tmax} = 50$ μm is found at 6500 MeV in Fig. 7.6, while now appears at 7500 MeV for an energy spread of $\delta E = 15\%$. We have calculated the relative differences in the $(\sigma, \bar{E}_0)$-space of G1 in respect to the monoenergetic beam. For example, when considering $\delta E = 15\%$, the ranges indicate a contrast up to a 50% between both, and up to 25% for the position of the maximum temperature. These differences depend on the parameters of the beam and depend on the region of the $(\sigma, \bar{E}_0)$-space, finding the higher discrepancies for intermediate and central hot-spots[3].

In respect to the temperatures, found in the right panel, we find that $T_{\rm x=0}$ does not change significantly, neither does $T_{\rm max}$, but this happens only in the edge hot-spot region. In the central and intermediate hot-spot regions, the isolines of $T_{\rm max}$ and $T_{\rm hs}$ also tend to narrow, tearing down any constant behaviour. This means that, for the same energy, achieving a central hot-spot with the same temperature requires now higher fluxes. For instance, at $\bar{E}_0 = 9400$ MeV, in the monoenergetic case $T_{\rm max} = 14$ keV and $T_{\rm hs} = 14$ keV, are found at $\sigma \approx 2.4 \cdot 10^{18}$ cm^{-2} and $\sigma \approx 4.3 \cdot 10^{18}$ cm^{-2}, respectively, while for an energy dispersion of $\delta E = 15\%$, they are found at $\sigma \approx 6.3 \cdot 10^{18}$ cm^{-2} and $\sigma \approx 5 \cdot 10^{18}$ cm^{-2}. When computing the relative differences between the G1

[3]We advance that the results of G1 and G2 cases are almost identical, so the relative differences between the G2 and the monoenergetic beam are equivalent to those presented for G1.

and the monoenergetic cases, we have found discrepancies up to 25% for the hot-spot temperature and up to 50% for the maximum temperature, depending on the selected $(\sigma, \bar{E}_0)$-values.

On the other hand, in Fig. 7.8 (G2) we show the solutions when considering a Gaussian beam separated from the target. As foreseen in Figs. 7.4 and 7.5, the results of the G2 case do not differ drastically from the G1 case. Still, minor differences can be found, as for instance: x_{Tmax} isolines are less vertical in the G2 beam, in such a way that, when increasing the flux, for the same $\bar{E}_0$ the position of the maximum temperature is further from the edge in the G2 case; the L_{h} isolines of the G1 scenario are mostly vertical and reach shorter ranges for larger values of $\bar{E}_0$, in comparison to the G2 case; at last, the G2 scenario reaches slightly higher hot-spot temperatures. We have also calculated the relative differences in the $(\sigma, \bar{E}_0)$-space of G2 in respect to G1. The most extreme discrepancy we have found is related to the position of the maximum temperature, up to 50% for intermediate energies and large fluxes. The range shows differences up to a 20%, but mostly negligible in all experiments. The contrast between G1 and G2 for the temperatures (T_{hs}, T_{max} and $T_{\mathrm{x=0}}$), as well as, for the radius of the hot-spot (R_{hs}), are found to be lower than 10%. The latter explains why the gain results are almost identical in Sect. 7.2 and in the following section.

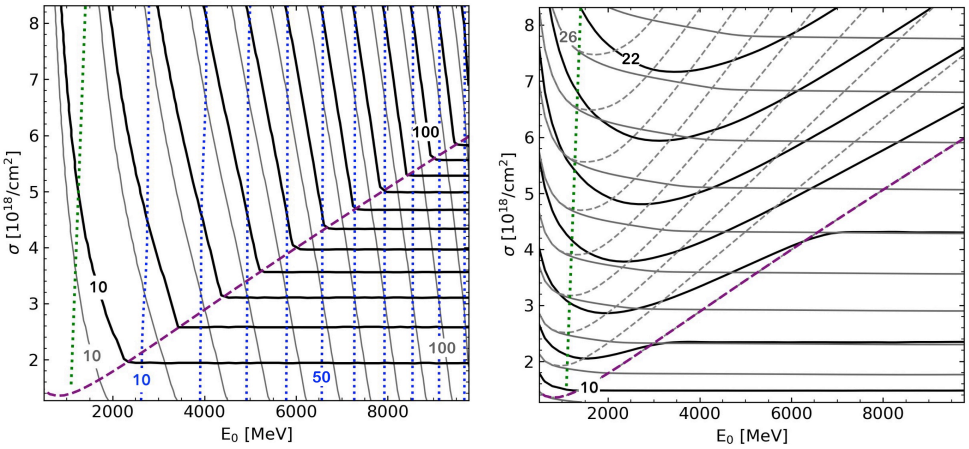

FIGURE 7.6— Isolines of the characteristic lengths (top panel, L_{h}, L_{hs} and x_{Tmax}) and temperatures (bottom panel, T_{hs}, T_{max} and $T_{\mathrm{x=0}}$) generated by monoenergetic vanadium beams in the $(\sigma, \bar{E}_0)$-space.

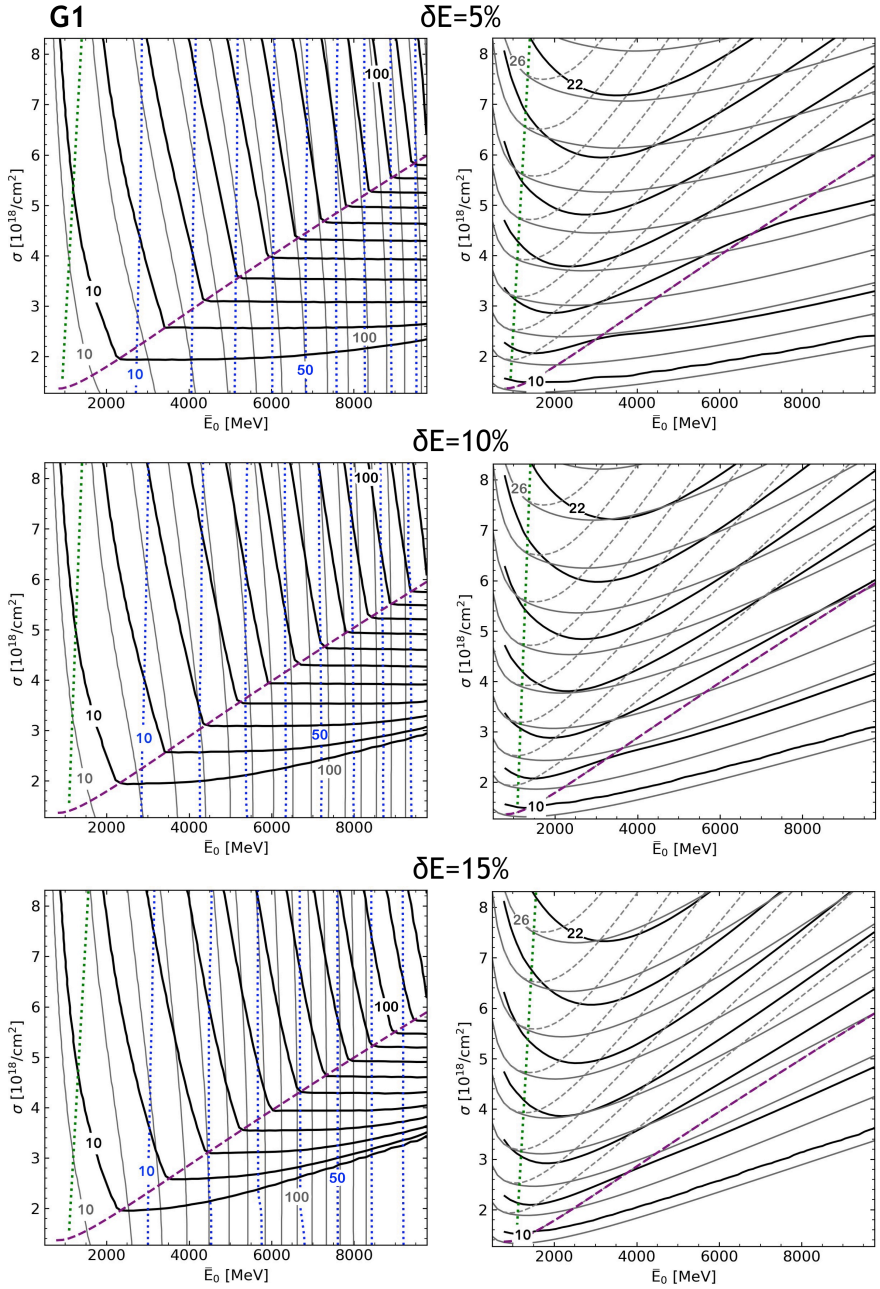

FIGURE 7.7— Similar to Fig 7.6, but considering a Gaussian ion beam generated at the edge of the plasma (G1), with $\delta E = 5\%$, 10% and 15%.

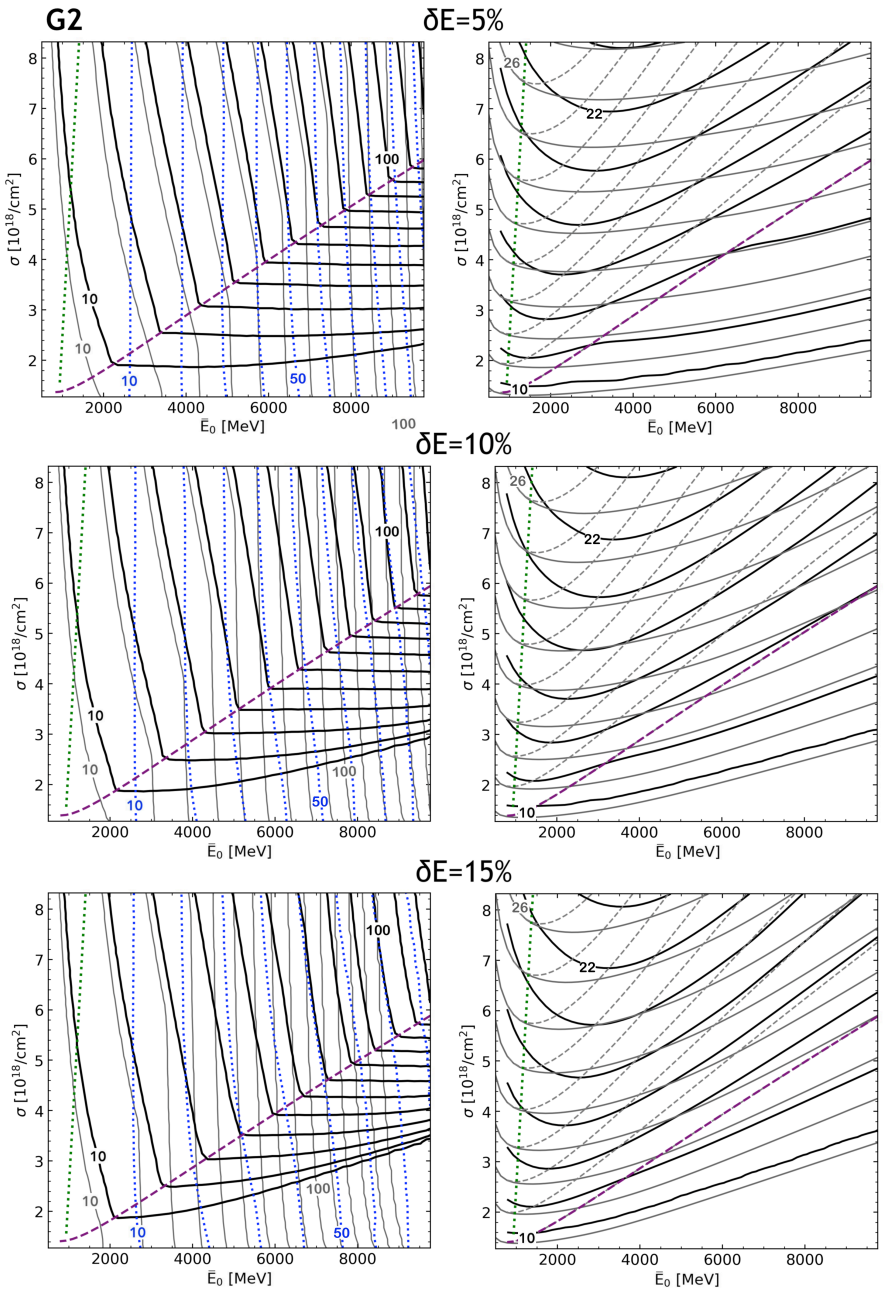

FIGURE 7.8— Similar to Fig 7.6, but considering a Gaussian ion beam generated at distance "d" from the edge of the plasma (G2), with $\delta E = 5\%$, 10% and 15%.

7.4 Burning gain and coupling results in the $(\sigma, \bar{E}_0)$-space

We also have determined the burning gains and coupling in the $(\sigma, \bar{E}_0)$-space of the same vanadium beams, as we show in Figs. 7.9 and 7.10. We consider the monoenergetic beam ($\delta E = 0\%$) and the three previous energy spreads. The DT fuel is assumed with a radius of $R_{\rm F} = 50$ μm (for calculating Eq. 3.61) and the ion beams with a radius of $r_{\rm b} = 15$ μm. The rest of the conditions of the beam and the plasma match those of Fig. 7.7. In all panels, the thick black line at low σ or low $\bar{E}_0$ represents the ignition curve (as in Fig. 7.5). In Fig. 7.9, the other black line represents the isoline of $L_{\rm h} = 100$ μm, in order to study those cases in which the range of the projectiles is less than the beam diameter. The first result we can address is the lack of significant differences between G1 and G2, either for the burning gain or the coupling. This is a consequence of finding very similar results for the hot-spot parameters between G1 and G2 (as shown in Fig. 7.7 and 7.8). We can still analyse the differences between a monoenergetic and a Gaussian beam.

In Fig. 7.9 we see that the maximum value of $G_{\rm burn}$ is in the order of 4500. The monoenergetic beam ($\delta E = 0\%$) is the one with easier access to the highest gains, which are found for $(\sigma, \bar{E}_0)$-parameters close to the ignition curve, this is either low projectile energy or flux. In comparison, for quasi-monoenergetic beams, some areas of favourable gain disappear or require larger fluxes to be achieved. As shown in Fig. 7.5, for larger energy spreads, the ignition curve becomes more confining, restricting the maximum gains to low projectile energy values. For instance, for any of the quasi-monoenergetic beams presented, it is impossible to reach a burning gain of 3500-4000 at $\bar{E}_0 = 5000$ MeV, while the monoenergetic case does have access to such gains. Additionally, the isoline of $L_{\rm h} = 100$ μm shifts towards lower energies, reducing more the region where the study is possible. If still available, same gain values are displaced to elevated fluxes when the energy spread increases. For example, at 5000 MeV, a burning gain of 2000-2500 is found at $\sigma \approx 2 \cdot 10^{18}$ cm^{-2} for the monoenergetic case and at $\sigma \approx 2.3 \cdot 10^{18}$ cm^{-2} for $\delta E = 15\%$. In this case, similar gains can be obtained if the flux is tuned to a higher value.

At last, in Fig. 7.10 we show the coupling results ($\Delta E_{\rm hs}/E_{\rm b}$). Again, for larger energy spreads, we find that the restriction of the ignition conditions makes the palette of couplings of the central hot-spot region to become more compact, with a minor displacement to higher fluxes. Aside from this, we do not find drastic changes in the results with respect to the monoenergetic beam. We could argue that the G2 case offers slightly more $(\sigma, \bar{E}_0)$-area with $\Delta E_{\rm hs}/E_{\rm b} \approx 1$, in respect to G1. This is found, for instance, when comparing the coupling of both cases at $\sigma \approx 2 \cdot 10^{18}$ cm^{-2} and $\bar{E}_0 = 2000$ MeV, for $\delta E = 15\%$.

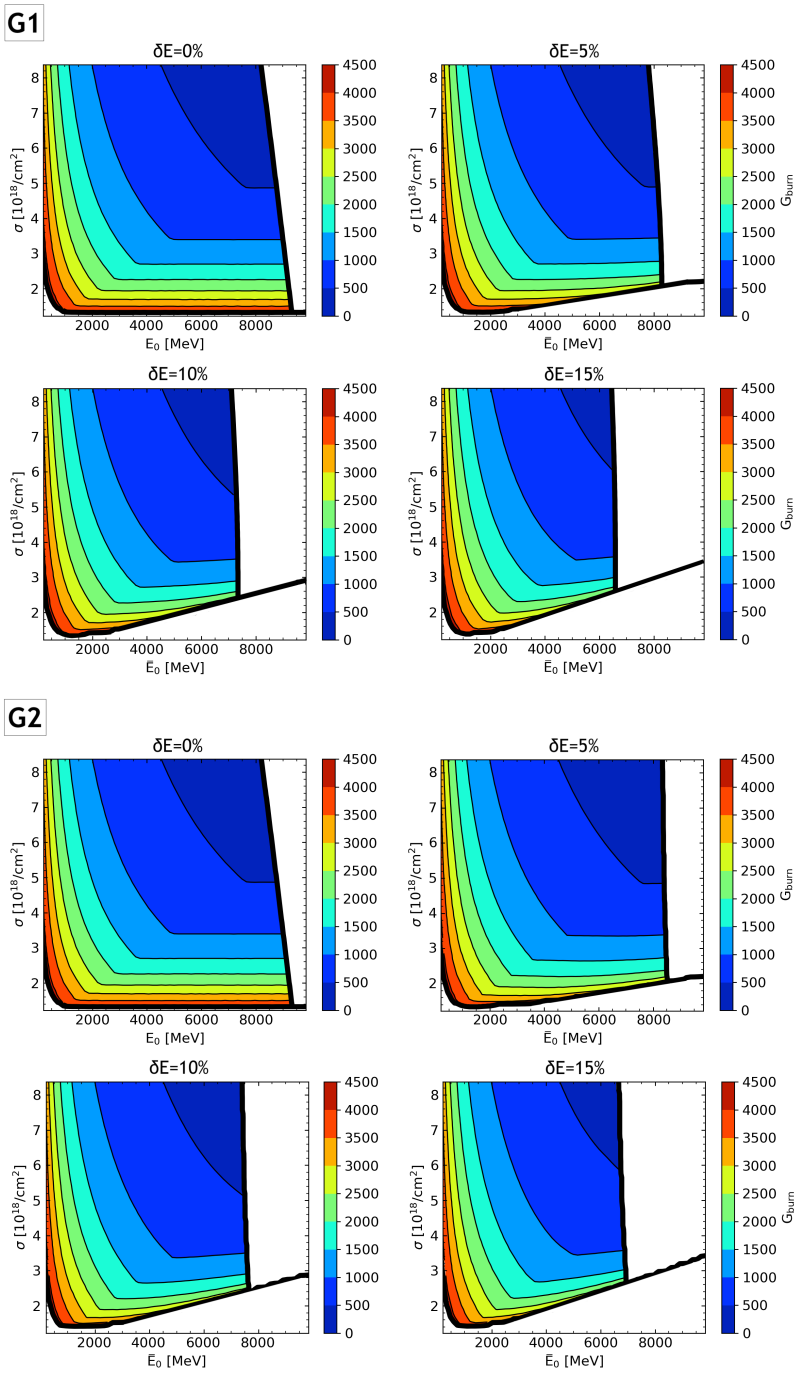

FIGURE 7.9— Burning gains in the $(\sigma, \bar{E}_0)$-space, considering a Gaussian ion beam generated at the edge of the plasma (G1) and another generated at distance "d" from the edge of the plasma (G2), with δE=0% (monoenergetic beam), 5%, 10% and 15%.

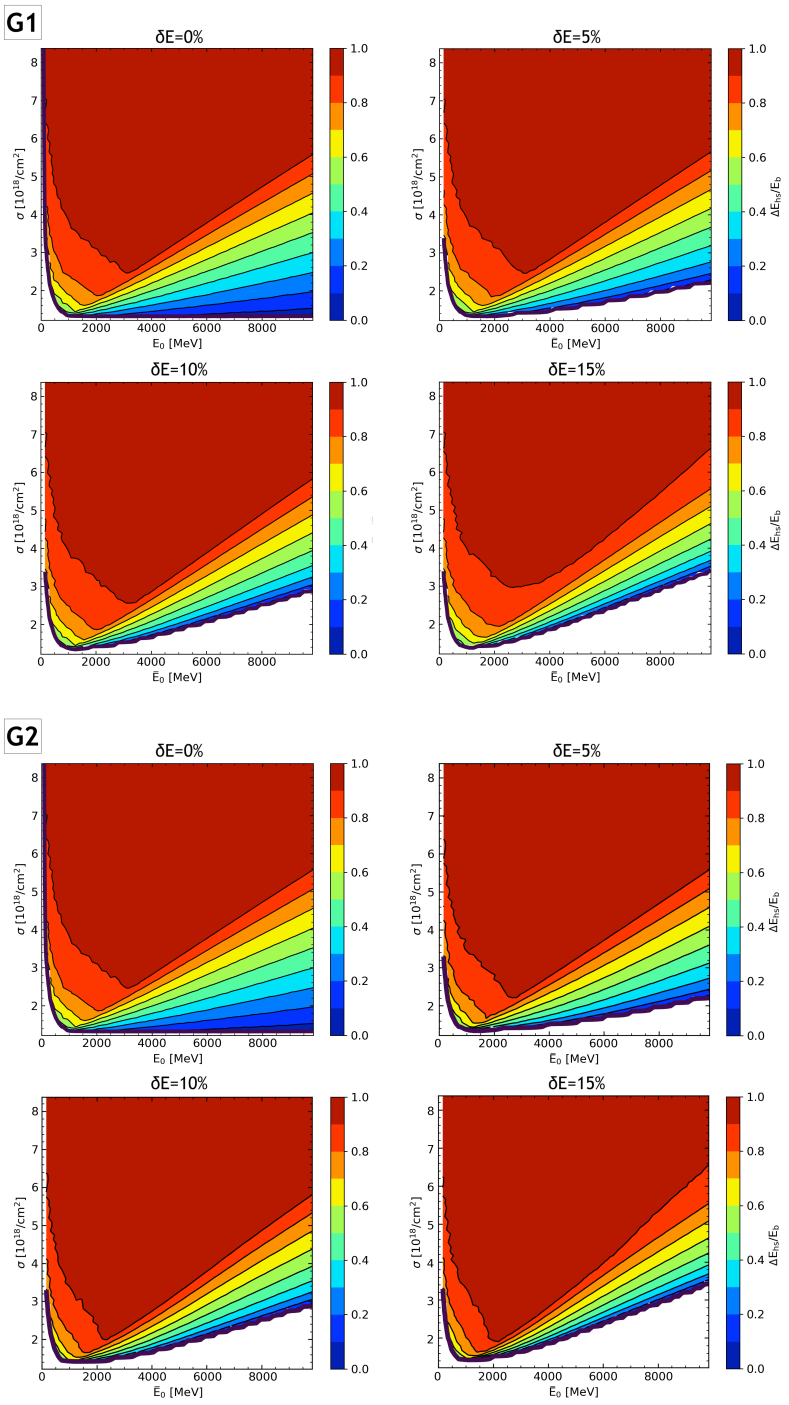

FIGURE 7.10— Coupling results in the $(\sigma, \bar{E}_0)$-space, considering a Gaussian ion beam generated at the edge of the plasma (G1) and another generated at distance "d" from the edge of the plasma (G2), with δE=0% (monoenergetic beam), 5%, 10% and 15%.

7.5 Implications of the distance between the beam source and the fuel

A particular detail that needs to be addressed is how the results of G2 are independent of the separation distance (d), as explained in Sect. 3.12. In the presence of a corona, the effect of the distance would be substantial: the farther the source is, the larger the energy losses before entering the core, even more if an energy distribution is considered. On the other hand, if the beam source is too distant from the fuel, the beam time might increase until our condition of $\tau_{\rm proc} > \tau_{\rm beam}$ and $\tau_{\rm hyd} > \tau_{\rm beam}$ is not fulfilled. In such situation would be necessary to compute the internal process taking place in the plasma simultaneously with the beam interaction. This raises the question of the maximum distance at which the beam can be colocated before our criteria is broken. To address this, we study when the beam time is equivalent to the characteristic time of the processes (as explained in Sect. 3.9.1, we take $\tau_{\rm fus,dep}$ to represent the rest). To exemplify when the distance needs to be taken into account, in Fig. 7.11, we display the threshold "d" at which $\tau_{\rm beam} = \tau_{\rm fus,dep}$, for the same experiments as in Fig. 7.8. It is found that the maximum distance corresponds to higher energies and lower fluxes, which are associated to larger beam and fusion times. As in previous experiments, increasing the energy spread magnifies the results, thus finding the shorter threshold distances for the energy spread of $\delta E = 15\%$. Note how the results range from $d \approx 0.25$ to 3 mm, which are typical values considered in the literature (e.g. Honrubia et al., 2009, 2014; Khatami & Khoshbinfar, 2020). In additional simulations we have performed, it is also found that lighter beams (p^+ or C^{6+}) requires shorter "d" values for our approximation to be valid.

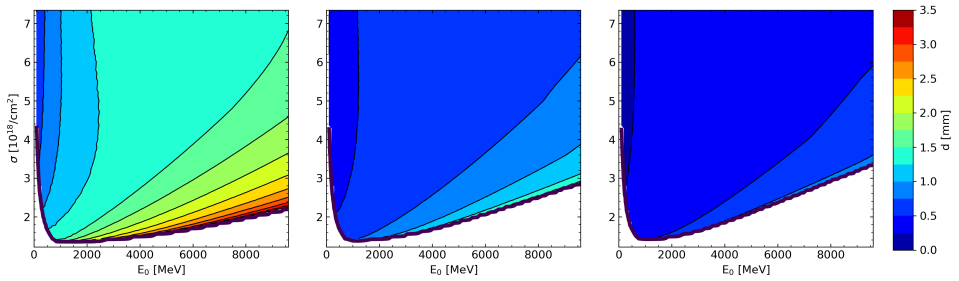

FIGURE 7.11— Threshold distance such that $\tau_{\rm beam} = \tau_{\rm fus,dep}$ for the same experiments as in Fig. 7.8.

The deductions from this chapter imply that a quasi-monoenergetic beam in general complicates the creation of a suitable hot-spot. In the $(\sigma, \bar{E}_0)$-space the region where the ignition is possible is reduced. This is due to a decrease in the maximum temperatures achieved by quasi-monoenergetic beams. Also, we find that for similar projectile energies, when a quasi-monoenergetic beam is considered, the ranges become larger and the position of the maximum temperature is found closer to the edge of the plasma. Between the G1 and G2 cases, we find similar results for all parameters. As an exception, for the same $\bar{E}_0$, the position of the maximum temperature is closer to the edge in the G1 case. When inspecting the central hot-spots in $(\sigma, \bar{E}_0)$-space, the constant behaviour of the hot-spot parameters we find with monoenergetic beams, disappears when a Gaussian energy distribution is considered for the projectiles, such that larger flux is needed for achieving the similar conditions. At last, with a quasi-monoenergetic beam, the optimal burning gains are restricted, in comparison to the monoenergetic case. In the G2 case, it is necessary to check the distance at which the source is located, in order to fulfil the conditions of $\tau_{\text{proc}} > \tau_{\text{beam}}$ and $\tau_{\text{hyd}} > \tau_{\text{beam}}$. All the discrepancies with the monoenergetic case are accentuated when the energy spread is increased.

8

Conclusions and future research

The ion fast ignition (IFI) scheme is one of the possible candidates to achieve nuclear fusion, within the inertial confinement approach. This implies applying a high energy particle beam to heat a precompressed fuel of DT. Several numerical studies have been carried out to advance the capabilities and limitations of this scheme, however, previous literature may lack a complete perspective of the process. In this context, the current research aimed to provide a systematic study of the beam-plasma interaction, considering a wide range of scenarios. Our extensive results should expand the knowledge on this topic, tackling new regimes not previously explored in a systematic way. To do so, we have developed a computational application capable of performing a massive number of simulations and an analysis of the ion beam-plasma interaction in different scenarios of interest in the IFI context. Thus, we model the state of the plasma during and just after the heating due to the beam. From this information, we foresee its capacity to achieve fuel burning. Given a specific fuel set-up, our particular approach delves into determining what beam characteristics are required to retrieve a heated plasma with certain properties. Describing the connection between the beam attributes and the resulting plasma via simulations is key for the advancement of FI. On a practical level, this allows to tune the experiment configuration in such a way that the desired outline is achieved or, conversely, given some experimental constrains, we predict the result to be found. Once the space of parameters is explored, we analyse typical experimental conditions and search for those values that optimize the outcome. To the best of our knowledge, there are no previous works that perform an analysis of this magnitude and characteristics.

The tools we have created to perform the desired systematic study include

several scenarios and free parameters. The simpler case consists of a monoenergetic ion beam interacting with a pure DT plasma without corona. Then, we can consider a plasma with corona, a plasma with impurities at different concentrations or a quasi-monoenergetic ion beam. In any of these cases, we can select the parameters of the beam and the plasma. The plasma is determined by the radius of the fuel sphere, its composition, its initial temperature and its density, the latter being not necessarily constant. The beam can have any charge, radius, flux and projectile energy, as well as energy dispersion and distance from the fuel, if considered. The modelling of the interaction includes a spatial-temporal simulation of the stopping of the beam and the heating of the plasma, returning the final field of temperatures. With this result, we perform a posterior analysis of the possibility of ignition and a preliminary estimation of the burning gain. Our computational approach is thought to massively calculate arrays with different values of the flux and the projectile energy. Hence, in order to perform the systematic study, we need to extract key characteristics from the temperature field recovered for each set of parameters. From the distribution of temperatures of the heated region we extract the range of the beam within the plasma, the mean temperature of the heated region, the maximum temperature and its position. Then, we analyse if within the heated region there is a hot-spot able to achieve ignition. If existent, such hot-spot is characterised by a length and a temperature. At last, we calculate the self-heating, ignition and burning gains, as well as the coupling between the hot-spot and the beam.

Among other results, our primal investigation considers the simplest case of a monoenergetic ion beam interacting with a pure DT plasma without corona. The rest of cases presented before (plasma with corona, doped plasma and quasi-monoenergetic beam) are studied independently, that is, only one of the three is considered, while the rest of characteristics match the simplest case. With this approach, we can study each scenario separately and differentiate the effect in the solutions. Hence, the first results to tackle are those for the reference case of a monoenergetic ion beam interacting with a pure DT plasma without corona, representing the most ideal case. We proceed to summarise the most interesting behaviours found in function of the particle flux of the beam and the energy of the projectiles. The utmost outcome we evaluate is the parameter space where it is worth performing the study, that is, mostly, the beam characteristics that achieve ignition. With our simulations, we can also determine what kind of beam will produce an edge, intermediate or central hot-spot, which can be addressed as regions of study in the flux-energy space. As previous literature already stated, we find that finding central hot-spots is easier if the charge of the beam is increased. We remind that the central hot-spots

are of special interest, as the consequent burning is more symmetric. In respect to the characteristics of the heated region, we show how the temperature and the length increase as the flux-energy parameters do. In the case of central hot-spots we find a particular scenario: the position of the maximum temperature is almost independent of the flux, so its value is tunable by the energy of the projectile. On the other hand, in the central hot-spot cases, we find that the length and temperature of the hot-spot are independent of the energy and only increase with the flux. Then, when studying the burning gain, we find that the maximum values are located close to the ignition threshold, this is, either for low fluxes or energies. In general, the burning gain increases for heavier ions of the beam and shorter radius, while for the fuel, the results improve for denser and initially colder plasmas and bigger radius of the sphere. Al last, the coupling between the hot-spot and the beam energies is found to be better as the flux and energy increase, at least for the edge and intermediate hot-spots. For the central hot-spots, the coupling worsens for high energies and low fluxes. Hence, there is a compromise between the burning gain and the coupling, if a central hot-spot is to be created.

At this point, we can evaluate the rest of scenarios in respect to the reference case we have just described. First, we analyse the implications of including a corona surrounding the core of the fuel. As expected, the projectiles suffer stopping in this preliminar plasma, so, the most remarkable result is a displacement of all results to higher energies. The general behaviour is the same as in the reference case, but the projectiles require more energy to achieve the same depth, temperature and gain. Additionally, the coupling worsens for all cases. Second, we consider the inclusion of dopants in the fuel. Among other things, this means increasing the density in respect to the pure DT plasma. When either the atomic number or the concentration of the impurity increase, the general behaviour of all magnitudes is the same, but displaced towards higher energies and fluxes, as well as reaching higher temperatures. More importantly, the inclusion of dopants makes the ignition more restrictive and limits the maximum values of the burning gain achievable, which is highly detrimental in the IFI context. Third, we simulate quasi-monoenergetic beams with a Gaussian distribution of energies, we considered two cases, one where the beam is located at the edge of the plasma (G1) and another located at a certain distance (G2). In either case, the ignition threshold becomes more restrictive, this is, beams of high projectile energy require more flux for the condition to be fulfilled. This is due to the distribution of temperatures becoming with colder and flatter, this is, with larger ranges. We find that the G1 and G2 cases do not differ drastically, returning very similar solutions. When observing the characteristics of the heated region, the values corresponding to edge and intermediate hot-

spot, are very similar between the monoenergetic and the quasi-monoenergetic beam. However, for central hot-spots, we find drastic differences in respect to the monoenergetic beam. For both G1 and G2, central hot-spot constant behaviour with energy is lost. Reaching the same conditions for the plasma requires more flux for the same projectile energy. Additionally, considering a quasi-monoenergetic beam complicates achieving the same burning gains as in the monoenergetic case: either the maximum values are not reached or the values require higher fluxes. Overall, larger energy spreads in quasi-monoenergetic beams return worsened results.

Descriptions of the behaviour extracted from the results found for each scenario, such as explained in the previous paragraph, yield a greater view on the performance of IFI depending on the conditions selected. In respect to the systematic study, we have filled some blank spaces of knowledge by widening the space of parameters studied, using various approximations. More interestingly, our focus on connecting the initial conditions and the characteristics of the beam with the state of the resulting heated plasma provides a great advantage: our work provides the capability to formulate a conceptual experiment, with some input parameters, and predict the resulting plasma state; alternatively, if the objective is to create a specific hot-spot for the fusion, we offer the needed input characteristics. These are some of the main contributions provided by the current thesis to the field.

Nevertheless, further research is badly needed in all directions to meet the requirements of a future IFI experiment, such us optimizing the production of fusion materials, the development of containers resistant to high energies and the mechanisms responsible for initiating plasma ignition. In our framework, a better theoretical examination of the beam, the plasma and their interaction would be of great use, as well as computational simulations that forecast the process with precision.

In this sense, even if this work serves as a solid foundation, we could expand even further the IFI studies and perform more realistic simulations. Future works should simulate, if necessary, more realistic experiments, considering all our computed scenarios together, this is, a doped plasma with corona and a quasi-monoenergetic beam. Another factor to improve would be the posterior evolution of the hot-spot. Currently, we preliminarily approximate the fusion success with the burning gain (which could improve with a more accurate revision), however, we could compute a more realistic simulation of the explosion. On the one hand, we could consider a zero dimensional heating model to study the interaction of ion beams with durations longer than the times characteristic of the internal plasma processes. This comes as a natural extension of the mainframe proposed in this thesis, and inspired by the works of Zou et al.

(2016); Mehrangiz (2017) and Fetsch & Fisch (2023). Thus, we combine the beam interaction with the temporal evolution of the temperature and volume of the hot-spot, as it absorbs the surrounding cold material and expands during the ignition and burning process. On the other hand, we could perform a complete 3D-temporal simulation in which we study the deposition of energy of the alpha particles within the cold plasma, thus providing a realistic description of the evolution of the sphere. The latter could be easily implementable, as we already have a code that calculates the stopping of particles, however, the computational cost would increase significantly. Another significant improvement could be:

- Considering ion beams with lifetimes on the order or shorter than the equilibrium time of the plasma. This is inspired by the articles of Badziak & Domański (2019) and Badziak & Domański (2021), in which they treat ion beam pulses of picoseconds and femtoseconds, following the line of study about the characteristic times carried out in the current thesis.

- Modelling a two-temperature plasma for its ions and electrons. This would improve the approximation in the case of a plasma without thermodynamic equilibrium.

- Tackling the scenario of hybrid ion charge beams, such as Mehrangiz & Khoshbinfar (2020) and Deng et al. (2021) propose.

- If necessary, an extension of the model to partially ionised ion beams could be implemented, allowing for a more rigorous study in the range of possibilities that this change introduces. For this purpose, it is required to develop a stopping model that takes into account the influence of the bound electrons present in the beam ions. This is, a collisional-radiative model that takes into account the time evolution of the electronic states and the number of bound electrons of the beam ions.

Furthermore, our interaction model will also benefit from plenty of potential refinements, among them, we consider: implementing non-collimated, dispersive and non-homogeneous beams; using more realistic energy distributions for the quasi-monoenergetic beams; including other configurations, such as multi-beam interaction or the presence of a re-entrant cone; computing 2D-simulations of the process and incorporating the hydrodynamic processes of the system. Although not mentioned in this thesis, our computational package is able to calculate the stopping over a plasma where the ions have bound electrons (Rodríguez-Beltrán, 2018). This would serve to study other plasmas, besides the fusion ones. In this sense, we need to estimate the atomic structure and the atomic

kinetic of the ions in the plasma by solving the set of rate equations in the collisional-radiative formalism. This calculation is performed by the MIXKIP computational package, created by our team (Espinosa et al., 2017). At last, besides to improving our physical model, in the computational sense, our code could benefit from polishing and optimization. Currently, the systematic analysis is mostly based on large arrays of projectile energy and flux. It would be of great use to enable other parameters to be calculated similarly. An endgame goal would be to release an open-source version for the public to use.

The bottom line is, through a systematic study, we offer a more general perspective on what kind of experimental conditions and beam characteristics are necessary to bring the plasma to a desired state of fusion. Currently, Fast Ignition is not the most popular approach in the path for achieving nuclear fusion. However, it is absolutely necessary to explore any viable option, in order to learn enough and assure the better alternative is found. In this context, we hope the contents of this thesis serve as a spark for the community, to continue future investigations towards the noble purpose of finding a clean energy source for this planet.

Scientific Production

Publications

- Pablo R. Beltrán, Juan Miguel Gil, Rafael Rodríguez, Guadalupe Espinosa (2023). "Beam-plasma interaction in fast ignition nuclear fusion: Hot-spot properties and gains for different initial plasma temperatures." *Nuclear Instruments and Methods in Physics Research Section B: Beam Interactions with Materials and Atoms.* Elsevier. DOI:https://doi.org/10.1016/j.nimb.2023.07.007

- Pablo R. Beltrán, Juan Miguel Gil, Rafael Rodríguez, Guadalupe Espinosa (2019). "Simulation of the ion beam-plasma interaction processes for point-like ions in doped DT plasmas." *X-Ray Spectrometry.* Wiley Online Library. DOI:10.1002/xrs.3083

- Juan Miguel Gil, Pablo R. Beltrán, Rafael Rodríguez, Guadalupe Espinosa (2023). "Simulation and characterization of hot spots generated in deuterium–tritium plasma by fast quasi-monoenergetic ion beams." *Nuclear Instruments and Methods in Physics Research Section B: Beam Interactions with Materials and Atoms* Elsevier. DOI:10.1016/j.nimb.2023.03.035

- Guadalupe Espinosa, Juan Miguel Gil, Rafael Rodríguez, Pablo R. Beltrán (2023). "Analytical model for the temperature field of a plasma heated by fast and monoenergetic ion beams." *Nuclear Instruments and Methods in Physics Research Section B: Beam Interactions with Materials and Atoms.* Elsevier. DOI:10.1016/j.nimb.2023.06.017

- Rafael Rodríguez, Guadalupe Espinosa, Juan Miguel Gil, Pablo R. Beltrán (2018). "Monochromatic and mean radiative properties of astrophysical plasma mixtures in nonlocal thermodynamic equilibrium regime." *X-Ray Spectrometry.* Wiley Online Library. DOI:10.1002/xrs.2997

- Juan Miguel Gil, Pablo R. Beltrán, Rafael Rodríguez, Guadalupe Espinosa (2018). "Bound electron stopping power model of partially stripped ions in partially ionized plasmas." *X-Ray Spectrometry.* Wiley Online Library. DOI:10.1002/xrs.3116

- Juan Miguel Gil, Rafael Rodríguez, Guadalupe Espinosa, Pablo R. Beltrán (2019). "Simulation of Plasma Microscopy Properties and Ion Beam-Plasma Interaction Processes In Plasmas by Using Mixkip/Rapcal/Stopp Code." *International Journal of Computational Methods.* World Scientific. DOI:10.1142/S0219876219400097

- Rafael Rodríguez, Guadalupe Espinosa, Juan Miguel Gil, Pablo R. Beltrán (2019). "Generation and Parametrization of Mean Plasma Radiative Properties Databases for Astrophysics and Nuclear Fusion Applications." *International Journal of Computational Methods.* World Scientific. DOI:10.1142/S0219876219400036

- Juan Miguel Gil, Rafael Rodríguez, Guadalupe Espinosa, Pablo R. Beltrán (2018). "Computational Package for the Simulation of Plasma Microscopy Properties and Ion Beam-Plasma Interaction in High Energy Density Plasmas." *Proceedings of the International Conference on Computational Methods* Vol: 5, pags: 454-466. Scientech Publisher LLC. ISSN:2374-3948

Conferences

- P. R. Beltrán, J.M. Gil, R. Rodríguez and G. Espinosa. Effects of impurities in DT plasmas on burning gains and self-heating and ignition curves in ion fast ignition scheme. Poster. International Symposium on fusion nuclear technology (ISFNT15). Las Palmas de Gran Canaria. 10-15, September, 2023.

- J.M. Gil, P. R. Beltrán, R. Rodríguez and G. Espinosa. Characterization of hot spots generated in DT plasmas by fast quasi-monoenergetic ion beams: self-heating/igniton curves and burning. Poster. International Symposium on fusion nuclear technology (ISFNT15). Las Palmas de Gran Canaria. 10-15, September, 2023.

- P. R. Beltrán, J.M. Gil, R. Rodríguez and G. Espinosa. Beam-plasma interaction in fast ignition nuclear fusion: hot-spot gains for different initial conditions. Poster. ICACS & SHIM 2022. Helsinki, Finlandia. 19-24, June, 2022.

- Espinosa Vivas, Guadalupe, Gil de la Fe, Juan Miguel, Rodríguez Pérez, Rafael, Rodríguez Beltrán, Pablo. Analytical model for the temperature field of a plasma heated by fast and monoenergetic ion beams. Poster. ICACS & SHIM 2022. Helsinki, Finlandia. 19-24, June, 2022.

- Juan Miguel Gil de la Fe, Rafael Rodríguez Pérez, Guadalupe Espinosa Vivas, Pablo Rodríguez Beltrán. MIXKIP/STOPP: an atomic kinetics and ion transport computational package for the simulation of the ion beam-plasma interaction processes in high energy density plasmas. Poster. The 27th International Conference on Atomic Physics. Toronto, Canada. 17-22, July, 2022.

- P. R. Beltrán, J.M. Gil, R. Rodríguez and G. Espinosa. Simulation of ion beam-plasma interaction processes for point-like ions in partially ionized plasmas. Poster. 19th International Conference Physics of Highly Charged Ions (HCI-2018). NOVA School of Science and Technology (FCT NOVA), Lisboa, Portugal. 3-7, September, 2018.

- J.M. Gil, P. R. Beltrán, R. Rodríguez and G. Espinosa. Calculations of stopping power of partially stripped ions in partially ionized plasmas. Poster. 19th International Conference Physics of Highly Charged Ions (HCI-2018). NOVA School of Science and Technology (FCT NOVA), Lisboa, Portugal. 3-7, September, 2018.

- R. Rodríguez, G. Espinosa, J.M. Gil and P. R. Beltrán. Monochromatic and mean radiative properties of astrophysical plasma mixtures in non-local thermodynamic equilibrium regime. Poster. 19th International Conference Physics of Highly Charged Ions (HCI- 2018). NOVA School of Science and Technology (FCT NOVA), Lisboa, Portugal. 3-7, September, 2018.

References

Afshari, M., Hornung, J., Kleinschmidt, A., et al. 2020, AIP Advances, 10

Alam, M. S. 2013, Dust-Ion-Acoustic Waves in Dusty Plasmas with Superthermal Electrons

Aristotle, A. & Aristotle. 1933, Metaphysics, Vol. 1 (Harvard University Press Cambridge, MA)

Atzeni, S. 1999, Physics of plasmas, 6, 3316

Atzeni, S. & Caruso, A. 1984, Nuovo Cim., B, 80, 71

Atzeni, S. & Meyer-Ter-Vehn, J. 2004, The Physics of Inertial Fusion: Beam-Plasma Interaction, Hydrodynamics, Hot Dense Matter (Oxford: Oxford University Press)

Atzeni, S. & Tabak, M. 2005, Plasma Phys Control Fusion, 47, B769

Atzeni, S., Temporal, M., & Honrubia, J. 2002, Nuclear fusion, 42, L1

Badziak, J. & Domański, J. 2019, Laser and Particle Beams, 37, 288

Badziak, J. & Domański, J. 2021, Nuclear Fusion, 61, 046011

Barbarino, M. 2020, Nature Physics, 16, 890

Beltran, P., Gil, J., Rodriguez, R., Espinosa, G., & Barriga-Carrasco, M. 2020, X-Ray Sepctrom, 49, 173

Bethe, H. 1930, Annalen der Physik, 5, 325

Betti, R. & Zhou, C. 2005, Physics of plasmas, 12

Betti, R., Zhou, C., Anderson, K., et al. 2007, Physical review letters, 98, 155001

Bodansky, D. 2007, Nuclear energy: principles, practices, and prospects (Springer Science & Business Media)

Bohm, D. & Pines, D. 1951, Physical Review, 82, 625

Bohm, D. & Pines, D. 1953, Physical Review, 92, 609

Bosch, H. & Hale, G. 1992, Nucl Fusion, 32, 611

Brown, L. S., Preston, D. L., & Singleton Jr, R. L. 2005, Physics Reports, 410, 237

Campbell, E., Sangster, T., Goncharov, V., et al. 2021, Philosophical Transactions of the Royal Society A, 379, 20200011

Cayzac, W. 2013, PhD thesis, Université Sciences et Technologies-Bordeaux I

Chadwick, J. 1932, Nature, 129, 312

Char, N. & Csik, B. 1987, IAEA bulletin, 3, 1987

Chu, P. K. & Lu, X. 2013, Low temperature plasma technology: methods and applications (CRC press)

Committee, P. S., Council, N. R., et al. 1995, Plasma science: from fundamental research to technological applications (National Academies Press)

Cornford, F. M. 2014, Plato's cosmology: the Timaeus of Plato (Routledge)

Craxton, R., Anderson, K., Boehly, T., et al. 2015, Physics of Plasmas, 22

Crookes, W. 1879, American Journal of Science, 3, 241

Dalton, J. 1817, A new system of chemical philosophy, Vol. 1 (Weale)

Davis, J., Petrov, G., & Mehlhorn, T. 2011, Plasma Physics and Controlled Fusion, 53, 045013

Debayle, A., Honrubia, J., Dhumseres, E., & Tikhonchuk, V. 2010, Phys Rev E, 82, 036405

Denavit, J. 1992, Physical Review Letters, 69, 3052

Deng, H., Shao, F., Zou, D., et al. 2021, Physics of Plasmas, 28

Destrée, P. 2003, L'Antiquité Classique, 72, 318

Duderstadt, J. J. & Moses, G. A. 1982

Durant, W. 2011, Our Oriental Heritage: The Story of Civilization, Volume I, Vol. 1 (Simon and Schuster)

Eddington, A. S. 1979, in A Source Book in Astronomy and Astrophysics, 1900–1975 (Harvard University Press), 281–290

Esirkepov, T. Z., Bulanov, S., Nishihara, K., et al. 2002, Physical review letters, 89, 175003

Espinosa, G., Rodriguez, R., Gil, J., et al. 2017, Phys Rev E, 95, 033201

Espinosa-Vivas, G., Gil, J., Rodriguez, R., & Rodriguez-Beltran, P. 2023, Nucl Instr Meth B, 542, 230

Fernandez, JC Albright, B., Beg, F., Foord, ME Hegelich, B., et al. 2014, Nucl Fusion, 54, 054006

Fernandez, J., Honrubia, J., Albright, B., et al. 2009, Nucl Fusion, 49, 065004

Fetsch, H. & Fisch, N. J. 2023, Physical Review E, 108, 045206

Fraley, G., Linnebur, E., Mason, R., & Morse, R. 1974, Phys Fluids, 17, 474

Frank Fleschner. 2023, Wendelstein 7-X reaches milestone: Power plasma with gigajoule energy turnover generated for eight minutes, `https://www.ipp.mpg.de/5322229/01_23`, [Online; accessed 22 February 2023]

Freidberg, J. P. 2008, Plasma physics and fusion energy (Cambridge university press)

Fuentes, C. D. E. 2018, Proyecto Final de Carrera, Universidad Politécnica de Madrid

Gasparyan, O., Gus'kov, S. Y., Illin, D., Sherman, V., & Zmitrenko, N. 2013, J Russ Laser Res, 34, 33

Gauthier, M., Blancard, C., Chen, S., et al. 2013, High Energy Density Physics, 9, 488

Gil, J., Rodriguez-Beltran, P., Rodriguez, R., & Espinosa-Vivas, G. 2023, Nucl Instr Meth B, 540, 7

Green, J., Ovchinnikov, V., Evans, R., et al. 2008, Physical review letters, 100, 015003

Guo, Z. 2023

Gus'kov, S., Il'in, D., & Sherman, V. 2014a, Plasma Phys Rep, 40, 572

Guskov, S., Krokhin, O., & Rozanov, V. 1976, Nuc Fusion, 16, 957

Gus'kov, S., Zmitrenko, N., Il'in, D., & Sherman, V. 2014b, J Exp Theor Phys, 119, 958

Gus'kov, S., Zmitrenko, N., Il'in, D., & Sherman, V. 2015, Plasmas Phys Rep, 41, 725

Gus' kov, S. Y., Demchenko, N., Zmitrenko, N., et al. 2017, Journal of Russian Laser Research, 38, 173

Gus' kov, S. Y., Zmitrenko, N., Il'in, D., et al. 2009, Plasma physics reports, 35, 709

Gus'kov, S., Il'in, D., & Sherman, V. 2011, Plasma Phys Rep, 37, 1020

Gus'kov, S. & Sherman, V. 2016, J Exp Theor Phys, 123, 363

Gus'kov, S. Y., Il'in, D., Limpouch, J., Klimo, O., & Sherman, V. 2010, Plasma Physics Reports, 36, 473

Hegelich, B., Jung, D., Albright, B., et al. 2011, Nuclear Fusion, 51, 083011

Hegelich, B. M., Albright, B., Cobble, J., et al. 2006, Nature, 439, 441

Honrubia, J., Fernandez, J., Hegelich, B., Murakami, M., & Enriquez, C. 2014, Laser Part Beams, 32, 419

Honrubia, J., Fernández, J., Temporal, M., Hegelich, B., & Meyer-ter Vehn, J. 2009, Physics of Plasmas, 16

Honrubia, J. & Murakami, M. 2015, Phys Plasmas, 22, 012703

Hu, S., Nichols, K., Shaffer, N., et al. 2024, Physics of Plasmas, 31

ITER. 2023, On the road to ITER: Milestones, `https://www.iter.org/proj/ITERMilestones`, last updated: 22 December 2023

Jung, D., Albright, B., Yin, L., et al. 2013a, New Journal of Physics, 15, 123035

Jung, D., Gautier, C., Johnson, R., et al. 2012, in APS Division of Plasma Physics Meeting Abstracts, Vol. 54, NO7–007

Jung, D., Yin, L., Albright, B., et al. 2013b, New Journal of Physics, 15, 023007

Jung, D., Yin, L., Albright, B. J., et al. 2011, Physical Review Letters, 107, 115002

Kamenetskii, D. A. F. 1972, Plasma: The Fourth State of Matter (MacMillan)

Keçebaş, A. & Kayfeci, M. 2019, in Solar Hydrogen Production (Elsevier), 3–29

Kemp, A. & Divol, L. 2012, Phys Rev Lett, 109, 195005

Khatami, S. & Khoshbinfar, S. 2020, Chinese Journal of Physics, 66, 620

Kidder, R. 1976, Nucl Fusion, 16, 405

King, M., Wilson, R., Bacon, E. F., et al. 2023, The European Physical Journal A, 59, 132

Kodama, R., Norreys, P., Mima, K., et al. 2001, Nature, 412, 798

Langmuir, I. 1928, Proceedings of the National Academy of Sciences, 14, 627

Li, C. & Petrasso, R. 1993a, Phys Rev Lett, 70, 3059

Li, C. & Petrasso, R. 1993b, Phys Rev Lett, 70, 3063

Liseikina, T. & Macchi, A. 2007, Applied physics letters, 91

Macchi, A., Cattani, F., Liseykina, T. V., & Cornolti, F. 2005, Physical review letters, 94, 165003

Maynard, G. 1987, PhD thesis, Universite de Paris-Sud

McCrory, R., Bahr, R., Betti, R., et al. 2001, Nuclear fusion, 41, 1413

Mehlhorn, T. 1980, Sandia National Laboratories

Mehlhorn, T. A. 1981, Journal of Applied Physics, 52, 6522

Mehrangiz, M. 2017, International Journal of Advanced Research in Science, Engineering and Technology, 4

Mehrangiz, M. & Khoshbinfar, S. 2020, Contributions to Plasma Physics, 60, e201900061

Miley, G. 1982, in Unconventional Approaches to Fusion (Springer), 397–415

MIT. 2004, Helium-3 neutron proportional counters, `http://web.mit.edu/8.13/www/JLExperiments/38/tgm-neutron-detectors.pdf`, rchived from the original (PDF) on 21 November 2004

Mitchell, M. 2023, Physical World

Moynihan, M. & Bortz, A. B. 2023, in Fusion's Promise: How Technological Breakthroughs in Nuclear Fusion Can Conquer Climate Change on Earth (And Carry Humans To Mars, Too) (Springer), 175–205

Nezam, Z. Z., Ghasemizad, A., & Khoshbinfar, S. 2020, Nuclear Instruments and Methods in Physics Research Section A: Accelerators, Spectrometers, Detectors and Associated Equipment, 969, 164050

Nuckolls, J., Wood, L., Thiessen, A., & Zimmerman, G. 1972, Nature, 239, 139

'Nuclear fusion', Wikipedia contributors. 2024, Nuclear fusion — Wikipedia, The Free Encyclopedia, [Online; accessed 6-May-2024]

Peter, T. 1991, Phys. Rev. A, 43, 1998

Peter, T. & Meyer-ter Vehn, J. 1991, Physical Review A, 43, 2015

Piel, A. 2010, Plasma Physics

Pines, D. & Bohm, D. 1952, Physical Review, 85, 338

Pohle, W. 1971, Isis, 62, 36

Rhodes, R. 2012, The making of the atomic bomb (Simon and Schuster)

Ribeyre, X., Tikhonchuk, V., Breil, J., Lafon, M., & Le Bel, E. 2011, Physics of Plasmas, 18

Robinson, A., Zepf, M., Kar, S., Evans, R., & Bellei, C. 2008, New J Phys, 10, 013021

Rodríguez-Beltrán, P. 2018, Master's thesis

Roth, M. 2009, Plasma Phys Contr Fusion, 51, 014004

Roth, M., Bedacht, S., Busold, S., et al. 2014, in IPAC2014 conference 15-20 June

Roth, M., Cowan, T., Key, M., et al. 2001, Phys. Rev. Lett., 86, 436

Roth, M. & Schollmeier, M. 2017, arXiv preprint arXiv:1705.10569

Rubel, M. 2019, Journal of Fusion Energy, 38, 315

Rutherford, E. 1911, The London, Edinburgh, and Dublin Philosophical Magazine and Journal of Science, 21, 669

Rutherford, E. 1919, The London, Edinburgh, and Dublin Philosophical Magazine and Journal of Science, 37, 581

Schwoerer, H., Pfotenhauer, S., Jäckel, O., et al. 2006, Nature, 439, 445

Segre, E. G. 1989, Physics today, 42, 38

Shang, W., Betti, R., Hu, S., et al. 2017, Physical review letters, 119, 195001

Shea, D. A. & Morgan, D. L. 2010, The helium-3 shortage: Supply, demand, and options for congress, Vol. 22 (Congressional Research Service Washington, DC)

Spitzer, L. 1951, A proposed stellarator, Tech. rep., Princeton Univ., NJ Forrestal Research Center

Spitzer, L. 1962, Physics of Fully Ionized Gases (New York: John Wiley and Sons)

Stacey, W. 2010, The quest for a fusion energy reactor: an insider's account of the INTOR Workshop (Oxford University Press)

Stacey, W. M. 2018, Nuclear reactor physics (John Wiley & Sons)

Tabak, M. & Callaham-Miller, D. 1998, Nucl Instr Meth, 415, 75

Tabak, M., Hammer, J., Glinsky, M., et al. 1994, Phys Plasmas, 1, 1626

Tabak, M., Hinkel, D., Atzeni, S., Campbell, E. M., & Tanaka, K. 2006, Fusion science and technology, 49, 254

Tabak, M., Norreys, P., Tikhonchuk, V., Tanaka, K., et al. 2014, Nucl. Fusion, 54, 54001

Tao, T., Zheng, G., Jia, Q., Yan, R., & Zheng, J. 2023, High Power Laser Science and Engineering, 11, e41

Temporal, M. 2006, Physics of plasmas, 13

Theobald, W., Betti, R., Stoeckl, C., et al. 2008, Physics of Plasmas, 15

Thomson, J. J. 1897, The London, Edinburgh, and Dublin Philosophical Magazine and Journal of Science, 44, 293

Vasaru, G. 1993, Tritium isotope separation (CRC press)

Waltham, C. 2002, arXiv preprint physics/0206076

Whitlock, J. 2010, Canadian Nuclear FAQ. Retrieved, 09

Wilson, Tom and Hancock, Alice. 2023, US scientists repeat fusion power breakthrough, `https://www.ft.com/content/a9815bca-1b9d-4ba0-8d01-96ede77ba06a`, online; accessed: 6 August 2023

Woodward, A. 2022, Nuclear-Fusion Breakthrough Accelerates Quest to Unlock Limitless Energy Source, online; accessed: 13 December 2022

World-Nuclear-News. 2023, ITER delays revision of project's timeline, `https://www.iter.org/proj/ITERMilestones`, online; accessed: 27 December 2023

Yin, L., Albright, B., Hegelich, B., & Fernández, J. 2006, Laser and Particle Beams, 24, 291

Žáková, B. M. 2015

Zel'dovich, Y. B. & Raizer, Y. P. 2001, Physics of schock waves and high-temperature hydrodynamic phenomena (New York: Dover publications)

Zou, D., Hu, L., Wang, W., et al. 2016, High Energy Density Phys, 18, 1